



# SENS4ICE

SENSORS AND CERTIFIABLE HYBRID ARCHITECTURES  
FOR SAFER AVIATION IN ICING ENVIRONMENT

## Final report on hybrid ice detection development

### SENS4ICE Deliverable D4.2

Lead beneficiary (organisation):	SAFRAN Aerosystems
Document manager	A. Orazzo
Actual submission date:	06 FEB 2024
Dissemination level	Public
Grant Agreement number:	824253
Project acronym:	SENSE4ICE
Project title:	SENSors and certifiable hybrid architectures FOR safer aviation in ICing Environment
Funding scheme:	Research and Innovation Action
Project coordinator:	DLR (German Aerospace Center)
Project website:	<a href="http://www.sens4ice-project.eu">www.sens4ice-project.eu</a>



This project has received funding from the European Union's Horizon 2020 research and innovation programme under grant agreement No 824253.



<b>File name</b>	<b>SENS4ICE_D4.2_Final_report_on_HIDS_development_Safran_20240201.docx</b>
------------------	--

## APPROVALS

Role	Name	Organisation	Date
Coordinator	Schwarz	DLR	2024/Jan/29
WP leader	Deiler	DLR	2023/Dec/14
Task leader	Orazio	SAFRAN Aerosystems	2023/Dec/13
Other (quality)	Behrendt	L-UP	2023/Dec/18

## DOCUMENT HISTORY

Version	Date	Modification	Author
V1	12 SEP 2023	Evaluation of IID; Conclusions	Deiler
V2	22 SEP 2023	FT overview; Evaluation of HIDS; Conclusions	Orazio & Thillays
V3	20 NOV 2023	Final Version after Revisions	Orazio, Thillays & Deiler
V4	18 DEC 2023	Quality review	Behrendt

## LIST OF AUTHORS

Name	Organisation
SAFRAN Aerosystems	Annagrazia Orazio
SAFRAN Aerosystems	Bruno Thillays
DLR	Christoph Deiler

## DISTRIBUTION LIST

This deliverable report is public.





## TABLE OF CONTENTS

Executive summary .....	14
1. Overview on SENS4ICE Flight Test campaigns .....	14
1.1 North America FT campaign .....	14
1.2 European FT campaign .....	17
2. Evaluation of Indirect Ice Detection algorithm .....	21
2.1 Indirect Ice Detection Algorithm .....	21
2.2 IID implementation .....	24
2.3 IID results for North America FT campaign .....	29
2.4 IID results for European FT campaign .....	44
2.5 Ways forward for Indirect Detection algorithm .....	85
3. Evaluation of Hybrid Ice Detection System .....	86
3.1 HIDS general description .....	86
3.2 HIDS results for North America FT campaign .....	88
3.3 HIDS results for European FT campaign .....	98
3.4 Ways forward for HIDS .....	115
4. Conclusions .....	116
5. References .....	117

## GLOSSARY

Acronym	Signification
A/C	Aircraft
AIP	Atmospheric Icing Patch
AMPERA	Atmospheric Measurement of Potential and Electric field on Aircraft
BCPD	Back-scatter Cloud Probe with Polarization Detection
CER	Contrôle Essais Réception / Dedicated ATC for tests & acceptance
CM2D	Cloud Multi-Detection Device
CCP	Cloud Combination Probe
DID	Direct Ice Detection
DIDS	Direct Ice Detections Sensor
FDAU	Flight Data Acquisition Unit
FL	Flight Level





FOD	Fiber Optic Detector
FT	Flight Test
FTI	Flight Test Instrumentation
HIDS	Hybrid Ice Detection System
HSI	High Speed Imager
IAGOS	In-service Aircraft for a Global Observing System
IAR	Ice Accretion Rate
IC	Icing Condition
ICD	Ice Crystal Detector
IDS	Collins Ice Differentiator System
IID	Indirect Ice Detection
IPS	Ice Protection Systems
L	litre
LAS	Large aspherical particles
LILD	Local Ice Layer Detector
LWC	Liquid Water Contents
MVD	Median Volume Diameter
PC	Personal Computer
PFIDS	Primary In-Flight Ice Detection Sensor
PIP	Precipitation Imaging Probe
SAFIRE	Service des avions français instrumentés pour la recherche en environnement (French facility for airborne research)
SAT	Static Air Temperature
SRP	Short Range Particulate
TAS	True Airspeed
TAT	Total Air Temperature
TRL	Technology Readiness Level
TWC	Total Water Content
UAV	Unmanned Aerial Vehicle
UTC	Coordinated Universal Time
wrt	With Respect To
$\mu$ P	microPhysics



## TABLE OF FIGURES

Figure 1: Phenom 300 instrumented for North America FT campaign (image Embraer/ SENS4ICE project).....	15
Figure 2: Basic HIDS architecture for North America Flight tests. ....	16
Figure 3: North America flight campaign ground tracks (image DLR/ SENS4ICE project)....	16
Figure 4: Safire ATR 42 instrumented for European FT campaign (image DLR/ SENS4ICE project) .....	17
Figure 5: Basic HIDS architecture for European Flight tests. ....	18
Figure 6: European flight campaign ground tracks (image Safire, Map data from OpenStreetMap/ SENS4ICE project).....	19
Figure 7: Expected icing influence on aircraft aerodynamics (lift and drag coefficient); adapted from [11].....	21
Figure 8: Measured aircraft performance variation based on dynamic Phenom 300 flight test data throughout a large flight envelope (2.2 million data points): estimated drag polar and convex hulls ( $P_{90}$ , $P_{99}$ , $P_{99.9}$ & $P_{100}$ ).....	23
Figure 9: Measured aircraft performance variation based on ATR 42 flight test data at several flight conditions (1.45 million data points): estimated drag polar and convex hulls ( $P_{90}$ , $P_{99}$ , $P_{99.9}$ & $P_{100}$ ). .....	23
Figure 10: Basic principle of the IID method based on the aircraft power imbalance. ....	23
Figure 11: Visualization of HIDS concept used within SENS4ICE (pictures credit DLR/ Embraer/ Safire/ SENS4ICE project). ....	24
Figure 12: Aircraft drag polar for Phenom300 prototype used for the SENS4ICE North America icing flight test campaign: calculated lift and drag coefficient from flight test data ( <b>blue dots</b> ), pre-campaign reference drag polar ( <b>gray line</b> , no SENS4ICE aircraft modification) and adapted campaign reference drag polar considering aircraft modifications ( <b>magenta line</b> ); clean air flight test data with aircraft in final configuration with all modification required for SENS4ICE in February 2023. ....	27
Figure 13: Aircraft drag polar for Safire ATR 42-320 (MSN78) used for the SENS4ICE European icing flight test campaign: calculated lift and drag coefficient from flight test data ( <b>blue dots</b> ), pre-campaign reference drag polar ( <b>gray line</b> , no SENS4ICE aircraft modification) and adapted campaign reference drag polar considering aircraft modifications ( <b>magenta line</b> ); clean air flights in final aircraft configuration with all modification required for SENS4ICE on March 22nd and 23rd, 2023..	27
Figure 14: Flight track from SENS4ICE North America icing campaign flight on February 23rd, 2023 (Chicago O'Hare, KORD, to St. Louis Regional Airport, KALN): geodetic position and altitude with indication of icing encountered. ....	29
Figure 15: Time history of IID system performance during specific icing encounter from the first example flight (February 23 <sup>rd</sup> , 2023, 17:41:49 UTC to 17:55:29 UTC): altitude and indicated airspeed (top), nominal drag estimation and IID detection output (second plot), and MVD and LWC of encountered icing conditions (third plot), and static air temperature and average engine fan speed (bottom); detection threshold at 10% relative drag increase.....	31
Figure 16: Time history of IID system performance during specific icing encounter from the first example flight (February 23 <sup>rd</sup> , 2023, 18:00:19 UTC to 18:11:39 UTC): altitude and indicated airspeed (top), nominal drag estimation and IID detection output (second plot), and MVD and LWC of encountered icing conditions (third plot), and static air temperature and average engine fan speed (bottom); detection threshold at 10% relative drag increase.....	32
Figure 17: Aircraft drag polar from SENS4ICE North America icing campaign flight on February 23rd, 2023 from Chicago O'Hare to Alton: calculated lift and drag coefficient from flight data measurements and drag polar reference (red line) for the Phenom300 prototype with SENS4ICE modifications (high-lift devices and gear retracted); drag coefficient data including the indication of nominal drag estimation calculated by IID. ....	33
Figure 18: Aircraft drag polar from example flight (selected data from Figure 17): calculated lift and drag coefficient from flight data measurements and reference for the Phenom300 prototype (red line) with SENS4ICE modifications; data excluding high engine fan speeds ( $N_1$ ) and significant negative	



temperature offsets  $\Delta ISA$ ; drag coefficient data including the indication of nominal drag estimation calculated by IID. .... 33

Figure 19: Schematic illustration of engine thrust model adjustment to counteract non-linear behavior with high engine fan speeds: reduction of max. thrust with fan speeds near ( $N1, max$ ) while maintaining the same thrust level for idle and medium fan speeds which correspond to the engine state for icing encounters. .... 34

Figure 20: Aircraft drag polar from example flight (same data as in Figure 17) after engine thrust model adjustment: calculated lift and drag coefficient from flight data measurements and reference for the Phenom300 prototype with SENS4ICE modifications; drag coefficient data including the indication of nominal drag estimation calculated by IID with **adjusted engine thrust during data replay**35

Figure 21: Time history of IID system performance during specific icing encounter from the first example flight (February 23<sup>rd</sup>, 2023, 17:41:49 UTC to 17:55:29 UTC): altitude and indicated airspeed (top), nominal drag estimation and IID detection output (second plot), and MVD and LWC of encountered icing conditions (third plot), and static air temperature and average engine fan speed (bottom); detection threshold at 10% relative drag increase; **adjusted engine thrust model behavior compared** to Figure 15. .... 36

Figure 22: Time history of IID system performance during specific icing encounter from the first example flight (February 23<sup>rd</sup>, 2023, 18:00:19 UTC to 18:11:39 UTC): altitude and indicated airspeed (top), nominal drag estimation and IID detection output (second plot), and MVD and LWC of encountered icing conditions (third plot), and static air temperature and average engine fan speed (bottom); detection threshold at 10% relative drag increase; **adjusted engine thrust model behavior** to Figure 16. .... 37

Figure 23: Flight track from SENS4ICE North America icing campaign flight on February 25<sup>th</sup>, 2023 (St. Louis Regional Airport, KALN to Toledo Express Airport, KTOL): geodetic position and altitude with indication of icing encountered. .... 38

Figure 24: Time history of IID system performance during specific icing encounter from the first example flight (February 25<sup>th</sup>, 2023, 12:19:09 UTC to 12:33:20 UTC): altitude and indicated airspeed (top), nominal drag estimation and IID detection output (second plot), and MVD and LWC of encountered icing conditions (third plot) including the indication of the amount of SLD (dashed lines), and static air temperature and average engine fan speed (bottom); detection threshold at 10% relative drag increase; **adjusted engine thrust model behavior**. .... 39

Figure 25: Time history of IID system performance during specific icing encounter from the first example flight (February 25<sup>th</sup>, 2023, 12:34:09 UTC to 12:44:09 UTC): altitude and indicated airspeed (top), nominal drag estimation and IID detection output (second plot), and MVD and LWC of encountered icing conditions (third plot) including the indication of the amount of SLD (dashed lines), and static air temperature and average engine fan speed (bottom); detection threshold at 10% relative drag increase; **adjusted engine thrust model behavior**. .... 40

Figure 26: Time history of IID system performance during specific icing encounter from the first example flight (February 25<sup>th</sup>, 2023, 12:45:49 UTC to 12:55:49 UTC): altitude and indicated airspeed (top), nominal drag estimation and IID detection output (second plot), and MVD and LWC of encountered icing conditions (third plot) including the indication of the amount of SLD (dashed lines), and static air temperature and average engine fan speed (bottom); detection threshold at 10% relative drag increase; **adjusted engine thrust model behavior**. .... 41

Figure 27: Time history of IID system performance during specific icing encounter from the first example flight (February 25<sup>th</sup>, 2023, 12:58:19 UTC to 13:08:19 UTC): altitude and indicated airspeed (top), nominal drag estimation and IID detection output (second plot), and MVD and LWC of encountered icing conditions (third plot) including the indication of the amount of SLD (dashed lines), and static air temperature and average engine fan speed (bottom); detection threshold at 10% relative drag increase; **adjusted engine thrust model behavior**. .... 42

Figure 28: Time history of IID system performance during specific icing encounter from the first example flight (February 25<sup>th</sup>, 2023, 13:10:49 UTC to 13:21:39 UTC): altitude and indicated airspeed (top), nominal drag estimation and IID detection output (second plot), and MVD and LWC of encountered icing conditions (third plot) including the indication of the amount of SLD (dashed lines), and static air temperature and average engine fan speed (bottom); detection threshold at 10% relative drag increase; **adjusted engine thrust model behavior**. .... 43



Figure 29: Aircraft drag polar from example flight on February 25<sup>th</sup>, 2023, **after engine thrust model adjustment**: calculated lift and drag coefficient from flight data measurements and reference for the Phenom300 prototype with SENS4ICE modifications; drag coefficient data including the indication of nominal drag estimation calculated by IID with **adjusted engine thrust during data replay**44

Figure 30:Figure: Flight track from SENS4ICE European icing campaign flight on April 24<sup>th</sup>, 2023 around Toulouse/ Marsant/ Cazaux: geodetic position and altitude with indication of icing encountered / built-up..... 45

Figure 31: Time history of IID system performance during the first example flight as230018 (April 24<sup>th</sup>, 2023,12:13 UTC to 16:56 UTC): altitude and indicated airspeed (top), nominal drag estimation and IID detection output (second plot), ice built-up on reference accretion ice sensor and static air temperature (dashed line 0degC) (third plot), and MVD and LWC of encountered icing conditions (solid line) including the indication of the amount of SLD (dashed lines) (bottom); **original detection threshold at 15% relative drag increase.** ..... 46

Figure 32: Time history of IID system performance during the first example flight as230018 (April 24<sup>th</sup>, 2023,12:13 UTC to 16:56 UTC): altitude and indicated airspeed (top), nominal drag estimation and IID detection output (second plot), ice built-up on reference accretion ice sensor and static air temperature (dashed line 0degC) (third plot), and MVD and LWC of encountered icing conditions (solid line) including the indication of the amount of SLD (dashed lines) (bottom); **updated detection threshold at 10% relative drag increase.**..... 47

Figure 33: Time history of IID system performance during specific icing encounter from the first example flight (April 24<sup>th</sup>, 2023,12:30:00 UTC to 13:16:55 UTC): altitude and indicated airspeed (top), nominal drag estimation and IID detection output (second plot), ice built-up on reference accretion ice sensor and static air temperature (dashed line 0degC) (third plot), and MVD and LWC of encountered icing conditions (solid line) including the indication of the amount of SLD (dashed lines) (bottom); **updated detection threshold at 10% relative drag increase.**..... 48

Figure 34: Time history of IID system performance during specific icing encounter from the first example flight (April 24<sup>th</sup>, 2023,13:24:40 UTC to 13:53:20 UTC): altitude and indicated airspeed (top), nominal drag estimation and IID detection output (second plot), ice built-up on reference accretion ice sensor and static air temperature (dashed line 0degC) (third plot), and MVD and LWC of encountered icing conditions (solid line) including the indication of the amount of SLD (dashed lines) (bottom); **updated detection threshold at 10% relative drag increase.**..... 49

Figure 35: Time history of IID system performance during specific icing encounter from the first example flight (April 24<sup>th</sup>, 2023,14:18:20 UTC to 14:36:40 UTC): altitude and indicated airspeed (top), nominal drag estimation and IID detection output (second plot), ice built-up on reference accretion ice sensor and static air temperature (third plot), and MVD and LWC of encountered icing conditions (solid line) including the indication of the amount of SLD (dashed lines) (bottom); **updated detection threshold at 10% relative drag increase.** ..... 50

Figure 36: Evolution of ice accretion on the airframe during icing encounter: camera views on left & right wing and horizontal tail for specific moments during flight (increased brightness and contrast); corresponding to encounter and IID detection given in Fig.Figure 35; credit Safire / SENS4ICE project. .... 51

Figure 37: Time history of IID system performance during specific icing encounter from the first example flight (April 24<sup>th</sup>, 2023,14:42:29 UTC to 15:02:39 UTC): altitude and indicated airspeed (top), nominal drag estimation and IID detection output (second plot), ice built-up on reference accretion ice sensor and static air temperature (third plot), and MVD and LWC of encountered icing conditions (solid line) including the indication of the amount of SLD (dashed lines) (bottom); **updated detection threshold at 10% relative drag increase.** ..... 52

Figure 38: Evolution of ice accretion on the airframe during icing encounter: camera views on left & right wing and horizontal tail for specific moments during flight (increased brightness and contrast); corresponding to encounter and IID detection given in Figure 37; credit Safire / SENS4ICE project. .... 53

Figure 39: Time history of IID system performance during specific icing encounter from the first example flight (April 24<sup>th</sup>, 2023,15:10:39 UTC to 15:26:39 UTC): altitude and indicated airspeed (top), nominal drag estimation and IID detection output (second plot), ice built-up on reference accretion ice sensor and static air temperature (third plot), and MVD and LWC of encountered icing conditions (solid



line) including the indication of the amount of SLD (dashed lines) (bottom); **updated detection threshold at 10% relative drag increase.** ..... 54

Figure 40: Evolution of ice accretion on the airframe during icing encounter: camera views on left & right wing and horizontal tail for specific moments during flight (increased brightness and contrast); corresponding to encounter and indirect ice detection output given in Figure 39; credit Safire / SENS4ICE project. .... 55

Figure 41: Time history of IID system performance during specific icing encounter from the first example flight (April 24<sup>TH</sup>, 2023, 15:34:09 UTC to 16:03:19 UTC): altitude and indicated airspeed (top), nominal drag estimation and IID detection output (second plot), ice built-up on reference accretion ice sensor and static air temperature (third plot), and MVD and LWC of encountered icing conditions (solid line) including the indication of the amount of SLD (dashed lines) (bottom); **updated detection threshold at 10% relative drag increase.** ..... 57

Figure 42: Evolution of ice accretion on the airframe during icing encounter: camera views on left & right wing and horizontal tail for specific moments during flight (increased brightness and contrast); corresponding to encounter and indirect ice detection output given in Fig. Figure 41; credit Safire / SENS4ICE project. .... 58

Figure 43: Time history of IID system performance during specific icing encounter from the first example flight (April 24<sup>TH</sup>, 2023, 16:08:20 UTC to 16:28:20 UTC): altitude and indicated airspeed (top), nominal drag estimation and IID detection output (second plot), ice built-up on reference accretion ice sensor and static air temperature (third plot), and MVD and LWC of encountered icing conditions (solid line) including the indication of the amount of SLD (dashed lines) (bottom); **updated detection threshold at 10% relative drag increase.** ..... 59

Figure 44: Evolution of ice accretion on the airframe during icing encounter: camera views on left & right wing and horizontal tail for specific moments during flight (increased brightness and contrast); corresponding to encounter and indirect ice detection output given in Figure 43; credit Safire / SENS4ICE project. .... 60

Figure 45: Aircraft drag polar from example flight on April 24<sup>TH</sup>, 2023: calculated lift and drag coefficient from flight data measurements and reference for the SAFIRE ATR42-320 with SENS4ICE modifications; drag coefficient data including the indication of nominal drag estimation calculated by IID. .... 61

Figure 46: Aircraft drag polar from example flight on April 24<sup>TH</sup>, 2023: calculated lift and drag coefficient from flight data measurements and reference for the SAFIRE ATR42-320 with SENS4ICE modifications; drag coefficient data including the indication of ice accretion announced by Safire ice reference probe. .... 62

Figure 47: Aircraft drag polar from example flight on April 24<sup>TH</sup>, 2023: calculated lift and drag coefficient from flight data measurements and reference for the SAFIRE ATR42-320 with SENS4ICE modifications; drag coefficient data including the indication of confirmed IID detection output; **updated detection threshold at 10% relative drag increase.** ..... 62

Figure 48: Flight track from SENS4ICE European icing campaign flight on April 26<sup>th</sup>, 2023 (afternoon) around Toulouse/Cazaux: geodetic position and altitude with indication of icing encountered / built-up. .... 63

Figure 49: Time history of IID system performance during the second example flight as230021 (April 26<sup>th</sup>, 2023, 13:02 UTC to 17:13 UTC): altitude and indicated airspeed (top), nominal drag estimation and IID detection output (second plot), ice built-up on reference accretion ice sensor and static air temperature (dashed line 0degC) (third plot), and MVD and LWC of encountered icing conditions (solid line) including the indication of the amount of SLD (dashed lines) (bottom); **original detection threshold at 15% relative drag increase.** ..... 64

Figure 50: Time history of IID system performance during the second example flight as230021 (April 26<sup>th</sup>, 2023, 13:02 UTC to 17:13 UTC): altitude and indicated airspeed (top), nominal drag estimation and IID detection output (second plot), ice built-up on reference accretion ice sensor and static air temperature (dashed line 0degC) (third plot), and MVD and LWC of encountered icing conditions (solid line) including the indication of the amount of SLD (dashed lines) (bottom); **updated detection threshold at 10% relative drag increase.** ..... 65

Figure 51: Time history of IID system performance during the second example flight as230021 (April 26<sup>th</sup>, 2023, 13:02 UTC to 17:13 UTC): altitude and indicated airspeed (top), nominal drag estimation





and IID detection output (second plot), ice built-up on reference accretion ice sensor and static air temperature (dashed line 0degC) (third plot), and MVD and LWC of encountered icing conditions (solid line) including the indication of the amount of SLD (dashed lines) (bottom); **reduced detection threshold at 7% relative drag increase.** ..... 66

Figure 52: Time history of IID system performance during specific icing encounter from the second example flight (April 26<sup>TH</sup>, 2023, 15:43:19 UTC to 15:57:29 UTC): altitude and indicated airspeed (top), nominal drag estimation and IID detection output (second plot), ice built-up on reference accretion ice sensor and static air temperature (third plot), and MVD and LWC of encountered icing conditions (solid line) including the indication of the amount of SLD (dashed lines) (bottom); **updated detection threshold at 10% relative drag increase.** ..... 67

Figure 53: Evolution of ice accretion on the airframe during icing encounter: camera views on left & right wing and horizontal tail for specific moments during flight (increased brightness and contrast); corresponding to encounter and indirect ice detection output given in Figure 52; credit Safire / SENS4ICE project. .... 68

Figure 54: Time history of IID system performance during specific icing encounter from the second example flight (April 26<sup>TH</sup>, 2023, 16:09:59 UTC to 16:32:29 UTC): altitude and indicated airspeed (top), nominal drag estimation and IID detection output (second plot), ice built-up on reference accretion ice sensor and static air temperature (third plot), and MVD and LWC of encountered icing conditions (solid line) including the indication of the amount of SLD (dashed lines) (bottom); **updated detection threshold at 10% relative drag increase.** ..... 69

Figure 55: Evolution of ice accretion on the airframe during icing encounter: camera views on left & right wing and horizontal tail for specific moments during flight (increased brightness and contrast); corresponding to encounter and indirect ice detection output given in Figure 54; credit Safire / SENS4ICE project. .... 70

Figure 56: Aircraft drag polar from example flight on April 26<sup>TH</sup>, 2023: calculated lift and drag coefficient from flight data measurements and reference for the SAFIRE ATR42-320 with SENS4ICE modifications; drag coefficient data including the indication of nominal drag estimation calculated by IID. .... 71

Figure 57: Aircraft drag polar from example flight on April 26<sup>TH</sup>, 2023: calculated lift and drag coefficient from flight data measurements and reference for the SAFIRE ATR42-320 with SENS4ICE modifications; drag coefficient data including the indication of ice accretion announced by Safire ice reference probe. .... 72

Figure 58: Aircraft drag polar from example flight on April 26<sup>TH</sup>, 2023: calculated lift and drag coefficient from flight data measurements and reference for the SAFIRE ATR42-320 with SENS4ICE modifications; drag coefficient data including the indication of confirmed indirect ice detection; **updated detection threshold at 10% relative drag increase.** ..... 72

Figure 59: Aircraft drag polar from example flight on April 26<sup>TH</sup>, 2023: calculated lift and drag coefficient from flight data measurements and reference for the SAFIRE ATR42-320 with SENS4ICE modifications; drag coefficient data including the indication of confirmed indirect ice detection; **reduced detection threshold at 7% relative drag increase.** ..... 73

Figure 60: Flight track from SENS4ICE European icing campaign flight on April 27<sup>th</sup>, 2023 (morning) around Toulouse: geodetic position and altitude with indication of icing encountered / built-up. 74

Figure 61: Time history of IID system performance during the third example flight as230022 (April 27<sup>th</sup>, 2023, 06:36 UTC to 09:49 UTC): altitude and indicated airspeed (top), nominal drag estimation and IID detection output (second plot), ice built-up on reference accretion ice sensor and static air temperature (dashed line 0degC) (third plot), and MVD and LWC of encountered icing conditions (solid line) including the indication of the amount of SLD (dashed lines) (bottom); **original detection threshold at 15% relative drag increase.** ..... 75

Figure 62: Time history of IID system performance during the third example flight as230022 (April 27<sup>th</sup>, 2023, 06:36 UTC to 09:49 UTC): altitude and indicated airspeed (top), nominal drag estimation and IID detection output (second plot), ice built-up on reference accretion ice sensor and static air temperature (dashed line 0degC) (third plot), and MVD and LWC of encountered icing conditions (solid line) including the indication of the amount of SLD (dashed lines) (bottom); **updated detection threshold at 10% relative drag increase.** ..... 76





Figure 63: Time history of IID system performance during specific icing encounter from the third example flight (April 27<sup>TH</sup>, 2023,06:46:39 UTC to 07:09:59 UTC): altitude and indicated airspeed (top), nominal drag estimation and IID detection output (second plot), ice built-up on reference accretion ice sensor and static air temperature (third plot), and MVD and LWC of encountered icing conditions (solid line) including the indication of the amount of SLD (dashed lines) (bottom); **updated detection threshold at 10% relative drag increase.** ..... 77

Figure 64: Time history of IID system performance during specific icing encounter from the third example flight (April 27<sup>TH</sup>, 2023,07:39:59 UTC to 07:54:59 UTC): altitude and indicated airspeed (top), nominal drag estimation and IID detection output (second plot), ice built-up on reference accretion ice sensor and static air temperature (third plot), and MVD and LWC of encountered icing conditions (solid line) including the indication of the amount of SLD (dashed lines) (bottom); **updated detection threshold at 10% relative drag increase.** ..... 78

Figure 65: Time history of IID system performance during specific icing encounter from the third example flight (April 27<sup>TH</sup>, 2023,08:06:39 UTC to 08:26:39 UTC): altitude and indicated airspeed (top), nominal drag estimation and IID detection output (second plot), ice built-up on reference accretion ice sensor and static air temperature (third plot), and MVD and LWC of encountered icing conditions (solid line) including the indication of the amount of SLD (dashed lines) (bottom); **updated detection threshold at 10% relative drag increase.** ..... 79

Figure 66: Evolution of ice accretion on the airframe during icing encounter: camera views on left & right wing and horizontal tail for specific moments during flight (increased brightness and contrast); corresponding to encounter and indirect ice detection output given in Figure 65; credit Safire / SENS4ICE project. .... 80

Figure 67: Time history of IID system performance during specific icing encounter from the third example flight (April 27<sup>TH</sup>, 2023,09:08:20 UTC to 09:45:00 UTC): altitude and indicated airspeed (top), nominal drag estimation and IID detection output (second plot), ice built-up on reference accretion ice sensor and static air temperature (third plot), and MVD and LWC of encountered icing conditions (solid line) including the indication of the amount of SLD (dashed lines) (bottom); **updated detection threshold at 10% relative drag increase.** ..... 81

Figure 68: Evolution of ice accretion on the airframe during icing encounter: camera views on left & right wing and horizontal tail for specific moments during flight (increased brightness and contrast); corresponding to encounter and indirect ice detection output given in Figure 67; credit Safire / SENS4ICE project. .... 82

Figure 69: Aircraft drag polar from example flight on April 27<sup>TH</sup>, 2023: calculated lift and drag coefficient from flight data measurements and reference for the SAFIRE ATR42-320 with SENS4ICE modifications; drag coefficient data including the indication of nominal drag estimation calculated by IID. .... 83

Figure 70: Aircraft drag polar from example flight on April 27<sup>TH</sup>, 2023: calculated lift and drag coefficient from flight data measurements and reference for the SAFIRE ATR42-320 with SENS4ICE modifications; drag coefficient data including the indication of ice accretion announced by Safire ice reference probe. .... 84

Figure 71: Aircraft drag polar from example flight on April 27<sup>TH</sup>, 2023: calculated lift and drag coefficient from flight data measurements and reference for the SAFIRE ATR42-320 with SENS4ICE modifications; drag coefficient data including the indication of confirmed indirect detection; **updated detection threshold at 10% relative drag increase.** ..... 84

Figure 72: Schematic representation of HIDS Arbitration function. .... 87

Figure 73: ATR HIDS, on the left, and HIDS-PC user interface, on the right (image credit Safran). 87

Figure 74:  $\mu$ Physics and A/C data for FT1475-2. The red lines represent the calculated average values of each parameters during the icing encounters. Such values are reported in Table 7. .... 88

Figure 75: Ice Detection signal of DIDSs and IID for FT1475-2. From the bottom to the top:  $\mu P$ , IID, PFIDS, SRP, IDS and AIP. .... 89

Figure 76: Ice Detection signal of DIDSs and IID for IC2 of FT1475-2 From the bottom to the top:  $\mu P$ , IID, PFIDS, SRP, IDS and AIP. .... 91

Figure 77: FT1475-2 Results of HIDS arbitration for the couple PFIDS/IID, on the left, and the couple SRP/IID, on the right. From the top to the bottom: LWC curve and  $\mu P$  ice flag; IID ice flag; DID IAR or



LWC curve and ice flag; DID App O flag (not available for PFIDS since it cannot discriminate); HIDS Arbitration results; HIDS Arbitration status..... 92

Figure 78: FT1475-2 Results of HIDS arbitration for the couple IDS/IID, on the left, and the couple AIP/IID, on the right. From the top to the bottom: LWC curve and  $\mu P$  ice flag; IID ice flag; DID IAR or LWC curve (if available) and ice flag; DID App O flag; HIDS Arbitration results; HIDS Arbitration status. .... 92

Figure 79:  $\mu$ Physics and A/C data for FT1476-1. The red lines represent the calculated average values of each parameters during the icing encounters. Such values are reported in Table 9..... 93

Figure 80: Ice Detection signal of DIDSs and IID for the icing encounters of FT1476-1. From the bottom to the top:  $\mu P$ , IID, PFIDS, SRP, IDS. .... 94

Figure 81: App O detection signals of DIDSs for the icing encounters of FT1476-1. From the bottom to the top:  $\mu P$ , SRP, IDS..... 95

Figure 82: Ice Detection signal of DIDSs and IID for IC3 of FT1476-1. From the bottom to the top:  $\mu P$ , IID, PFIDS, SRP, IDS..... 96

Figure 83: FT1476-1 Results of HIDS arbitration for the couple PFIDS/IID, on the left, and the couple SRP/IID, on the right. From the top to the bottom: LWC curve and  $\mu P$  ice flag; IID ice flag; DID IAR or LWC curve and ice flag; DID App O flag (not available for PFIDS since it cannot discriminate); HIDS Arbitration results; HIDS Arbitration status..... 97

Figure 84: FT1476-1 Results of HIDS arbitration for the couple IDS/IID. From the top to the bottom: LWC curve and  $\mu P$  ice flag; IID ice flag; IDS ice flag; IDS App O flag; HIDS Arbitration results; HIDS Arbitration status..... 98

Figure 85: Flight as230018 A/C data,  $\mu P$  data, reference icing flags and IID outputs. From the top to the bottom: A/C altitude time history and IPS activation; Nevzorov measurements of LWC and TWC; Temperature time history (both SAT and TAT) and RICE probe ice flags;  $\mu P$  ice flags; IID relative drag increase and ice flags..... 99

Figure 86: Flight as230018 Ice Detection signal of DIDSs and IID for icing encounters. From the top to the bottom: RICE,  $\mu P$ , IID, AMPERA, LILD, FOD. .... 100

Figure 87: Flight as230018 time interval [14:19 – 14:28] UTC IC1 On the right,  $\mu P$ , A/C data and reference ice flags. On the left: DIDSs, IID and reference ice flags..... 101

Figure 88: Flight as230018 time interval [14:42 – 15:01] UTC IC2 On the right,  $\mu P$ , A/C data and reference ice flags. On the left: DIDSs, IID and reference ice flags during the time interval [14:42 – 15:01] UTC. On the left: DIDSs, IID and reference ice flags..... 102

Figure 89: Flight as230018 Results of HIDS arbitration for the couple AMPERA/IID. From the top to the bottom: TWC curve and RICE ice flag; AMEPRA TWC measurements and ice flags; IID ice flags; HIDS Arbitration results; HIDS Arbitration status. .... 103

Figure 90: Flight as230018 Results of HIDS arbitration for the couple LILD/IID. From the top to the bottom: LWC curve and RICE ice flag; LILD IAR measurements and ice flags; IID ice flags; HIDS Arbitration results; HIDS Arbitration status..... 104

Figure 91: Flight as230018 Results of HIDS arbitration for the couple FOD/IID. From the top to the bottom: LWC curve and RICE ice flag; FOD IAR measurements and ice flags; IID ice flags; HIDS Arbitration results; HIDS Arbitration status..... 104

Figure 92: Flight as230021 A/C data,  $\mu P$  data, reference icing flags and IID outputs. From the top to the bottom: A/C altitude time history and IPS activation; Nevzorov measurements of LWC and TWC; Temperature time history (both SAT and TAT) and RICE probe ice flags;  $\mu P$  ice flags; IID relative drag increase and ice flags..... 105

Figure 93: Flight as230021 Ice Detection signal of DIDSs and IID for aicing encounters. From the top to the bottom: RICE,  $\mu P$ , IID, AMPERA, LILD, FOD. .... 106

Figure 94: Flight as230021 time interval [14:52 – 15:01] UTC IC1 On the right,  $\mu P$ , A/C data and reference ice flags. On the left: DIDSs, IID and reference ice flags..... 107

Figure 95: Flight as230021 time interval [15:46 – 15:54] UTC IC2 On the right,  $\mu P$ , A/C data and reference ice flags. On the left: DIDSs, IID and reference ice flags..... 108



Figure 96: Flight as230021 Results of HIDS arbitration for the couple AMPERA/IID. From the top to the bottom: TWC curve and RICE ice flag; AMPERA TWC measurements and ice flags; IID ice flags; HIDS Arbitration results; HIDS Arbitration status. .... 108

Figure 97: Flight as230021 Results of HIDS arbitration for the couple LILD/IID. From the top to the bottom: LWC curve and RICE ice flag; LILD IAR measurements and ice flags; IID ice flags; HIDS Arbitration results; HIDS Arbitration status. .... 109

Figure 98: Flight as230021 Results of HIDS arbitration for the couple FOD/IID. From the top to the bottom: LWC curve and RICE ice flag; FOD IAR measurements and ice flags; IID ice flags; HIDS Arbitration results; HIDS Arbitration status. .... 109

Figure 99: Flight as230022 A/C data,  $\mu P$  data, reference icing flags and IID outputs. From the top to the bottom: A/C altitude time history and IPS activation; Nevzorov measurements of LWC and TWC; Temperature time history (both SAT and TAT) and RICE probe ice flags;  $\mu P$  ice flags; IID relative drag increase and ice flags. .... 110

Figure 100: Flight as230022 Ice Detection signal of DIDSs and IID for icing encounters. From the top to the bottom: RICE,  $\mu P$ , IID, AMPERA, LILD, FOD. .... 111

Figure 101: Flight as230022 IC1 On the right,  $\mu P$ , A/C data and reference ice flags during the time interval [07:14 – 07:23] UTC. On the left: DIDSs, IID and reference ice flags during the time interval [07:14 – 07:27] UTC. .... 112

Figure 102 Flight as230022 time interval [09:20 – 09:39] UTC IC2 On the right,  $\mu P$ , A/C data and reference ice flags. On the left: DIDSs, IID and reference ice flags. .... 112

Figure 103: Flight as230022 Results of HIDS arbitration for the couple AMPERA/IID. From the top to the bottom: TWC curve and RICE ice flag; AMPERA TWC measurements and ice flags; IID ice flags; HIDS Arbitration results; HIDS Arbitration status. .... 113

Figure 104: Flight as230022 Results of HIDS arbitration for the couple LILD/IID. From the top to the bottom: LWC curve and RICE ice flag; LILD IAR measurements and ice flags; IID ice flags; HIDS Arbitration results; HIDS Arbitration status. .... 114

Figure 105: Flight as230022 Results of HIDS arbitration for the couple FOD/IID. From the top to the bottom: LWC curve and RICE ice flag; FOD IAR measurements and ice flags; IID ice flags; HIDS Arbitration results; HIDS Arbitration status. .... 114

Figure 106: Schematic activation and monitoring of IPS provided by HIDS. .... 115

## TABLE OF TABLES

Table 1: Overview of DIDS tested during North America FT campaign. .... 15

Table 2: Synthesis of North America Flight Test campaign. .... 17

Table 3: Overview of DIDS tested during European FT campaign. .... 18

Table 4: Synthesis of European Flight Test campaign. .... 20

Table 5: Detection threshold values and confirmation time for the different IID implementations for the SENS4ICE flight test benches. .... 28

Table 6: Number of icing encounters for FT1475-2 and number of IC /APP O Flags raised by each detector. Note that IID and PFIDS are not able to discriminate between APP C and APP O icing conditions. .... 90

Table 7: Characteristics of IC1 and IC2 for FT1475-2. .... 90

Table 8: IID and DIDSs response time for IC2. .... 90

Table 9: Characteristics of IC1, IC2, IC3, IC4 and IC 5 for FT1476-1. .... 93

Table 10: Number of icing encounters for FT 1475-1 and number of IC /APP O Flags raised by each detector. Note that IID and PFIDS are not able to discriminate between App. C and App. O icing conditions. .... 95

Table 11: IID and DIDSs response time for the 5 App O conditions of FT 1476-1. .... 96

Table 12: Summary of the number of IPS activation, reference ice flags and indirect ice detection for the flight as230018. .... 99





Table 13: IID and DIDSs response time for the icing encounter during the time interval [14:19:00 – 14:28:00] UTC of flight as230018.....	101
Table 14: IID and DIDSs response time for the icing encounter during the time interval [14:42:00 – 15:01:00] UTC of flight as230018.....	101
Table 15: Summary of the number of IPS activation, reference ice flags and indirect ice detection for the flight as230021. ....	105
Table 16: IID and DIDSs response time for the icing encounter during the time interval [14:52:00 – 15:01:00] UTC of flight as230021.....	106
Table 17: IID and DIDSs response time for the icing encounter during the time interval [15:46:00 – 15:57:00] UTC of flight as230021.....	107
Table 18: Summary of the number of IPS activation, reference ice flags and indirect ice detection for the flight as230022. ....	110
Table 19: IID and DIDSs response time for the icing encounter during the time interval [07:14:00 – 07:23:00] UTC of flight as230022.....	111
Table 20: IID and DIDSs response time for the icing encounter during the time interval [09:20:00 – 09:39:00] UTC of flight as230022.....	111

If not acknowledged otherwise, images courtesy of the SENS4ICE consortium partners.

This document reflects only the consortium's view. The European Commission and the European Climate, Infrastructure and Environment Executive Agency (CINEA) are not responsible for any use that may be made of the information it contains.

This document is one of the four final public deliverables for the EU-funded project SENS4ICE (Grant Agreement No 824253, 2019-2023):

- D4.1 Sensor evaluation results and final roadmaps for future technology development and exploitation
- D4.2 Final report on hybrid ice detection development
- D4.3 Final report on airborne demonstration and atmospheric characterisation
- D4.4 Final report on evaluation of technologies developed in SENS4ICE and technical project results





## Executive summary

Aim of this deliverable is to report the analysis of the data obtained during the two SENS4ICE FT (flight test) campaigns on two different aircraft types in order to assess the overall performance of the indirect and hybrid ice detection approach and evaluate their capabilities to detect and characterize different icing conditions and the aircraft status during the flight.

Through the analysis of FT data, the advantages of the hybrid ice detection approach are undeniable: HIDS (hybrid ice detection system) can guarantee an early ice detection, thanks to the fast and reliable direct ice detection technologies developed within the SENS4ICE project, together with a continuous monitoring of the aircraft performance during the icing conditions encounter and even after. Indeed, the indirect detection algorithm was able to detect aircraft performance degradation due to the presence of residual ice accretion on the airframe after leaving the icing clouds. These capabilities clear the way for the use of HIDS as a Primary Ice Detection system, since it is based on dissimilar ice detection sources and can provide an automatic control and monitoring of the aircraft Ice Protection Systems. Actually, the proven capability of IID (indirect ice detection) to detect residual ice accretion on the whole airframe provides a direct measurement of ice protection efficiency. HIDS could even enable significant reduction in fuel consumption thanks to a more efficient use of IPS (ice protection systems), thanks to the indirect detection, associated to the monitoring of remaining ice.

Thanks to the flight tests campaigns and the promising results obtained, the hybrid ice detection approach has been validated during real icing conditions and may be consequentially considered TRL5, according to the Horizon 2020 TRL definitions.

With regard to the capabilities of DIDS (direct ice detection systems) and HIDS in Appendix O icing conditions, it can be pointed out that only a relatively small part of the envelope was encountered during the FT campaign, mainly FZDZ (freezing drizzle). Covering the whole Appendix O, including the rare FZRA (freezing rain), to properly assess the performance of the SENS4ICE technologies, can hardly be met in a single flight campaign or project.

Additional research is thus necessary in order to further mature the hybrid approach in Appendix O conditions, as well as, to improve such technology on a system level. Indeed, all the aspects linked to safety issues, implementation of the IID/HIDS algorithm within aircraft avionics, etc., were out of the scope of SENS4ICE research and innovation project. Nevertheless, all these subjects will be crucial to address HIDS airworthiness.

## 1. Overview on SENS4ICE Flight Test campaigns

Two flight test campaigns were performed in early 2023 in order to test in natural in-flight icing conditions, both the direct ice detection technologies developed with the SENS4ICE project and the HIDS, the onboard computer that includes the implementation of the Indirect Ice Detection algorithm in real time:

- The North America FT campaign (late February/early March 2023) with the Embraer Phenom 300,
- The European FT campaign (April 2023) with the French ATR 42 environmental research aircraft of Safire.

Note that the two flight campaigns are described in greater detail in SENS4ICE deliverable D4.3 “Final report on airborne demonstration and atmospheric characterisation” [7] and a short overview is presented in the following sections.

### 1.1 North America FT campaign

An experimental prototype of Phenom 300 was used to perform the FT campaign. The aircraft was instrumented with two different reference probes, a Cloud Combination Probe (CCP) and an Ice Crystal Detector (ICD), and with several cameras in order to monitor ice accretion on the A/C sensitive surfaces during the flights, see Figure 1.

In this document,  $\mu\text{P}$  (“microPhysics”) refers to the global results of all these probes, analyzed by DLR Institute of Atmospheric Physics.





Figure 1: Phenom 300 instrumented for North America FT campaign (image Embraer/ SENS4ICE project).

In this campaign, four different DIDS were tested: Aerotex AIP, Collins IDS, Honeywell SRP and SAFRAN PFIDS, together with HIDS/IID. Some details on each direct detection technology are reported in Table 1. For further details on DIDSs see SENS4ICE deliverable D4.1 “Sensor evaluation results and final roadmaps for future technology development and exploitation” ref. [5].

Sensor/Developer	Sensor Type	Sensor Principle	Provided data	Sensor Maturity before FT (TRL)
AIP/AeroTex	Atmospheric	Isothermal with inertial separation at different sensors along aircraft	ICE flag; APP O flag; LWC	TRL 4
IDS/Collins	Atmospheric	Thermal response to heat impulse	ICE flag; APP O flag	TRL 5
SRP/Honeywell	Atmospheric	Collecting backscattered light from particles	ICE flag; APP O flag; LWC; MVD; Dmax; DV99	TRL 6
PFIDS/Safran	Accretion	Optical reflection from ice accretion	ICE flag; IAR	TRL 6

Table 1: Overview of DIDS tested during North America FT campaign.

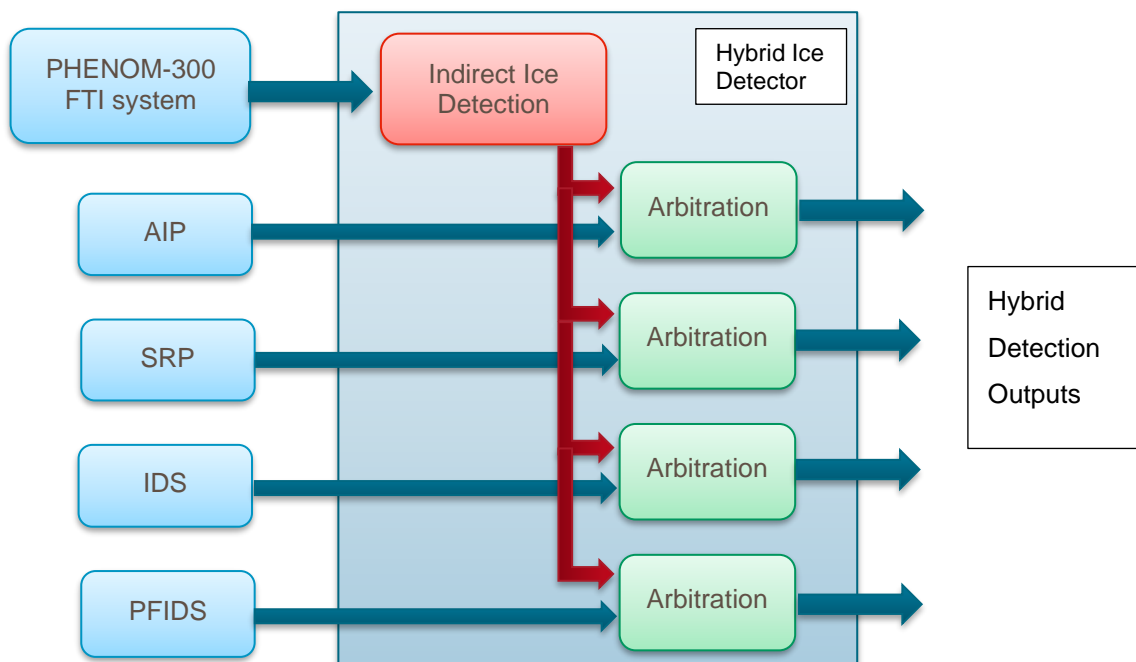


Figure 2: Basic HIDS architecture for North America Flight tests.

The flight tests were conducted from Alton/St. Louis Regional Airport (KALN). The Phenom 300 flew mainly over the southeast, south and west regions of Lake Michigan, see Figure 3, since the probability of encountering SLD conditions was higher in this area, as described in [1].

15 flights were conducted (including ferry flight and check flights) for a total of 25 flight hours. In total more than 4 hours and 23 minutes were spent in icing conditions and 42 minutes in Appendix O conditions.

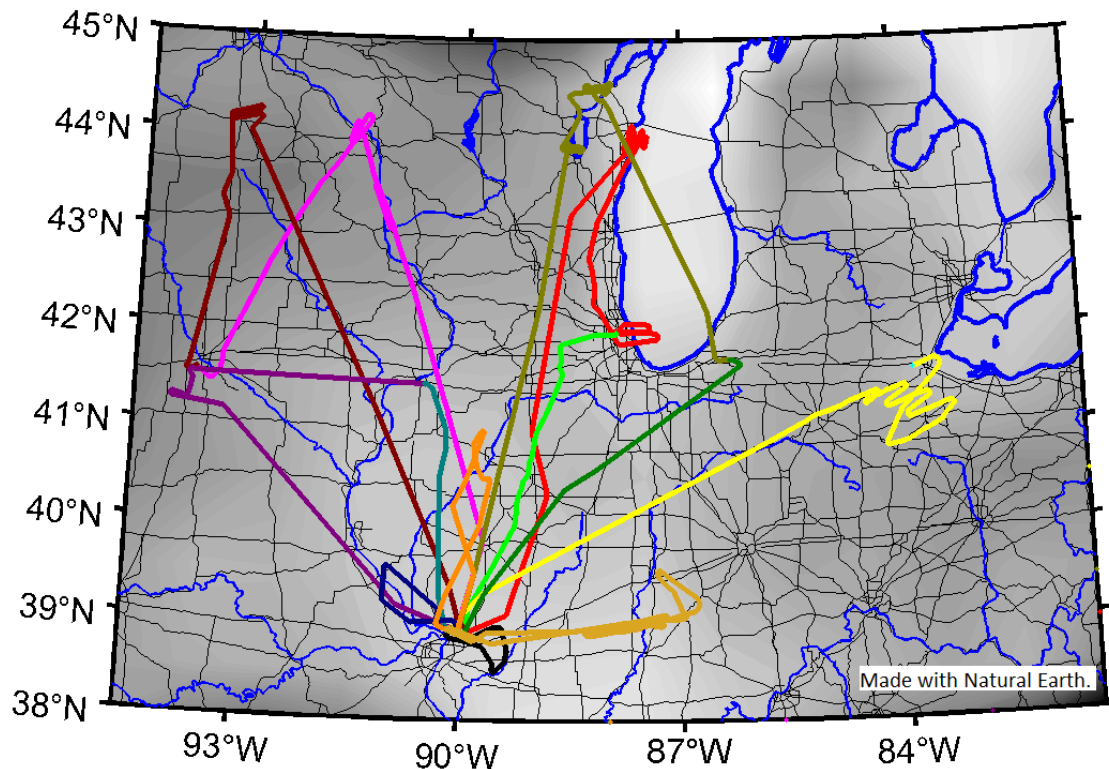


Figure 3: North America flight campaign ground tracks (image DLR/ SENS4ICE project).



The performed flights are summarized in Table 2.

No	Date	Flight ID	Duration	Comments
1	22/02/2023	1474-1	0:39	Check Flight
2	23/02/2023	1475-1	2:45	Appendix O
3	23/02/2023	1475-2	1:12	Appendix C
4	25/02/2023	1476-1	2:03	Appendix O
5	25/02/2023	1476-2	1:37	Appendix O
6	01/03/2023	1477-1	2:45	Appendix O
7	01/03/2023	1477-2	2:12	Appendix O
8	06/03/2023	1478-1	1:07	Appendix C
9	06/03/2023	1478-2	-	Dry Air
10	08/03/2023	1479-1	2:21	Appendix O
11	08/03/2023	1479-2	0:40	Return to base
12	08/03/2023	1480-1	-	Check Flight
13	09/03/2023	1481-1	1:23	Appendix C
14	10/03/2023	1482-1	2:15	Appendix O
15	10/03/2023	1482-2	1:08	Appendix C

Table 2: Synthesis of North America Flight Test campaign.

In this document the flights 1475 and 1476 are analysed in detail. These two flights were selected in order to provide an example of DIDSs and HIDS/IID performance in both Appendix C (FT 1475 leg 2) and Appendix O (FT 1476 leg 1) conditions.

## 1.2 European FT campaign

This campaign was led thanks to the SAFIRE team and its ATR 42 environmental research aircraft. The aircraft was equipped with several cameras for ice accretion monitoring and different reference probes: Cloud Combination Probe (CCP), Nevzorov Probe, Precipitation Imaging Probe (PIP), High Speed Imager (HSI) and Backscatter Cloud Probe with Polarization Detection. The installation of these reference probe is reported in Figure 4.



Figure 4: Safire ATR 42 instrumented for European FT campaign (image DLR/ SENS4ICE project)

In this document,  $\mu\text{P}$  (“microPhysics”) refers to the global results of all these probes, including CM2D, analyzed by DLR Institute of Atmospheric Physics.

**DISCLAIMER:** For Appendix C conditions the reference measurement results for MVD are only valid for a low concentration of large aspherical particles (parameter LAS N), see SENS4ICE deliverable D4.3 [7]. This was



not necessarily the case particularly for the European flight campaign and is checked specifically for individual icing encounters for the analyses presented in this document.

The direct detectors tested in this campaign, together with HIDS/IID, are INTA FOD, DLR LILD, ONERA AMPERA and DLR CM2D. Note that the latter sensor, which can be considered as a reference probe, was not used for hybridization with indirect detection and it is not analysed in this document, as it is a technology for scientific purposes. Some details on each direct detection technology are reported in Table 3. For further details on DIDSs see ref. [5].

Sensor/Developer	Sensor Type	Sensor Principle	Provided data	Sensor Maturity before FT (TRL)
FOD / INTA	Accretion	Latent heat measured with fiber optic	ICE flag; APP O flag; LWC; IAR; Ice thickness	TRL5
LILD / DLR	Accretion	Ultrasonic wave attenuation/phase change	ICE flag; APP O flag; IAR; Ice thickness	TRL3-4
AMPERA / ONERA	Atmospheric	Measurement of aircraft electrical potential	ICE flag; TWC	TRL4-5
CM2D / DLR	Atmospheric	Single particle optical backscatter + isothermal measurement of water content	LWC; Particle Size Distribution (PDS)	TRL5

Table 3: Overview of DIDS tested during European FT campaign.

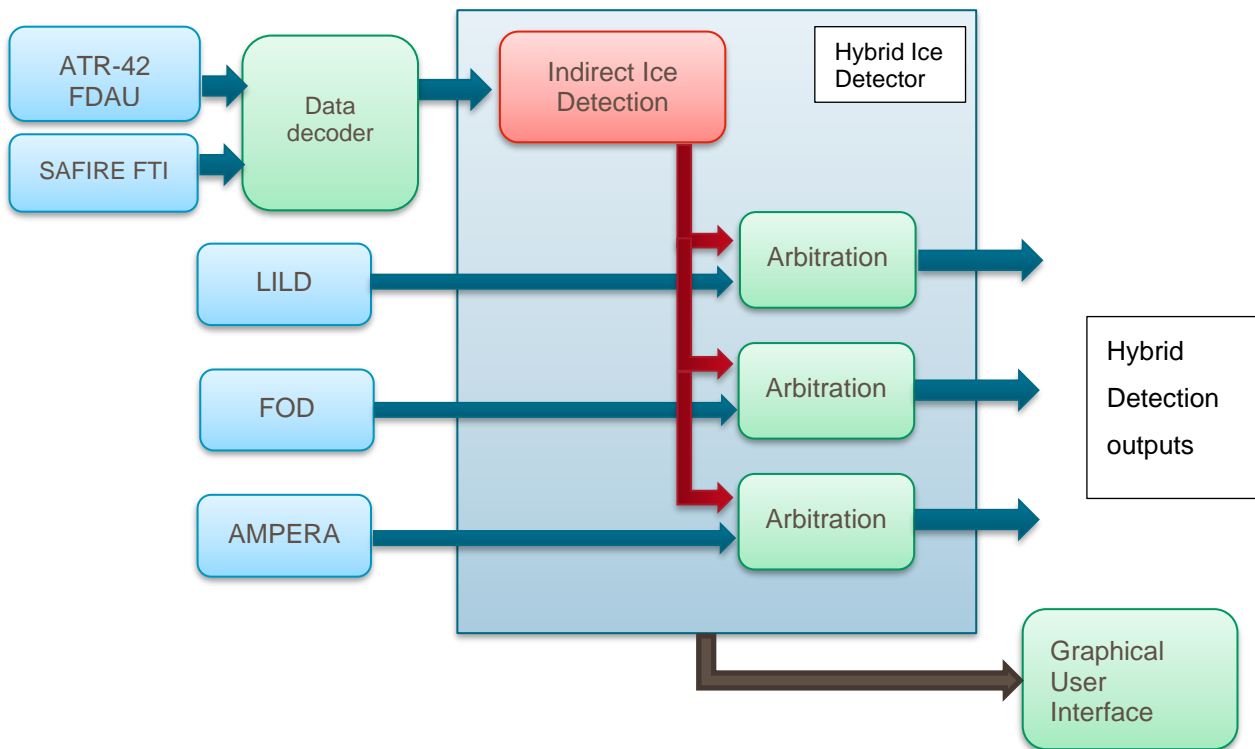


Figure 5: Basic HIDS architecture for European Flight tests.



SAFIRE ATR 42 was based at Francazal airport in Toulouse (LFBF) for the European SENS4ICE flight campaign and realized 15 flights, for a total of about 50 flight hours by flying over France, especially the south regions, see Figure 6.

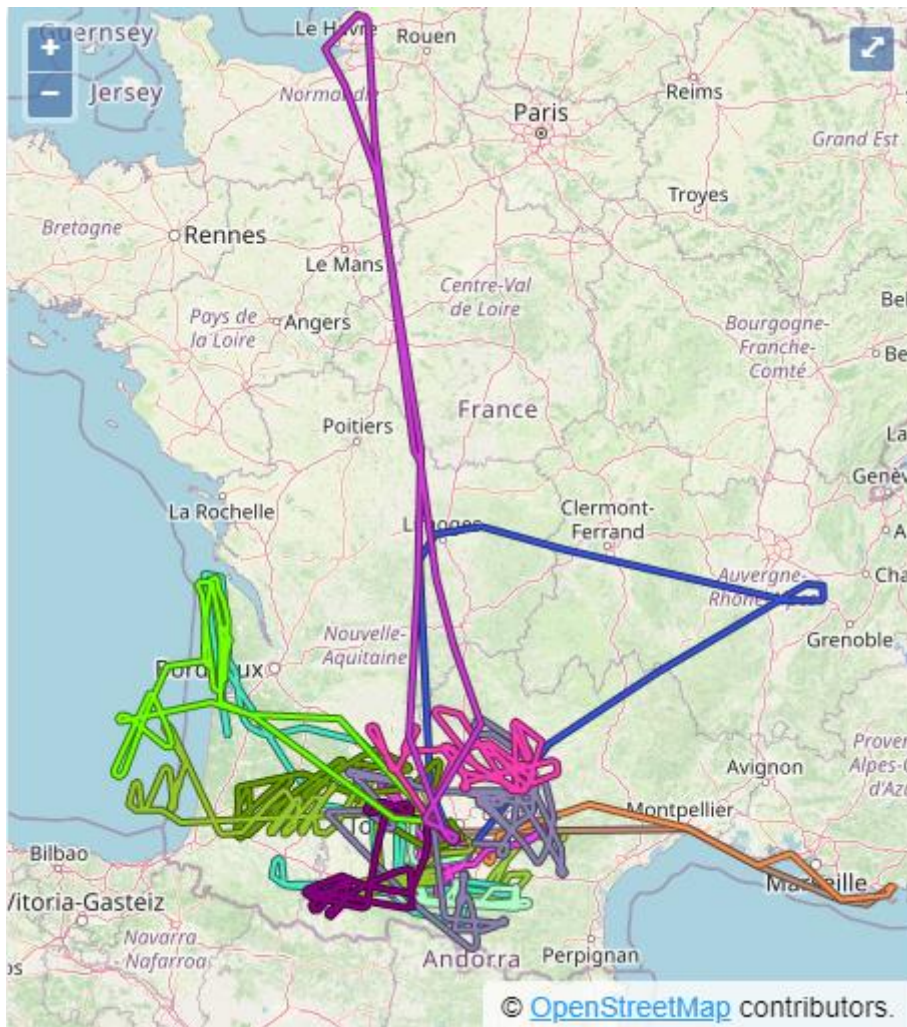


Figure 6: European flight campaign ground tracks (image Safire, Map data from OpenStreetMap/ SENS4ICE project).

Icing conditions were encountered during almost all flights and some SLD conditions were detected as well. An overview of the performed FT is reported in Table 4.



Flight name	Date	From	To	Depart (local)	Arrival (local)	Flight ID	Flight Hours	Comments
EMI	21/03/2023	LFBF	LFBF	14h30	15h35	as230006	1.1	
CAL	22/03/2023	LFBF	LFBF	11h50	13h25	as230007	1.6	Toulouse CER
TEST	24/03/2023	LFBF	LFBF	10h25	12h00	as230008	1.6	Toulouse CER
1	03/04/2023	LFBF	LFBF	08h00	11h40	as230009	3.7	Toulouse CER
2	04/04/2023	LFBF	LFTH	13h30	14h55	as230010	1.4	Airways
3	04/04/2023	LFTH	LFBF	15h05	16h30	as230011	1.4	Airways
4	06/04/2023	LFBF	LFBF	07h05	07h40	as230012	0.6	Cazaux CER - Aborted
5	14/04/2023	LFBF	LFBF	06h25	11h30	as230013	4.9	Cazaux and Toulouse CER
6	15/04/2023	LFBF	LFBF	08h00	10h25	as230014	2.4	Toulouse CER LFBF Extra opening
7	18/04/2023	LFBF	LFBF	15h55	19h10	as230015	3.3	CER Toulouse
8	20/04/2023	LFBF	LFBF	14h35	16h25	as230016	2.8	Airways LFBF-LFBL-LFLS
9	22/04/2023	LFBO	LFBO	07h55	10h55	as230017	3.0	CER Marsant
10	24/04/2023	LFBF	LFBF	14h20	19h00	as230018	4.7	CER Marsant/Cazaux
11	25/04/2023	LFBF	LFBF	13h00	18h00	as230019	5.0	Toulouse CER
12	26/04/2023	LFBF	LFBF	08h25	10h55	as230020	2.5	Toulouse CER
13	26/04/2023	LFBF	LFBF	15h30	19h10	as230021	3.7	Cazaux CER
14	27/04/2023	LFBF	LFBF	8h30	12h00	as230022	3.5	Toulouse CER
15	27/04/2023	LFBF	LFBF	14h00	17h50	as230023	3.8	Airways LFBF - LFOH

Table 4: Synthesis of European Flight Test campaign.

In this document the flights as230018, as230021 and as230022 are analysed in detail. These flights were selected in order to state direct detectors and HIDS/IID performance in different icing conditions, Appendix C and Appendix O and severe icing, as it is described in the following paragraphs.

## 2. Evaluation of Indirect Ice Detection algorithm

### 2.1 Indirect Ice Detection Algorithm

Within SENS4ICE the “indirect ice detection” (IID) was further developed and matured and is one important project pillar [9]. It is a novel methodology and system for the on-board surveillance of aircraft flight performance used for ice detection purposes. It was originally formulated and presented as a performance-based ice detection methodology, e.g., in Ref. [10]. It utilizes the effect of aircraft performance degradation due to ice accretion. The idea of the IID is not restricted to an application on large transport aircraft but can also enable a reliable ice detection for aircraft systems, such as small unmanned aerial vehicle (UAV), which currently have no ice detection system, but operate in hazardous environments with very different icing conditions.

One major effect of aircraft ice accretion is a significant drag increase due to surface roughness changes, parasitic influence of ice protuberances, and local flow separation. Another effect of icing is a change of the aircraft lift behavior, causing e.g., earlier or more abrupt flow detachment with increasing angle of attack and/or a reduction in aircraft lift slope. Both together significantly alter the aircraft flight performance which can be monitored during flight. Figure 7 illustrates the typical icing-induced change of the lift and drag curves as generally described, e.g., in the AGARD report 344 [11]. Icing will also change the aircraft's flight dynamics (e.g., pitching and rolling moment). In addition, the control characteristics are negatively affected by icing and change the aircraft dynamics differently according to the specific occurrence of ice accretion. But these changes are very difficult to detect during flight, for what the IID relies on the icing-related change of aircraft flight performance [10, 9].

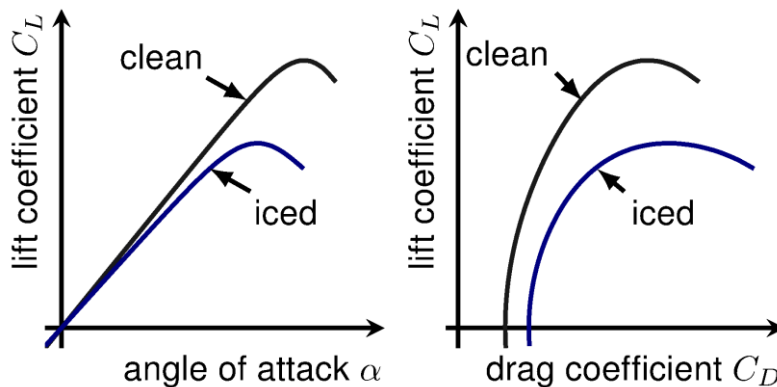


Figure 7: Expected icing influence on aircraft aerodynamics (lift and drag coefficient); adapted from [11].

Hence, aircraft flight performance monitoring can provide crucial information to the pilots about the current (limited/degraded) aircraft capabilities while only requiring the sensor information that is available on all modern airliners and business jets. The advantage of the developed methodology is that it relies only on the change in flight performance (i.e., steady flight states) contrary to the many failed attempts (see for detailed information about this in [10]) based on the estimation of changes in the aircraft's dynamic behavior or a combination of both. The change/ degradation in the flight performance is an indicator of ice accretion that is both robust and highly available: unlike the approaches based on the detection of changes in the aircraft dynamical behavior, it can be used also during steady flight conditions (most of an operating flight) and can detect icing effects significantly before entering into stall. Although other direct ice measuring approaches for the detection of icing conditions or ice accretion on the airframe could deliver a partly similar information, the indirect detection using the performance monitoring approach would not require (potentially costly) modifications of existing and future aircraft. It is important to highlight that the method within the IID is focused on the flight performance changes without any specific need for additional dynamic aircraft excitations. Such an excitation is not acceptable during normal operations and especially not when flying with an aircraft that has a reduced (unknown) maximum-lift angle of attack due to icing.

The basic assumption for the indirect ice detection using performance monitoring is the possibility to discriminate between (very slow and low) performance variation of a single aircraft over lifetime in service (or



within a fleet of same type) and the (much faster) performance variation caused by icing. Factors causing the flight performance variations across airplanes from the same type are for example:

- production tolerances,
- aircraft skin repairs,
- aircraft skin contamination (e.g., dirt),
- engine aging causing reduced efficiency, or
- engine contamination.

The aircraft flight performance can be seen as follows:

**Flight Performance** = Nominal Aircraft Performance + Expectable Variation + **Variation to be detected**

whereby the “*Expectable Variation*” part gathers the effects mentioned previously and the “**Variation to be detected**” is subject to the indirect ice detection approach. The first step is to determine the typical and most extreme flight performance variation (“*Expectable Variation*”) encountered during regular airline operations (due to a real performance variation or sensor errors). There are different approaches to reveal this variation from operational flight data. In Refs. [10, 12] the determination of the performance variation from 75,689 flights with Boeing B737 aircraft operated by a German airline is presented. The results underpinned the above mentioned assumption and revealed that it is possible to successfully monitor the aircraft performance using the regular sensors and with a level of precision that permits to detect the performance degradation induced by the ice accretion at a very early stage (before this degradation of the performance reaches a critical level).

In a second step, flight data for the Embraer Phenom 300 prototype (North America FT campaign) and the ATR 42 test aircraft (European FT campaign) serving as flight test benches in SENS4ICE were processed to obtain the measured performance variation during flight. The resulting performance variation (without icing) is given in Figure 8 for the Phenom 300 prototype and in Figure 9 for the ATR 42 test bench. The measured performance variation in this case results from the non-filtered measurements which are also not corrected for external disturbances. Therefore, the measured variation does include (external) effects on the aircraft, e.g., resulting from encountered atmospheric disturbances or conducted manoeuvres, together with additional influences on the performance calculation like measurement noise. This is in contrast to the results given in Refs. [10, 12], where the data were corrected for most of these effects. But for the design of the IID, it is essential to also evaluate the measured performance variation of a single aircraft, which is mainly the variation between the actual aircraft and the reference model together with the named additional influences. Hence, in this case the 90% quantile is more relevant than the higher ones, because it can be reliably assumed that the variation above results from the external influence which can be ignored for the ice detection and circumvented (e.g., for large scale atmospheric disturbances or dynamic manoeuvres) or filtered (e.g., for measurement noise) within the designed algorithm. If the measurements of the flight condition are available with sample rate (and frame rate for transmission to the IID) above e.g., 20 Hz and are not filtered or corrected for e.g., measurement noise, the IID must account for a higher observed performance variation (“*Expectable Variation*”). But it is assumed to be able to reliably detect a performance degradation due to icing fast. If the rate is significantly lower (e.g., 5 Hz) and/or the data are already low-pass filtered, the IID will observe a smaller performance variation and the detection of the degradation might be slower than for the higher measurement rate case. Consequently, within the application of the IID approach, the potential detection speed and accuracy is directly related to the quality of the flight data measurements.

The basic idea of the herein-proposed detection method is to compare the current (possibly ice-influenced) aircraft flight performance characteristics with a known reference, as schematically represented in Figure 10. The flight performance can be formulated as a power imbalance (change of total energy)  $\dot{E}_{tot}$  in both cases (current state and reference), which allows to represent the changed aircraft characteristics in only one significant value and reduces the detection module complexity. Moreover, it combines the influences of aerodynamics and engines on the aircraft performance.

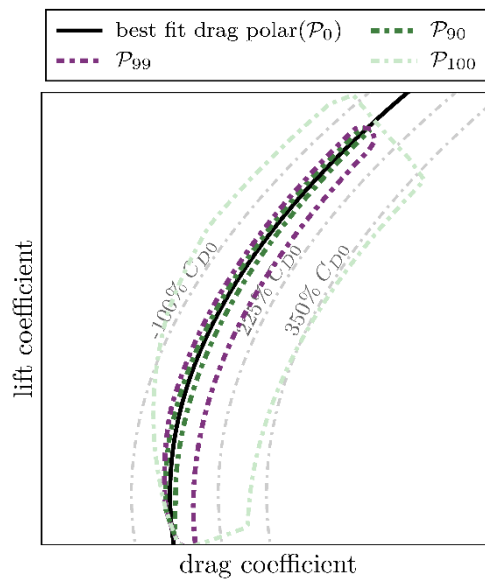


Figure 8: Measured aircraft performance variation based on dynamic Phenom 300 flight test data throughout a large flight envelope (2.2 million data points): estimated drag polar and convex hulls ( $P_{90}$ ,  $P_{99}$ ,  $P_{99.9}$  &  $P_{100}$ ).

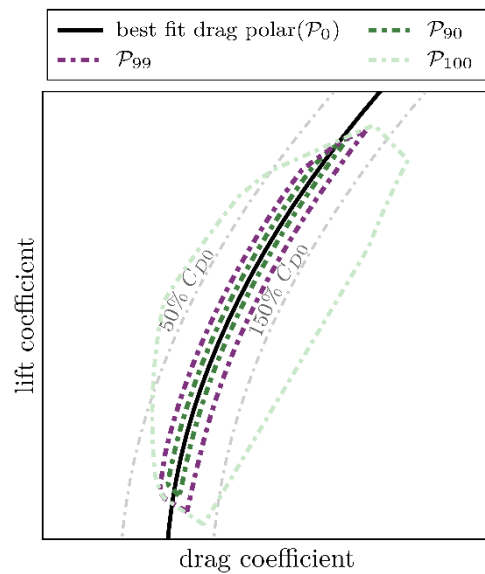


Figure 9: Measured aircraft performance variation based on ATR 42 flight test data at several flight conditions (1.45 million data points): estimated drag polar and convex hulls ( $P_{90}$ ,  $P_{99}$ ,  $P_{99.9}$  &  $P_{100}$ ).

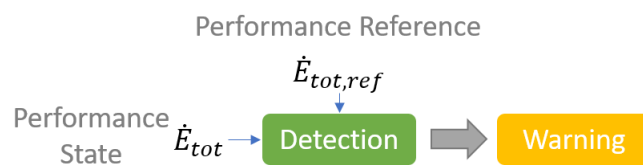


Figure 10: Basic principle of the IID method based on the aircraft power imbalance.



The power imbalance  $\dot{E}_{tot}$  is analytically derived through

$$\dot{E}_{tot} = V_{TAS} \cdot \dot{V}_{TAS} \cdot m_{AC} + \frac{1}{2} \cdot V_{TAS}^2 \cdot \dot{m}_{AC} + g \cdot \dot{H} \cdot m_{AC} + g \cdot H \cdot \dot{m}_{AC} \quad (1)$$

with the altitude change (with respect to time)  $\dot{H}$  referenced to the surrounding air and the speed change (with respect to time)  $\dot{V}_{TAS}$ . Note that the gravitational acceleration is assumed to be constant and its variation with time can be neglected for the calculation of the power imbalance. The following scaling/conversion of this power imbalance into an equivalent drag coefficient variation according to Ref. [10] is used:

$$\Delta C_{\bar{D}} \approx \frac{\dot{E}_{tot,ref} - \dot{E}_{tot}}{V_{TAS} \cdot \bar{q} \cdot S} \quad (2)$$

This nondimensional value is well comparable to a predefined threshold and indicates an abnormal performance variation when exceeding the threshold value, independent from any flight point. Moreover, it is well interpretable in terms of aerodynamics and flight mechanics by aerospace engineers and allows a direct assessment of the magnitude of aerodynamic degradation caused by icing within the IID. The equivalent drag coefficient is calculated by comparison of the current determined power imbalance  $\dot{E}_{tot}$  and a predefined reference value  $\dot{E}_{tot,ref}$ . The latter is a function of certain aircraft flight parameters like altitude, speed and load factor, the aircraft configuration (e.g., mass, high lift system configuration) and propulsion system state.

The equivalent drag coefficient is well comparable to a predefined threshold value and indicates an abnormal performance variation when exceeding. This is further independent from any flight point. Note that a drag coefficient value is well interpretable in terms of aerodynamics and flight mechanics by aerospace engineers and allows a direct assessment of the magnitude of aerodynamic degradation caused by icing. Within the IID, this drag coefficient is normalized with the aircraft's zero-lift drag coefficient and compared to a predefined threshold.

## 2.2 IID implementation

The indirect ice detection is implemented as a modular set of functions, including the core detection algorithm, the required data preprocessing and a subsequent detection result filtering to prevent false detections. The filtering also helps to achieve the necessary system robustness and reliability. Within SENS4ICE, the indirect ice detection is part of the HIDS and allows with its specific implementation detecting performance degradations and therefore the ice accretion on the two very different testing aircraft (see Figure 11). This is possible through the generic formulation of the detection methodology itself, not relying in specific information about the aircraft: the required aircraft-specific adaption of the detection is achieved by considering the aircraft-specific reference, which is an input to the algorithm and not part of the core implementation.

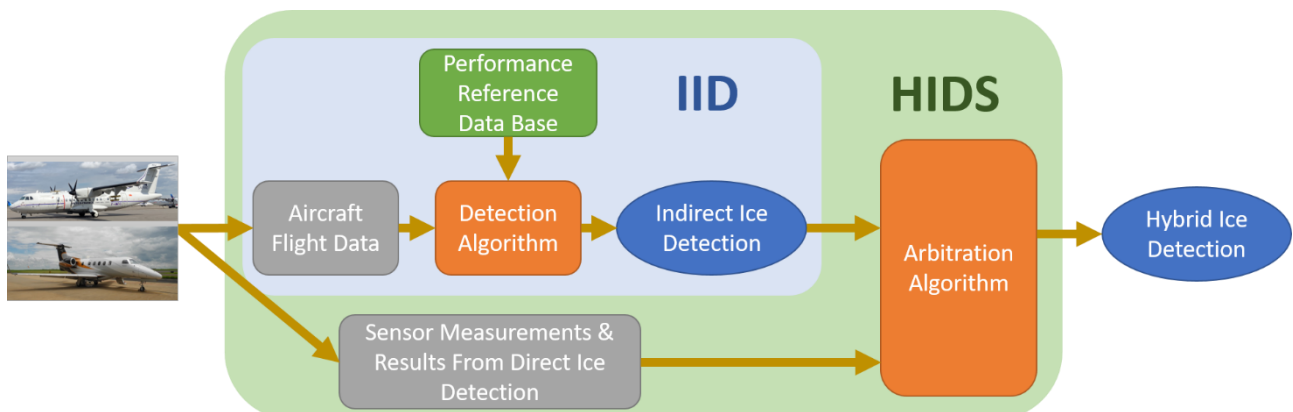


Figure 11: Visualization of HIDS concept used within SENS4ICE (pictures credit DLR/ Embraer/ Safire/ SENS4ICE project).



With regard to a highly adaptable use of the IID for different aircraft types, this formulation of the detection methodology is a significant advantage for prototyping the specific system implementation compared to more integrated approaches. Such implementations would require more specific information about the aircraft inside the core detection algorithm. Hence, there are still several needs for adjustments inside the IID for a specific aircraft type, which concern

1. the flight data preprocessing,
2. the flight performance reference data base,
3. the indirect ice detection threshold and confirmation times,
4. the detection reliability conditions,

which are further detailed below.

The IID is currently implemented in MATLAB®/Simulink including several parts formulated in code originating from the SENS4ICE project partners. Basically, the methodology can be implemented in different formats depending on the framework to run with. For SENS4ICE a very agile prototyping and dynamic testing was required for which MATLAB®/Simulink is very handy. Furthermore, for flight testing the HIDS runs on a dSpace MicroAutoBox in real time, and the Simulink model can be easily transferred to the hardware including a full intellectual property protection required for several parts of the IID. Future exploitation will presumably provide a code implementation running with aircraft avionic systems.

#### Flight Data Preprocessing

The available measurements about the aircraft's current flight state, the configuration and the atmospheric conditions are significantly aircraft dependent. Nevertheless, for modern transport aircraft, there is a minimum set of required measurements, e.g., for indication in the cockpit or use in flight controllers, which is almost sufficient for the IID calculations. But the number measurements, the units and their quality are different for different aircraft: for example, modern highly automated aircraft are equipped with doubled or tripled sensor systems in order to provide a fail-safe avionics system for automatic flight control, whereas older aircraft might only provide a minimum set of sensors sufficient for manual flight controls. Another example are the different propulsion systems, which require a different treatment of measured data for calculating the total aircraft thrust.

Hence, within the flight data pre-processing a data selection for the required data sets must be performed. For the IID it is essential to have all measurements about the flight state referenced to the current centre of gravity position, which means that accelerations and flow measurements must be corrected for position offsets. For the specific implementation in the SENS4ICE project, two individual data pre-processing functions are used, providing mutual parts but also aircraft-specific implementations reflecting the different propulsion systems of the ATR 42 (turboprops) and the Phenom 300 (jet engines) or the individual sensor positions of the different sensor equipment. Consequently, this is a part of the IID which requires a deeper insight in the aircraft and avionics system but the necessary effort for development is not different as for any other aircraft-specific avionic functions (e.g., flight management system or flight control functions).

For example, the IID requires the following information about the current aircraft state:

- acceleration, rotational rates and attitude,
- atmospheric conditions, altitude, airspeed, inflow angles,
- engine (and propeller) state,
- aircraft configuration and weight and balance,

which is processed and provided to the detection algorithm in a fixed format. The highest available sample time, e.g., commonly available for the acceleration measurements, defines the overall sample time for the IID input data, knowing that some data will not be updated between different time stamps in the input data. Nevertheless, normally the low sampled data also reflects slow processes or dynamics, which makes this acceptable. But for an ideal implementation of the IID, a high sample rate for high resolution data measured with high accuracy is of course favourable to ensure a highly reliable and fast detection of the flight performance degradation.

#### Flight Performance Reference Data Base

The IID relies on an accurate flight performance reference which allows to compute an expected current flight performance to be compared to the measured one within the detection module. As discussed above, the reference data base must allow to compute the reference power imbalance  $\dot{E}_{\text{tot,ref}}$  and is not restricted to a



certain type of implementation. In Ref. [10] a multi-dimensional table was found to be the most suitable way but for the SENS4ICE project a different implementation was chosen for several reasons. In SENS4ICE, the IID consists of a performance reference data base splitting engine and aerodynamic influence into individual parts. Having this separation, it is easy to adapt the reference aerodynamics to the specific conditions given by the flight test benches having several external probes attached to the test aircraft influencing the aircraft's flight performance.

The flight performance reference in SENS4ICE is based on certain a priori knowledge and information obtained from a specific flight data evaluation. Using existing and well-known aircraft types eases off course the flight performance reference generation in the presented case. Nevertheless, for new aircraft designs or the application of the IID to other aircraft types, the performance reference can be based on the design models and initial prototype flight test results. This means, that the IID implementation does not require an existing aircraft fleet but can be part of the aircraft design and certification process from the beginning with a validation during e.g., first production flights.

The flight test case-specific adaption of the aerodynamic performance reference is formulated as an additional part to the "base" aircraft reference, which allows a very fast adaption of the reference data base prior to the icing flight tests. Having the final configuration of the aircraft only available a few days before the icing flight test campaign and with only one initial test flight to retrieve the aerodynamic changes compared to the "base" aircraft aerodynamics already available through the extensive flight data evaluation, this is the most practical and suitable approach. Using a kind of delta approach to the aerodynamic reference, the performance reference is highly adaptable with the small but very specific information available from an initial test flight in dry air with dedicated test conditions prior to the campaign. Note, that this is a special condition and therefore not contrary but complementary to the argumentation in Ref. [10] being in favour of an integrated multi-dimensional reference table for a tail number-specific implementation of the performance reference in an aircraft fleet of similar type.

Having a representation of the aircraft drag polar given by

$$C_D = C_{D0} + k_1 \cdot C_L + k_2 \cdot C_L^2 \quad (3)$$

a linear parameter extension was already foreseen in the IID implementation allowing the adaptation of the aircraft aerodynamics to the SENS4ICE aircraft modifications:

$$C_D = (C_{D0} + \Delta C_{D0}) + (k_1 + \Delta k_1) \cdot C_L + (k_2 + \Delta k_2) \cdot C_L^2. \quad (4)$$

For the North America flight test campaign, the final configuration of the aircraft with all modifications, i.e. external sensors and pods mounted on wing pylons or at the fuselage, was available for a check flight before the campaign in February 2023. Moreover, the ferry flights from Brazil, where the prototype was modified at Embraer facilities, to the United States, where the flight test campaign took place, served as an additional source of information for the corresponding changes of the aerodynamics due to aircraft modifications with SENS4ICE equipment (compared to the "base" aircraft).

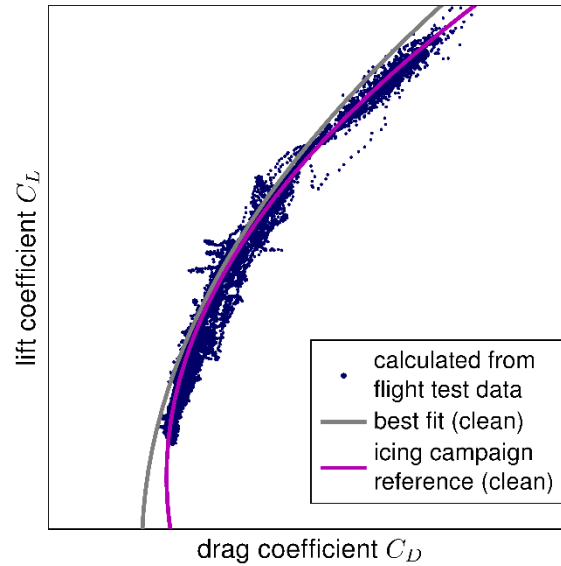


Figure 12: Aircraft drag polar for Phenom300 prototype used for the SENS4ICE North America icing flight test campaign: calculated lift and drag coefficient from flight test data (**blue dots**), pre-campaign reference drag polar (**gray line**, no SENS4ICE aircraft modification) and adapted campaign reference drag polar considering aircraft modifications (**magenta line**); clean air flight test data with aircraft in final configuration with all modification required for SENS4ICE in February 2023.

For the European flight test campaign, the final configuration of the aircraft with all modifications, i.e. external sensors and pods mounted on wing pylons or at the fuselage, was available in mid-March 2023 for check flights two weeks before the campaign start. With two specific test flights on March 22nd and 23rd, 2023, the corresponding changes of the aerodynamic compared to the “base” aircraft aerodynamics were determined. The latter were already available through the extensive flight data evaluation of Safire’s ATR 42-320 (MSN 78, see Figure 9). Figure 13 shows the drag polar calculated from flight test data of the clean air flights with the aircraft in campaign configuration together with the pre-campaign reference used to design the IID and the modified drag polar used for the icing flight tests.

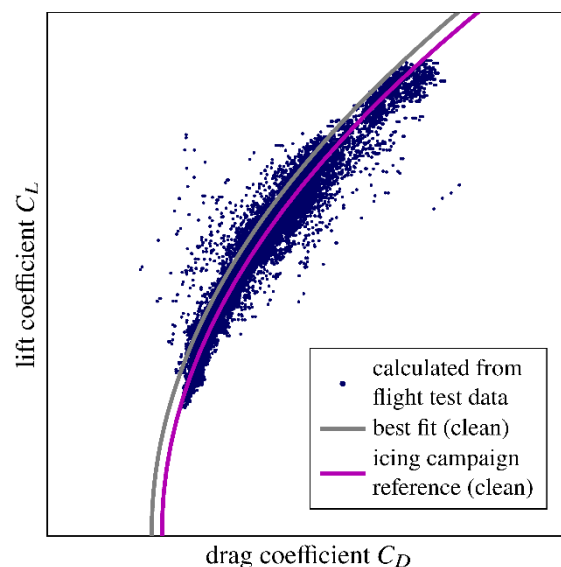


Figure 13: Aircraft drag polar for Safire ATR 42-320 (MSN78) used for the SENS4ICE European icing flight test campaign: calculated lift and drag coefficient from flight test data (**blue dots**), pre-campaign reference drag polar (**gray line**, no SENS4ICE aircraft modification) and adapted campaign reference drag polar considering aircraft modifications (**magenta line**); clean air flights in final aircraft configuration with all modification required for SENS4ICE on March 22nd and 23rd, 2023.



Moreover, for both flight test benches ATR and Embraer delivered detailed information about the propeller respectively engine thrust based on the inflight measurements of propeller and engine states. Note, that in case of the Phenom 300 a numerical engine thrust model was shared which does not represent the correct engine performance but provides a sufficient estimation for the IID implementation. Having this available for SENS4ICE, the definition of a different reference model formulation for the propulsion system influence on the reference flight performance is of no additional value. Consequently, the flight performance reference consists of different data bases and reference model formulations adapted to the SENS4ICE purposes, but is still generally valid for different aircraft implementation if required.

#### Detection Threshold and Confirmation Time

Abnormal flight performance can result from different sources as initially discussed. But if resulting from ice accretion on the airframe it is assumed to be persistent and constantly increasing. In this case, the flight performance degradation is leading to the indirect ice detection, but must not be subject to false alarms. Therefore, a detection threshold on the equivalent drag coefficient has to be defined which ensures that the degradation is significant and critical for the further flight. For practical reasons, the detection is not done on the absolute value of the equivalent drag increase but on a relative value with the zero-lift drag coefficient as base. In a nominal case, the additional drag coefficient is zero and there is no relative change to the normal drag condition.

During normal operation flight there is a constant fluctuation of measured flight performance, sometimes also exceeding the threshold. One simple reason is that the data used for the detection is processed online in near real time and therefore affected by measurement noise which is not filtered although the measurements are calibrated and corrected for constant known errors. To reduce the overall effort of the data processing and computations necessary for detection, the input data are not filtered for noise but the equivalent drag coefficient is. A low-pass filtering allows to remove the higher frequency fluctuations resulting from noise. Furthermore, flight performance is also affected by atmospheric disturbances, which are accounted for by monitoring the performance in the aerodynamic frame, but this relies on an accurate measurement of the inflow with high resolution. This is commonly not available on transport aircraft because e.g., the flight control system does not require those. Hence, the measured flight performance will also contain some fluctuations for which a reliable detection algorithm has to account for. As these will also lead to a short-time exceedance of the detection threshold from time to time, the detection module requires the implementation of a confirmation time, which is set large enough to prevent a false detection resulting from other effects leading to a threshold exceedance.

The confirmation time is chosen in accordance with the modelling accuracy of the whole IID system chain and quality of flight data. A high quality and accuracy of flight data measurements together with a highly accurate performance reference data base can lead to relatively short confirmation times whereas lower data quality and/or performance reference accuracy must lead to longer confirmation times in order to prevent false detections. To ensure that the equivalent drag exceeds the threshold most of the time (more than 50%) within a considered time frame weighted moving averages are used. These are based on a certain confirmation time frame and different for the positive detection and the reset after leaving the icing situation. For the detection, the confirmation time frame is chosen relatively short to ensure fast response behaviour but for reset that confirmation time must be much longer to guarantee the threshold is reliably undershot and the icing-related performance degradation is not present anymore. The corresponding values are given in Table 5.

	<b>SAFIRE ATR 42-</b>	<b>Embraer Phenom</b>
detection threshold as relative drag coefficient increase	15 %	10 %
confirmation timeframe for detection (threshold exceeded more than 50%)	20 s	20 s
confirmation time for reset (threshold undershot more than 50%)	180 s	180 s

Table 5: Detection threshold values and confirmation time for the different IID implementations for the SENS4ICE flight test benches.



### Indirect Detection Reliability Conditions

The IID is designed to run continuously during the whole flight and to monitor the aircraft flight performance, and a potential degradation, independently from any specific flight phase or manoeuvre, as discussed in Ref. [10]. This also includes considering different aircraft configurations for different settings of the high lift system and gear extension. Nevertheless, the implementation in SENS4ICE is currently experimental and limited to one aircraft configuration without flaps or gear extended because of the flight test in icing conditions being only performed in this configuration for flight safety reasons. For all other aircraft configurations, the IID is designed to detect that the configuration is not reflected in the current implementation, freeze and set an unreliability flag allowing the HIDS to discard the current IID output. Freezing in this case allows to not load the moving average filters with unreliable data leading to a false positive detection when the IID is reactivated after a configuration change. A similar procedure is applied for short-term effects on the flight performance not included in the reference flight performance data base to reduce the overall effort for calculations in the IID like the use of speed-brakes. During these phases, the IID also freezes and the output unreliability is set.

## 2.3 IID results for North America FT campaign

Results from two different flights of the North America icing flight test campaign are presented and evaluated. During these flights the flight test crew successfully encountered different icing conditions including classical App. C and the rare SLD conditions (App. O).

### FLIGHT 1475

The first selected flight took place on February 23rd, 2023, departing from Chicago O'Hare Airport at 17:18 UTC (11:18 local) and searching for icing conditions on the way back south to St. Louis Regional Airport in Alton, Illinois. After around 1h of flight, the aircraft landed on St. Louis Regional Airport having successfully encountered App. C icing conditions two times during flight. An overview of the flight is given in Figure 14 including the flight track and icing encounters. Note that the information about the icing conditions found is resulting from the evaluation of atmospheric conditions measured with the reference probes during flight.

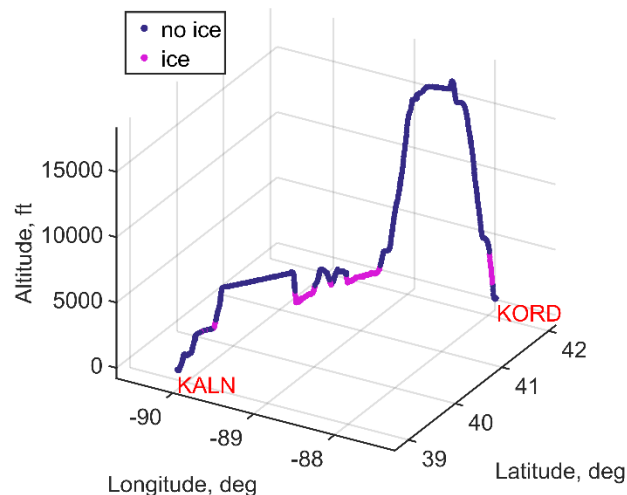


Figure 14: Flight track from SENS4ICE North America icing campaign flight on February 23rd, 2023 (Chicago O'Hare, KORD, to St. Louis Regional Airport, KALN): geodetic position and altitude with indication of icing encountered.

The IID performance during this example is evaluated for the two major icing encounters in the middle of the flight. These are visualized as time history plots in Figure 15 and Figure 16. The top plot contains the altitude and indicated airspeed for each flight segment respectively icing encounter. It is clearly visible that the aircraft



was intentionally descending into the (expected) icing conditions and climbing again out of these after a certain encounter time. The second plot (from top) shows the nominal drag estimation (based on clean aircraft zero-lift drag) and gives a direct impression about the performance degradation. In parallel, the IID detection output is given allowing a direct comparison of drag increase and IID detection performance. Note that the shown data are a result of the online IID calculation within the HIDS system implementation directly fed with aircraft data/measurements. The third plot (from top) contains the information about the encountered icing conditions. The measured droplet size (MVD) and liquid water content (LWC) describe the atmospheric icing conditions, in the presented case classical App. C conditions with smaller droplets. The bottom plot contains the measured static air temperature as well as the averaged engine fan speed (left and right, assuming symmetric thrust conditions). During the descend into the icing conditions the temperature decreases significantly and increases again after leaving the conditions, indicating an atmospheric inversion layer. This allows a direct assessment about the icing encountered leading to airframe ice accretion and hence a performance degradation, together with the possibility to cross-check the detection reset with the flight through warm air and consequently de-icing. The averaged engine fan speed is directly linked to the total engine thrust and therefore gives an information about the forces applied to the aircraft in combination with the aerodynamic performance degradation.

Figure 15 shows the first icing encounter during the flight after descend to an altitude of 3,500 ft. The encounter starts at 17:42 UTC leading to a noticeable performance degradation due to ice accretion at around 17:44 UTC. The detection threshold was constantly exceeded at 17:45:50 UTC causing a confirmed detection 10 s later (17:46 UTC). This means that the IID icing indication was present within 2 min after the performance degradation was starting. The performance degradation and drag was further increased during the whole encounter and reached a maximum of more than 30% before leaving the conditions and starting the full airframe de-icing in warmer air with higher speed, leading to a detachment of all ice formation on the airframe. During climb, the reference performance of the flight test aircraft with SENS4ICE modifications was restored and the monitored degradation decreased leading to a reset of the IIDSIIID at around 17:55:05 UTC.

Between 17:52:30 UTC and 17:53:10 UTC, a significant peak in the drag estimation is visible. At first sight, it seems very unrealistic that this is a consequence of the performance degradation caused by icing. Looking to the averaged engine fan speed, it becomes clear that this peak in performance degradation is directly linked to the increase of engine fan speed and therefore thrust (including the applied filtering in the IID). Knowing that the engine thrust information embedded in the IID originates from an approximation of the Pratt & Whitney PW535E engine behavior leads directly to the conclusion that the used model is not capable of correctly representing the engine thrust at the given flight condition: thrust increase at low altitude, low speed and significant negative temperature offset  $\Delta ISA$  (lower temperature compared to normal conditions in the given altitude). A detailed evaluation of this behavior was part of the initial post-flight data analysis and subject to a proposal for the IID implementation modification given below.

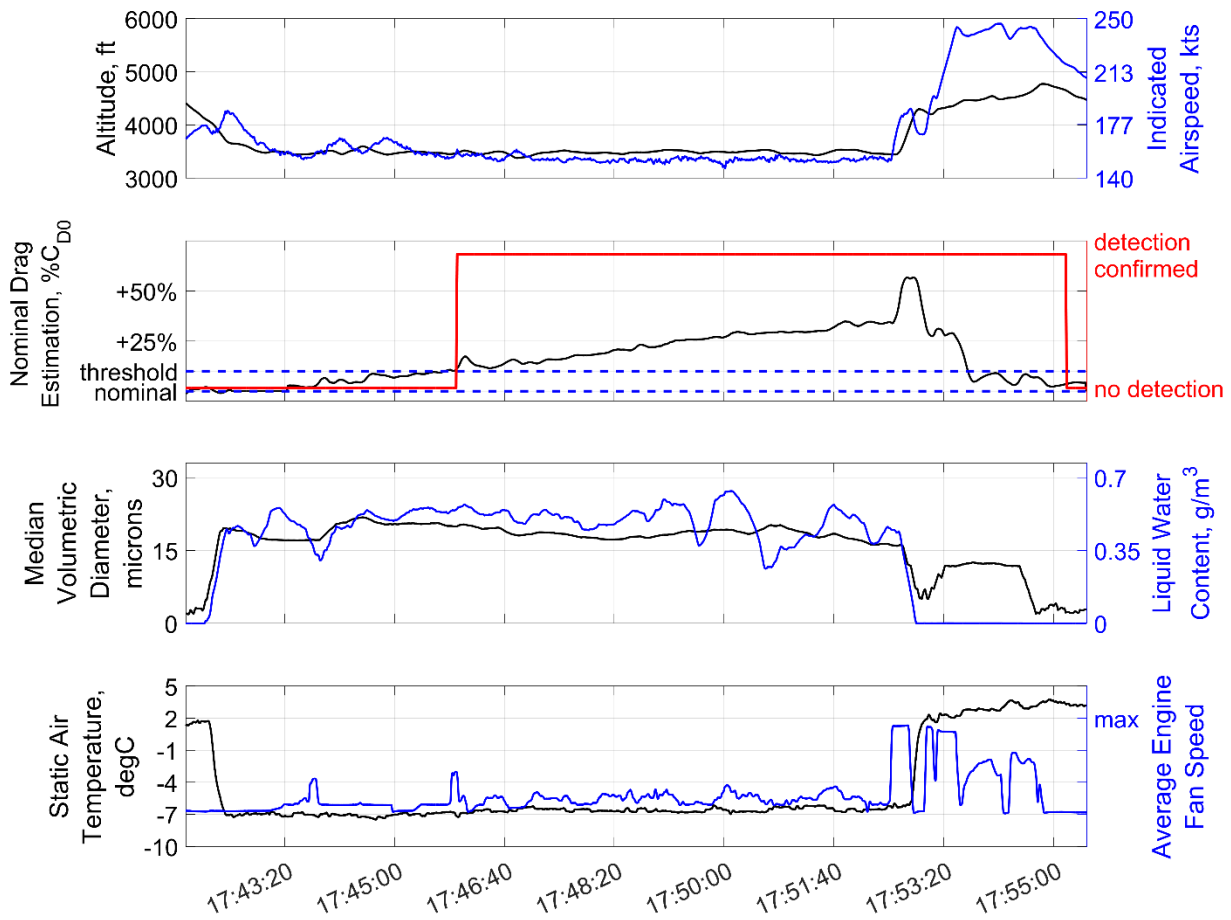


Figure 15: Time history of IID system performance during specific icing encounter from the first example flight (February 23<sup>rd</sup>, 2023, 17:41:49 UTC to 17:55:29 UTC): altitude and indicated airspeed (top), nominal drag estimation and IID detection output (second plot), and MVD and LWC of encountered icing conditions (third plot), and static air temperature and average engine fan speed (bottom); detection threshold at 10% relative drag increase.

A similar time history plot for the second encounter of the example flight is given in Figure 16. The aircraft descended into icing conditions and reached the target altitude of 3,500 ft at 18:01:40 UTC. The encounter started already during the descent leading directly to a noticeable performance degradation of around 5% when leveling off. The drag was constantly increasing during the encounter exceeding the detection threshold at around 18:03:10 UTC. This caused a confirmed ice detection within less than two minutes after the beginning of the icing encounter. The performance degradation further increased during the flight in the icing clouds reaching again a maximum of around 30% before the aircraft was accelerated again for climbing out the cloud layer. After reaching 6,000 ft with warmer air, the airframe was de-iced and the nominal flight performance was restored resetting the IID detection output at 18:11:30 UTC. With full engine thrust applied between 18:08:00 UTC and 18:08:40 UTC, a similar peak in the nominal drag estimation to the first encounter could be observed underpinning the above discussed finding.

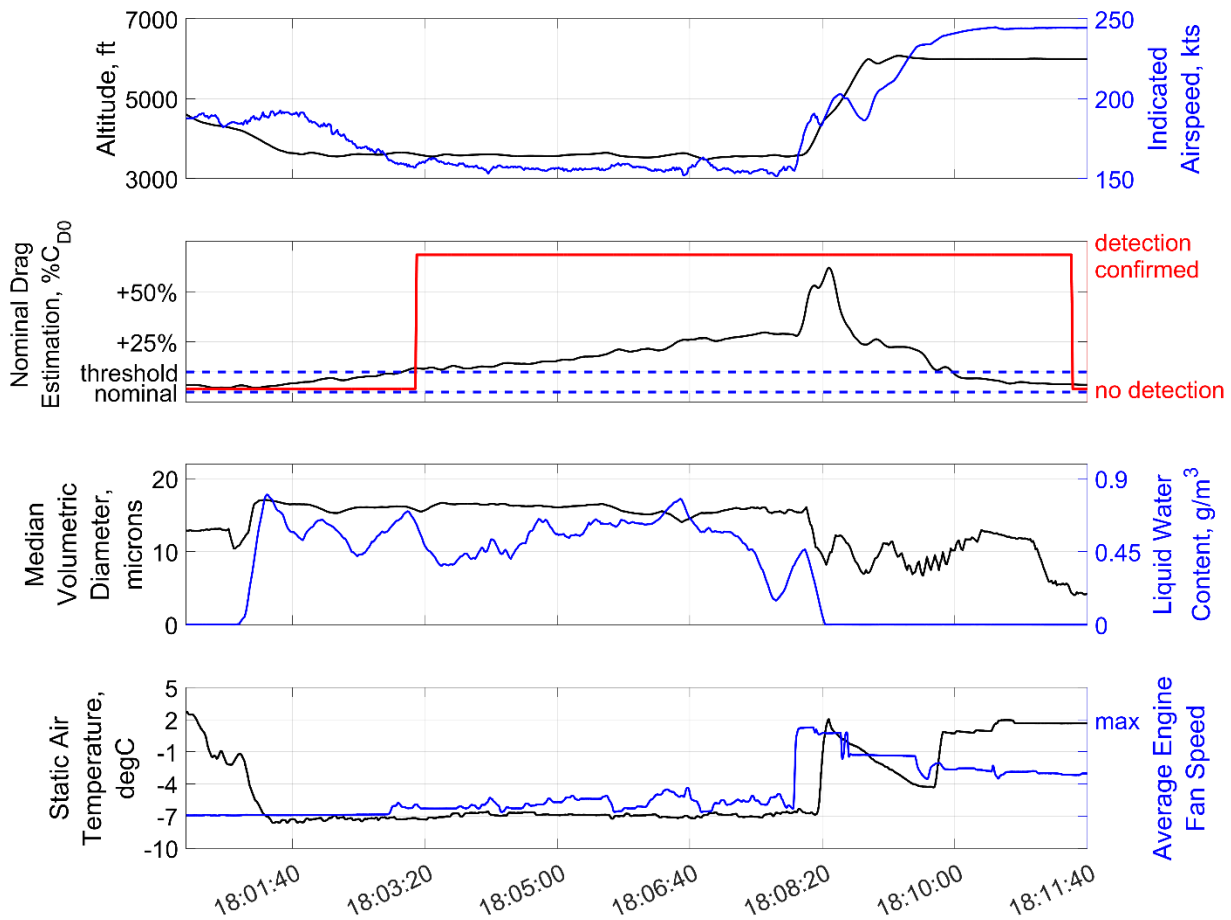


Figure 16: Time history of IID system performance during specific icing encounter from the first example flight (February 23<sup>rd</sup>, 2023, 18:00:19 UTC to 18:11:39 UTC): altitude and indicated airspeed (top), nominal drag estimation and IID detection output (second plot), and MVD and LWC of encountered icing conditions (third plot), and static air temperature and average engine fan speed (bottom); detection threshold at 10% relative drag increase.

### Aerodynamic Degradation due to icing

Figure 17 shows the aircraft drag polar calculated from the measured data for the whole flight (flaps retracted, gear up and no spoiler deflection). For each data point available in the measurement, the lift and drag coefficient is calculated based on the available inertial and inflow measurements as well as the given engine thrust model (see, e.g., Ref. [13] for detailed information on the equations). The plot further contains the aerodynamic reference used for the flight test reflecting the Phenom 300 prototype characteristics with all SENS4ICE modifications (red line). Furthermore, the drag polar data includes an indication of the corresponding IID calculated nominal drag estimation (normalized with base aircraft zero-lift drag). Blue marks indicate a nominal drag, which means that there is no increase detected. The more the aircraft is degraded, the more the drag increases and the marks are moving to the right getting lighter. Orange marks indicate the maximum calculated drag increase, which has to be taken with caution in the presented case for the already mentioned reasons. Anyway, the cyan marks show a drag increase of around 30% (compared to the nominal value) which was approximately the maximum present during the icing encounters as shown in Figure 15 and Figure 16. Without any further modifications of the IID, it can be already stated that the IID is capable of reliably and correctly indicating the current aircraft performance degradation caused by airframe icing.

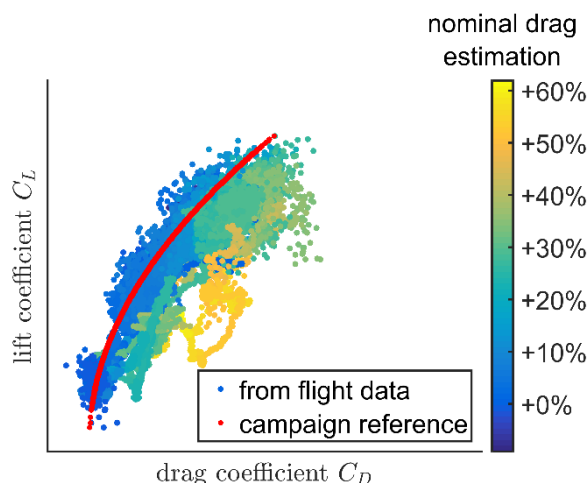


Figure 17: Aircraft drag polar from SENS4ICE North America icing campaign flight on February 23rd, 2023 from Chicago O'Hare to Alton: calculated lift and drag coefficient from flight data measurements and drag polar reference (red line) for the Phenom300 prototype with SENS4ICE modifications (high-lift devices and gear retracted); drag coefficient data including the indication of nominal drag estimation calculated by IID.

Figure 18 shows the similar illustration of calculated lift and drag data, but now only for a certain selection of flight data excluding high engine fan speeds and larger negative temperature offsets ( $\Delta ISA < -5^\circ C$ ). It is directly visible that the large calculated drag increase has vanished. Now a clear discrimination of clean (blue marks) and iced aircraft (cyan marks) is visible in the plot (only some orange marks indicating very large drag increase left). Hence, this underpins the above presented assumption that the used (approximated) engine thrust model over-predicts the true engine thrust in certain parts of its envelope, i.e., high engine fan speeds and large negative temperature offsets.

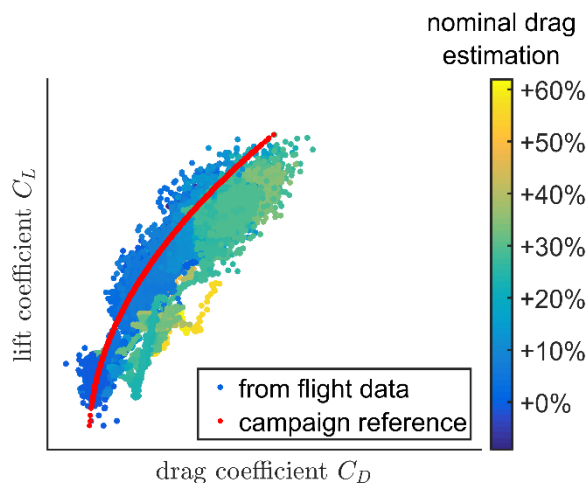


Figure 18: Aircraft drag polar from example flight (selected data from Figure 17): calculated lift and drag coefficient from flight data measurements and reference for the Phenom300 prototype (red line) with SENS4ICE modifications; data excluding high engine fan speeds ( $N_1$ ) and significant negative temperature offsets  $\Delta ISA$ ; drag coefficient data including the indication of nominal drag estimation calculated by IID.



### Post-Flight IID Evaluation and Initial Adjustment

With the first flight test data analysis available, the IID performance is further evaluated post-flight using the design model and replayed flight test data. The IID model is available for MATLAB®/Simulink including an emulation of the interface to the HIDS used during flight test. Furthermore, the IID design model allows to directly access individual signals within the IID to further evaluate the system behavior and performance to specific influences, like the full thrust scenario which is of main concern for the evaluation. It also enables changes of the detection parameters, e.g., threshold and confirmation times.

After finding that the used engine thrust model might overpredict the engine thrust sometimes, simple model adjustments were introduced to verify the assumption. It is clear that the engine thrust is strongly dependent on the engine fan speed and normally shows a highly nonlinear behavior for high fan speeds. Exactly this behavior must be modified by a reduction of the maximum values without changing the engine thrust for lower fan speeds or idle. Figure 19 visualizes this required model adjustment schematically. Note that the engine thrust is further dependent on other parameters like airspeed, altitude/pressure, temperature offset etc., which are not included in this simple figure, but expand the curve to a multi-dimensional space. The dashed line for the adjusted model indicates the slight reduction of the nonlinear behavior and maximum thrust value is reduced while preserving the low fan speed behavior.

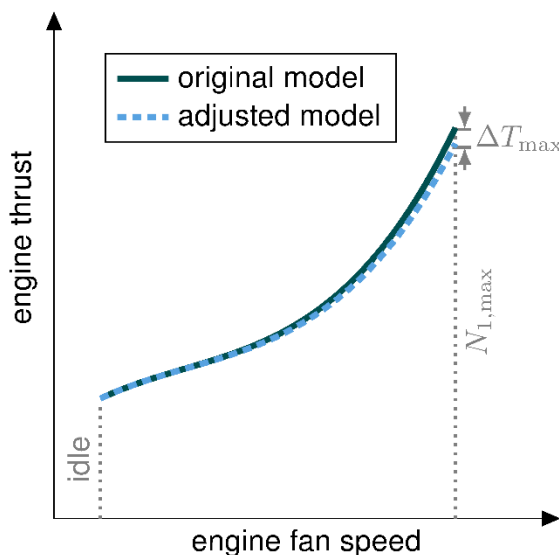


Figure 19: Schematic illustration of engine thrust model adjustment to counteract non-linear behavior with high engine fan speeds: reduction of max. thrust with fan speeds near ( $N_{1,max}$ ) while maintaining the same thrust level for idle and medium fan speeds which correspond to the engine state for icing encounters.

A simple linear formulation of the adjustment function allows to directly achieve the new engine thrust model behavior using the original model output  $T_{model}$ :

$$T_{adjusted} = T_{model} \cdot f_T + b_T. \quad (5)$$

During the preliminary post-flight evaluation, it was found that a few percent of reduction (values for  $f_T \geq 0.95$ ) and an offset  $b_T$  of several hundred Newton is enough to achieve much better results. Furthermore, as the data was gathered in flight from different aircraft buses with different sample rates, a suitable synchronization and therefore collinearity of data might not be given. This means that the acceleration and engine state measurement might be shifted against each other. Hence, it was further checked if the consideration of such shift in the IID process will additionally enhance the results, especially in the high thrust scenario. But it was found that such shift has no significant impact if considered to be between 0 and 100 ms in both directions.

Figure 20 contains the flight test aircraft drag polar for the whole flight including the icing encounters, now calculated with the adjusted engine thrust, similar to Figure 17. It further contains again the flight test reference polar and an indication of the IID estimated nominal drag, this time also from a post-flight replay with the adjusted engine thrust characteristics in the performance state calculation. The maximum drag change as well as the maximum predicted performance degradation from the IID are both significantly reduced compared to



the online flight test results presented in Figure 17 as a direct consequence of the model adjustment. The maximum drag increase is limited to around 35% of the nominal estimate which is the assumed impact of the ice formation on the airframe on the aerodynamics during the icing encounters (with still some larger values present but not affecting the IID behavior). These preliminary results give a good confidence that the source of the unreliably large drag increase is related to the full thrust scenarios.

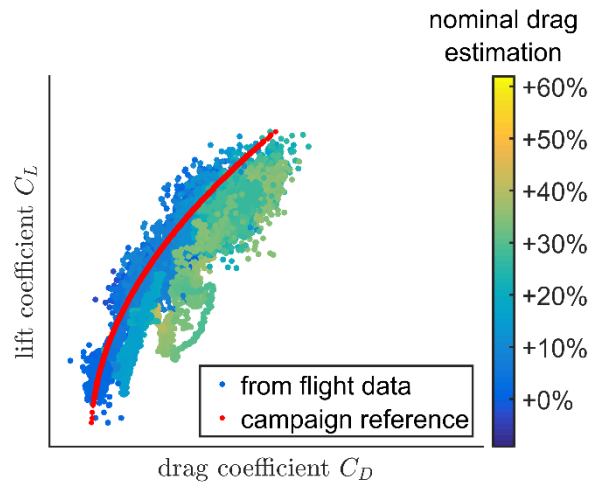


Figure 20: Aircraft drag polar from example flight (same data as in Figure 17) after engine thrust model adjustment: calculated lift and drag coefficient from flight data measurements and reference for the Phenom300 prototype with SENS4ICE modifications; drag coefficient data including the indication of nominal drag estimation calculated by IID with **adjusted engine thrust during data replay**

In addition to the evaluation of the aircraft aerodynamics the time histories of the IID performance during the encounters were analyzed. Figure 21 shows the IID output for the replayed flight test data of the first icing encounter (see Figure 15) with the given adjustments. The calculated drag increase has changed compared to the flight test implementation by removing some peaks in the time histories correlated with high engine fan speeds: at around 17:45:55 UTC, the engine is spooled up for a few seconds causing a small peak in the nominal drag estimation in Figure 15 which is not existing anymore. Also, the large predicted increase starting from 17:52:30 UTC while climbing out of the icing cloud is now removed and the maximum degradation predicted by the IID remains at around 35% which is more reasonable. Similar results are obtained for the second encounter shown in Figure 22 where the questionable peak in the nominal drag estimation could be significantly reduced, too.

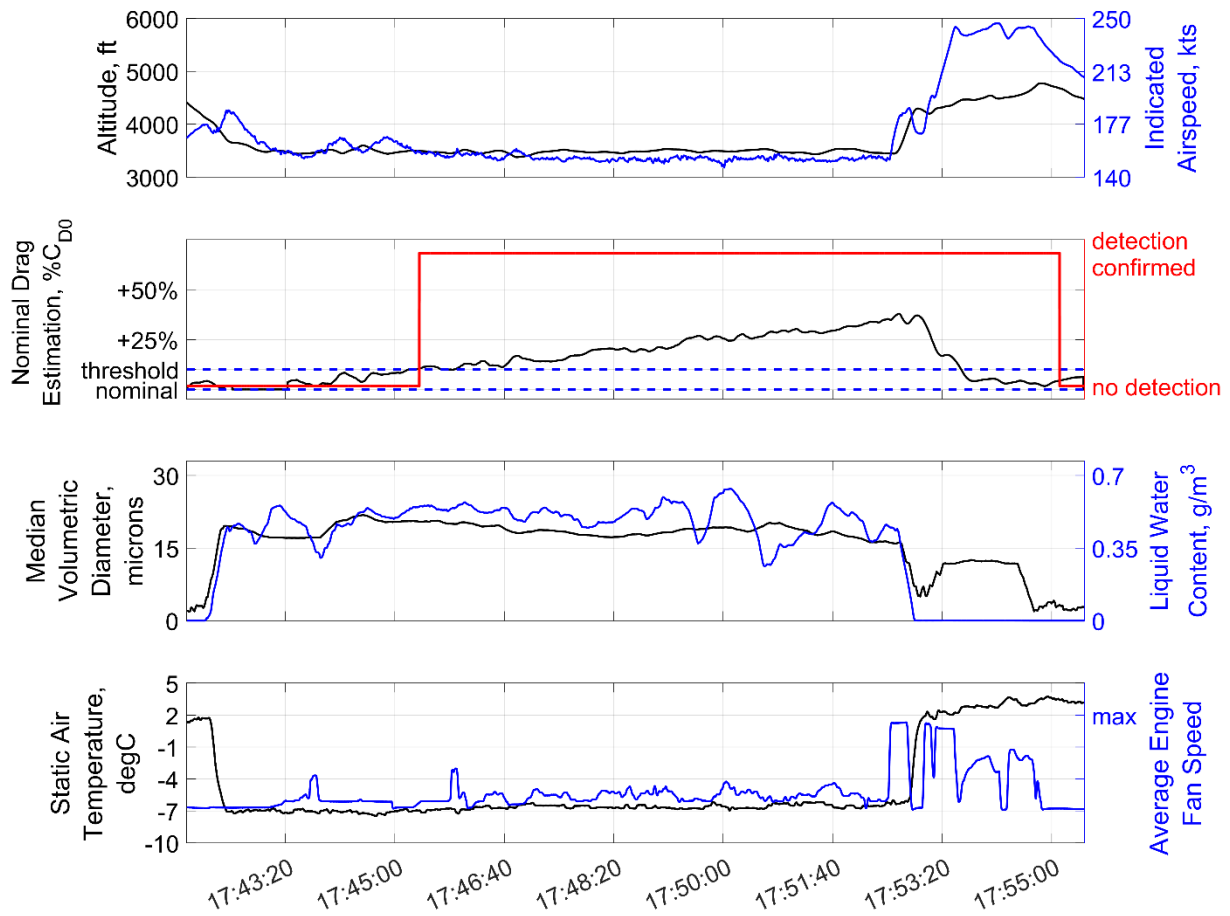


Figure 21: Time history of IID system performance during specific icing encounter from the first example flight (February 23<sup>rd</sup>, 2023, 17:41:49 UTC to 17:55:29 UTC): altitude and indicated airspeed (top), nominal drag estimation and IID detection output (second plot), and MVD and LWC of encountered icing conditions (third plot), and static air temperature and average engine fan speed (bottom); detection threshold at 10% relative drag increase; **adjusted engine thrust model behavior compared** to Figure 15.

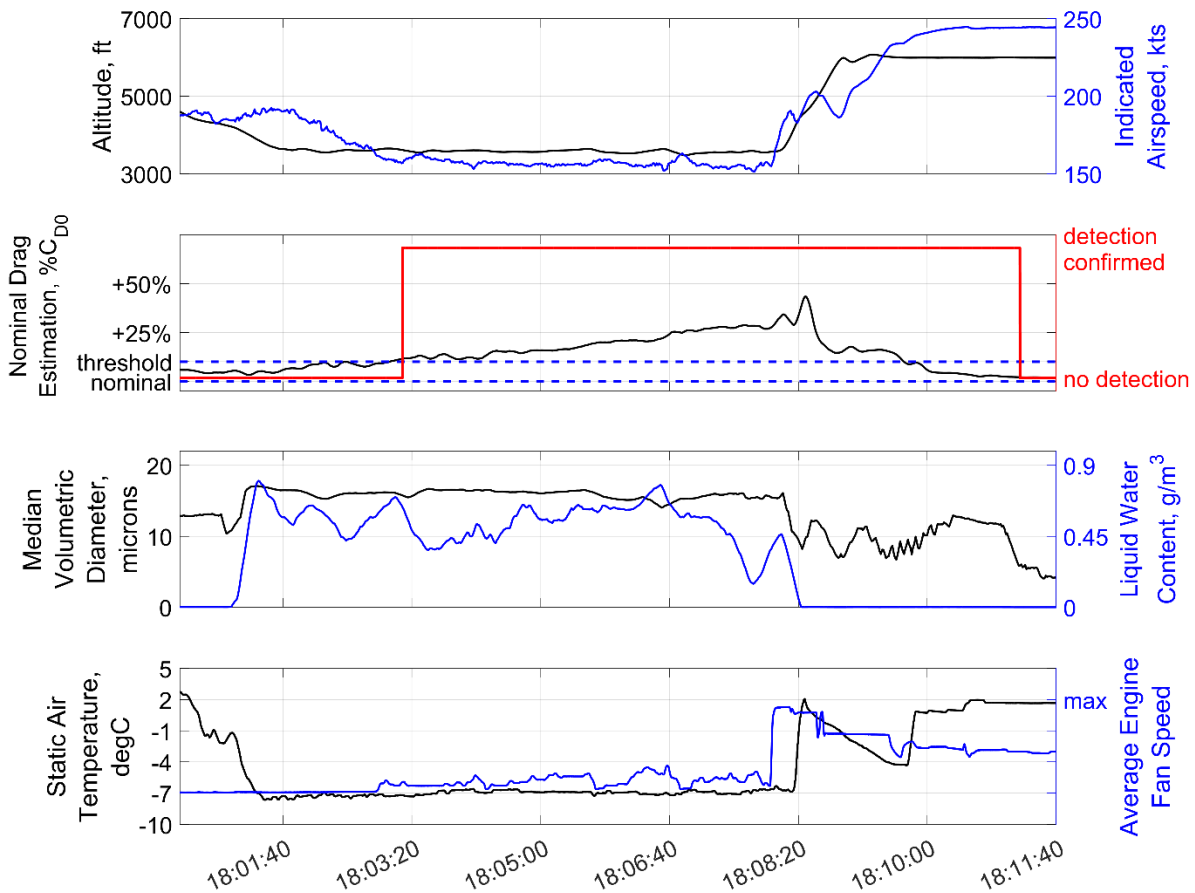


Figure 22: Time history of IID system performance during specific icing encounter from the first example flight (February 23<sup>rd</sup>, 2023, 18:00:19 UTC to 18:11:39 UTC): altitude and indicated airspeed (top), nominal drag estimation and IID detection output (second plot), and MVD and LWC of encountered icing conditions (third plot), and static air temperature and average engine fan speed (bottom); detection threshold at 10% relative drag increase; **adjusted engine thrust model behavior** to Figure 16.

## FLIGHT 1476

The second selected flight on February 25<sup>th</sup>, 2023, left St. Louis Regional Airport in Alton, Illinois, in a north easterly direction to the great lakes at 11:38 UTC (5:38 local) reaching Eugene F. Kranz Toledo Express Airport in Toledo, Ohio, at 13:42 UTC (7:42 local). Within the vicinity of the great lakes after around 40min of flight icing conditions were found leading to 5 successful encounters also including App. O conditions respectively SLD. Note that during the encounters the total amount of SLD was low compared to the other supercooled water drops with lower size, as it was expected due to the rarity of SLD in the atmosphere. An overview of the flight is given in Figure 23 including the flight track and icing encounters.

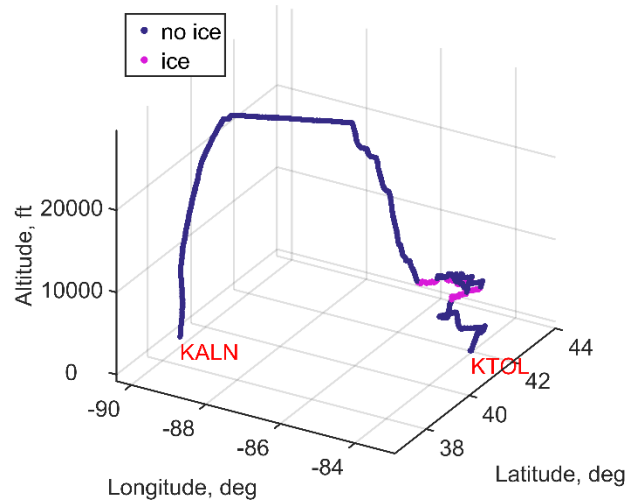


Figure 23: Flight track from SENS4ICE North America icing campaign flight on February 25th, 2023 (St. Louis Regional Airport, KALN to Toledo Express Airport, KTOL): geodetic position and altitude with indication of icing encountered.

The IID performance during this example is evaluated for the five icing encounters near Toledo. These are visualized as time history plots in Figure 24 and Figure 28. The plots are similar to the visualization of the IID behavior during the encounters of the previous flight (1475) in Figure 16 and Figure 17 or Figure 21 and Figure 22. Note that during these encounters drops above  $100\ \mu\text{m}$  were present resulting in a positive evaluation in terms of App. O and SLD. Nevertheless, two important remarks must be made in order to further evaluate the IID results:

1. The overall liquid water content was lower during these 5 encounters in flight 1476 than it had been during the encounters in flight 1475, although the droplet distribution was different. This has a direct effect on the visible performance degradation during the encounters which is successfully detected by the IID. The maximum values reached after a comparable time in icing conditions (flight 1746 compared to flight 1475, both up to 7min) are lower because less ice was gathered in total on the aircraft, which is mainly related to the total amount of water drops collected. Note that this does not imply any severity, criticality or safety evaluation for the aircraft or flight operation, but basically is required as background knowledge to interpret the IID results during the encounters including SLD.
2. The presence of SLD in the clouds which then cause icing on the aircraft when flown through does not directly imply a change of the ice accretion on the airframe. For the ice formation and the resulting shapes affecting the aircraft's aerodynamics the total amount of SLDs in relation to smaller droplets is important. A few SLDs in the clouds with a total amount of smaller drops several magnitudes larger might not affect the resulting ice formation whereas, the presence of a majority of SLD in the icing conditions will of course strongly affect the appearance of ice shapes on the aircraft. Hence, the IID results for this flight 1476, which had only a very small amount of SLD in the conditions, are not consequently representative for an expectable performance degradation as it could result from App. O conditions with a larger amount of SLD. For the IID and the performance degradation the negative impact of ice shapes on aerodynamics is important and this could be similar or worse when caused solely by classical App. C conditions than for the conditions encountered also including SLD. Furthermore, every encounter is different, so it is per se very difficult to compare the specific results in order to make general conclusions.

Figure 24 to Figure 28 now contain in the third plot (from top) in addition to the information about the encountered icing conditions given by measured droplet size (MVD) and liquid water content (LWC) (all drops, solid lines) an information about the SLD part of the conditions (dashed line). In the plots, the icing encounters can be again defined as starting during the descend when the temperature decreases significantly and ending



with its increase again after leaving the conditions. Remind that although liquid water might be present, icing can only occur for temperatures below 0°C.

Note that for some time the estimated drag jumps to the nominal value due to an unreliable estimation caused by the deployment of the aircraft spoilers. During this time the calculation is stopped and the IID output is marked as unreliable with nominal drag estimation values. This is the case in Figure 24 until 12:20 UTC during the descent and between 12:30:50 UTC and 12:31:40 UTC to reduce the speed after climb out.

During all encounters the IID was able to reliably detect the performance degradation 2 min or less after the ice built up started. The confirmed detection remained every time until the aircraft left the conditions and was completely de-iced again. For these encounters, the time to restore the nominal flight performance and to reset the detection flag took approximately the same time as the aircraft stayed in the conditions itself. This shows the **great value of the IID because it reliably indicates the aircraft degradation being possibly critical for the aircraft operation especially if the degradation is unknown, which is also monitored once the icing conditions are already left**. This is one of the keys related to the layered safety concept provided by SENS4ICE including the HIDS approach.

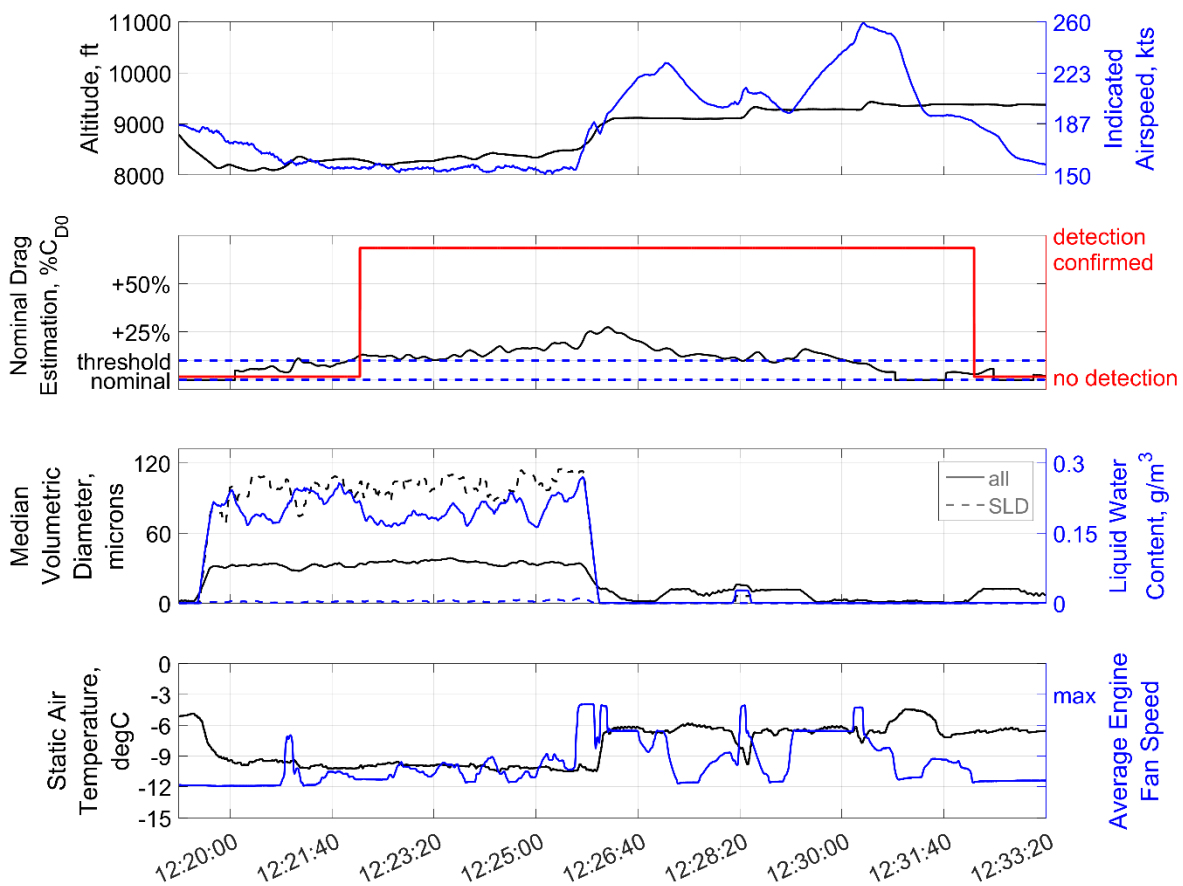


Figure 24: Time history of IID system performance during specific icing encounter from the first example flight (February 25<sup>th</sup>, 2023, 12:19:09 UTC to 12:33:20 UTC): altitude and indicated airspeed (top), nominal drag estimation and IID detection output (second plot), and MVD and LWC of encountered icing conditions (third plot) including the indication of the amount of SLD (dashed lines), and static air temperature and average engine fan speed (bottom); detection threshold at 10% relative drag increase; **adjusted engine thrust model behavior**.

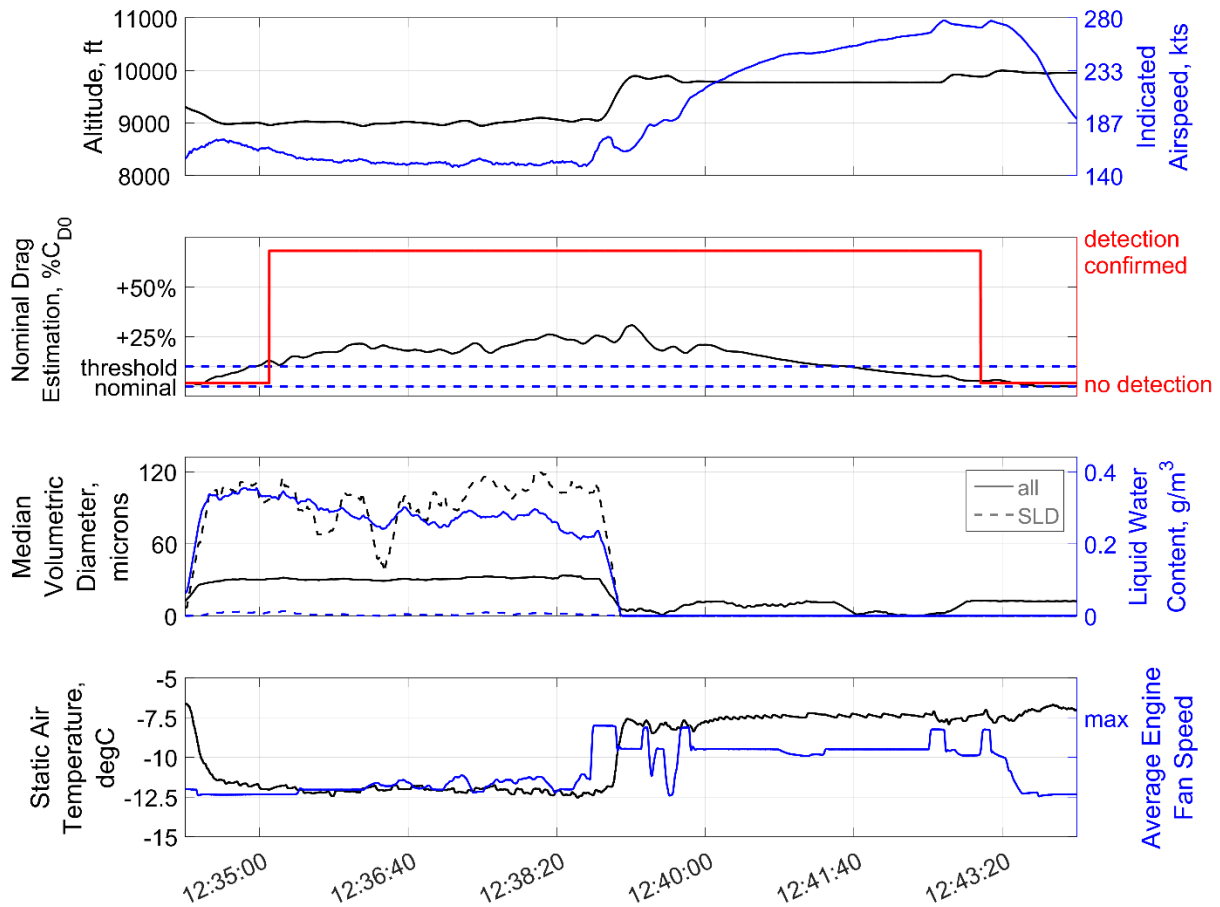


Figure 25: Time history of IID system performance during specific icing encounter from the first example flight (February 25<sup>th</sup>, 2023, 12:34:09 UTC to 12:44:09 UTC): altitude and indicated airspeed (top), nominal drag estimation and IID detection output (second plot), and MVD and LWC of encountered icing conditions (third plot) including the indication of the amount of SLD (dashed lines), and static air temperature and average engine fan speed (bottom); detection threshold at 10% relative drag increase; **adjusted engine thrust model behavior**.

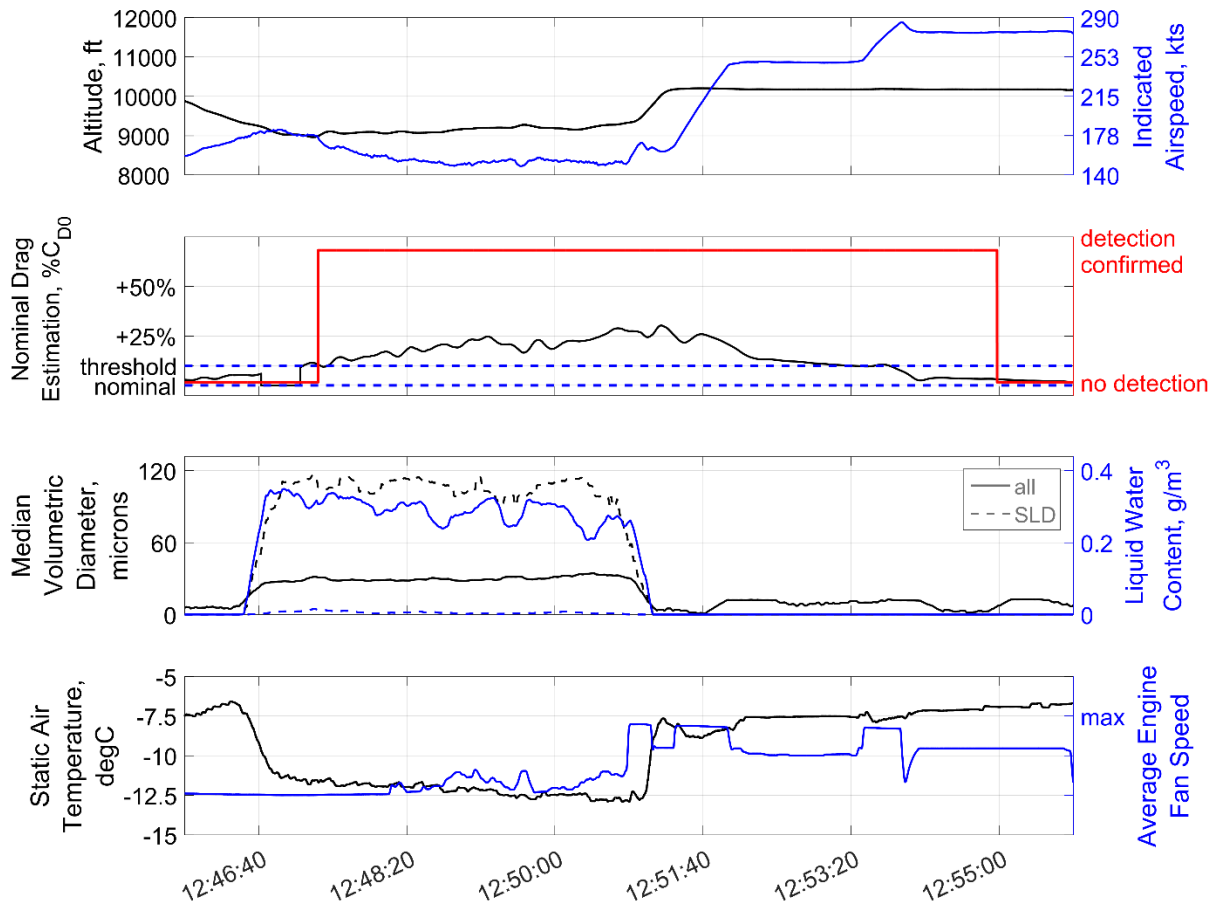


Figure 26: Time history of IID system performance during specific icing encounter from the first example flight (February 25<sup>th</sup>, 2023, 12:45:49 UTC to 12:55:49 UTC): altitude and indicated airspeed (top), nominal drag estimation and IID detection output (second plot), and MVD and LWC of encountered icing conditions (third plot) including the indication of the amount of SLD (dashed lines), and static air temperature and average engine fan speed (bottom); detection threshold at 10% relative drag increase; **adjusted engine thrust model behavior**.

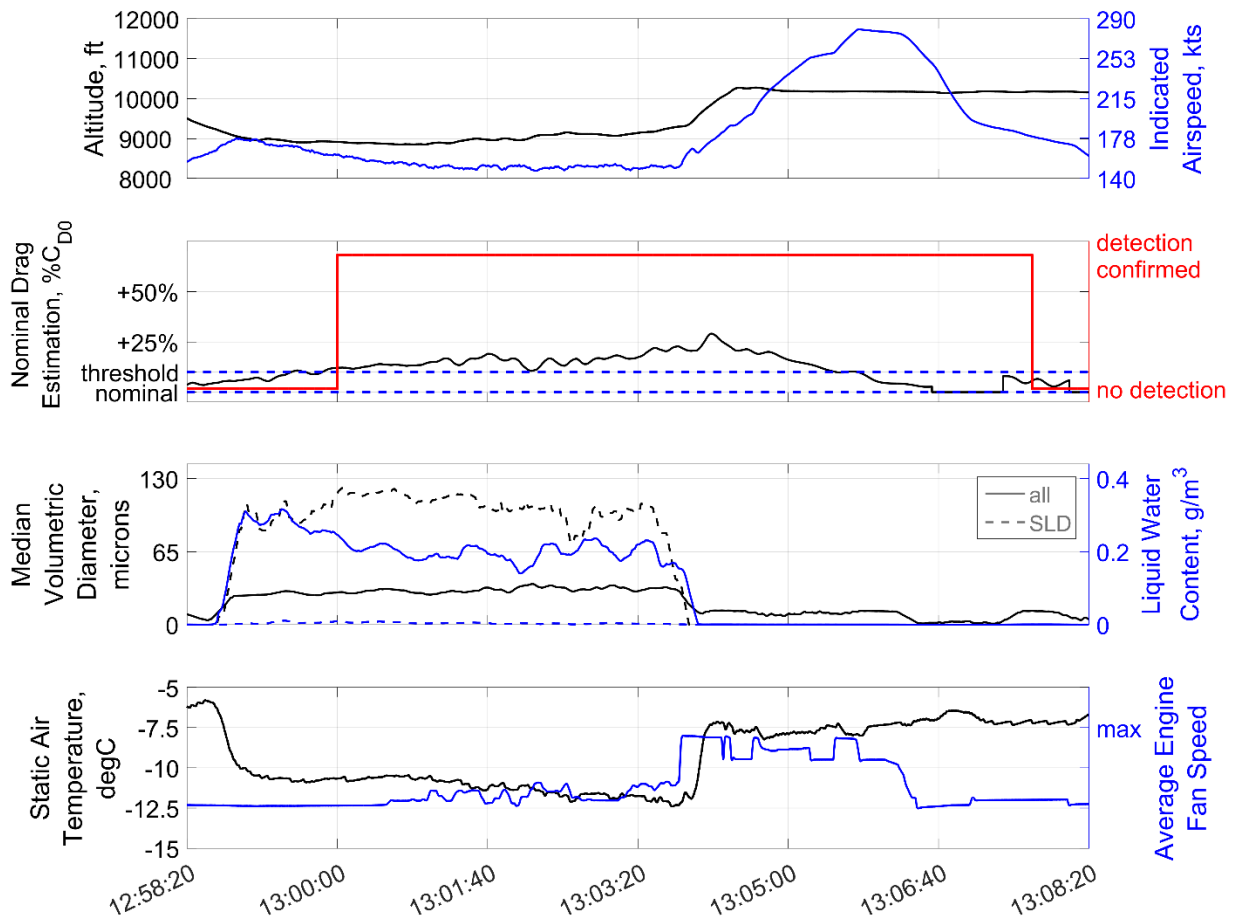


Figure 27: Time history of IID system performance during specific icing encounter from the first example flight (February 25<sup>th</sup>, 2023, 12:58:19 UTC to 13:08:19 UTC): altitude and indicated airspeed (top), nominal drag estimation and IID detection output (second plot), and MVD and LWC of encountered icing conditions (third plot) including the indication of the amount of SLD (dashed lines), and static air temperature and average engine fan speed (bottom); detection threshold at 10% relative drag increase; **adjusted engine thrust model behavior**.

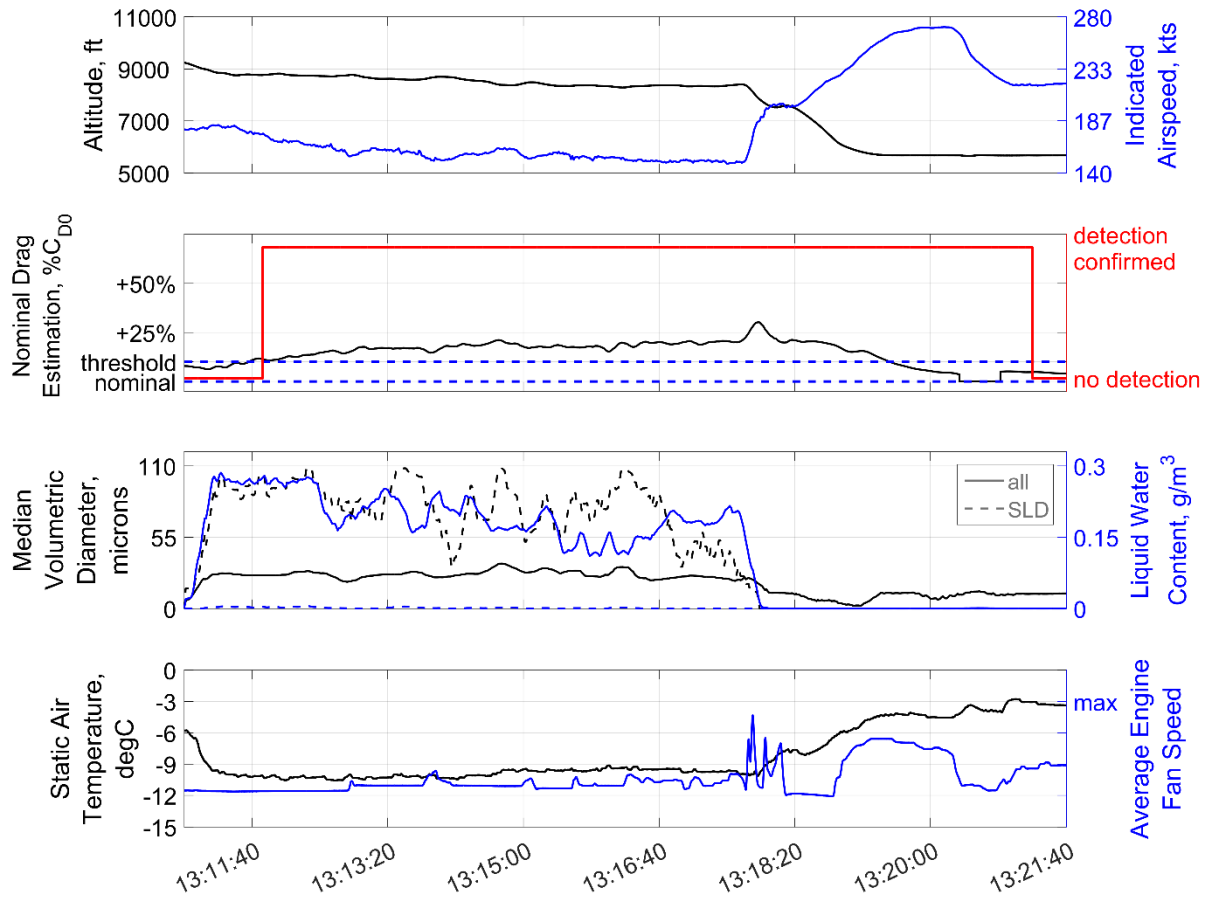


Figure 28: Time history of IID system performance during specific icing encounter from the first example flight (February 25<sup>th</sup>, 2023, 13:10:49 UTC to 13:21:39 UTC): altitude and indicated airspeed (top), nominal drag estimation and IID detection output (second plot), and MVD and LWC of encountered icing conditions (third plot) including the indication of the amount of SLD (dashed lines), and static air temperature and average engine fan speed (bottom); detection threshold at 10% relative drag increase; **adjusted engine thrust model behavior**.

### **Aerodynamic Degradation due to icing**

Figure 29 shows the aircraft drag polar calculated from the measured data for the whole flight (flaps retracted, gear up and no spoiler deflection) similar to Figure 20. For each data point available in the measurement, the lift and drag coefficient is calculated based on the available inertial and inflow measurements as well as the given engine thrust model including the adjustment described above. Again, the plot contains the aerodynamic reference used for the flight test reflecting the Phenom 300 prototype characteristics with all SENS4ICE modifications (red line).

The maximum degradation is correlated with a nominal drag estimation of around 30%, but having 25% change in average related to icing in a more continuous manner, meaning that the degradation is kind of saturated is visible in Figure 24 to Figure 28. Knowing that the main degradation is related to an increase of surface fraction on (mainly) unprotected aircraft parts, this is reasonable. This is well comparable to the results for the previous flight in App. C conditions.

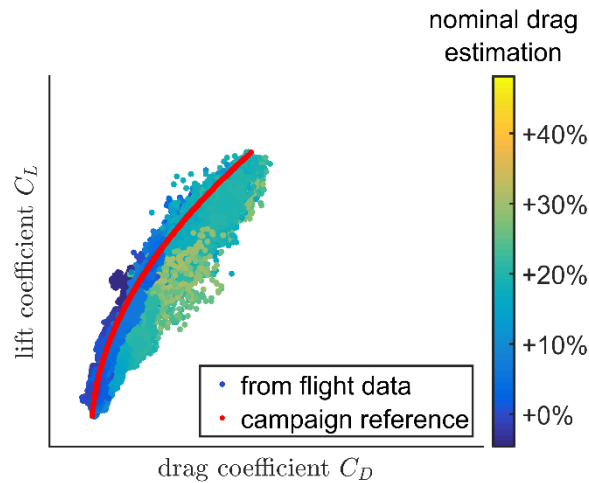


Figure 29: Aircraft drag polar from example flight on February 25<sup>th</sup>, 2023, **after engine thrust model adjustment**: calculated lift and drag coefficient from flight data measurements and reference for the Phenom300 prototype with SENS4ICE modifications; drag coefficient data including the indication of nominal drag estimation calculated by IID with **adjusted engine thrust during data replay**

## Conclusions on the North America SLD flight test IID results

Hence, with the currently available results from the SENS4ICE North America flight test campaign and the example flights, the degradation of App. C and App. O seem very similar in built-up and magnitude which consequently does not allow to discriminate by the IID alone. Anyway, this was initially anticipated by SENS4ICE and therefore the HIDS concept was developed. **The major result from both flights detailed above and the whole flight test is that the IID is well capable of detecting and announcing any flight performance degradation related to icing until the aircraft is again free of ice again.** For the SENS4ICE layered safety approach this means that the IID is able to fulfil the expectations in monitoring the aircraft operational capabilities.

Note that this is not a general result for all parts of App. C and O, or other aircraft types, or potential IID implementations. Although the SENS4ICE flight test was very successful in finding SLD icing and having a reasonable icing encounter during the test flight, the conditions are only a relatively small part of the icing envelope and the ice accretion and hence performance degradation was limited due to flight safety reasons.

## 2.4 IID results for European FT campaign

Results from three different flights of the European icing flight test campaign are presented and evaluated. During these flights the flight test crew successfully encountered different icing conditions including classical App. C and the rare SLD conditions (App. O). Note that for safety reasons, the mechanical de-icing system of the ATR42, i.e. pneumatic boots, was activated according to the given operational requirements, which led mainly to intercycle ice shapes on the wing's and horizontal tail's leading edges.

### FLIGHT AS230018

Figure 30 contains an overview of the flight track from flight as 230018, which was conducted on April 24<sup>th</sup>, 2023 around the CERs Marsant and Cazaux west of Toulouse. (CER refers to specifically designated areas that were reserved for the test aircraft.) It can be clearly seen, that during the flight icing was encountered at a specific altitude and after a certain time, the aircraft descended to perform a full airframe de-icing in warmer air. A time history of the IID behavior during this specific flight is given in Figure 31 The four different plots contain: altitude and indicated airspeed (top), nominal drag estimation and IID detection output (second plot), ice built-up on reference accretion ice sensor and static air temperature (third plot), and MVD and LWC of



encountered icing conditions (solid line) including the indication of the amount of SLD (dashed lines) (bottom). During the flight testing a threshold for the detection of 15% relative drag increase compared to the nominal flight performance was applied. It could be seen, that the major icing events/ encounter also led to a confirmed detection of abnormal flight performance through the IID. But after the campaign it was found that a modified and reduced threshold of 10% could significantly enhance the IID performance and reactivity without any negative effect, e.g., false alarms. In addition, the intercycle ice led sometimes to a reduction of estimated drag increase below the detection threshold (e.g., Figure 31 around 12:55 UTC or around 13:05 UTC) resetting the IID although the flight performance is still degraded and the encounter continuous. This switching behavior is physically correct, but undesired. It could be overcome with further output filtering or enhanced output logics, but a more reliable IID behavior with even lower thresholds is even more favorable.

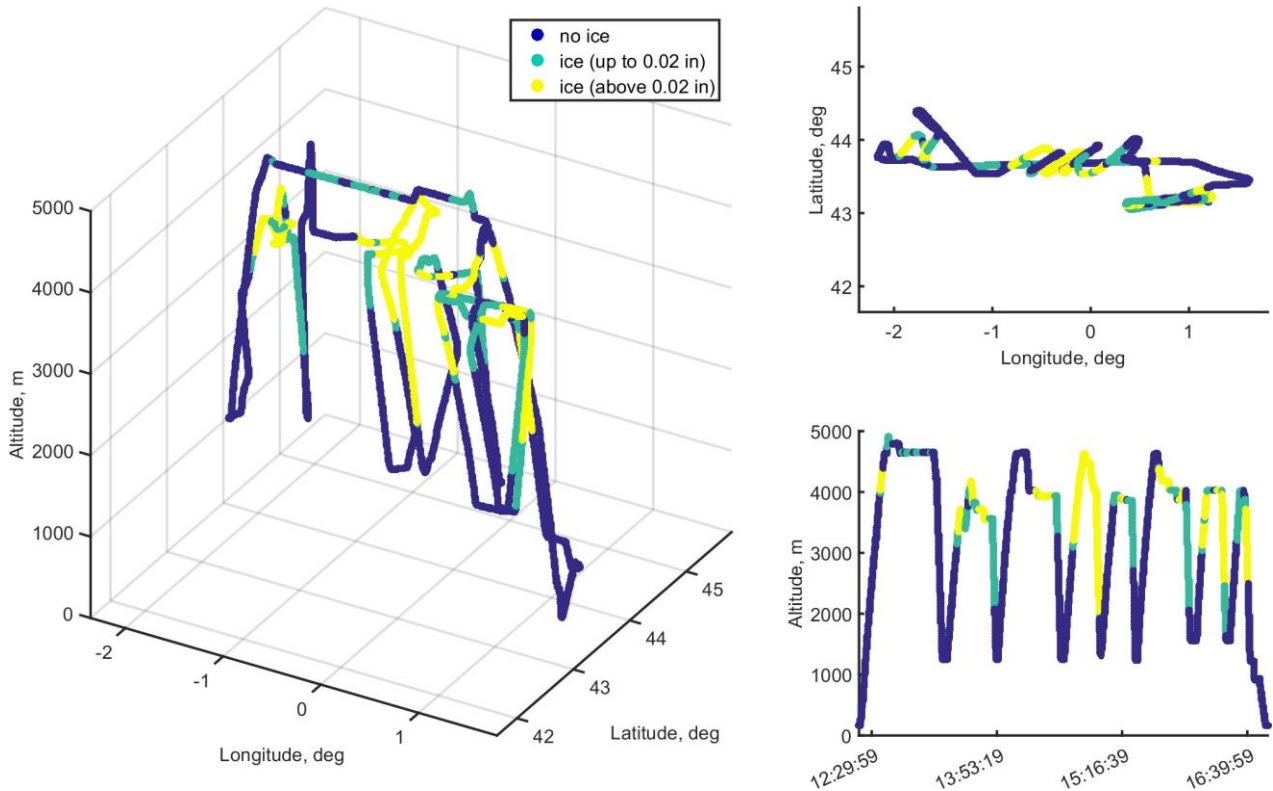


Figure 30: Figure: Flight track from SENS4ICE European icing campaign flight on April 24th, 2023 around Toulouse/ Marsant/ Cazaux: geodetic position and altitude with indication of icing encountered / built-up.

Figure 32 shows the same flight as a result from an IID post flight replay with a reduced threshold of 10% drag increase above nominal. There is no significant difference between both results except for the detection output, as the underlying code from the flight test used within the HIDS implementation (dSpace box) is similar to the replay on ground on the test hardware (desktop computer). The IID output now indicates the icing encounters in a continuous manner, without any switches between the detection state. Hence, **the results presented in the following will contain the reduced detection threshold (10%) instead of the more conservative flight test threshold (15%).**

Figure 33 and Figure 34 show the first to encounters (between 12:30:00 UTC and 13:16:55 UTC, and 13:24:40 UTC to 13:53:20 UTC) in more detail: in both cases the performance degradation is very slow in the beginning and the detection threshold (10%) is exceeded after around 10 min. The first encounter does not cause in the beginning any significant aerodynamic impact, which consequently is not visible in the IID output. Anyway, as long as icing conditions do not significantly alter the aircraft characteristics, there is no threat given and no safety issue for the further flight operations potentially present. The moment the drag increases due to more significant ice accretion on the airframe, the IID correctly and reliably indicates an abnormal flight performance (around 12:48 UTC). Similarly, during the second encounter, the degradation in the beginning is very low and does not exceed the threshold while nearly reaching is around 13:31UTC. The degradation was reduced again before rising significantly, presumably through a combination of the de-icing system and (static air) temperatures near 0°C. Nevertheless, at around 13:34 UTC, significant icing conditions were encountered



leading to an ice formation on the airframe again (indicated by the icing probe signal) which caused a fast and detectable performance degradation respectively aircraft drag increase (up to 25% above the nominal value of the drag estimation). Hence, the IID directly indicates the abnormal performance after exceeding the detection threshold (around 13:35 UTC).

Note that unfortunately the cameras observing the wings and horizontal tail had some malfunction during these first two encounters of this flight and no camera footage of the icing situation for these encounters is available.

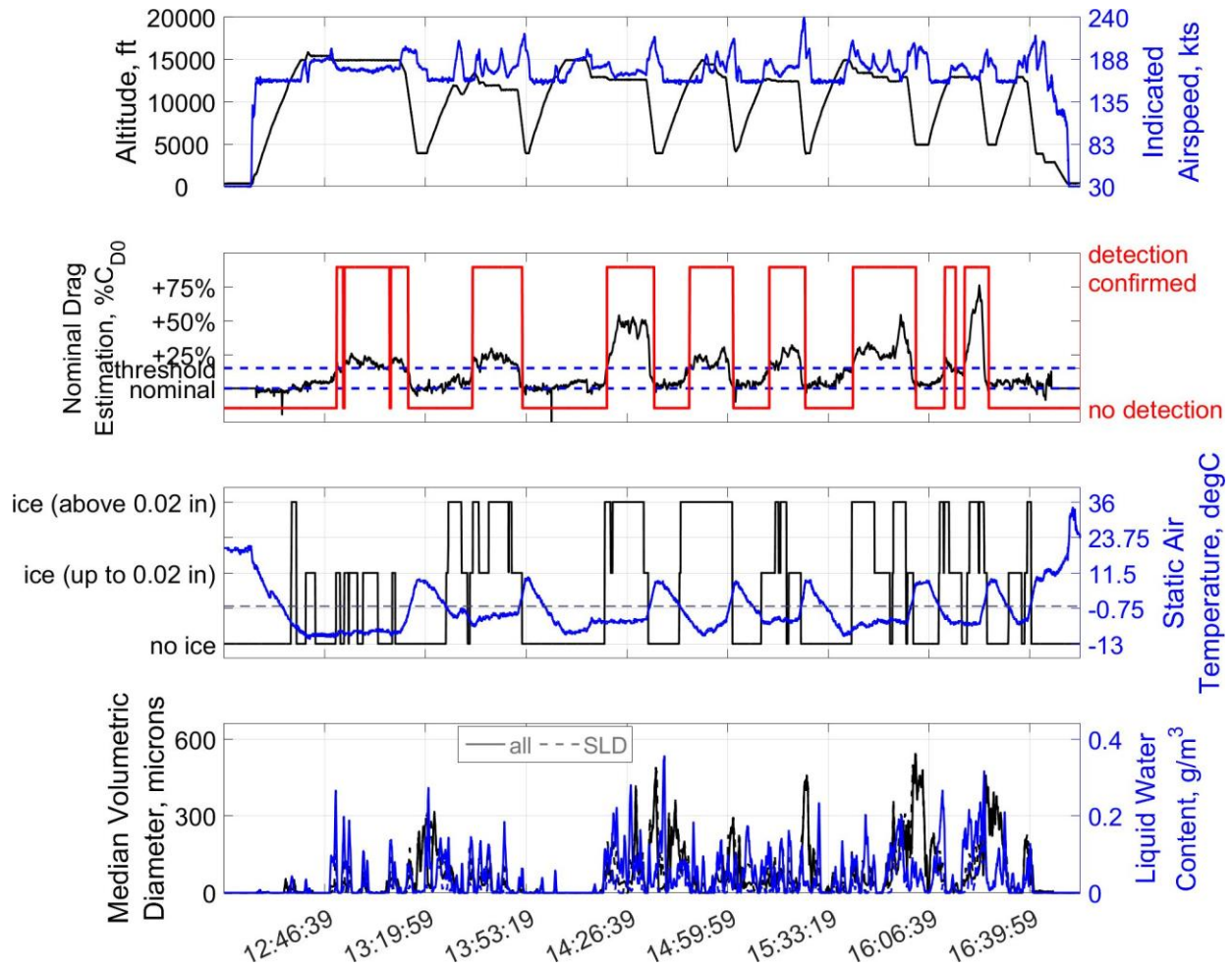


Figure 31: Time history of IID system performance during the first example flight as230018 (April 24th, 2023, 12:13 UTC to 16:56 UTC): altitude and indicated airspeed (top), nominal drag estimation and IID detection output (second plot), ice built-up on reference accretion ice sensor and static air temperature (dashed line 0degC) (third plot), and MVD and LWC of encountered icing conditions (solid line) including the indication of the amount of SLD (dashed lines) (bottom); **original detection threshold at 15% relative drag increase.**

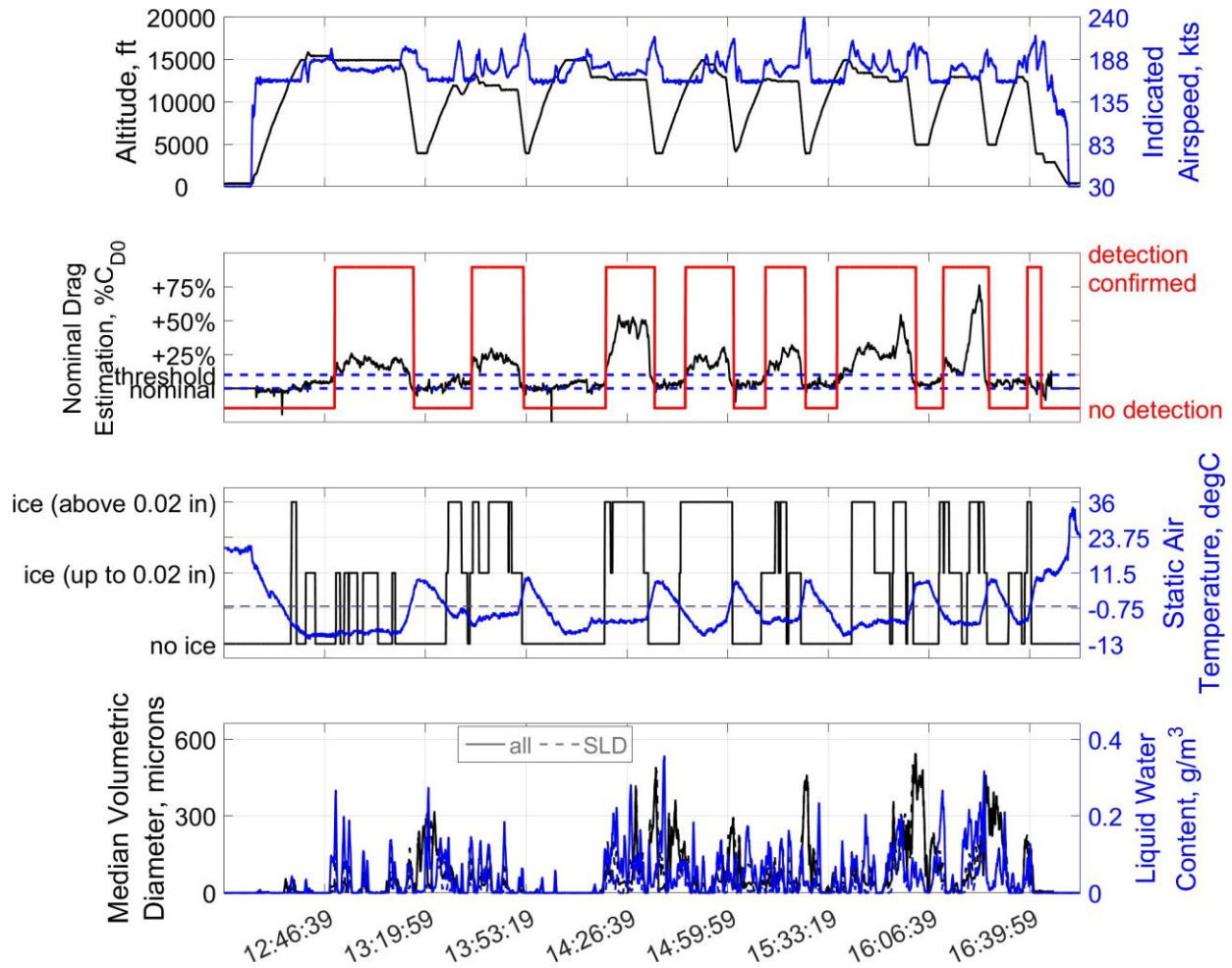


Figure 32: Time history of IID system performance during the first example flight as230018 (April 24th, 2023, 12:13 UTC to 16:56 UTC): altitude and indicated airspeed (top), nominal drag estimation and IID detection output (second plot), ice built-up on reference accretion ice sensor and static air temperature (dashed line 0degC) (third plot), and MVD and LWC of encountered icing conditions (solid line) including the indication of the amount of SLD (dashed lines) (bottom); **updated detection threshold at 10% relative drag increase.**

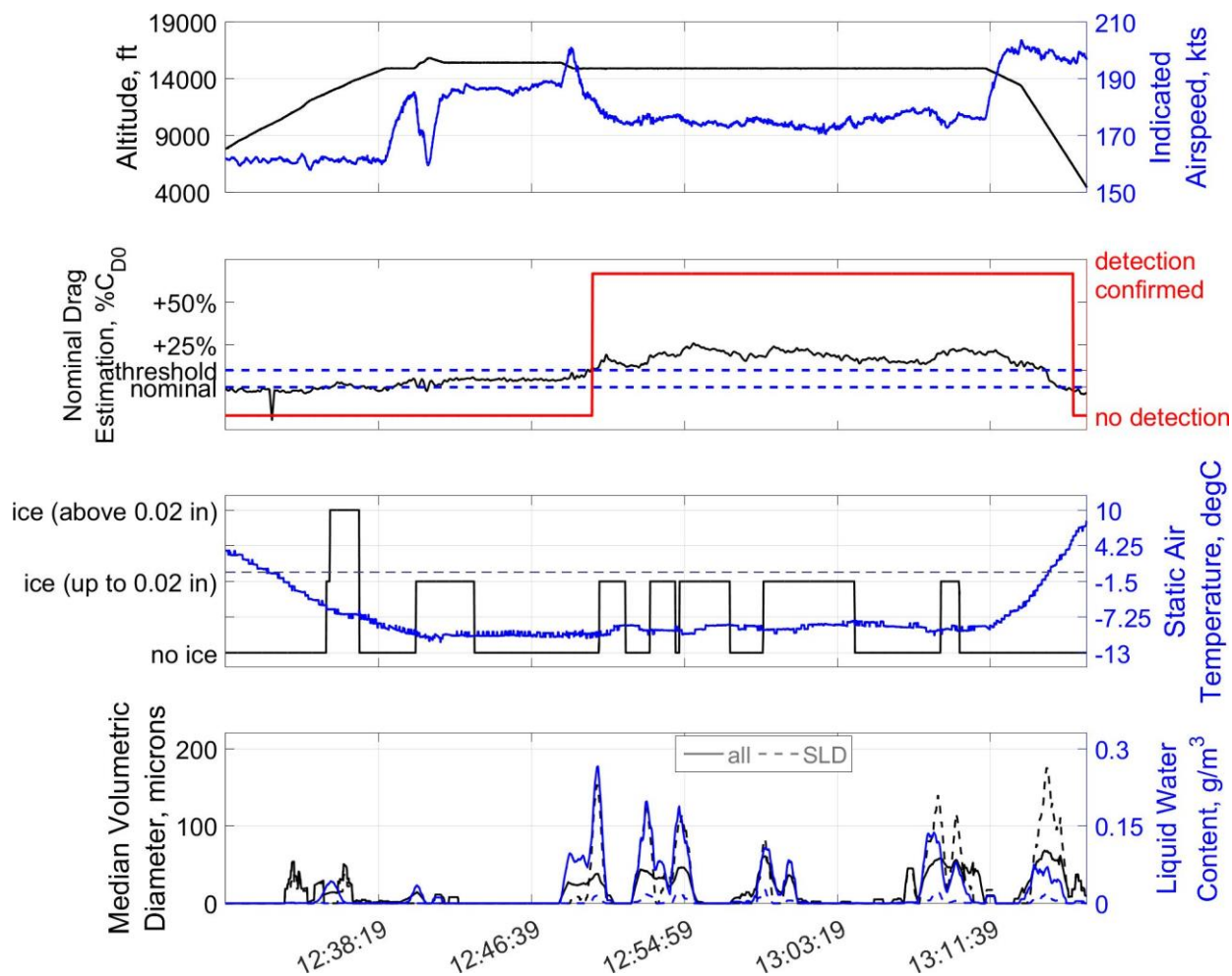


Figure 33: Time history of IID system performance during specific icing encounter from the first example flight (April 24TH, 2023, 12:30:00 UTC to 13:16:55 UTC): altitude and indicated airspeed (top), nominal drag estimation and IID detection output (second plot), ice built-up on reference accretion ice sensor and static air temperature (dashed line 0degC) (third plot), and MVD and LWC of encountered icing conditions (solid line) including the indication of the amount of SLD (dashed lines) (bottom); **updated detection threshold at 10% relative drag increase.**

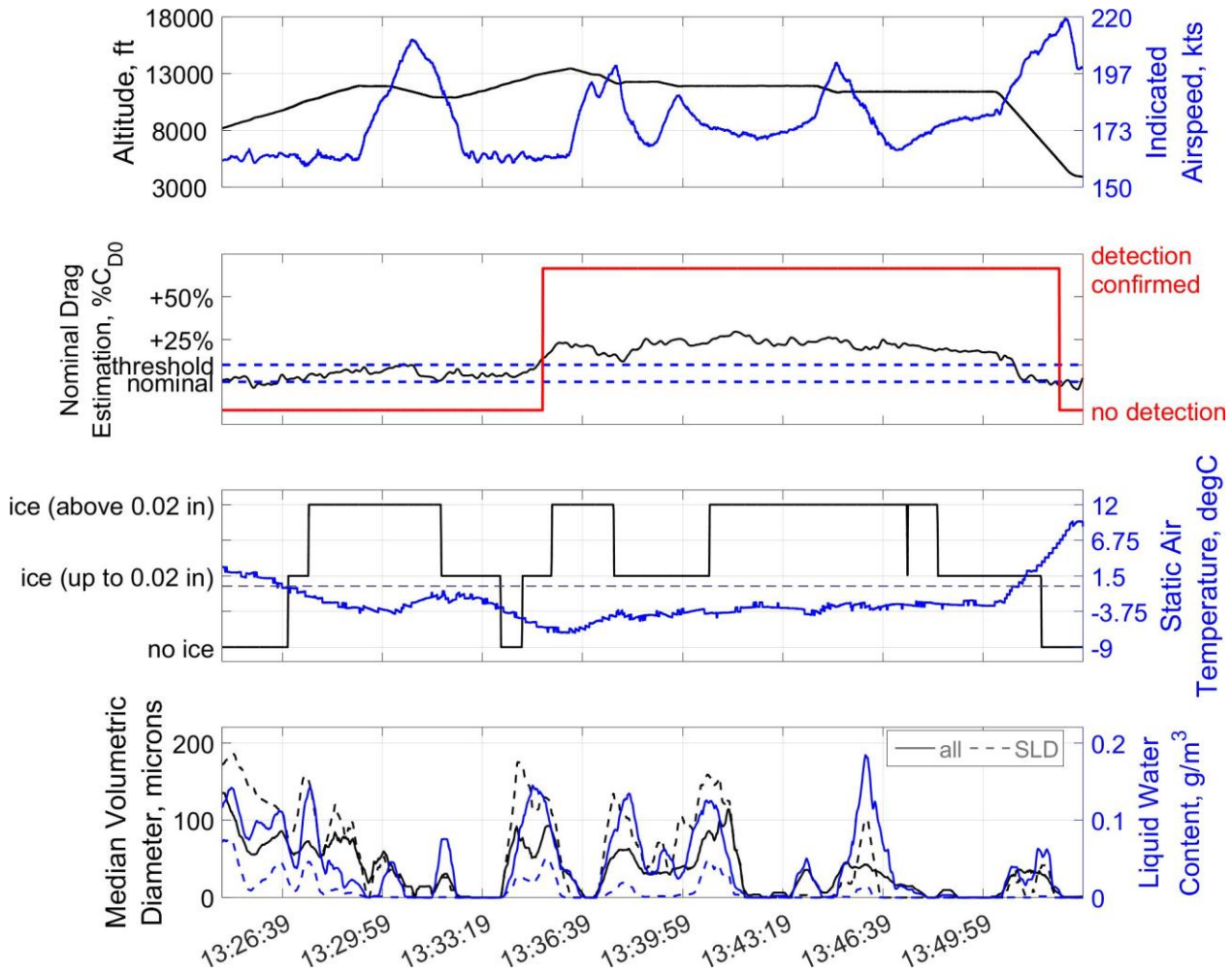


Figure 34: Time history of IID system performance during specific icing encounter from the first example flight (April 24TH, 2023, 13:24:40 UTC to 13:53:20 UTC): altitude and indicated airspeed (top), nominal drag estimation and IID detection output (second plot), ice built-up on reference accretion ice sensor and static air temperature (dashed line 0degC) (third plot), and MVD and LWC of encountered icing conditions (solid line) including the indication of the amount of SLD (dashed lines) (bottom); **updated detection threshold at 10% relative drag increase.**

Figure 35 shows the third encounter of this flight, which had a different profile than the previous ones. This time, the icing conditions led directly to a significant ice formation on the airframe (indicated through the jump in the reference ice probe signal) which is directly correlated with the strong icing situation also produced by SLDs in the air. The aircraft performance is continuously degraded until it reaches more than 50% relative drag increase compared to the nominal value. This degradation persists although the icing situation changes to even larger drops (see bottom plot at around 14:29 UTC). Due to the fact, that the de-icing boots were activated during the encounter, the aircraft was protected and a further aerodynamics degradation was prevented. The IID directly confirmed the ice formation on the airframe through the monitoring of the aircraft's flight performance within less than a minute after the encounters started. For this encounter pictures from the cameras indicating the airframe icing situation are available. Figure 36 shows a specific view on the leading edges of left and right wing (from below) together with the horizontal tail for different times. At 14:19:25 UTC when the encounter started, the airframe was free of visible ice accretion. But around two minutes later and a confirmed IID detection information, the airframe shows an icing layer which on the wings is already broken from the active de-icing system. During the next minutes the formation does not really change in total and although the boots allow to remove some ice, new formations built up, which then causes almost no change in the estimated drag resulting from the IID. It is interesting to see that at around 14:29 UTC, when large drops were encountered, the wings seem to have less ice than before – resulting in the reduction of the additional



drag estimated by the IID between 14:29 UTC and 14:31 UTC – because of presumably a good effectivity of the protection system. The drag rises again shortly after, where a more glaze ice looking ice formation is visible on the aircraft (14:32:37 UTC in Figure 36), which is presumably a result of the ongoing SLD icing situation. Anyway, this result shows that a currently present encounter might not have instantaneously a noticeable adverse effect on the aircraft aerodynamics. Monitoring only the icing conditions might consequently not give a correct indication on the criticality of the encounter even the situation looks dangerous in terms of water drops in the air, but the continuous monitoring of the ice formation and corresponding aerodynamics degradation will give the comprehensive view on the current layer situation required for a safe aircraft operation. After descending and passing through the 0°C temperature layer, the aircraft got free of ice again (14:36 UTC).

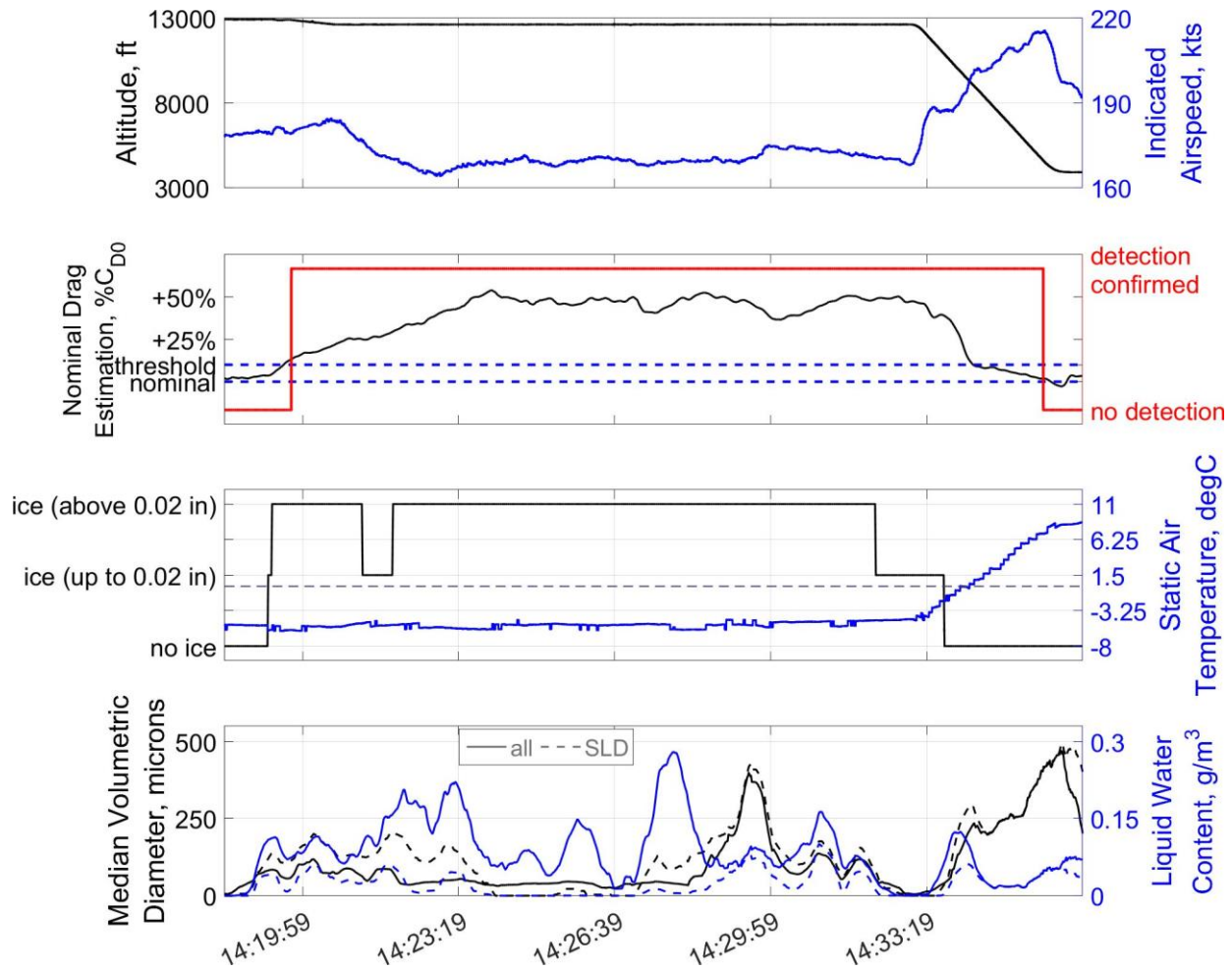


Figure 35: Time history of IID system performance during specific icing encounter from the first example flight (April 24<sup>th</sup>, 2023, 14:18:20 UTC to 14:36:40 UTC): altitude and indicated airspeed (top), nominal drag estimation and IID detection output (second plot), ice built-up on reference accretion ice sensor and static air temperature (third plot), and MVD and LWC of encountered icing conditions (solid line) including the indication of the amount of SLD (dashed lines) (bottom); **updated detection threshold at 10% relative drag increase.**

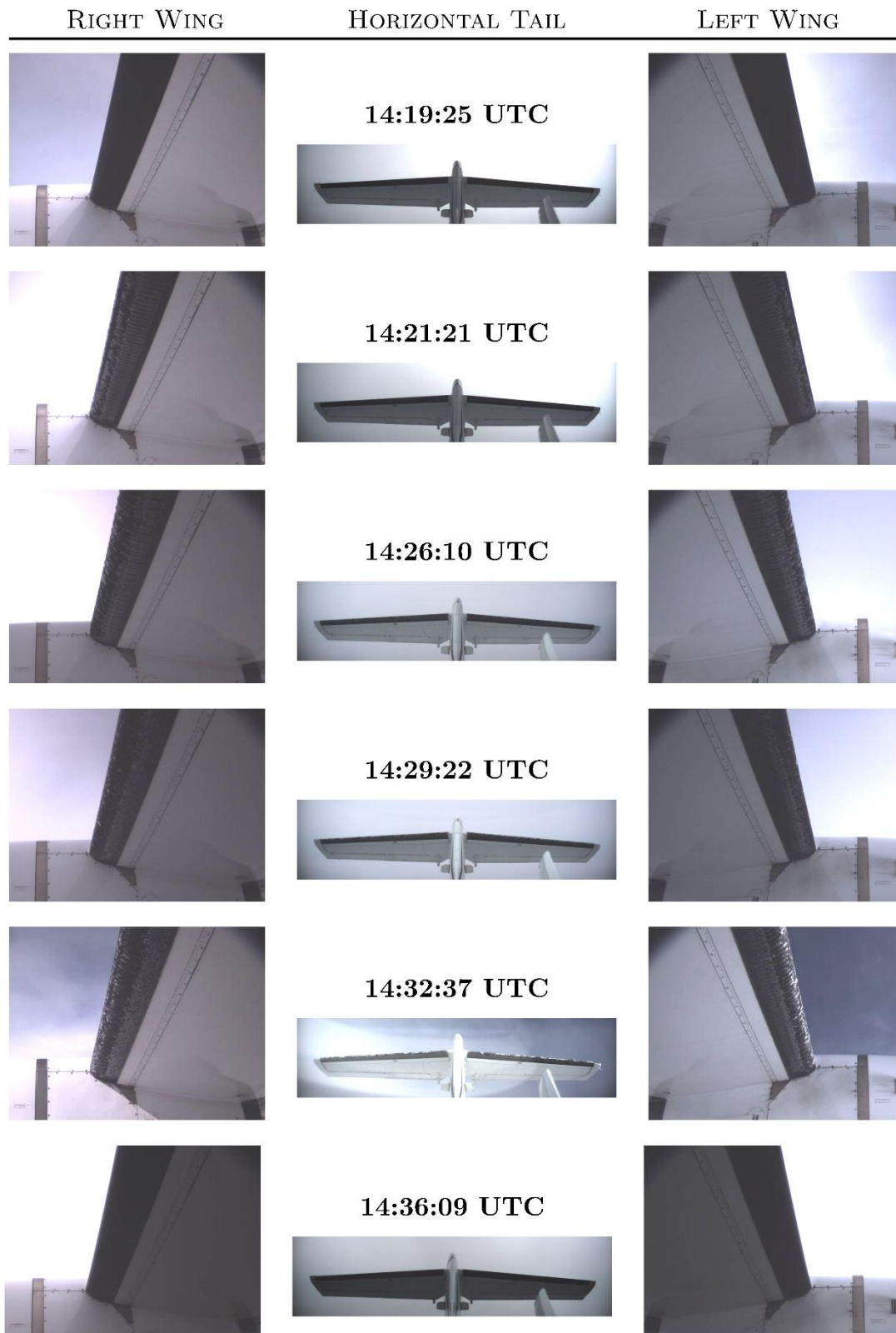


Figure 36: Evolution of ice accretion on the airframe during icing encounter: camera views on left & right wing and horizontal tail for specific moments during flight (increased brightness and contrast); corresponding to encounter and IID detection given in Fig. Figure 35; credit Safire / SENS4ICE project.



Similar results can be obtained for the next encounter between 14:42:29 UTC and 15:02:39 UTC given in Figure 37 (time history plot) and Figure 38 (camera footage). During the climb to FL140 the aircraft entered icing conditions leading to an airframe ice accretion indicated by the reference icing probe. At around 14:46 UTC, the aircraft's wings and empennage are visible free of ice, which means that ice formation was presumably only present on the unprotected surfaces resulting in less than 10% relative drag deviation. But, during the following climb the aircraft performance was notably degraded and the IID correctly announced the performance loss. At 14:49:15 UTC the wings' leading edges had some ice formation corresponding to the around 25% increase in the nominal drag estimation. The situation maintained almost constantly in terms of ice formation and degradation until the aircraft descended after 15:00 UTC into warmer air to remove the ice completely. Note that this encounter shows the advantage of the IID working throughout all flight conditions resulting in a fast and reliable information.

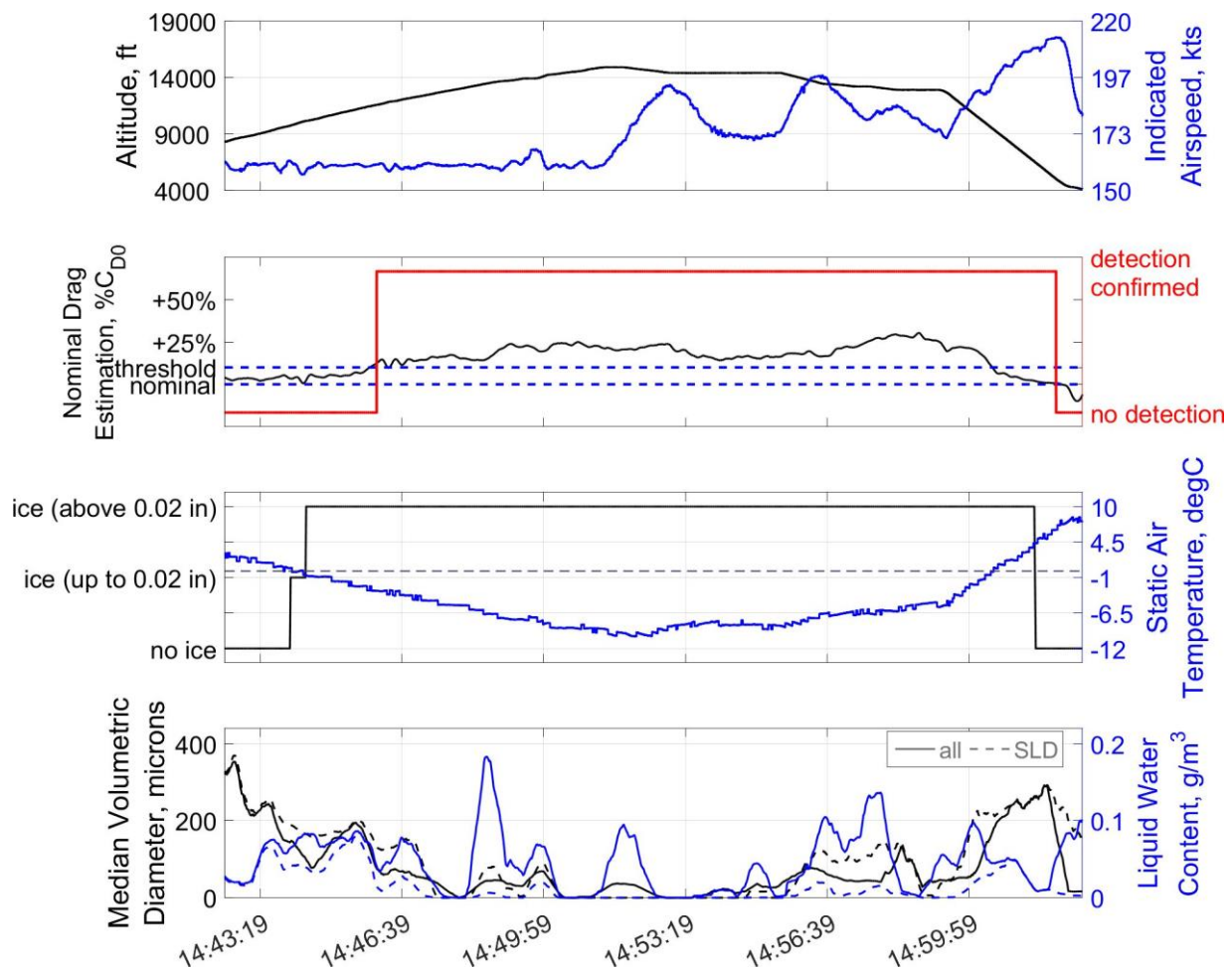


Figure 37: Time history of IID system performance during specific icing encounter from the first example flight (April 24<sup>th</sup>, 2023, 14:42:29 UTC to 15:02:39 UTC): altitude and indicated airspeed (top), nominal drag estimation and IID detection output (second plot), ice built-up on reference accretion ice sensor and static air temperature (third plot), and MVD and LWC of encountered icing conditions (solid line) including the indication of the amount of SLD (dashed lines) (bottom); **updated detection threshold at 10% relative drag increase.**

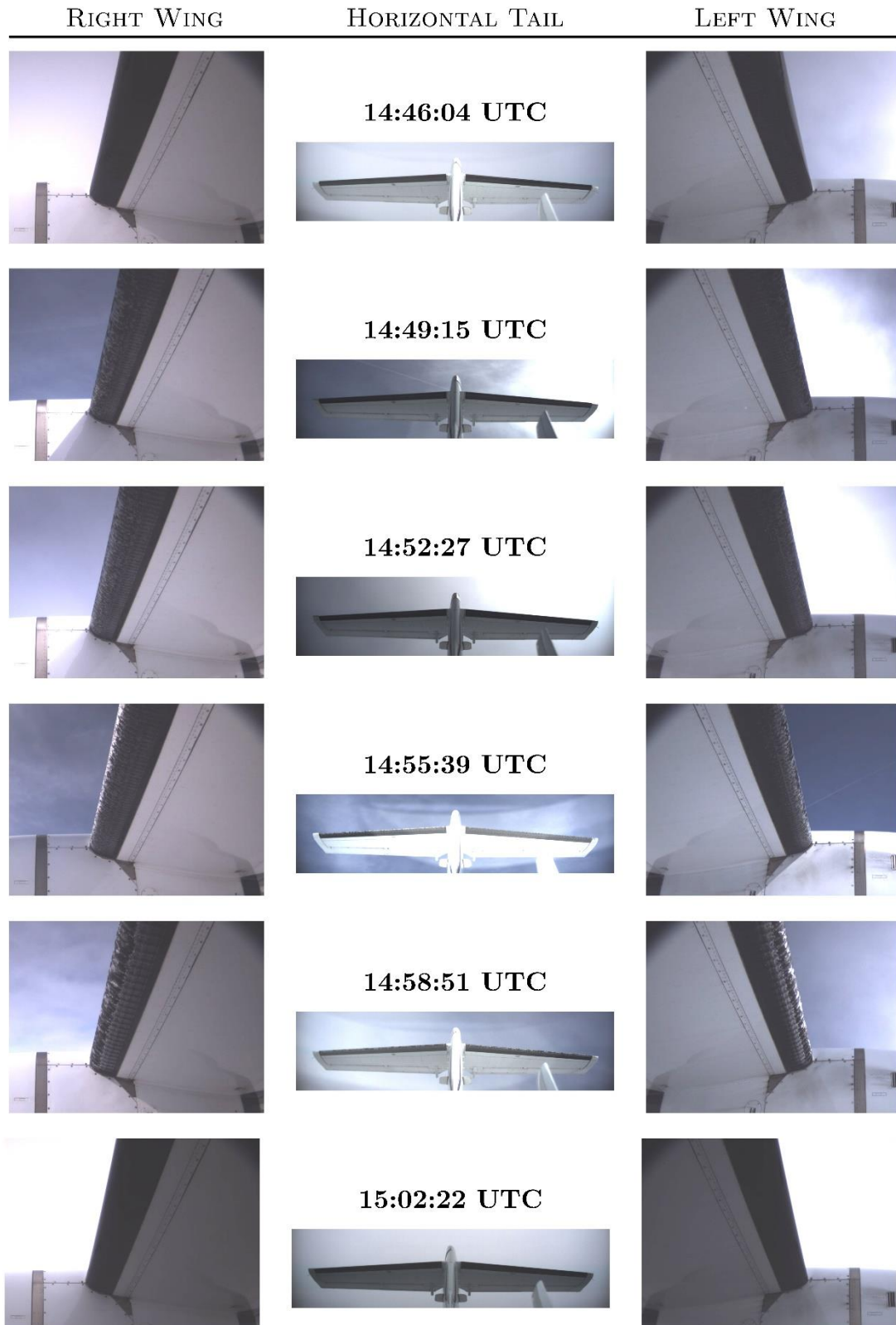


Figure 38: Evolution of ice accretion on the airframe during icing encounter: camera views on left & right wing and horizontal tail for specific moments during flight (increased brightness and contrast); corresponding to encounter and IID detection given in Figure 37; credit Safire / SENS4ICE project.



The next encounter in Figure 39 and Figure 40 was quite similar in terms of aerodynamic degradation characteristics and IID results. The aircraft climbed above FL120 and encountered icing conditions leading more or less directly to an indication of ice accretion on the reference probe. At 15:12:10 UTC the aircraft shows no ice accretion on the wing or empennage, but less than one minute later the IID provides an abnormal performance detection when the nominal drag estimation exceeds the 10% threshold. At 15:13:50 UTC light ice formation is clearly visible on the airframe. Again, the IID is able to fast and reliably indicate the aerodynamic degradation pointing to an ice contamination on the airframe. Throughout the encounter the degradation was increasing when the ice formation on the airframe rises (e.g., at 15:19:08 UTC). After the aircraft entered warmer air, the ice was removed and the nominal flight performance restored.

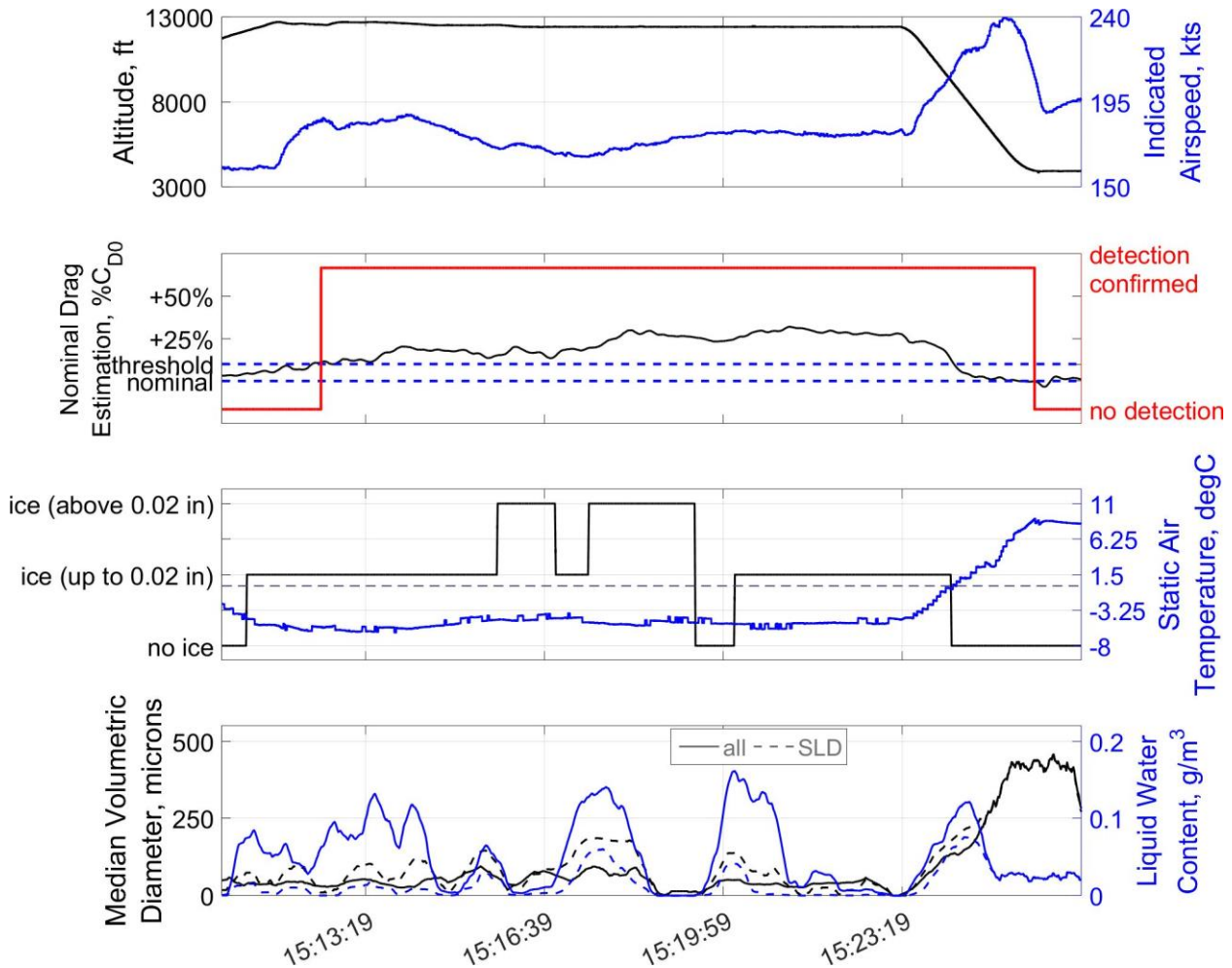


Figure 39: Time history of IID system performance during specific icing encounter from the first example flight (April 24<sup>th</sup>, 2023, 15:10:39 UTC to 15:26:39 UTC): altitude and indicated airspeed (top), nominal drag estimation and IID detection output (second plot), ice built-up on reference accretion ice sensor and static air temperature (third plot), and MVD and LWC of encountered icing conditions (solid line) including the indication of the amount of SLD (dashed lines) (bottom); **updated detection threshold at 10% relative drag increase.**

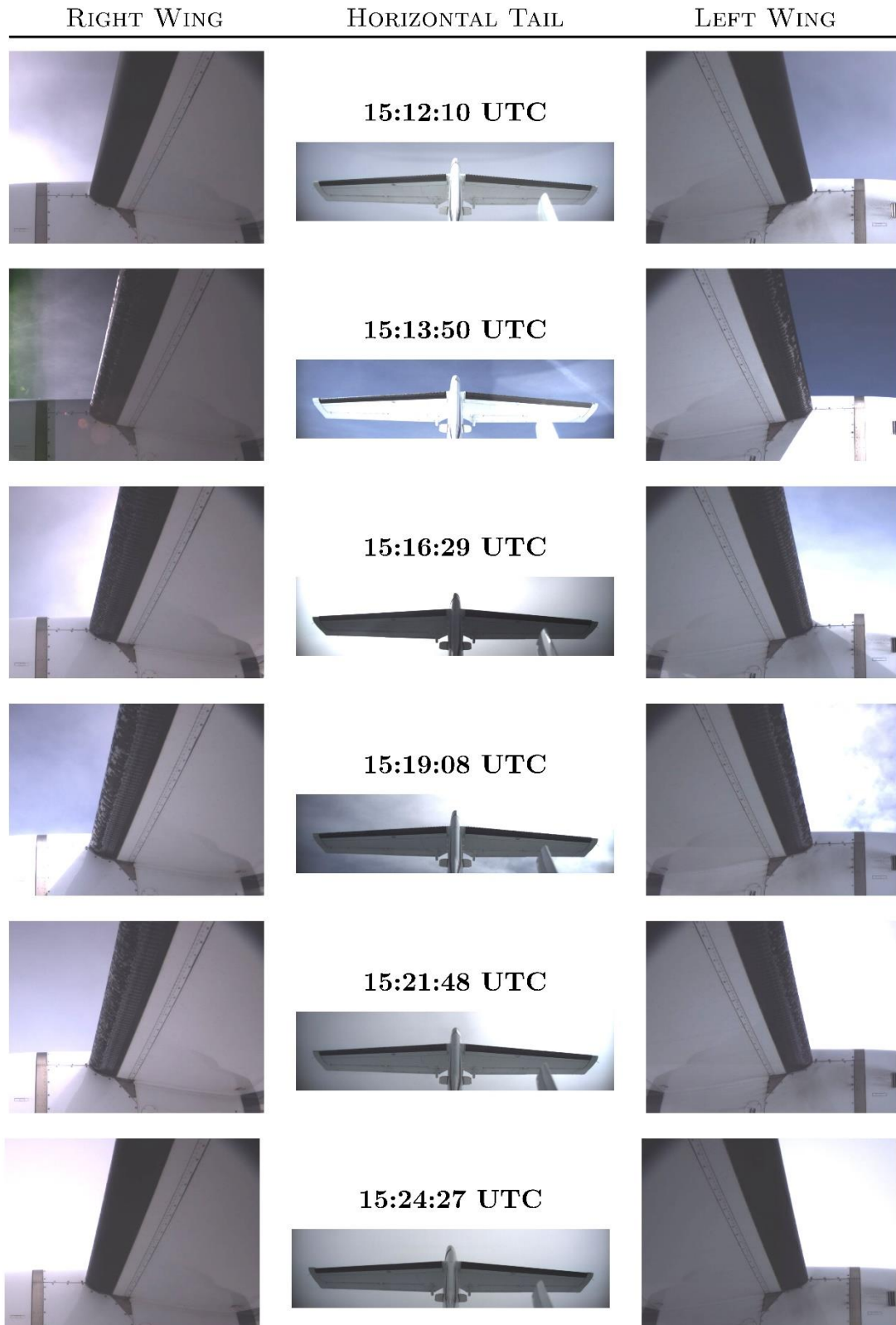


Figure 40: Evolution of ice accretion on the airframe during icing encounter: camera views on left & right wing and horizontal tail for specific moments during flight (increased brightness and contrast); corresponding to encounter and indirect ice detection output given in Figure 39; credit Safire / SENS4ICE project.



The sixth encounter of this flight presented herein (Figure 41 and Figure 42) has again a very interesting aerodynamic degradation characteristic showing the benefits of the IID for a comprehensive picture of the aircraft icing situation and for maintaining a safe flight condition during all-weather operations. Icing conditions are again encountered during the climb into the cloud layer and the drag estimation shows relatively fast a degradation compared to the nominal case for the flight test. Before level off, the IID confirms an abnormal flight performance and maintains this warning throughout the whole encounter. Ice accretion is visible on the airframe at 15:38 UTC whereas the reference accretion probe gives no indication. Also, the reference sensors do not show any icing conditions at around 15:39 UTC but the aircraft is still iced and nominal drag increased (10% to 15%). After 15:40 UTC the reference icing probe and the atmospheric reference sensors indicate icing conditions with significant accretion and the aerodynamics are further degraded (more than 25% relative increase compared to nominal values). Between 15:49 UTC and 15:54 UTC the reference accretion probe reduced the indication to small accretion and no ice and the conditions encountered also contained very small number of droplets but the aircraft was still degraded, correctly indicated by the IID. After 15:54 UTC SLDs are encountered again and there is visible significant ice accretion on the airframe which leads to a relative drag increase (constant rise during encounter to max. value) of about 50% above nominal. Descending to warmer air quickly removed the ice afterwards restoring the aircraft's nominal flight performance.

During the last encounter of this flight in Figure 43 and Figure 44 the maximum performance degradation was observed. Climbing into the icing conditions directly caused a positive ice indication from the reference probe when passing 0°C with supercooled liquid water present in the air. Around 16:11:20 UTC the IID also confirmed a performance degradation with estimated nominal drag increasing above the 10% threshold still in climb phase. Reaching the target altitude fewer icing conditions were found but the reference probe and IID still indicate icing, showing again, that the degradation is still present although icing conditions are already left. Looking to Figure 43 indicates that only light ice formation was visible on the airframe during this period. A new cloud with icing conditions was entered around 16:17 UTC and icing is still announced by the IID due to the still existing drag increase, but at 16:17:30 UTC the reference probe was reset to clean, while the estimated drag was increasing significantly. After 16:19 UTC IID and reference probe together with the measurements of atmospheric conditions clearly indicate icing conditions, also containing larger droplets with higher water content. The maximum estimated drag increase was above 75% at 16:23:10 UTC well matching the significant ice formation shown in Figure 44 at corresponding times. This encounter also shows the need for a comprehensive view on the aircraft icing situations and the monitoring of the aircraft capabilities not to be misled by individual indications. After descending into warmer air and leaving the icing conditions, the aircraft's nominal performance was restored and the IID detection output reset.

Note again, that during all encounters the de-icing system of the Safire ATR 42 was active and ice was shed from protected areas during the whole flight. Otherwise, the performance degradation might have been significantly higher with a potential threat to a safe flight operation. Hence, for some conditions the aerodynamic degradation maintained relatively constant because the overall accretion was kept on a certain level.



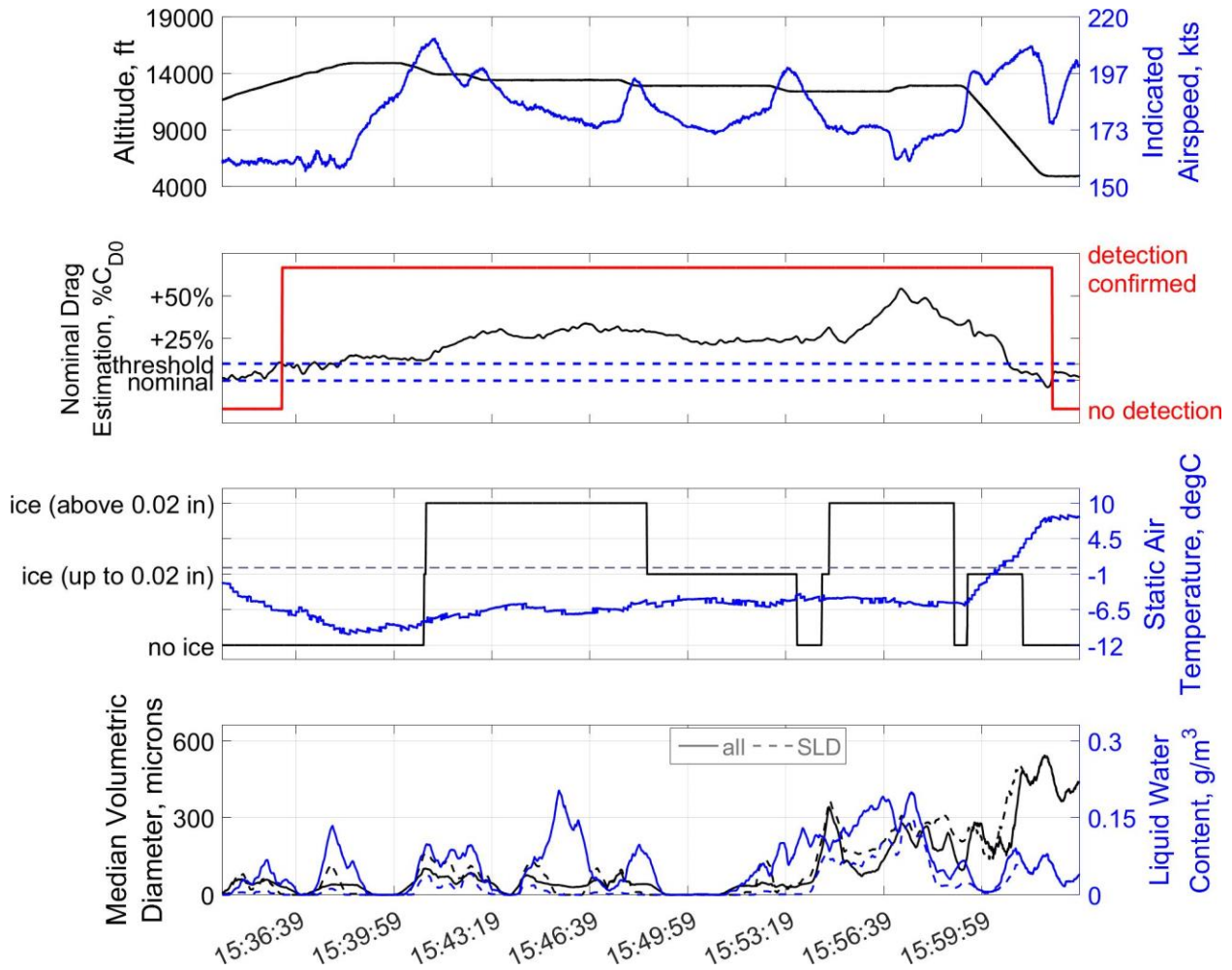


Figure 41: Time history of IID system performance during specific icing encounter from the first example flight (April 24<sup>TH</sup>, 2023, 15:34:09 UTC to 16:03:19 UTC): altitude and indicated airspeed (top), nominal drag estimation and IID detection output (second plot), ice built-up on reference accretion ice sensor and static air temperature (third plot), and MVD and LWC of encountered icing conditions (solid line) including the indication of the amount of SLD (dashed lines) (bottom); **updated detection threshold at 10% relative drag increase.**

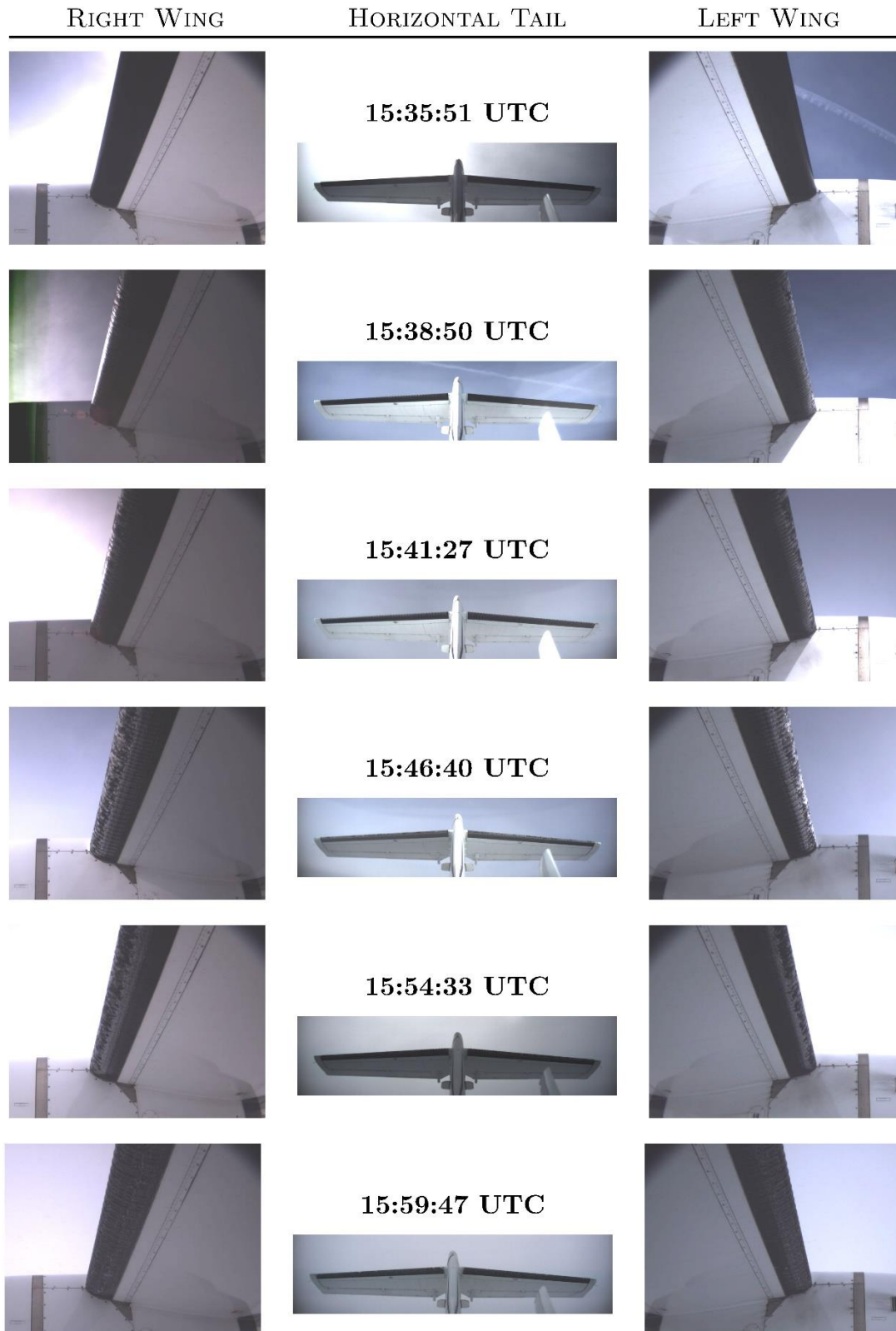


Figure 42: Evolution of ice accretion on the airframe during icing encounter: camera views on left & right wing and horizontal tail for specific moments during flight (increased brightness and contrast); corresponding to encounter and indirect ice detection output given in Fig. Figure 41; credit Safire / SENS4ICE project.

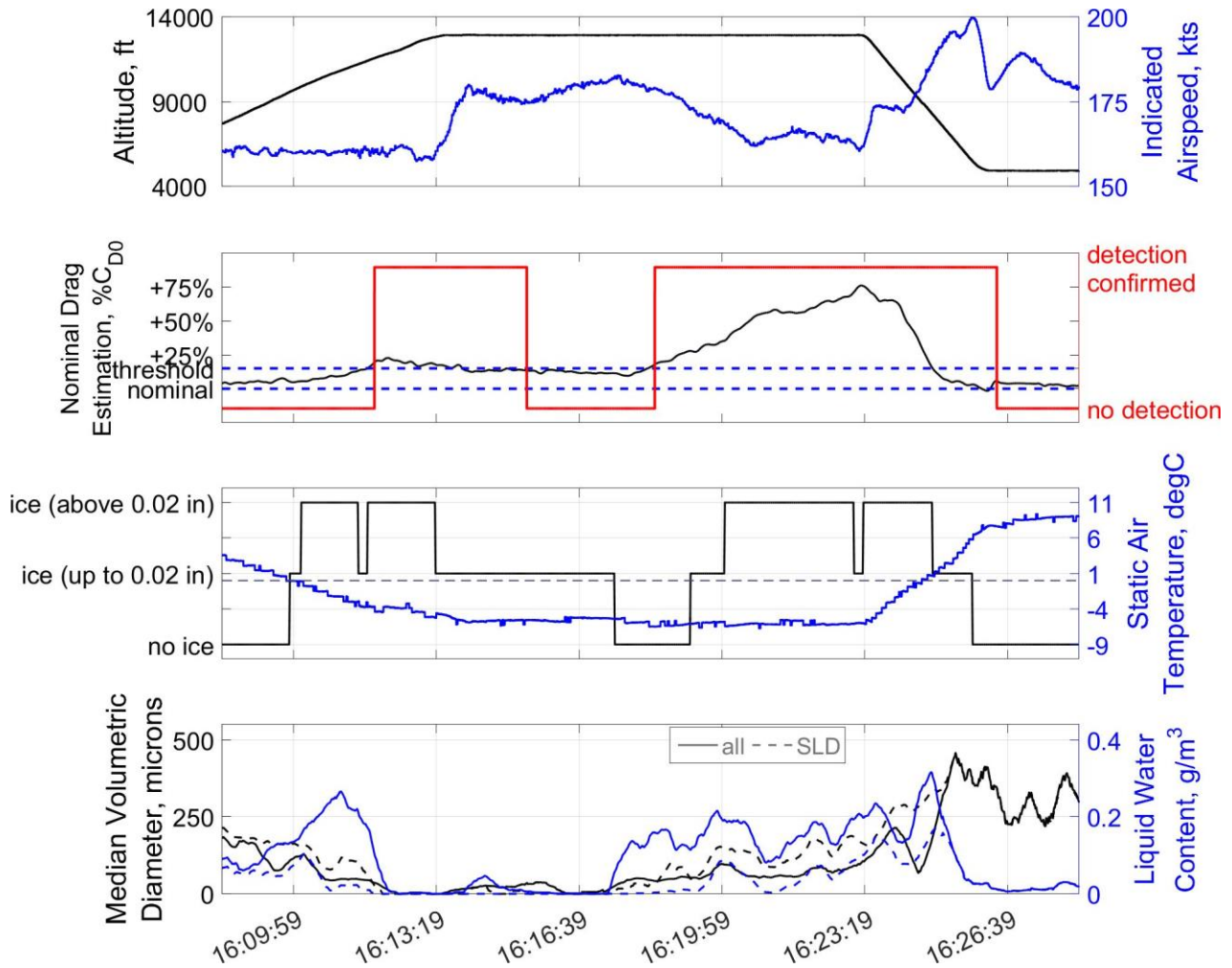


Figure 43: Time history of IID system performance during specific icing encounter from the first example flight (April 24<sup>TH</sup>, 2023, 16:08:20 UTC to 16:28:20 UTC): altitude and indicated airspeed (top), nominal drag estimation and IID detection output (second plot), ice built-up on reference accretion ice sensor and static air temperature (third plot), and MVD and LWC of encountered icing conditions (solid line) including the indication of the amount of SLD (dashed lines) (bottom); **updated detection threshold at 10% relative drag increase.**

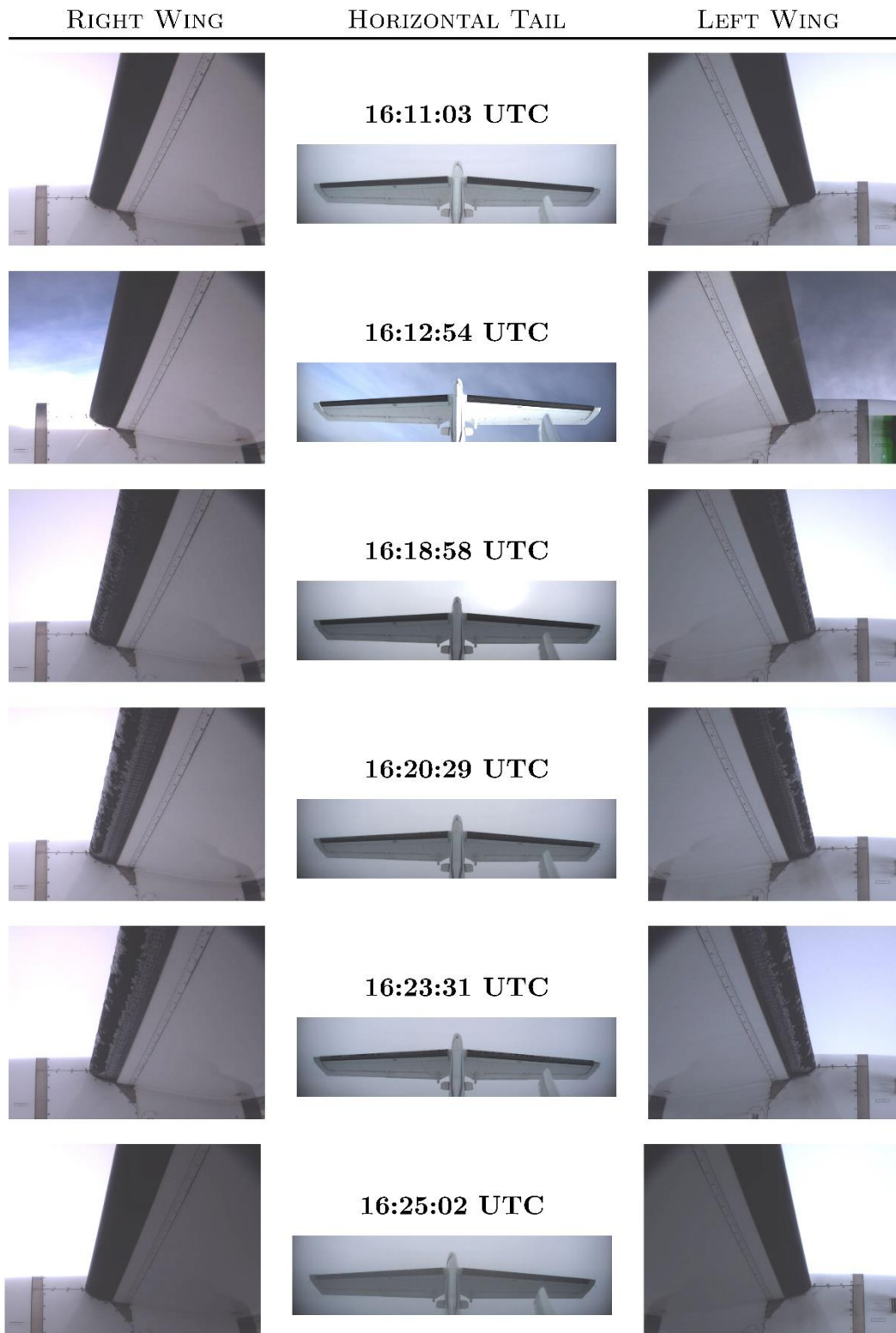


Figure 44: Evolution of ice accretion on the airframe during icing encounter: camera views on left & right wing and horizontal tail for specific moments during flight (increased brightness and contrast); corresponding to encounter and indirect ice detection output given in Figure 43; credit Safire / SENS4ICE project.



## Aerodynamic Degradation due to icing

Figure 45 shows the aircraft drag polar calculated from the measured data for the whole flight (flaps retracted, gear up). For each data point available in the measurement, the lift and drag coefficient is calculated based on the available inertial and inflow measurements as well as the given engine thrust. The plot contains the aerodynamic reference used for the flight test reflecting the SAFIRE ATR42-320 characteristics with all SENS4ICE modifications (red line).

The maximum degradation is correlated with a nominal drag estimation (change) of around 70%, but having 30 %to 40% change in average related to icing in a more continuous manner, means that the degradation is kind of saturated. This is also visible in the time history plots from this flight. Knowing that the main degradation is related to an increase of surface fraction on (mainly) unprotected aircraft parts, this is reasonable.

Figure 46 contains the aircraft drag polar including an indication of the ice accretion announced by the Safire reference probe. Overall, the drag increase (dots shifted to the right due to ice accretion) is well corresponding to the ice information given by the probe (cyan and yellow dots). But there are some blue dots in the shifted cloud indicating abnormal performance which is not directly correlated to the reference probe information. These are corresponding to the parts of the flight, where the performance was already or still degraded by the probe did not give any indication, e.g., in Figure 41. The results from the IID detection output are given Figure 47 as indication over the drag polar. There are only a few parts left, where the shifted drag is not directly marked yellow indicating a confirmed detection. Hence, this directly shows the advantage of the HIDS approach, which in combination of dissimilar technologies tries to overcome such individual shortages of direct sensors and IID.

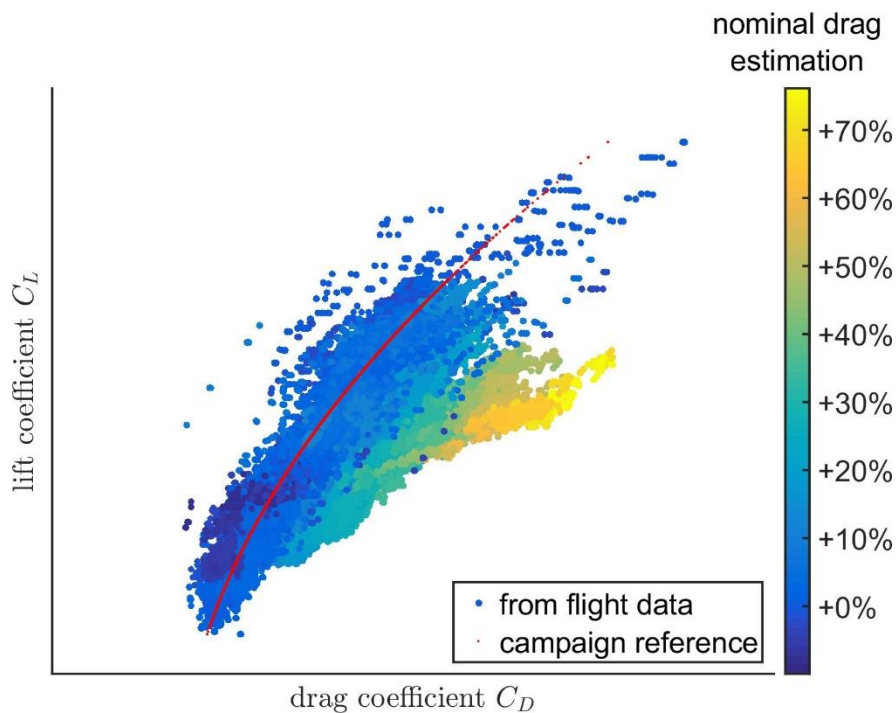


Figure 45: Aircraft drag polar from example flight on April 24<sup>TH</sup>, 2023: calculated lift and drag coefficient from flight data measurements and reference for the SAFIRE ATR42-320 with SENS4ICE modifications; drag coefficient data including the indication of nominal drag estimation calculated by IID.

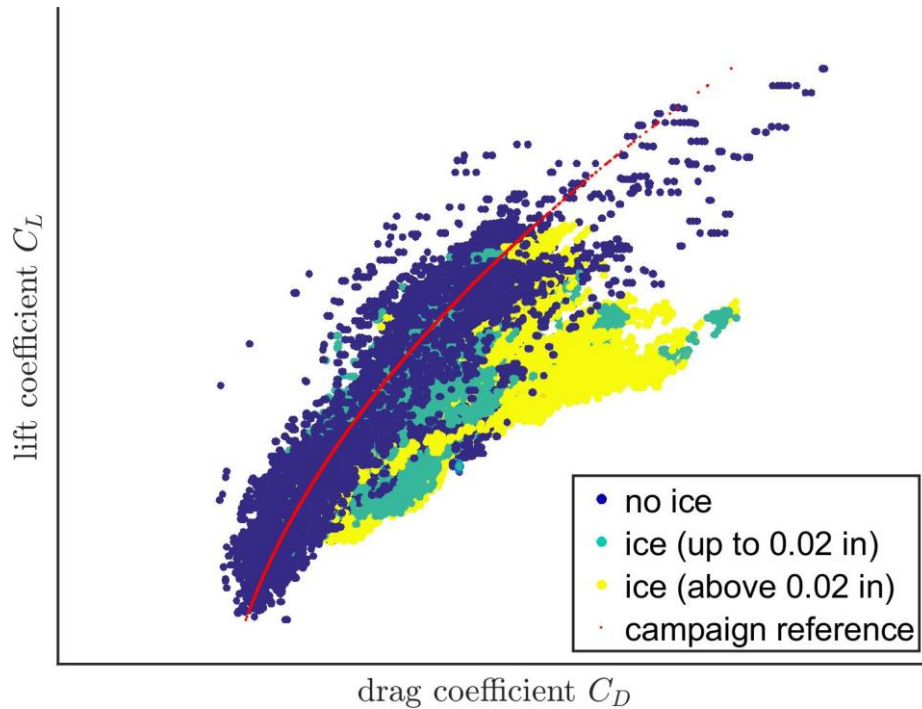


Figure 46: Aircraft drag polar from example flight on April 24<sup>TH</sup>, 2023: calculated lift and drag coefficient from flight data measurements and reference for the SAFIRE ATR42-320 with SENS4ICE modifications; drag coefficient data including the indication of ice accretion announced by Safire ice reference probe.

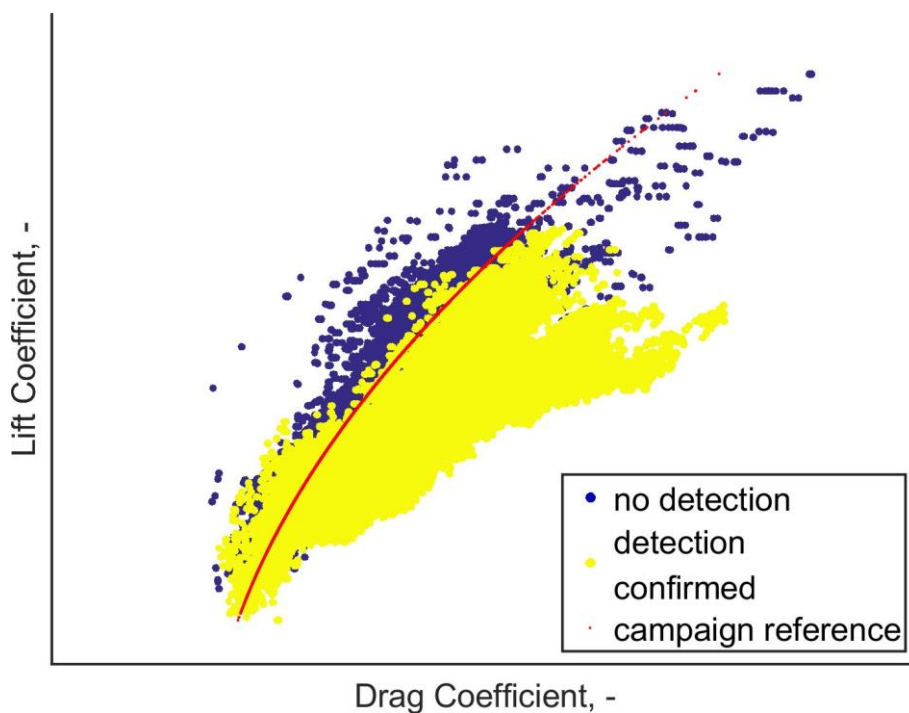


Figure 47: Aircraft drag polar from example flight on April 24<sup>TH</sup>, 2023: calculated lift and drag coefficient from flight data measurements and reference for the SAFIRE ATR42-320 with SENS4ICE modifications; drag coefficient data including the indication of confirmed IID detection output; **updated detection threshold at 10% relative drag increase.**



## FLIGHT AS230021

Flight as230021 took place in the afternoon of April 26<sup>th</sup>, 2023 around the Cazaux CER in southern France. Figure 48 contains the flight track including an indication of the icing encountered based on the Safire icing reference probe signal.

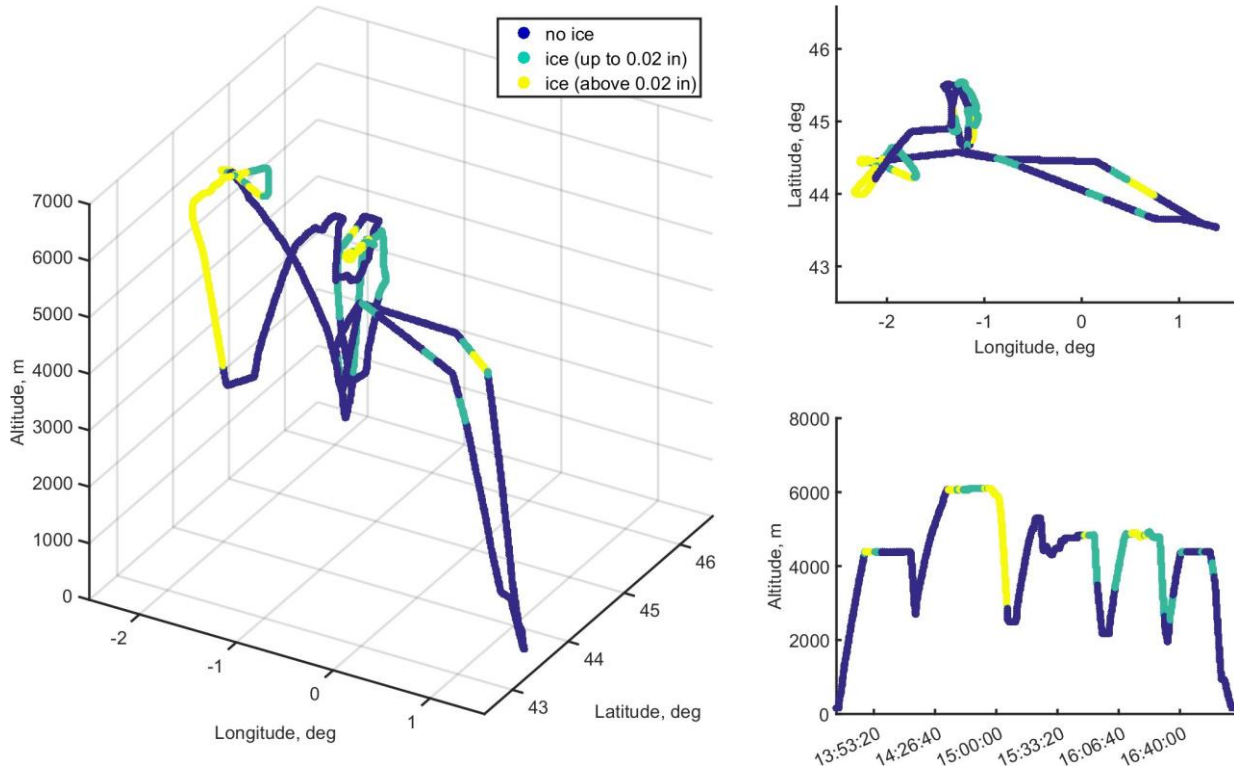


Figure 48: Flight track from SENS4ICE European icing campaign flight on April 26<sup>th</sup>, 2023 (afternoon) around Toulouse/Cazaux: geodetic position and altitude with indication of icing encountered / built-up.

Figure 49 contains the time history plot of the whole flight showing the IID results together with the aircraft flight information and the atmospheric conditions. Using the pre-campaign defined very conservative detection threshold, the major icing encounters were detected correctly (after around 15:45 UTC) because the aerodynamic degradation is significant. But the lighter encounters in the beginning of the flight with a much smaller change of flight performance could not be announced by the IID using the 15% threshold although the drag increase is estimated correctly. Hence, the updated threshold of 10% is the first choice to enhance the detection behavior (see Figure 50). However, during this flight, the degradation resulting from the first encounters is still below the 10% nominal drag increase not triggering the indirect ice detection in the offline data replay. This shows, that the threshold alone is no measure to define the quality of a detection system if not all encounters are announced: if the degradation is not significantly threatening the flight safety, there is basically no need to take any action for the flight operation. The announcement of the icing conditions is of course relevant to enhance the pilots' situational awareness, which can be done using direct sensor techniques. Again, the advantage of the HIDS is to create a comprehensive view on the icing situation which allows the pilots to decide about the current impact of the situation on the flight operation. If the detection threshold is chosen to early and reliably announce a critical performance degradation of the specific aircraft, not exceeding this threshold in consequence means not threat. But, this is only valid if – as shown for the examples – the IID can reliably estimate the current drag increase. Anyway, the IID is still under development and the best definition of the detection threshold is subject to further investigation. Therefore, another reduction of the threshold to 7% was used in the offline data replay shown in Figure 51. With the choice of this relatively small threshold, additional encounters in the beginning of this flight can be correctly detected. Keeping in mind the above written, these results point to the fact that an educated choice of the threshold including the knowledge about the specific aircraft concerned is essential but then the IID and/ or the implementation within the HIDS allows to provide a comprehensive view on the icing situation nowadays not available in modern aircraft.

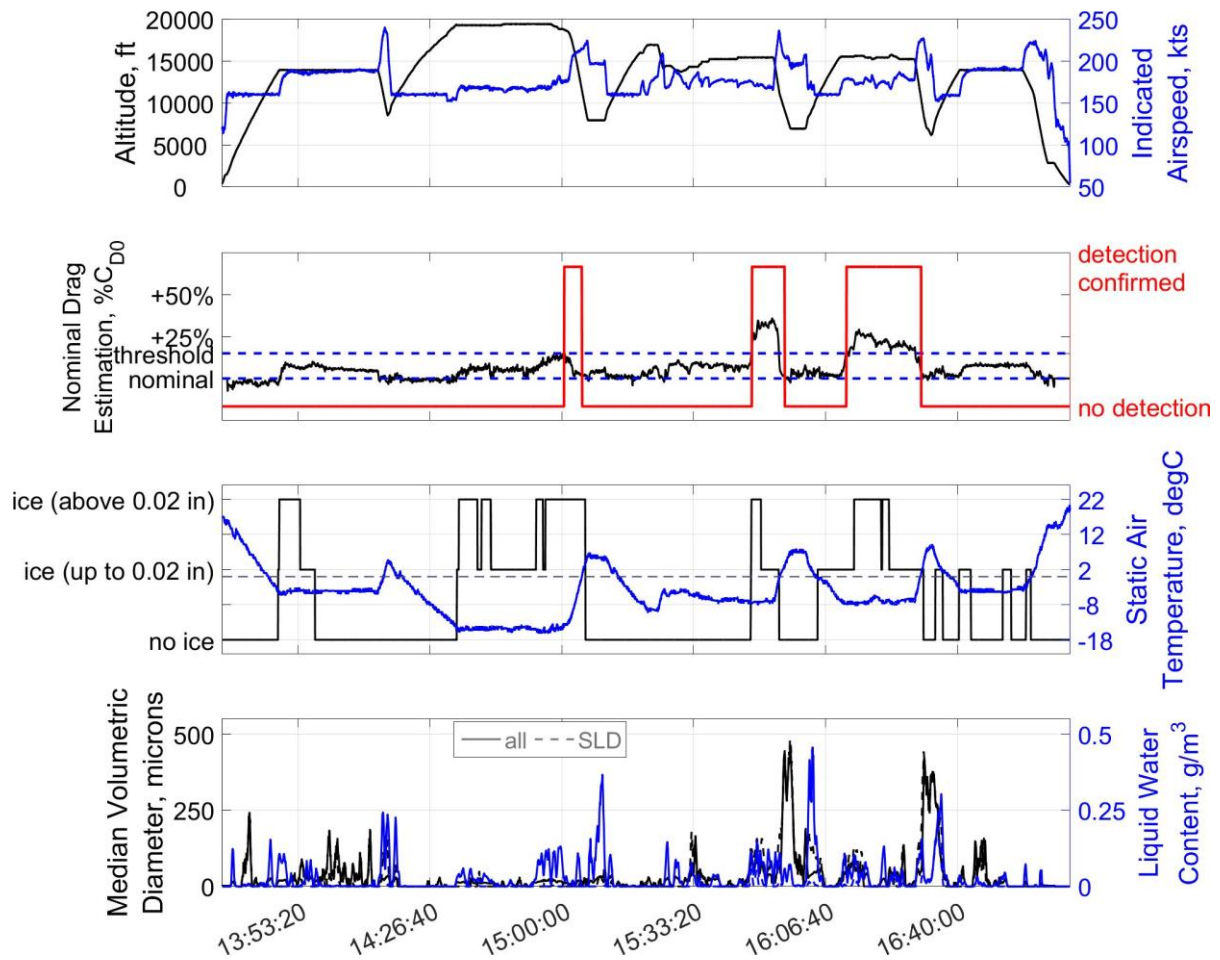


Figure 49: Time history of IID system performance during the second example flight as230021 (April 26<sup>th</sup>, 2023, 13:02 UTC to 17:13 UTC): altitude and indicated airspeed (top), nominal drag estimation and IID detection output (second plot), ice built-up on reference accretion ice sensor and static air temperature (dashed line 0degC) (third plot), and MVD and LWC of encountered icing conditions (solid line) including the indication of the amount of SLD (dashed lines) (bottom); **original detection threshold at 15% relative drag increase.**

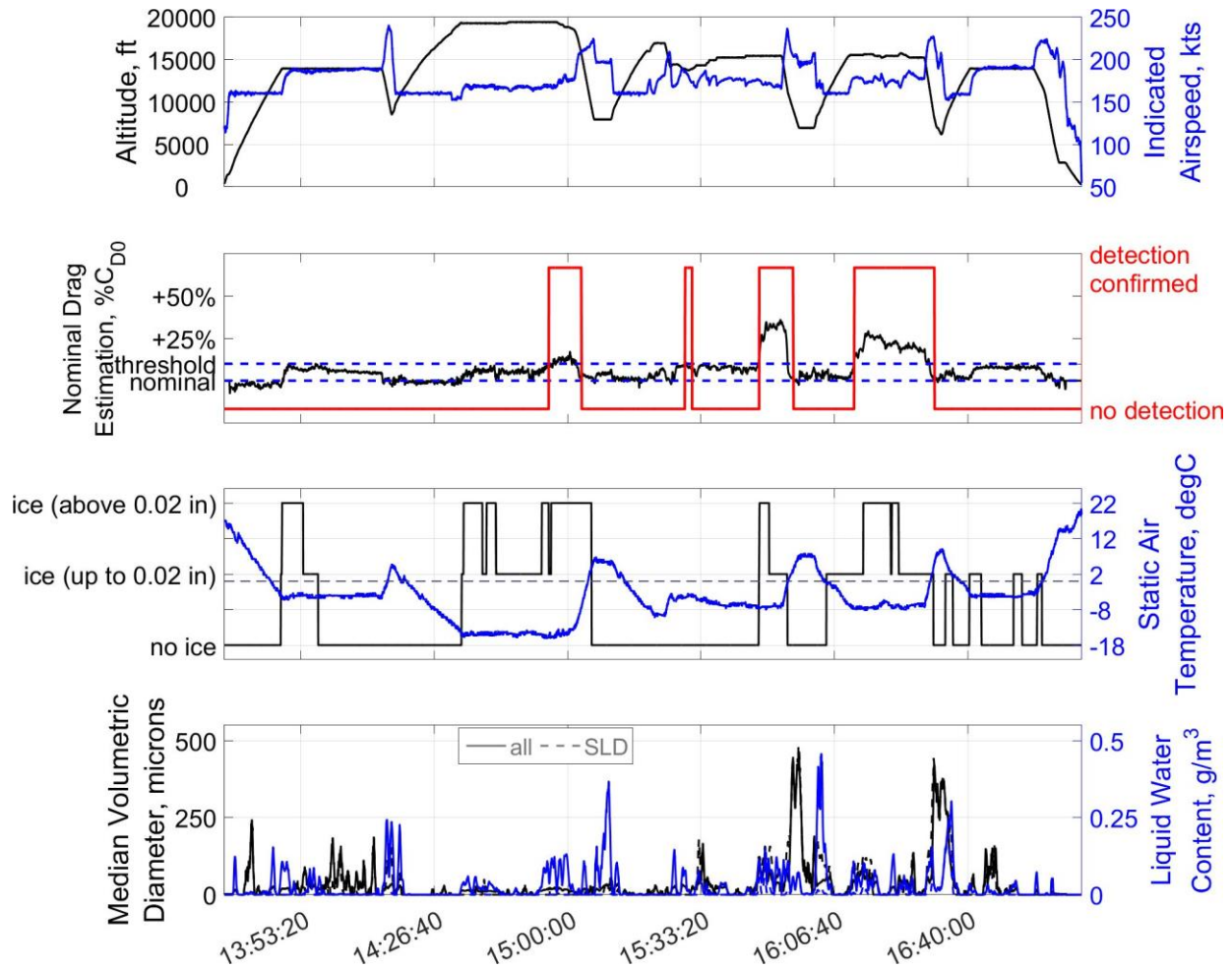


Figure 50: Time history of IID system performance during the second example flight as230021 (April 26<sup>th</sup>, 2023, 13:02 UTC to 17:13 UTC): altitude and indicated airspeed (top), nominal drag estimation and IID detection output (second plot), ice built-up on reference accretion ice sensor and static air temperature (dashed line 0degC) (third plot), and MVD and LWC of encountered icing conditions (solid line) including the indication of the amount of SLD (dashed lines) (bottom); **updated detection threshold at 10% relative drag increase.**

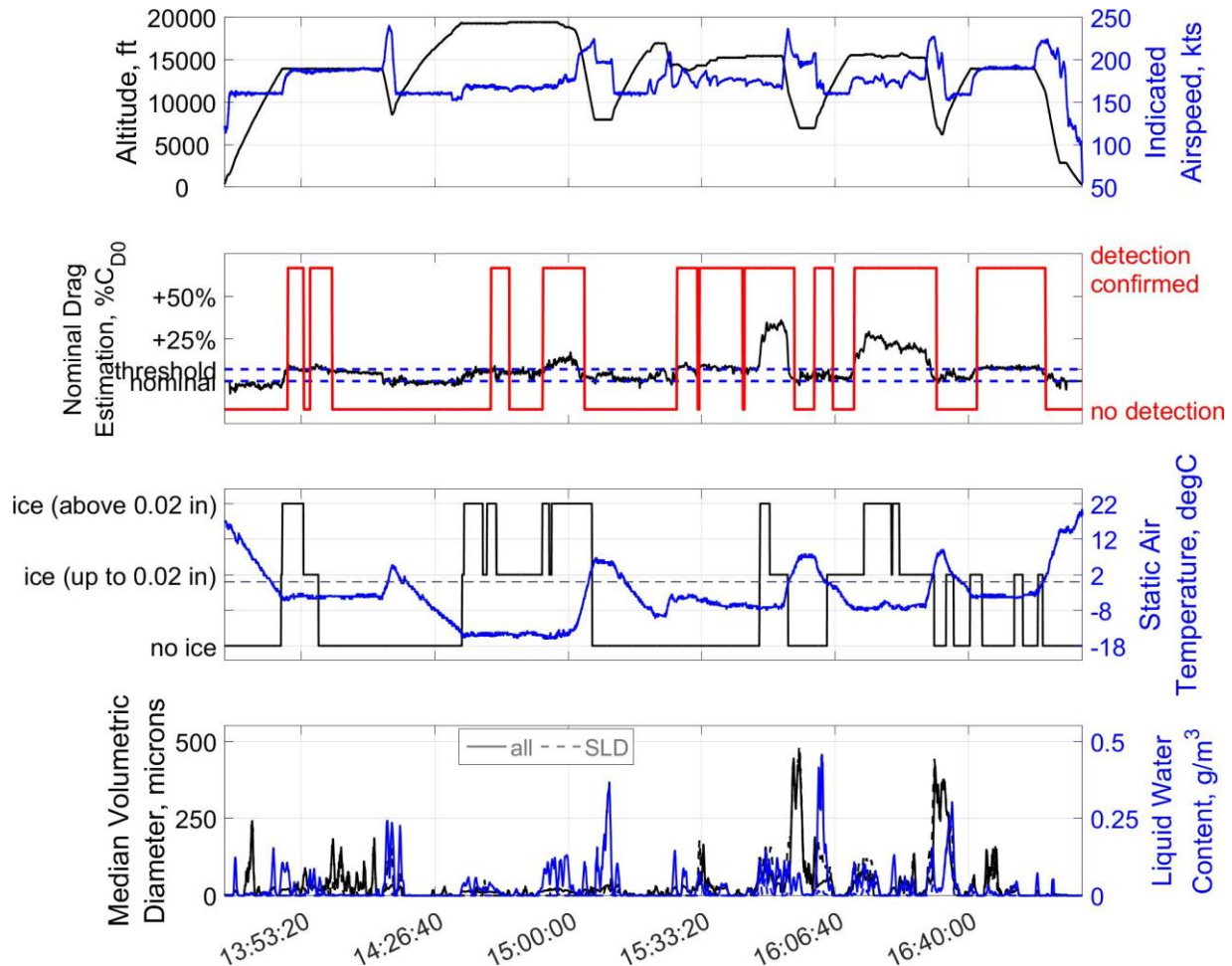


Figure 51: Time history of IID system performance during the second example flight as230021 (April 26<sup>th</sup>, 2023, 13:02 UTC to 17:13 UTC): altitude and indicated airspeed (top), nominal drag estimation and IID detection output (second plot), ice built-up on reference accretion ice sensor and static air temperature (dashed line 0degC) (third plot), and MVD and LWC of encountered icing conditions (solid line) including the indication of the amount of SLD (dashed lines) **reduced detection threshold at 7% relative drag increase.**

Figure 52 shows an extract from Figure 50 containing the updated detection threshold at 10% relative drag increase. During this part of the flight, it is interesting that the reference icing probe does not announce icing until around 15:48 UTC and also the reference measurements of atmospheric conditions indicate only very small amounts of water in the air. Anyway, a drag increase is already resulting from the IID calculations which corresponds to an existing ice accretion on the airframe (see Figure 53 at 15:47:33 UTC) already before the reference probe announce ice. The IID drag estimation do not exceed the threshold until around 15:48 UTC, but anyway, the indication of drag increase gives the full view on the icing situation. This is another proof for the complementarity of the IID to direct sensors and the advantage of the hybridization. At the time the reference icing probe announces a large ice formation the IID also confirms the abnormal flight performance due to icing caused by relatively large drops accumulating on the aircraft. It can be clearly seen in Figure 53 that the correct detection of drag increase from the IID is related to visible ice formation on the airframe although the de-icing system was active. The ice is then directly removed when the aircraft is descending to warmer air, restoring the nominal flight performance at around 15:55 UTC.

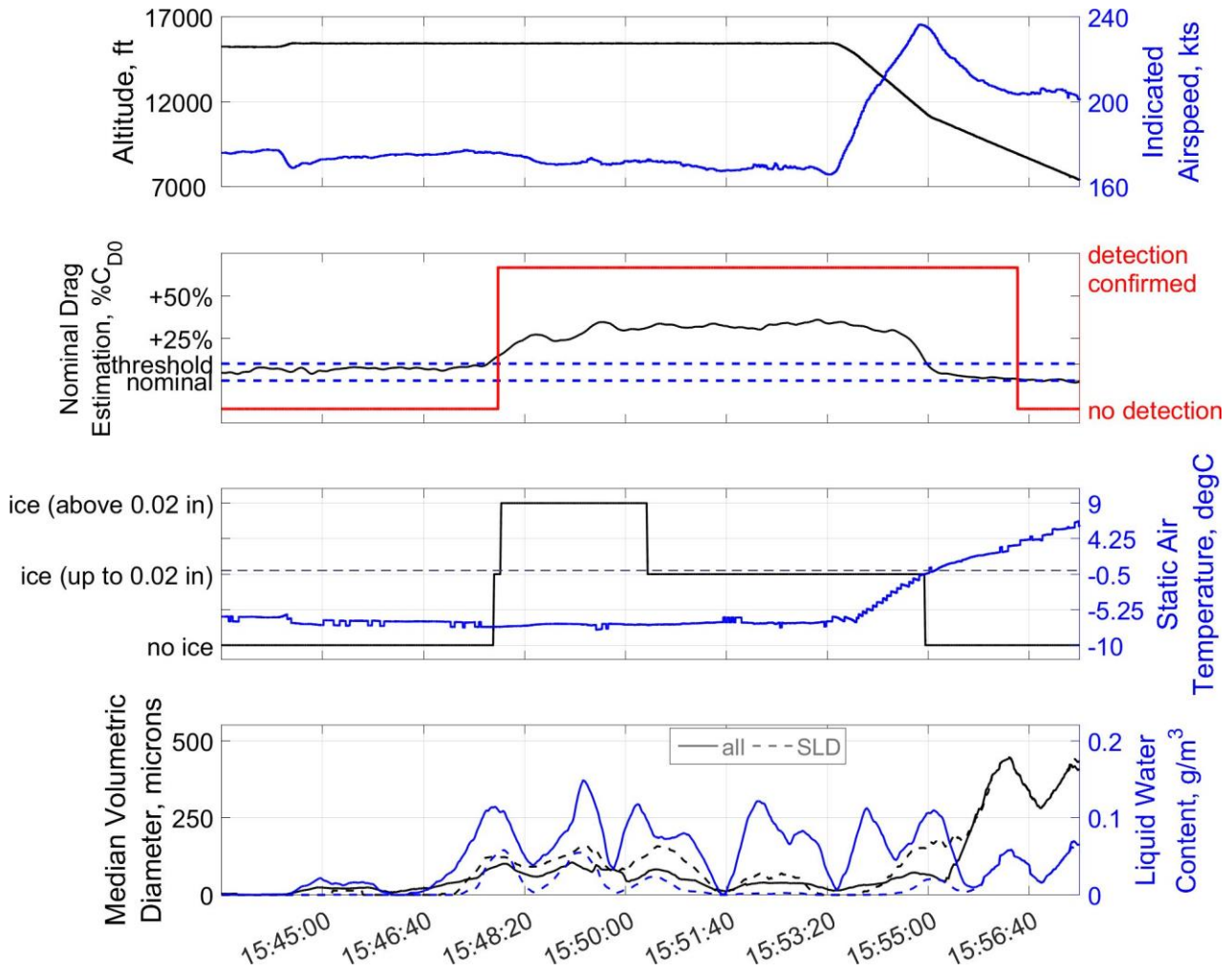


Figure 52: Time history of IID system performance during specific icing encounter from the second example flight (April 26<sup>TH</sup>, 2023, 15:43:19 UTC to 15:57:29 UTC): altitude and indicated airspeed (top), nominal drag estimation and IID detection output (second plot), ice built-up on reference accretion ice sensor and static air temperature (third plot), and MVD and LWC of encountered icing conditions (solid line) including the indication of the amount of SLD (dashed lines) (bottom); **updated detection threshold at 10% relative drag increase.**

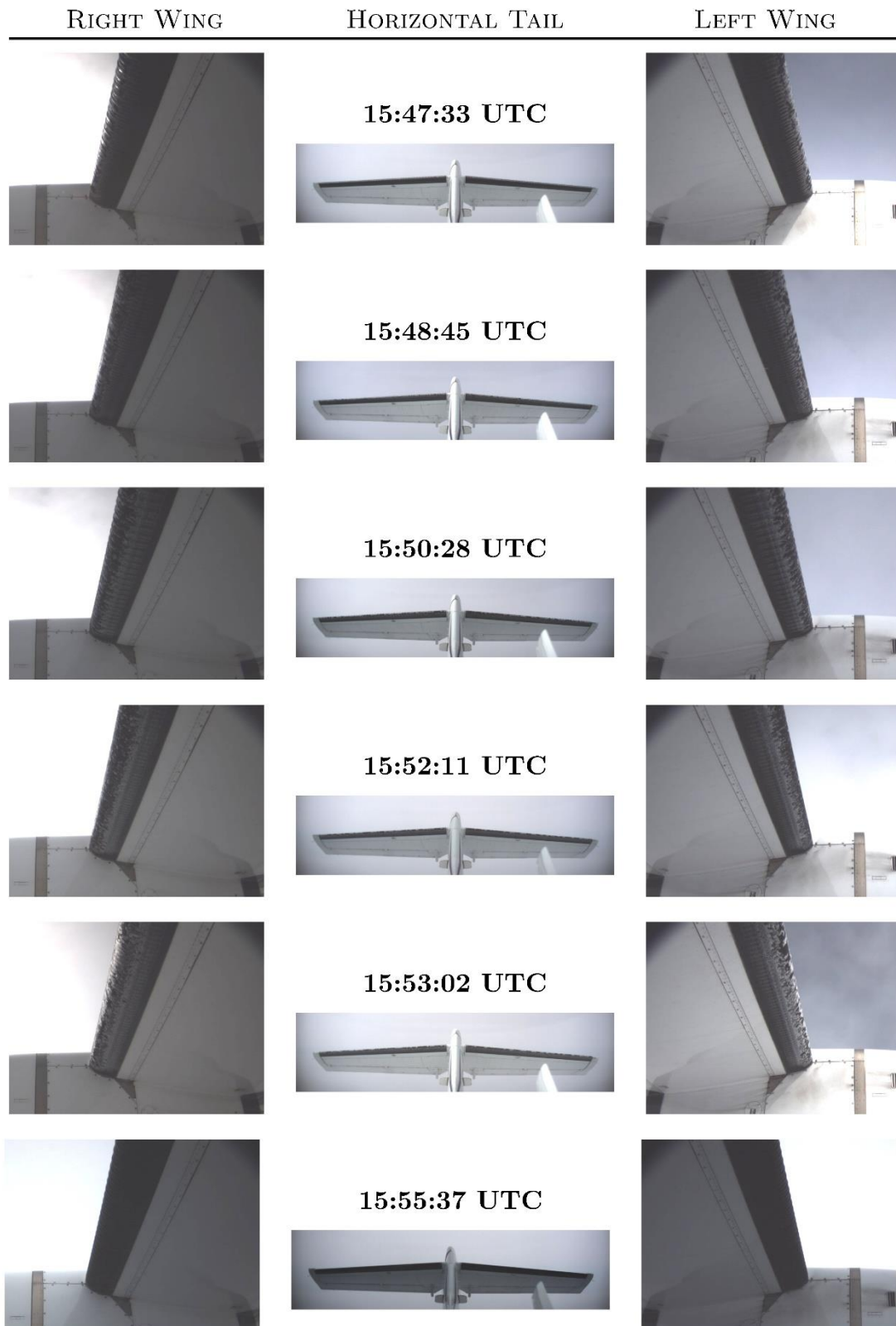


Figure 53: Evolution of ice accretion on the airframe during icing encounter: camera views on left & right wing and horizontal tail for specific moments during flight (increased brightness and contrast); corresponding to encounter and indirect ice detection output given in Figure 52; credit Safire / SENS4ICE project.



A second example extracted from this flight is given in Figure 54. The airframe is visible free of ice at 16:11:11 UTC (see Figure 55) and the flight performance at nominal level although the reference probe still indicates some ice. There is an encounter of supercooled water starting around 16:11:30 UTC resulting in ice accretion and a drag increase. The IID then correctly confirms the ice formation due to the resulting drag increase. During the whole encounter, light ice formation on the wing's leading edge is present, recurrently removed by the de-icing system keeping the estimated drag increase on a nearly constant level (see Figure 54 and Figure 55). After 16:29 UTC the aircraft descended to warmer air, the airframe is de-iced and the nominal flight performance restored. Again, this encounter shows, that monitoring the flight performance and aircraft capabilities for safe operation in hazardous conditions can be more comprehensive than using specific probes or information about the atmospheric conditions alone, because both were misleading in beginning of the data extract shown. Hence, hybridization of dissimilar technologies proves again its advantage compared to singular information.

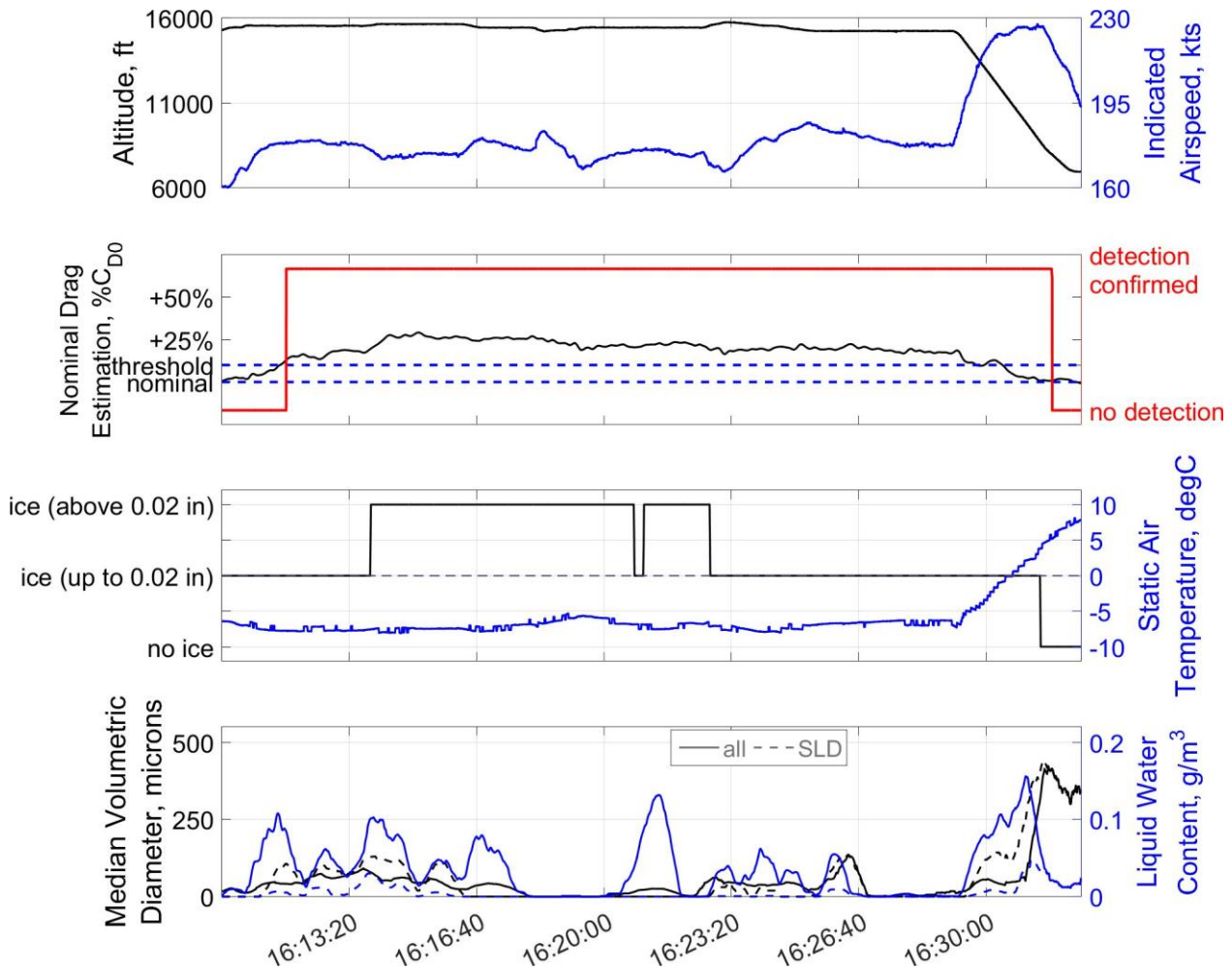


Figure 54: Time history of IID system performance during specific icing encounter from the second example flight (April 26<sup>th</sup>, 2023, 16:09:59 UTC to 16:32:29 UTC): altitude and indicated airspeed (top), nominal drag estimation and IID detection output (second plot), ice built-up on reference accretion ice sensor and static air temperature (third plot), and MVD and LWC of encountered icing conditions (solid line) including the indication of the amount of SLD (dashed lines) (bottom); **updated detection threshold at 10% relative drag increase.**

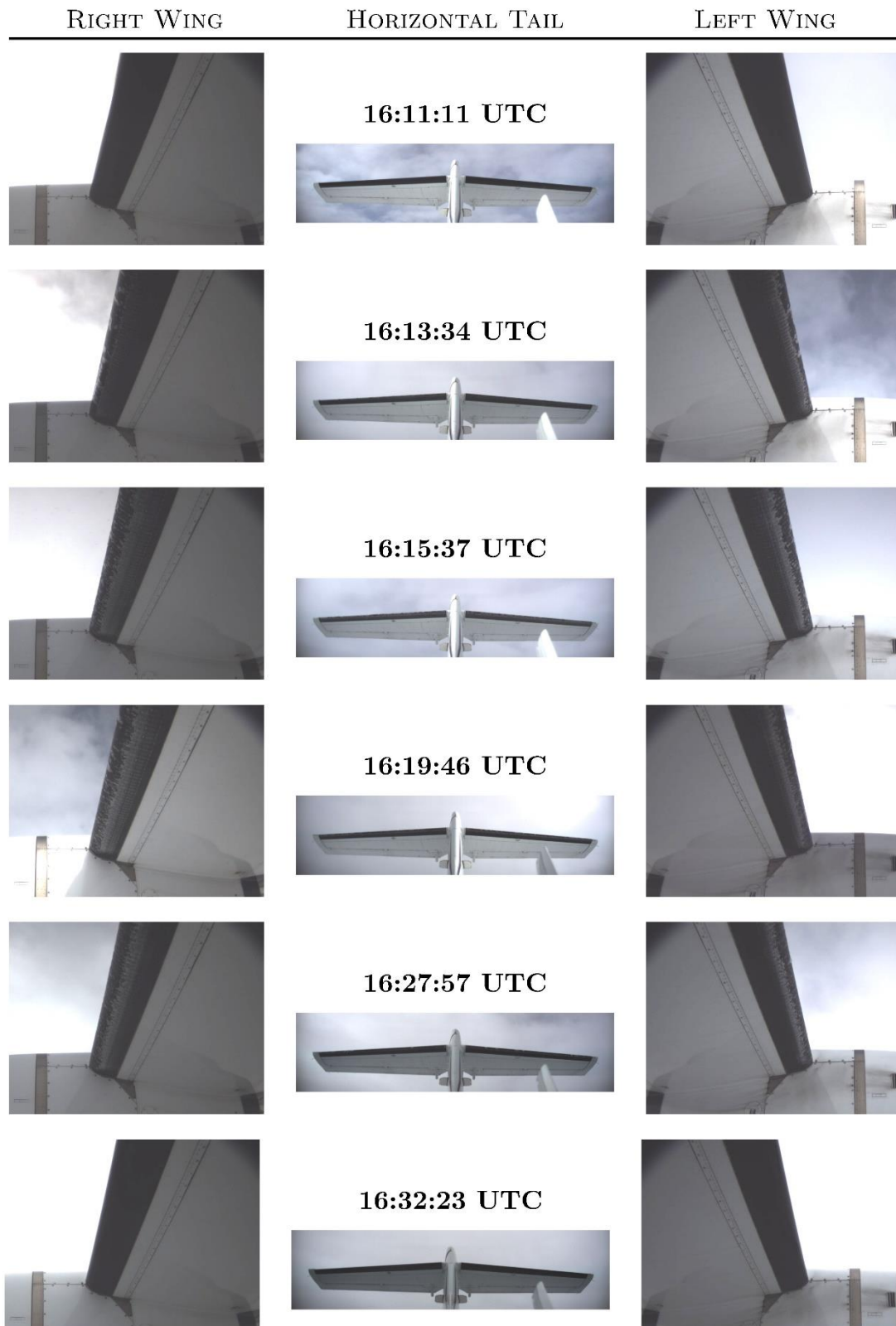


Figure 55: Evolution of ice accretion on the airframe during icing encounter: camera views on left & right wing and horizontal tail for specific moments during flight (increased brightness and contrast); corresponding to encounter and indirect ice detection output given in Figure 54; credit Safire / SENS4ICE project.



## Aerodynamic Degradation due to icing

Figure 56 shows again the aircraft drag polar calculated from the measured data for the whole flight (flaps retracted, gear up). The plot contains the aerodynamic reference used for the flight test reflecting the SAFIRE ATR42-320 characteristics with all SENS4ICE modifications (red line).

The maximum degradation is correlated with a nominal drag estimation change of around 35%, but having 25% to 30% change in average. This is also given in the time history plots from this flight. Although this flight contained also encounters of SLD, which could be a cause of significant aerodynamic degradations, the flight performance change observed was not as severe as it could have been expected. This does not mean that SLD icing is not a major threat to aircraft safety, but shows the need for a differentiated view on the icing situation and influence on the aircraft flight characteristics and operations. The main significance for a safe operation has the flight within a safe envelope, which must be continuously monitored despite the icing conditions encountered, as given by the IID. This is one key to success, although of course the confirmation about the icing conditions present must result from direct sensing techniques.

Figure 57 contains the aircraft drag polar including an indication of the ice accretion announced by the Safire reference probe. Overall, the drag increase (dots shifted to the right due to ice accretion) is well corresponding to the ice information given by the probe (cyan and yellow dots). But there again are also some blue dots in the shifted cloud indicating abnormal performance which is not directly correlated to the reference probe information. These are again corresponding to the parts of the flight, where the performance was already or still degraded by the probe did not give any indication, e.g., in Figure 52. The results from the indirect ice detection (updated detection threshold at 10%) output are given in Figure 58 as indication over the drag polar. There are only a few parts left, where the shifted drag is not directly marked yellow indicating a confirmed detection. Further reduction of the threshold to 7% additionally reduced the blue dots shifted to the right indicating that the IID is then able to additionally announce the smaller changes of flight performance due to the icing, but keeping in mind that this enhanced sensitivity might result in potential false alarms for certain flight conditions not tested here.

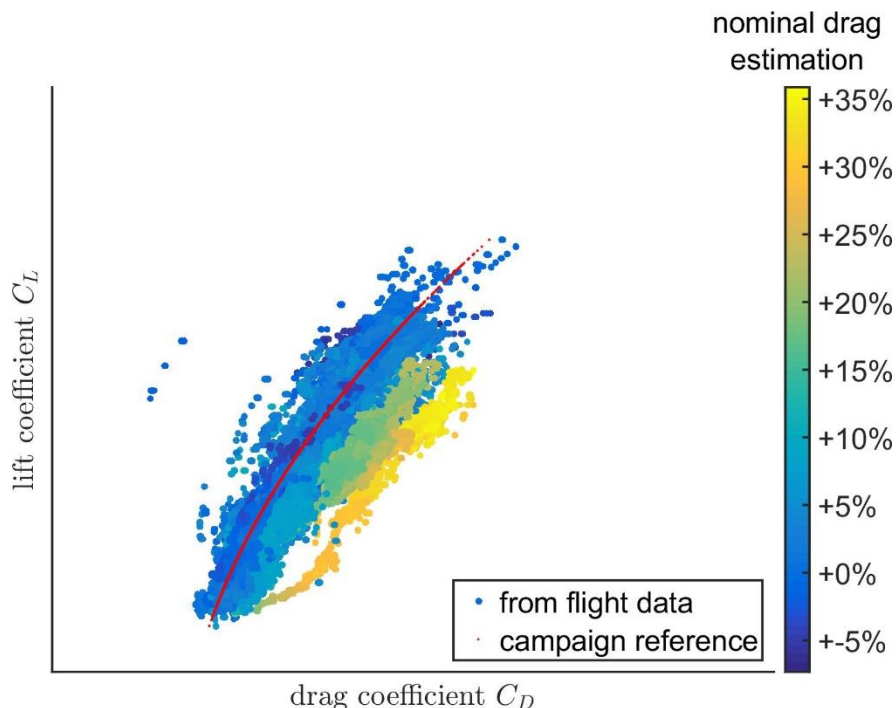


Figure 56: Aircraft drag polar from example flight on April 26<sup>TH</sup>, 2023: calculated lift and drag coefficient from flight data measurements and reference for the SAFIRE ATR42-320 with SENS4ICE modifications; drag coefficient data including the indication of nominal drag estimation calculated by IID.

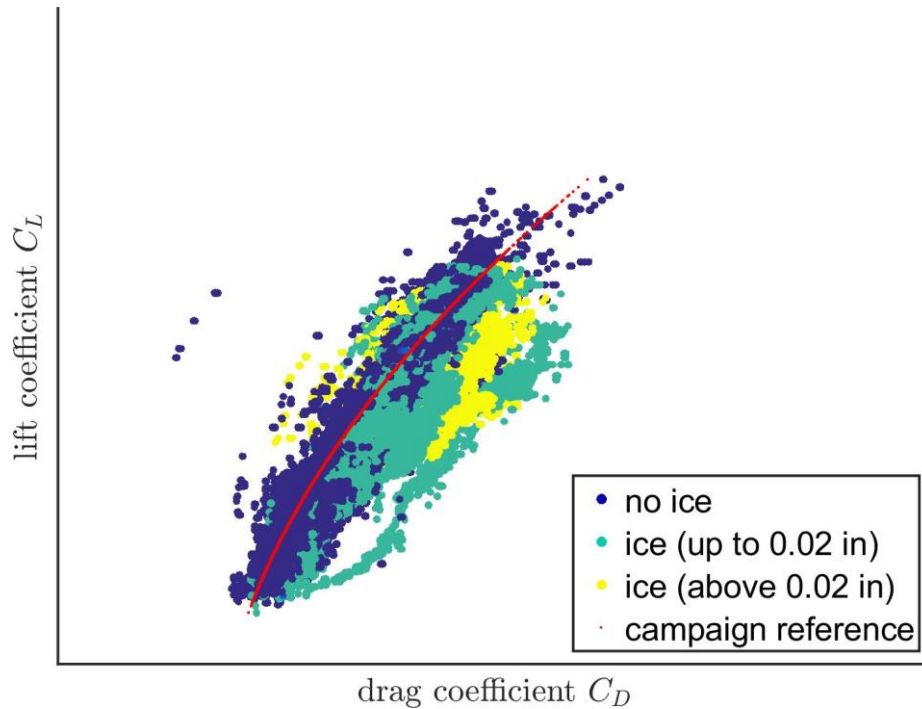


Figure 57: Aircraft drag polar from example flight on April 26<sup>TH</sup>, 2023: calculated lift and drag coefficient from flight data measurements and reference for the SAFIRE ATR42-320 with SENS4ICE modifications; drag coefficient data including the indication of ice accretion announced by Safire ice reference probe.

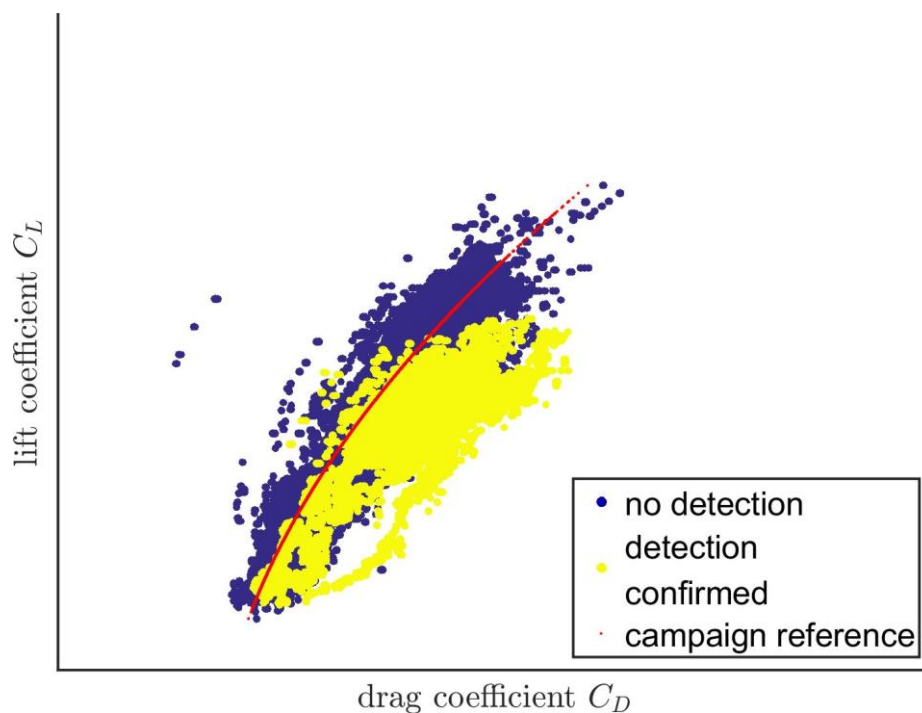


Figure 58: Aircraft drag polar from example flight on April 26<sup>TH</sup>, 2023: calculated lift and drag coefficient from flight data measurements and reference for the SAFIRE ATR42-320 with SENS4ICE modifications; drag coefficient data including the indication of confirmed indirect ice detection; **updated detection threshold at 10% relative drag increase.**

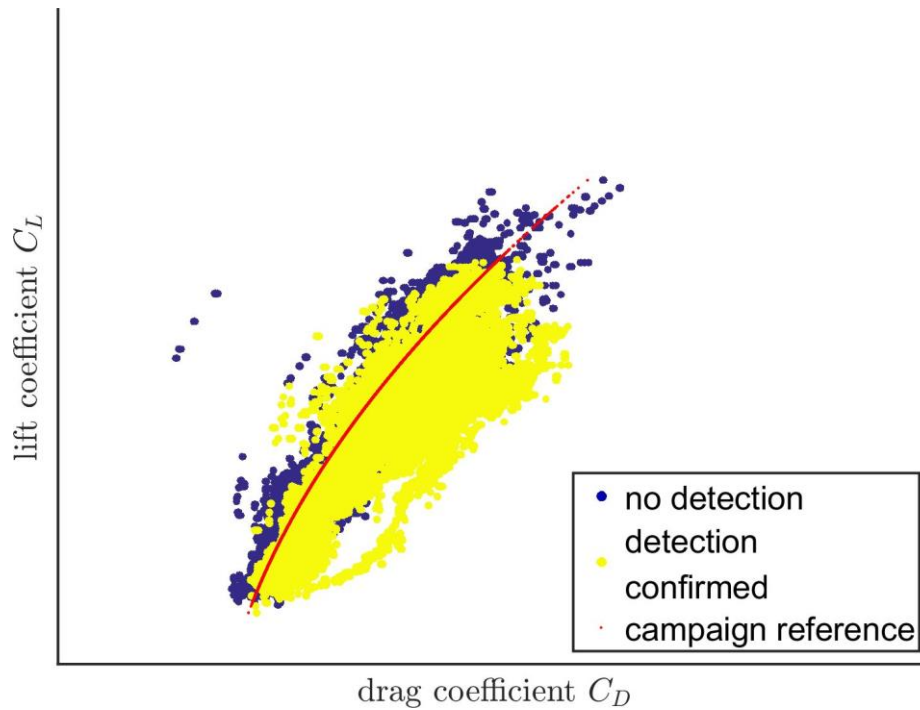


Figure 59: Aircraft drag polar from example flight on April 26<sup>th</sup>, 2023: calculated lift and drag coefficient from flight data measurements and reference for the SAFIRE ATR42-320 with SENS4ICE modifications; drag coefficient data including the indication of confirmed indirect ice detection; **reduced detection threshold at 7% relative drag increase.**

## FLIGHT AS230022

Flight as230022 took place in the morning of April 27<sup>th</sup>, 2023 around Toulouse. Figure 60 contains the flight track including an indication of the icing encountered based on the Safire icing reference probe signal. It is clearly visible, that also during this flight distinct cycles were flown to guarantee a full de-icing of the aircraft in warmer air (lower altitudes) after the different individual icing encounters.

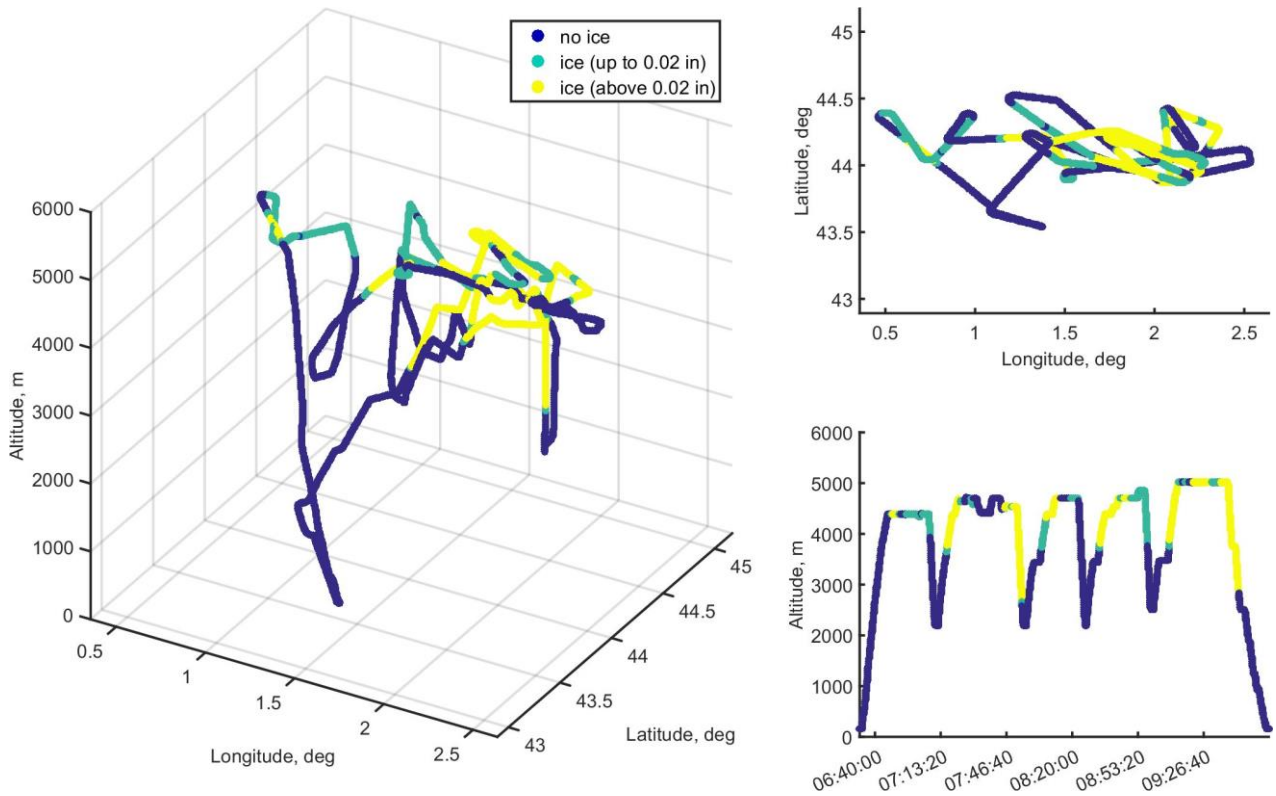


Figure 60: Flight track from SENS4ICE European icing campaign flight on April 27th, 2023 (morning) around Toulouse: geodetic position and altitude with indication of icing encountered / built-up.

Figure 61 contains the time history plot of the whole flight showing the IID results together with the aircraft flight information and the atmospheric conditions. Using the pre-campaign defined very conservative detection threshold, the major icing encounters were again detected correctly although the aerodynamic degradation only slightly exceeds the very conservative threshold. Again, the lighter encounters during the flight with small change of flight performance could not be announced by the IID using the 15% threshold, although the drag increase is also estimated correctly in these cases. With the updated threshold of 10% the detection behavior is more preferable because the increased sensitivity allows to also announce most of the remaining encounters, given in Figure 62. Note that the performance degradation resulting from icing on the aircraft being below the updated threshold of 10% does not pose a direct threat to the aircraft operation and can be also detected by an additional threshold reduction as discussed above from flight as230021.

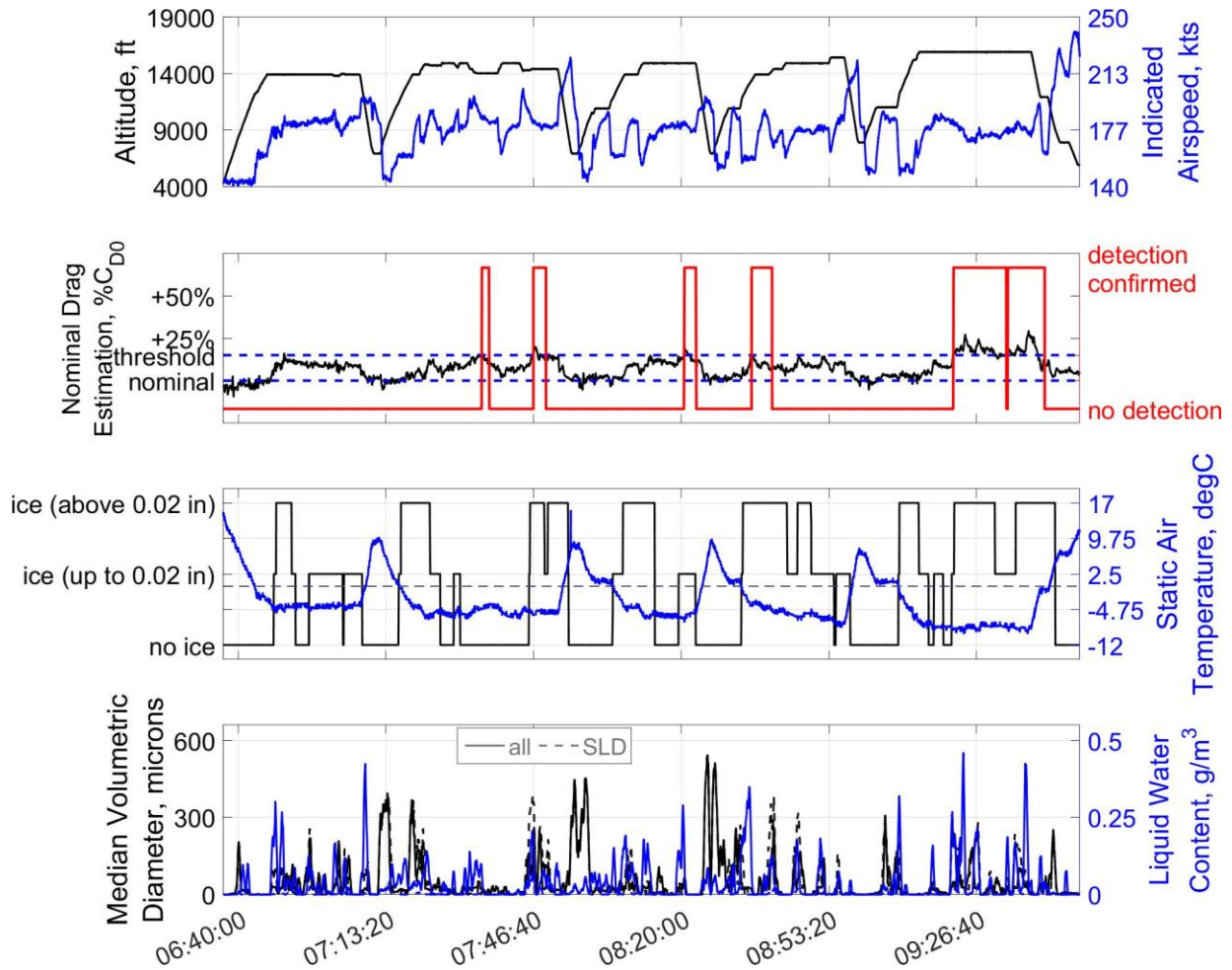


Figure 61: Time history of IID system performance during the third example flight as230022 (April 27<sup>th</sup>, 2023, 06:36 UTC to 09:49 UTC): altitude and indicated airspeed (top), nominal drag estimation and IID detection output (second plot), ice built-up on reference accretion ice sensor and static air temperature (dashed line 0degC) (third plot), and MVD and LWC of encountered icing conditions (solid line) including the indication of the amount of SLD (dashed lines) (bottom); **original detection threshold at 15% relative drag increase.**

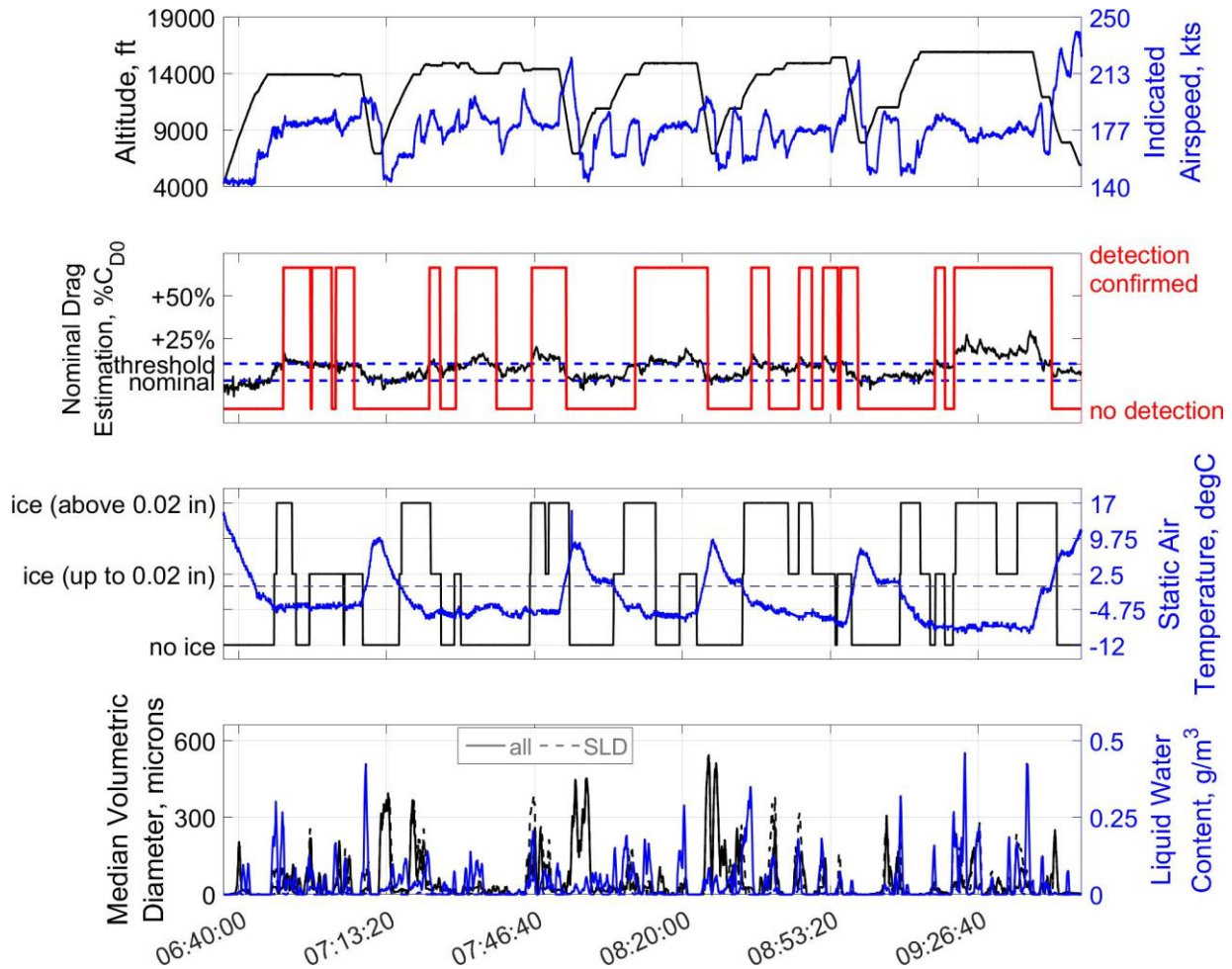


Figure 62: Time history of IID system performance during the third example flight as230022 (April 27<sup>th</sup>, 2023, 06:36 UTC to 09:49 UTC): altitude and indicated airspeed (top), nominal drag estimation and IID detection output (second plot), ice built-up on reference accretion ice sensor and static air temperature (dashed line 0degC) (third plot), and MVD and LWC of encountered icing conditions (solid line) including the indication of the amount of SLD (dashed lines) (bottom); **updated detection threshold at 10% relative drag increase.**

Figure 63 shows the first encounter of this flight starting around 06:46 UTC directly after the aircraft reached the targeted altitude at FL140. The reference ice accretion probe indicates a fast ice accretion which is also reflected by the nominal drag estimation reaching 10% increase within around one minute. Nevertheless, the aerodynamic degradation stagnated which did not right away trigger the IID output until 06:50 UTC when the threshold is exceeded slightly for a short time. Until round 07:07 UTC the aircraft was encountering icing several times, but the drag did not further increase significantly. Hence, the IID nominal drag estimation falls below the threshold and exceeds it again another two times forcing the detection output to show the given toggling characteristic. This is an undesired behavior which should be prevented by the detection logic. But in this case, the reset confirmation indicates a longer period of negative trend in the drag increase which is interpreted as intended by the IID logic. Unfortunately, the ice formation on the aircraft forces the IID to trigger the detection output almost right after reset again at around 06:56:40 UTC and 07:02 UTC. For a later implementation of the IID in an aircraft fleet in service, this behavior should be further prevented by a more robust detection logic around the threshold. With the results from the SENS4ICE flight test, it will be possible to further mature the IID because during the design phase, no specific information about the distinct impact of icing on the ATR 42 was available.

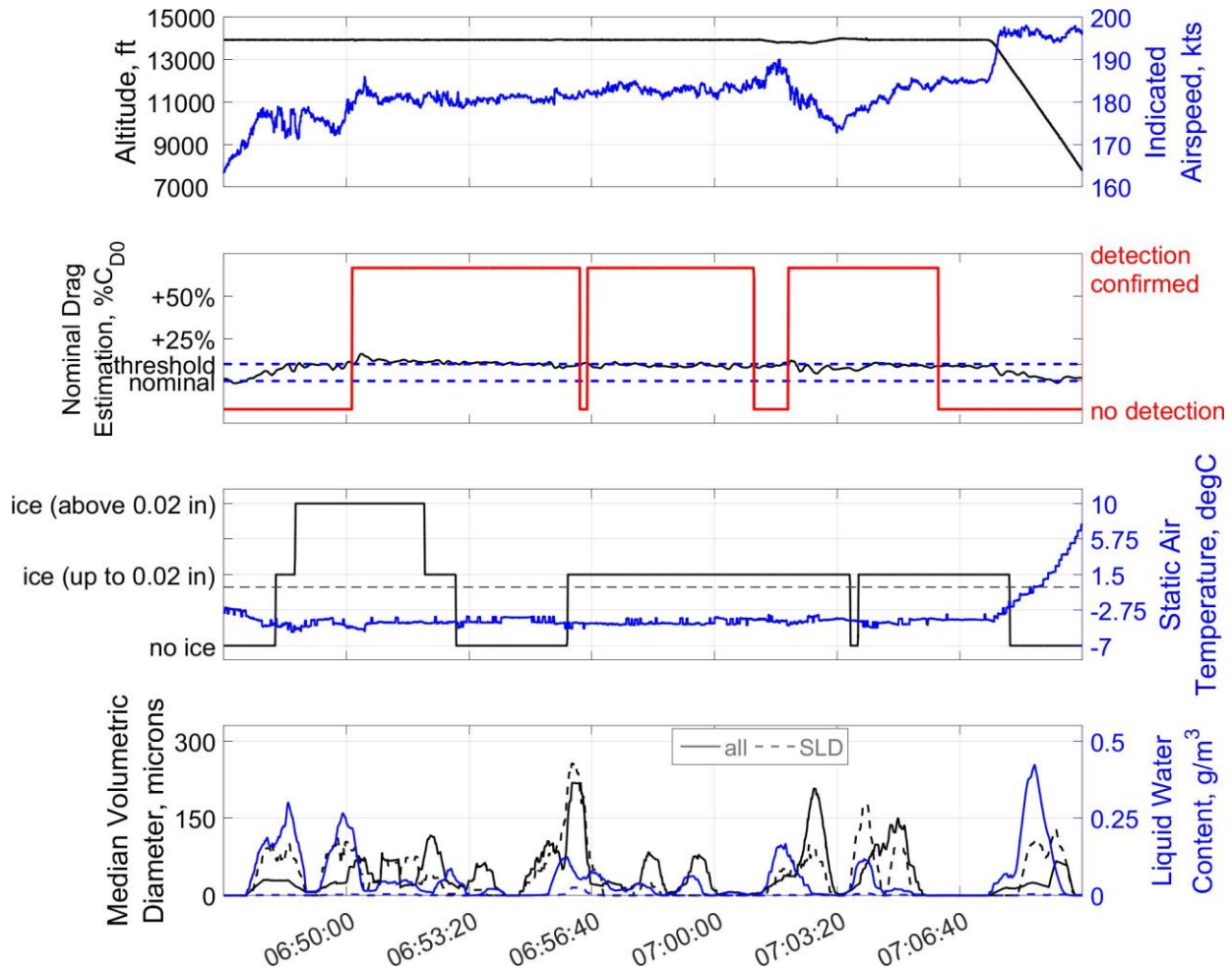


Figure 63: Time history of IID system performance during specific icing encounter from the third example flight (April 27<sup>th</sup>, 2023, 06:46:39 UTC to 07:09:59 UTC): altitude and indicated airspeed (top), nominal drag estimation and IID detection output (second plot), ice built-up on reference accretion ice sensor and static air temperature (third plot), and MVD and LWC of encountered icing conditions (solid line) including the indication of the amount of SLD (dashed lines) (bottom); **updated detection threshold at 10% relative drag increase.**

Figure 64 shows an important result from the SENS4ICE flight test concerning performance degradation and the detection behavior. Before the aircraft descended again from FL150 to FL140 after 7:43UTC the flight performance was still degraded from some ice accretion caused by a liquid water encounter after the last de-icing cycle in warmer air. The IID nominal drag estimation indicates the degradation while not triggering any warning because the magnitude of the increase is below the threshold. But, the reference probe did not indicate the presence of icing until the next encounter beginning around 07:45 UTC with large droplets. Then, the ice formation on the aircraft further degrades the flight performance directly resulting in an IID detection output. In parallel, also the reference accretion probe is indicating a significant ice formation. This example shows that the performance monitoring delivers valuable information about the current aircraft state even when the direct sensor did not indicate any icing conditions, as it could happen when the aircraft already left the clouds, the reference probes are free of ice but not the airframe itself.

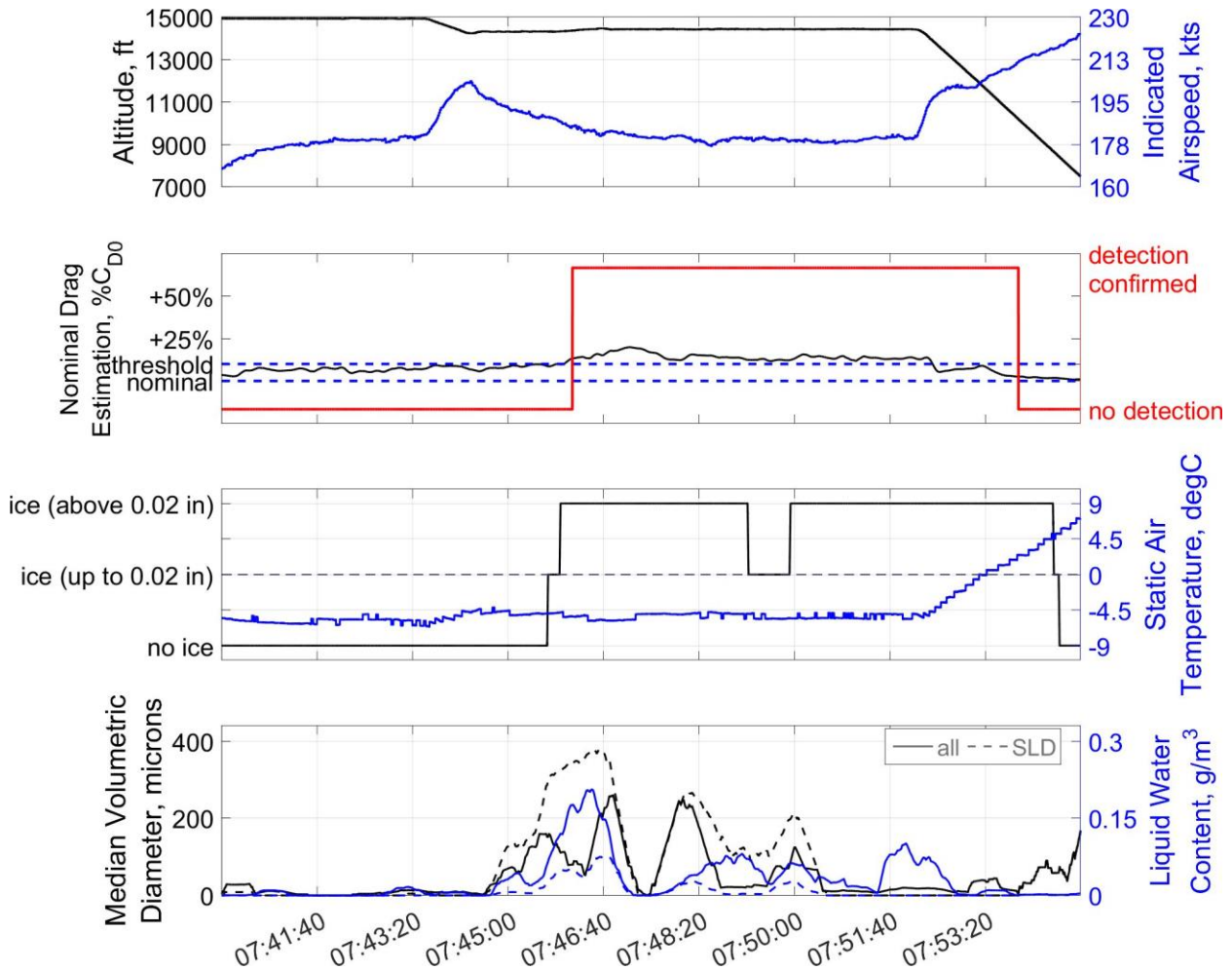


Figure 64: Time history of IID system performance during specific icing encounter from the third example flight (April 27<sup>TH</sup>, 2023, 07:39:59 UTC to 07:54:59 UTC): altitude and indicated airspeed (top), nominal drag estimation and IID detection output (second plot), ice built-up on reference accretion ice sensor and static air temperature (third plot), and MVD and LWC of encountered icing conditions (solid line) including the indication of the amount of SLD (dashed lines) (bottom); **updated detection threshold at 10% relative drag increase.**

Figure 65 contains the time histories of another encounter showing an interesting behavior of the aerodynamic degradation visible through the IID drag estimation. The aircraft reached a cloud layer and more significant icing started (above 0.02 in) at around 8.07 UTC indicated by the reference probe results. In parallel, the aircraft performance is degraded leading to an increase in drag exceeding the threshold around 8:09 UTC (see also the images given in Figure 66). After climbing to FL150 the aircraft left icing conditions (bottom plot in Figure 65) for e.g., around one minute at 8:17 UTC while the reference probe did also not indicate any icing. But there was still an additional drag present slowly decreasing until the next cloud was entered and icing condition present again. During this time the IID did still announce correctly the aircraft degradation. In Figure 66 pictures of the wing leading edges and horizontal tail at 8:17:35 UTC are provided, where the trace ice accretion leading to the degraded performance are still visible. At around 8:19 UTC another cloud was entered and the airframe collected again more ice leading to a slightly higher additional drag estimated by the IID. After the aircraft descended in warmer air, the ice was completely removed and the nominal performance restored (after 8:26 UTC).

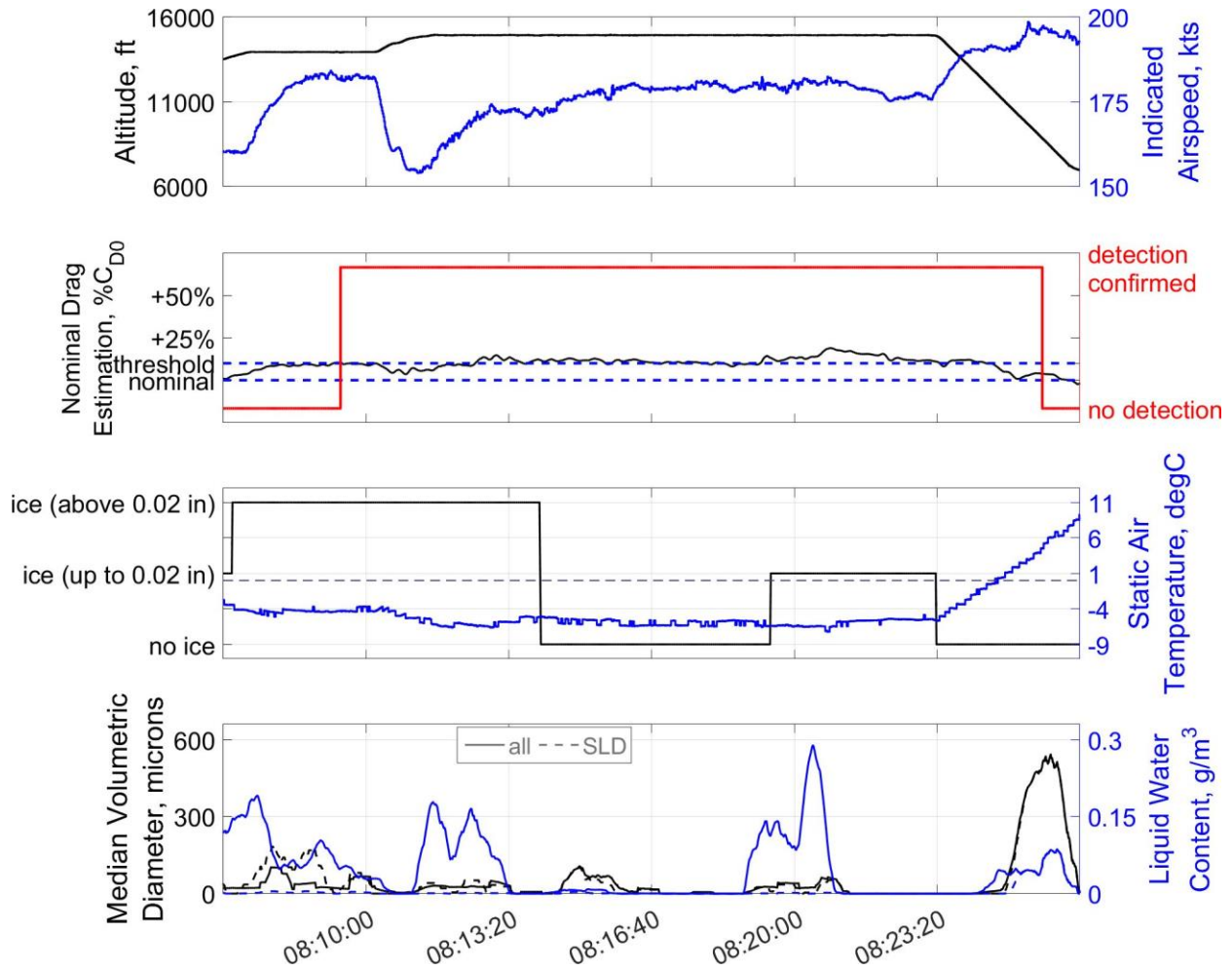


Figure 65: Time history of IID system performance during specific icing encounter from the third example flight (April 27<sup>TH</sup>, 2023, 08:06:39 UTC to 08:26:39 UTC): altitude and indicated airspeed (top), nominal drag estimation and IID detection output (second plot), ice built-up on reference accretion ice sensor and static air temperature (third plot), and MVD and LWC of encountered icing conditions (solid line) including the indication of the amount of SLD (dashed lines) (bottom); **updated detection threshold at 10% relative drag increase.**

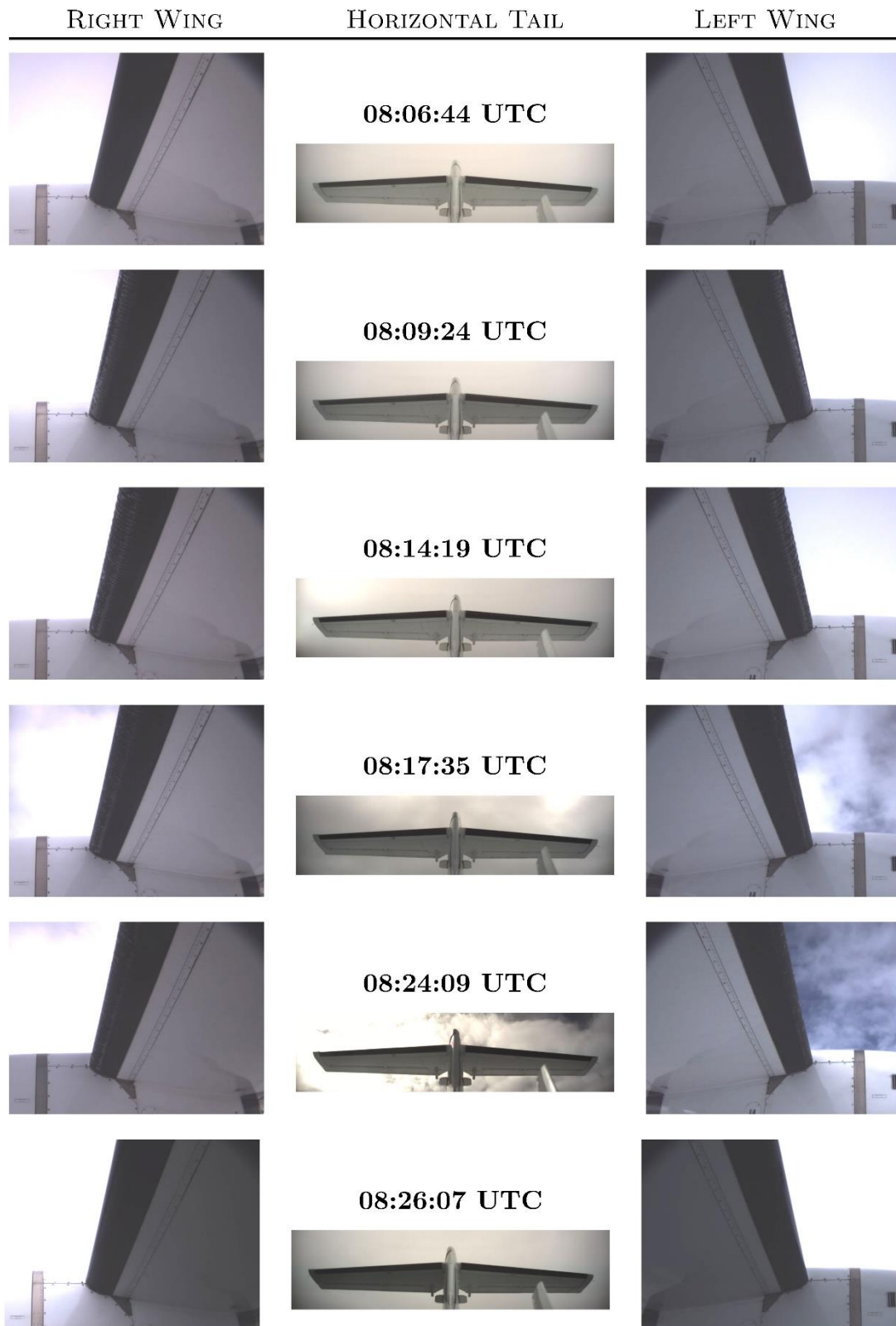


Figure 66: Evolution of ice accretion on the airframe during icing encounter: camera views on left & right wing and horizontal tail for specific moments during flight (increased brightness and contrast); corresponding to encounter and indirect ice detection output given in Figure 65; credit Safire / SENS4ICE project.



Figure 67 shows the time histories of last encounters of this flight. In the beginning during the climb, the reference probe indicated significant icing whereas the estimated drag only points to a slight performance loss. The icing on the probe might be a result from the supercooled conditions encountered before the climb, where ice can form on a surface even at outside temperature above 0°C, if the surface itself is cold enough. This might be speculation, but is relevant in terms of overall icing detection capabilities assessment, as this case might not be relevant for the overall evaluation of detection capabilities in order to assess the need for dissimilar technologies. When the aircraft reached the target altitude (FL160), the reference probe slowly reset its indication until a supercooled cloud was entered given by the rise in LWC and MVD. It is interesting that the performance degradation gets significant the same time the reference probe also indicates again an ice accretion, being very consistent this time. At 09:16:43 UTC only very few traces of ice were present on the airframe, but at 20 seconds later ice formation was clearly visible, leading to the said degradation (see also Figure 68). When the cloud was left the additional drag slowly decreased resetting the IID output and the reference probe indication of ice accretion. After 09:20 UTC icing conditions with large drops led again to airframe icing consistently detected by IID and the reference probe. With some variation in magnitude, the degradation was present and correctly detected until 09:43:20 when the aircraft was in descent reaching warmer air and the nominal flight performance was restored.

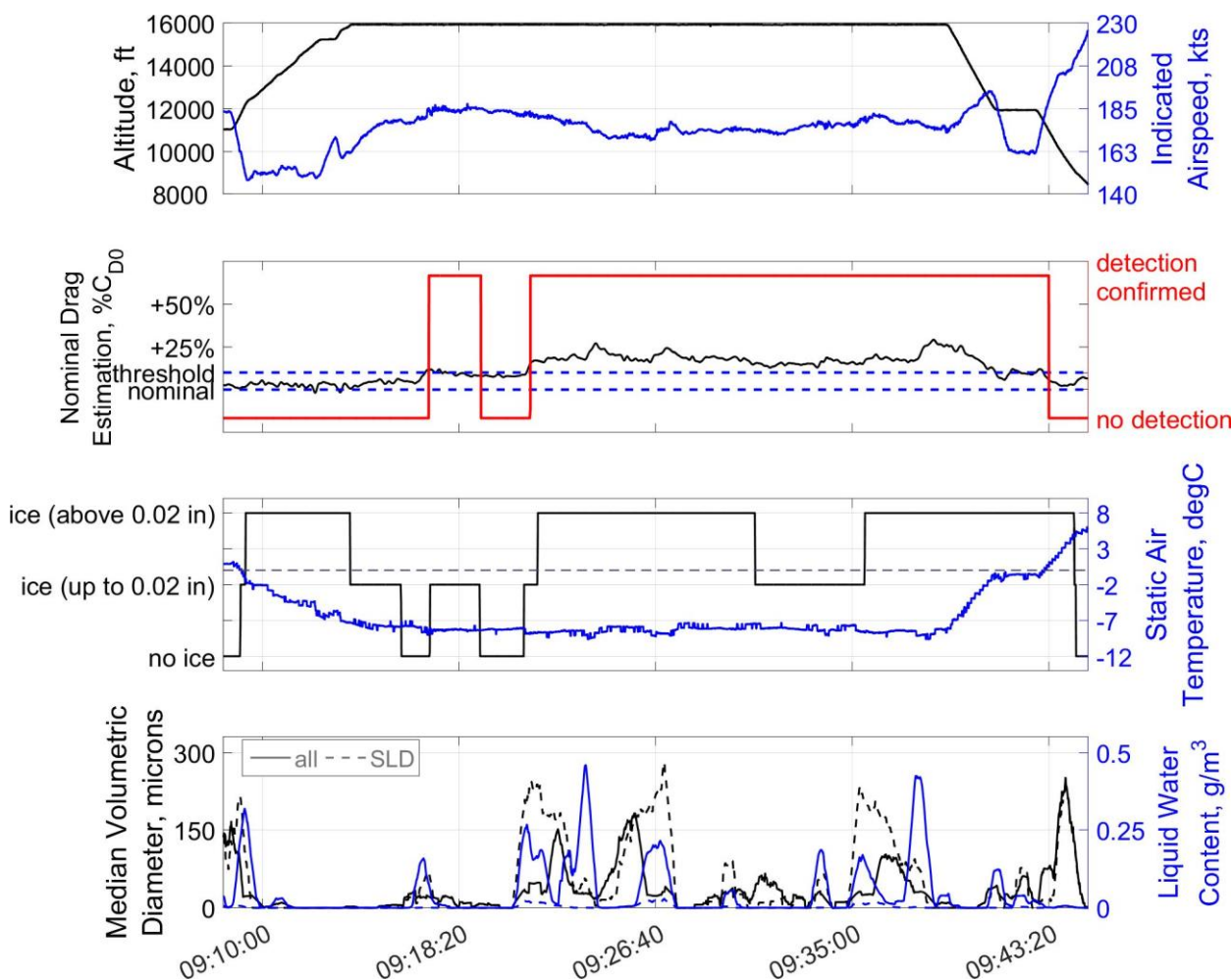


Figure 67: Time history of IID system performance during specific icing encounter from the third example flight (April 27<sup>th</sup>, 2023, 09:08:20 UTC to 09:45:00 UTC): altitude and indicated airspeed (top), nominal drag estimation and IID detection output (second plot), ice built-up on reference accretion ice sensor and static air temperature (third plot), and MVD and LWC of encountered icing conditions (solid line) including the indication of the amount of SLD (dashed lines) (bottom); **updated detection threshold at 10% relative drag increase.**

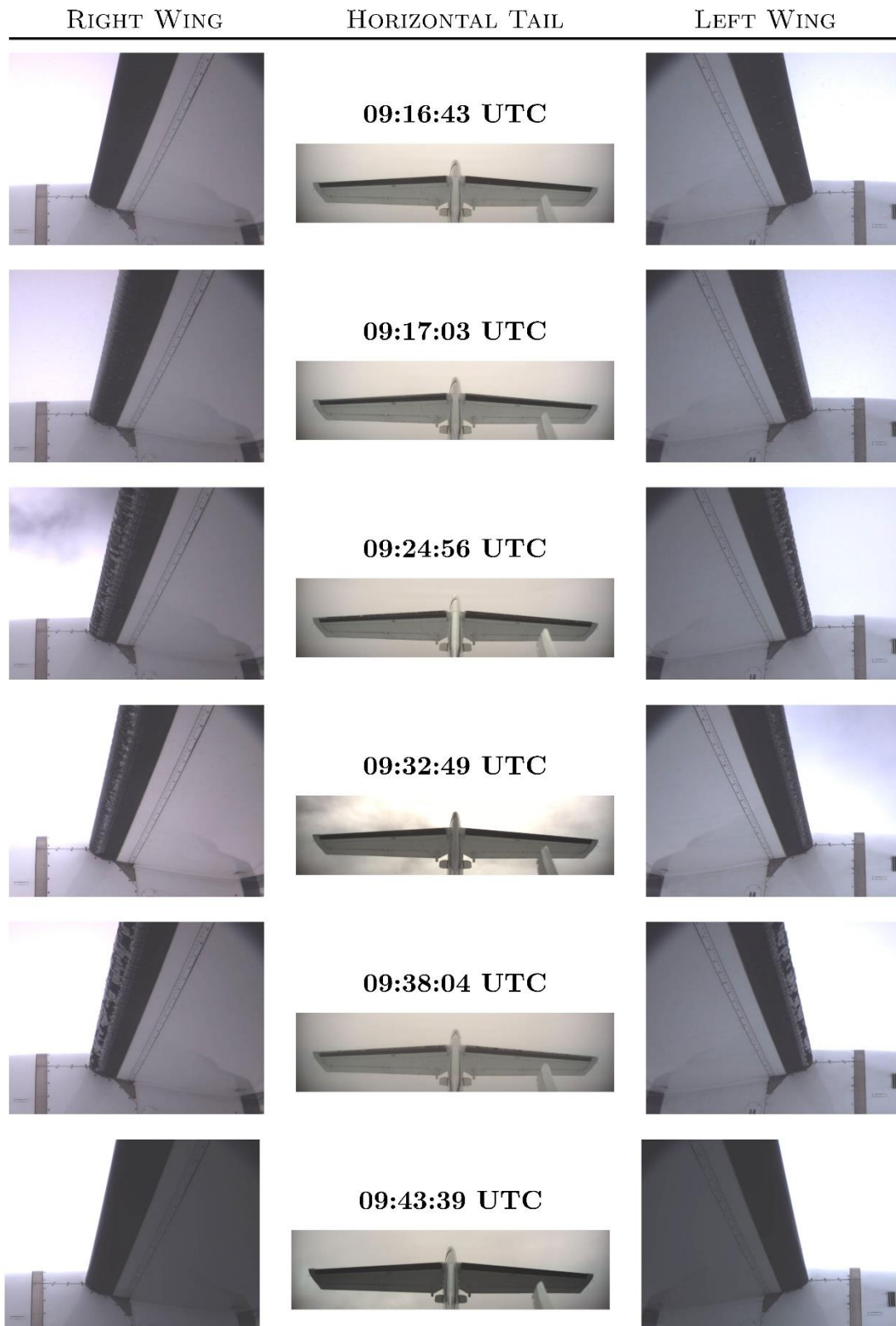


Figure 68: Evolution of ice accretion on the airframe during icing encounter: camera views on left & right wing and horizontal tail for specific moments during flight (increased brightness and contrast); corresponding to encounter and indirect ice detection output given in Figure 67; credit Safire / SENS4ICE project.



### Aerodynamic Degradation due to icing

Figure 69 contains the aircraft drag polar calculated from the measured data for the whole flight (flaps retracted, gear up). The plot contains again the aerodynamic reference used for the flight test reflecting the Safire ATR42-320 characteristics with all SENS4ICE modifications (red line).

The maximum degradation is correlated with a nominal drag estimation change of around 30%, but having 25% change in average. This flight contained also encounters of SLD, which could be a cause of significant aerodynamic degradations, but the flight performance change observed did not reflect this expectation as for flight as230021. Figure 70 contains again the aircraft drag polar including an indication of the ice accretion announced by the Safire reference probe. Overall, the drag increase (dots shifted to the right due to ice accretion) is well corresponding to the ice information given by the probe (cyan and yellow dots). But there again are also some blue dots in the shifted cloud indicating abnormal performance which is not directly correlated to the reference probe information. The results from the indirect ice detection (**updated detection threshold at 10%**) output are given Figure 71 as indication over the drag polar. There are again only a few parts left, where the shifted drag is not directly marked yellow indicating a confirmed detection.

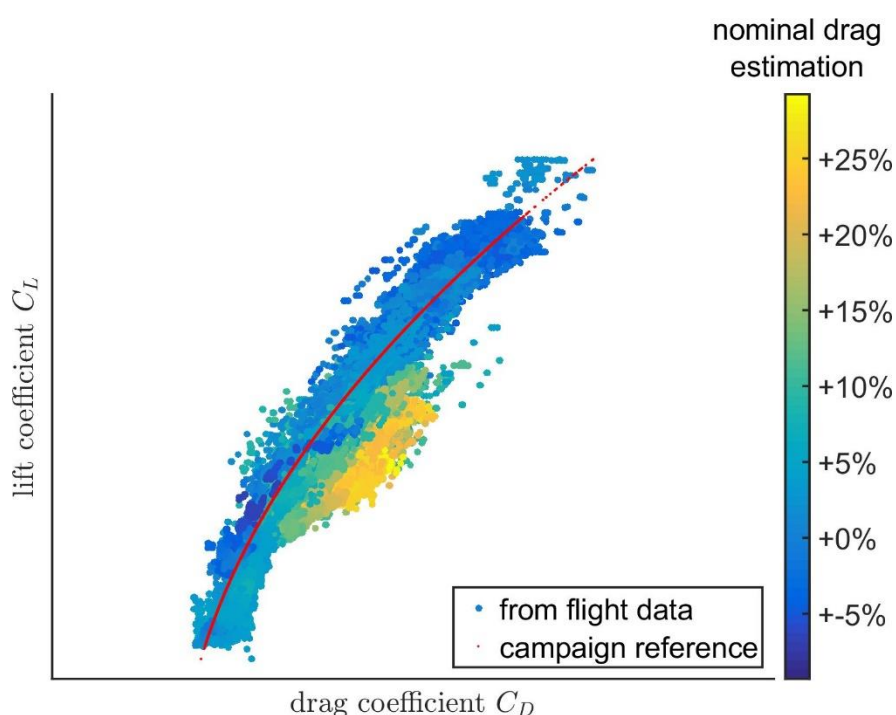


Figure 69: Aircraft drag polar from example flight on April 27<sup>TH</sup>, 2023: calculated lift and drag coefficient from flight data measurements and reference for the SAFIRE ATR42-320 with SENS4ICE modifications; drag coefficient data including the indication of nominal drag estimation calculated by IID.

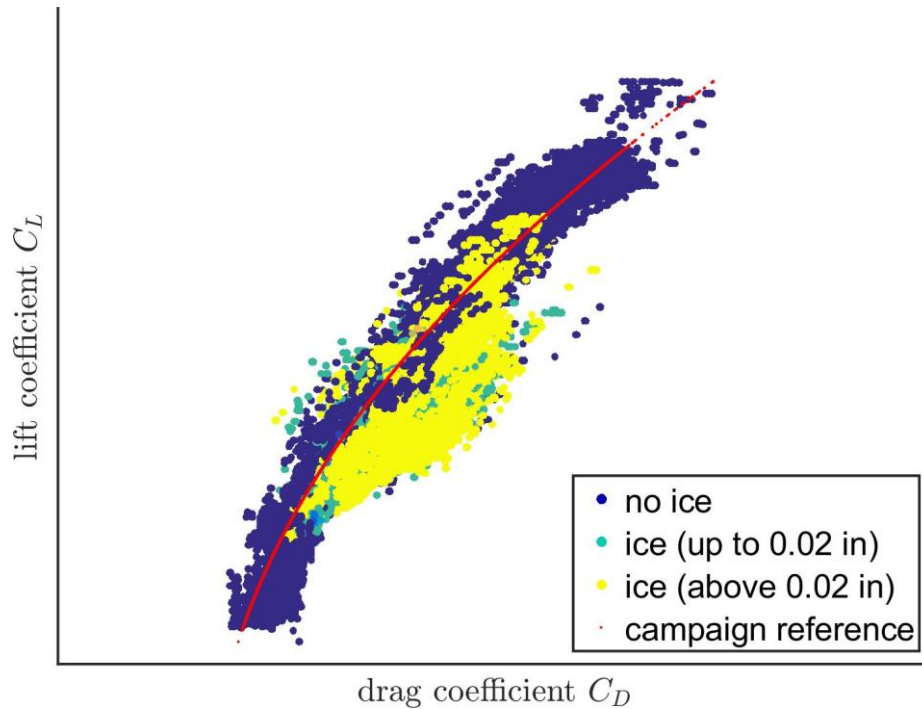


Figure 70: Aircraft drag polar from example flight on April 27<sup>TH</sup>, 2023: calculated lift and drag coefficient from flight data measurements and reference for the SAFIRE ATR42-320 with SENS4ICE modifications; drag coefficient data including the indication of ice accretion announced by Safire ice reference probe.

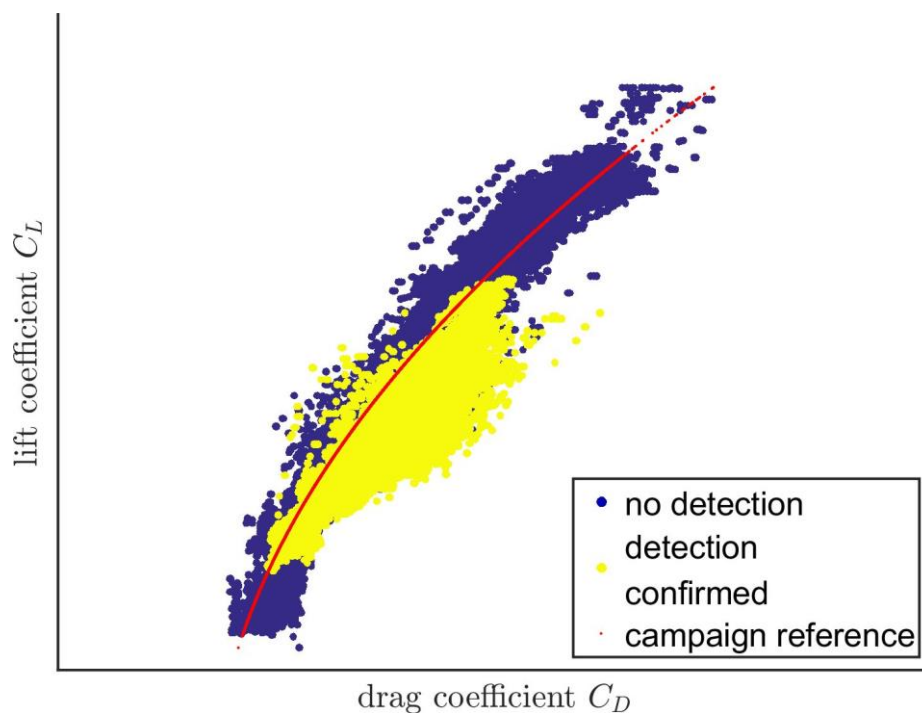


Figure 71: Aircraft drag polar from example flight on April 27<sup>TH</sup>, 2023: calculated lift and drag coefficient from flight data measurements and reference for the SAFIRE ATR42-320 with SENS4ICE modifications; drag coefficient data including the indication of confirmed indirect detection; **updated detection threshold at 10% relative drag increase.**



## 2.5 Ways forward for Indirect Detection algorithm

The Indirect Ice Detection algorithm developed in SENS4ICE showed very good performance during both flight test campaigns. The IID was well capable to detect the icing-related performance degradation and reliably monitor the corresponding drag increase. In addition, the further modification to the system made post-flight even enhanced the system performance to further detect flight performance degradations in a more sensitive and robust way. Nevertheless, the current version of the IID is an experimental demonstrator tailored to the specific flight test benches and their configurations during the SENS4ICE flight test campaigns (the maturity of the IID function could be considered TRL5 after the flight test campaigns). For an operational use within an in-service aircraft fleet, the algorithm must be further enhanced and implemented into the aircraft avionics, which was clearly not the scope of SENS4ICE.

The prototype running during the flight test campaigns was already designed to be highly adaptive to “known” changes of the aircraft flight performance, which was used to change the engine thrust representation in the IID for the Phenom 300 prototype. Also, the modification to the specific flight test bench prior to the flight test has proven the designed system flexibility. Hence, the algorithm seems highly applicable to other transport aircraft or even any fixed-wing aircraft design with reasonable effort. For smaller aircraft not equipped with direct ice detection technologies, the IID can be a valuable option for ice detection as the only detection source since its implementation into the avionics system could be easier than ice detectors hardware installation. In addition, the algorithm might give a high potential for monitoring the aircraft icing status in terms of present ice accretion degrading the flight characteristics and the effectiveness of countermeasures (anti-ice and de-icing systems) trying to prevent any negative impact of icing on the aircraft operations, both as standalone or as part of the hybrid approach. Such an evaluation might be possible with the data available from SENS4ICE flight test, but was not in the specific scope of the project.

Therefore, further work should explore the possibilities to implement the IID (mainly as standalone function) for new and/ or small aircraft configurations like, e.g., unmanned aerial vehicles, advanced air mobility applications or new transport aircraft targeting the sustainable aviation goals with mainly electric systems requiring completely new ice protections system designs. Also, the evaluations beyond the SENS4ICE scope based on the flight data and information gathered must be subject to further work to fully explore the IID potential for safer aviation in all icing conditions. Having an algorithm like the IID constantly running on aircraft during flight, an envelope opening for icing conditions defined within the App. O might be possible, if regulators agree, to achieve a partly certification for flight in additional icing conditions with existing aircraft if flight safety can be assured using the IID approach.





### 3. Evaluation of Hybrid Ice Detection System

This section is dedicated to the analysis of Hybrid Ice Detection System (HIDS) performance during the two SENS4ICE flights tests campaigns. As described in [6], two HIDS demonstrators were developed in order to meet the requirements and needs of the two aircraft FT architectures and of the different direct detectors. The DLR IID algorithms described in §2.2 were embedded in two HIDS demonstrators.

**DISCLAIMER:** The assessment of icing severity used in this section is only for research and development purposes based on engineering science judgement but not related to the aircraft operations.

#### 3.1 HIDS general description

HIDS allows to combine the direct ice detection, provided by the DIDSs installed outside the aircraft, measuring directly the local air flow characteristics and/or the ice accretion on a specific surface, and the indirect detection, provided by the IID, which evaluates the effect of ice accretion on aircraft flight performance.

During FT, HIDS main functions were to:

1. Initialize IID with some data not available through the A/C network, i.e. A/C weight, CG position, Fuel weight, before the takeoff;
2. Collect in real time all the aircraft data transferred through the FTI network in order to feed the IID algorithm;
3. Collect DIDS outputs, standardize each data format;
4. Run the IID algorithm;
5. Combine direct and indirect detection, via an internal function called *Arbitration*, in order to provide a synthetic and optimized ice detection information.

HIDS Arbitration function aims to extract a single, consistent output by coupling Indirect Detection with each Direct detector. As displayed in Figure 72, this function takes as input Direct and Indirect detection outputs, defines the validity on these two signals by considering the status of the detection sources, checks for inconsistencies, and combines them by considering A/C characteristics in icing conditions.

The Arbitration function, indeed, will raise an Ice Flag, only if  $TAT \leq TAT_{cr}$ , where  $TAT_{cr}$  is the maximum TAT at which ice accretion is possible on the airframe (for S4I FT,  $TAT_{cr} = 5^{\circ}C$  for Embraer and  $TAT_{cr} = 10^{\circ}C$  for ATR/SAFIRE), and thanks to direct detection IAR or LWC measurements, can provide an ICE SEVERITY signal based on specific thresholds provided by the A/C manufacturer. For SENS4ICE tests, standard thresholds were used:

- SEVERE ICE if  $IAR_{DIDS} > 7.5 \text{ cm/h}$  (=1.25 mm/min)
- SEVERE ICE if  $LWC_{DIDS} > 1.2 \text{ g/m}^3$

Since direct detection shall guarantee an early detection, while indirect detection needs a certain ice accretion on the airframe, the Arbitration function can provide the detection outputs after a certain delay,  $\Delta t$ , in order to wait for IID detection confirmation. This could reduce direct detection false alarms and warn the pilot only if a performance degradation that could put in danger the A/C safety is detected. This  $\Delta t$  can be a fixed value, or can be evaluated automatically by the HIDS if the DIDS can provide an accurate measure of the IAR and the maximum admissible ice thickness on the airframe,  $\tau_{MAX}$ , is known:  $\Delta t = \frac{(\tau_{MAX} - X\% \tau_{MAX})}{IAR_{DIDS}}$ .

Note that during the SENS4ICE FT campaigns, the arbitration function combined separately each DIDS installed on the A/C with IID.

On SAFIRE ATR 42, HIDS had to guarantee two more functions:

1. To record all the project level (“public”) data, shared with SENS4ICE consortium and used to perform the presented analyses;
2. To convert the aircraft data coming from ATR FDAU and SAFIRE FTI unit into the SENS4ICE IENA format, used for the North America FT campaign. For more details on Safire ATR42 see ref. [3].

Actually, in order to limit the difference between Embraer and ATR HIDS demonstrator, on Safire ATR42 was installed the HIDS-PC: a PC with a software developed by SAFRAN able to perform the A/C data decoding, also used for data recording. Moreover, the software installed on HIDS-PC was also used to monitor and



display in real time HIDS/IID and DIDSs outputs, as well as A/C data. This last function of HIDS-PC turned out to be a real asset for the European FT campaign since it allowed the SENS4ICE partners to participate in the FT campaign to easily obtain real time information during the flight.

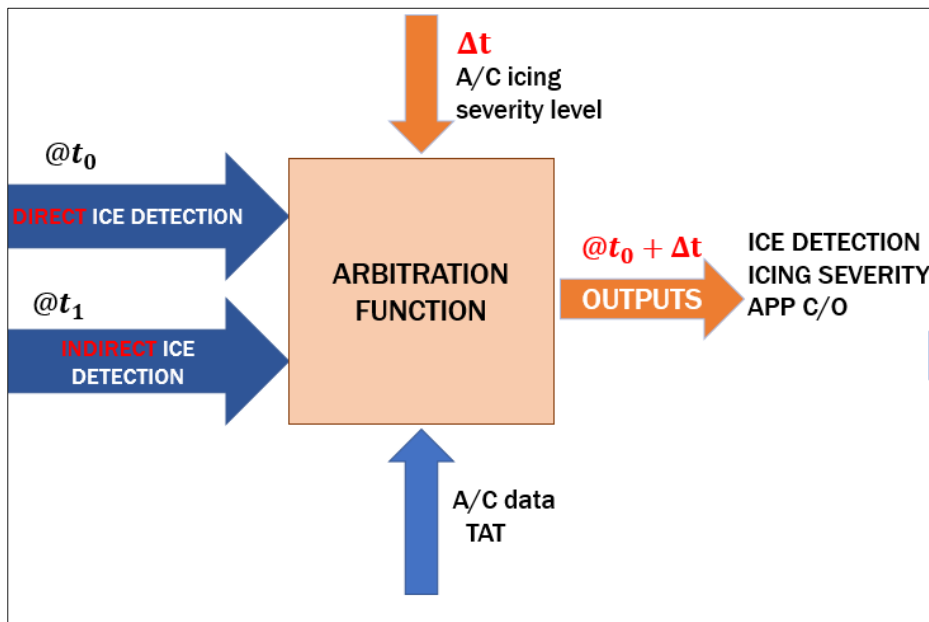


Figure 72: Schematic representation of HIDS Arbitration function.

Figure 73 shows the HIDS installed on Safire ATR 42 on the left, and the HIDS-PC interface on the right.



Figure 73: ATR HIDS, on the left, and HIDS-PC user interface, on the right (image credit Safran).

For the North America FT campaign, data recording and HIDS/IID and DIDS monitoring were operated by Embraer FT engineers.

The overall behaviour of HIDS during the two FT campaigns was very promising: HIDS was always able to receive and provide data through the A/C network, IID was always well initialized before the take-off, and all the encountered icing conditions were detected thanks to the combination of direct and indirect detection.



Regarding data recording during the European FT campaign, no problem was detected and the data were properly stored and shared with the involved partners.

In the following sections, detailed analyses of the selected flights are provided.

### 3.2 HIDS results for North America FT campaign

As indicated in §1.1 two flights are analysed in details in this document: FT1475-2 and FT1476-1.

The results of the analyses shown hereinafter are obtained by replaying offline the whole FT scenario by using post-processed data for IID, as described in §2.3, microphysics and DIDSs (AIP, SRP and IDS). The in-flight records were used for A/C data and PFIDS outputs.

#### FT1475-2

During FT1475-2, the A/C encountered 5 App. C icing conditions, of which only 2 can be considered as “stable” icing conditions, i.e. the A/C stayed in these conditions more than 2 minutes. These two conditions are labeled IC1 and IC2 in  $\mu$ Physics and A/C data for FT1475-2 are visible in Figure 74 where the LWC, MVD, SAT and A/C altitude and TAS time histories are reported.

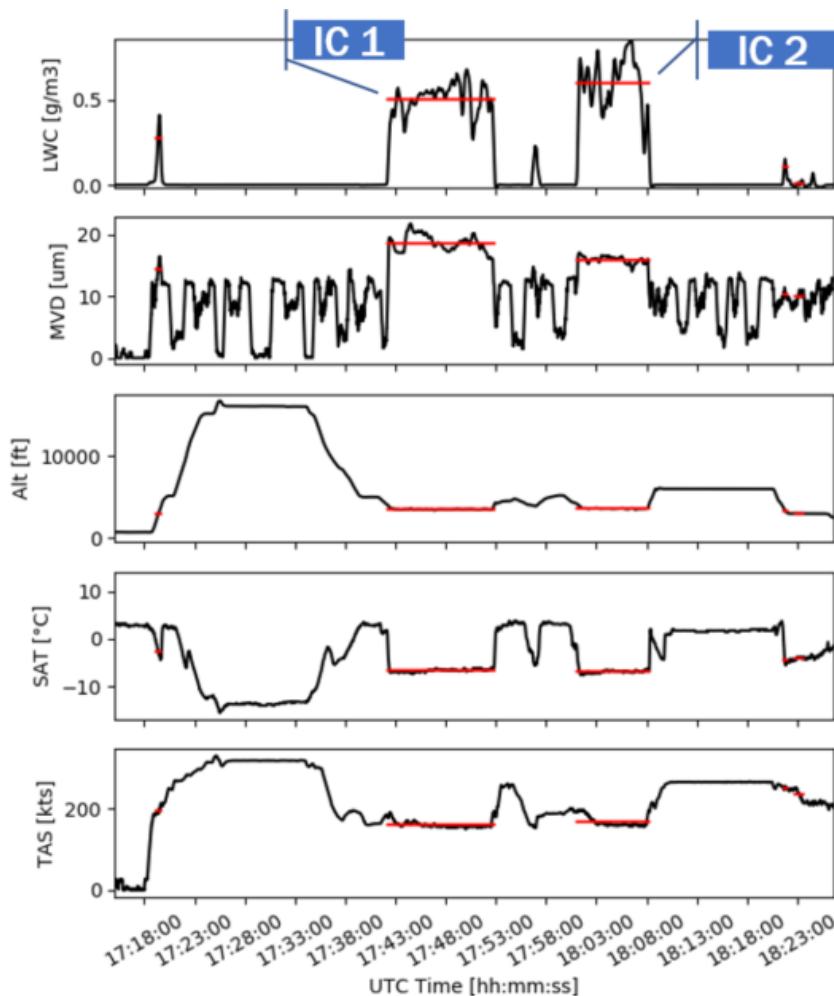


Figure 74:  $\mu$ Physics and A/C data for FT1475-2. The red lines represent the calculated average values of each parameters during the icing encounters. Such values are reported in Table 7.

Figure 75 compares the detection signals of direct detectors and the indirect detector for this flight with the  $\mu$ Physics Icing Flag, considered here as the reference. In Table 6 are reported the number of icing conditions and App. O conditions detected by each DIDS. No false detections were observed, with the exception of IDS,



and all DIDSs, but the SRP, detected the beginning and the end of each icing encounter in agreement with the  $\mu$ P ICE flag.

Honeywell's large-particle SRP variant, flown under SENS4ICE, uses direct detection to identify particles larger than 50 microns. At SENS4ICE request, its capability was extended to smaller particles ( $< 50 \mu m$ ) using new background signal analysis algorithms developed during the project, which showed promise in IWT testing. During flight test, ice particle MVD was between 15 -  $20 \mu m$ , and the new algorithm underestimated LWC as a result. Honeywell has flight-proven technology (BCPD under IAGOS EU-funded project) for detecting particles 4 -  $45 \mu m$ , which will be integrated with the flown large-particle design during productization to cover the full particle size range. In addition, algorithm improvements will be made to compensate for underestimation of LWC in small-MVD conditions by the large particle sensor as a redundancy.

The IDS false App. O detection has been investigated by sensor developers: they observed that the environmental conditions within the few seconds surrounding this event closely approached one of IDS App. O discrimination thresholds. They have already a plan to improve IDS algorithm and mitigate such kind of problem.

Note that between ~17:40 and ~17:55, DIDSs were disconnected from the SENS4ICE A/C network, for this reason they were not able to detect IC1.

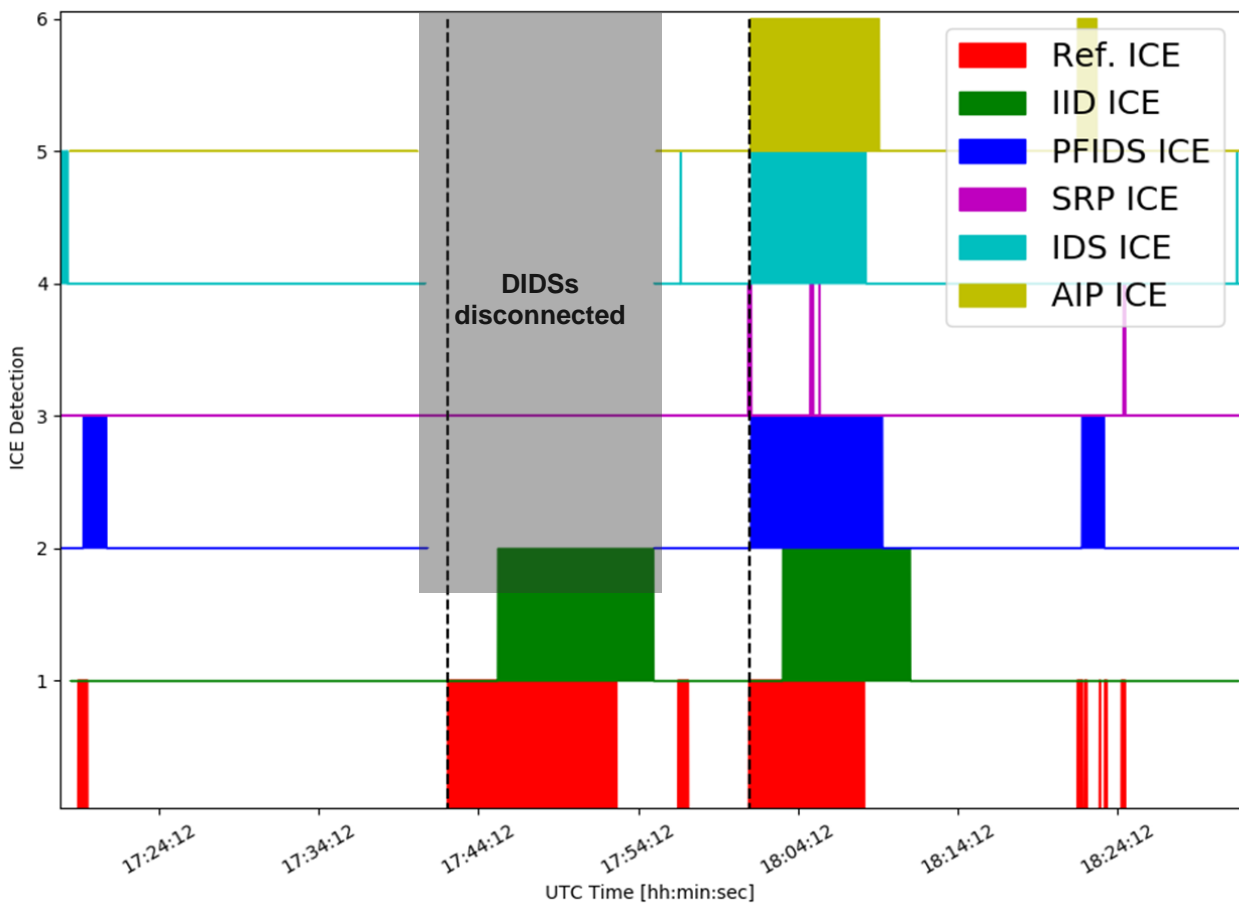


Figure 75: Ice Detection signal of DIDSs and IID for FT1475-2. From the bottom to the top:  $\mu$ P, IID, PFIDS, SRP, IDS and AIP.



FT1475-2	$\mu P$	IID	PFIDS	AIP	SRP	IDS
IC / APP O Flags	5 / 0	2 / -	3 / -	2 / 0	3 / 0	4 / 1

Table 6: Number of icing encounters for FT1475-2 and number of IC /APP O Flags raised by each detector. Note that IID and PFIDS are not able to discriminate between APP C and APP O icing conditions.

IC	ICE START ( $\mu P$ )	ICE END ( $\mu P$ )	Duration ( $\mu P$ )	LWC [g/m <sup>3</sup> ]	MVD [micron]	Alt [ft]	SAT [°C]	TAS [kts]	ED103 IAR [mm/min]	ED103 Resp time [s]
1	17:42:17	17:52:51	00:10:34	0.5	18.6	3500	-6.67	160.86	1.64	10.98
2	18:01:08	18:08:21	00:07:13	0.6	15.9	3610	-6.91	168.04	1.78	10.12

Table 7: Characteristics of IC1 and IC2 for FT1475-2.

Our analysis will be focused on IC1 and IC2, in particular IC2, since all DIDSs were correctly operating during this encounter.

The average values of the parameters characterizing these two conditions are indicated in Table 7. In this table are reported, as well, the start and the end of each icing encounter based on  $\mu P$  data, and the theoretical IAR and ice detector response time evaluated by using ED103B formula, see ref. [4]. Note that the standards reported in [4] are only addressed to direct ice detectors.

In Figure 76 details of each DIDS detection for IC2 are shown. As indicated in Table 8 all DIDSs provided an ICE signal within the time expected by ED103B for this condition, i.e. 10.12s. As expected, the indirect detection needs more time to detect a performance degradation due to ice accretion, indeed, the IID ICE flag was raised after 2 minutes from the IC encounter. Furthermore, Figure 76 shows that, if the DIDSs ICE flags dropped once the A/C exits the icing condition, the IID continued to detect a performance degradation.

Actually, Embraer engineers observed that the A/C left the clouds with moderate ice accreted on the unheated surfaces at 17:52, then the airframe was still iced up to 18:11. Indeed, IID is able to detect a performance degradation due to remaining residual ice.

DIDS	ICE FLAG raised @ [hh:min:sec]	ICE FLAG dropped @ [hh:min:sec]	Response time w.r.t. $\mu P$ [min:sec]
IID	18:03:13	18:11:11	02:05
PFIDS	18:01:16	18:09:29	00:08
SRP	18:01:05	18:01:17	-00:03
IDS	18:01:19	18:08:27	00:11
AIP	18:01:14	18:09:17	00:06

Table 8: IID and DIDSs response time for IC2.

In Figure 77 and Figure 78 are reported the results of HIDS arbitration function for each couple DIDS/IID. As described in §3.1, HIDS via the Arbitration function, associates direct and indirect detections, checks for the availability of two sources and provides a synthetic detection output.

The Arbitration function checks also the reliability of DIDS and IID, in particular it creates a new IID ICE signal, called **IID ICE Valid**, based on the reliability of IID outputs and on the TAT value:

- if IID outputs are reliable and TAT < 5°C → IID ICE output is valid;
- if IID outputs are unreliable (for example when high lift devices are used and/or the landing gear is down) and/or the TAT ≥ 5°C → IID ICE output is not valid.

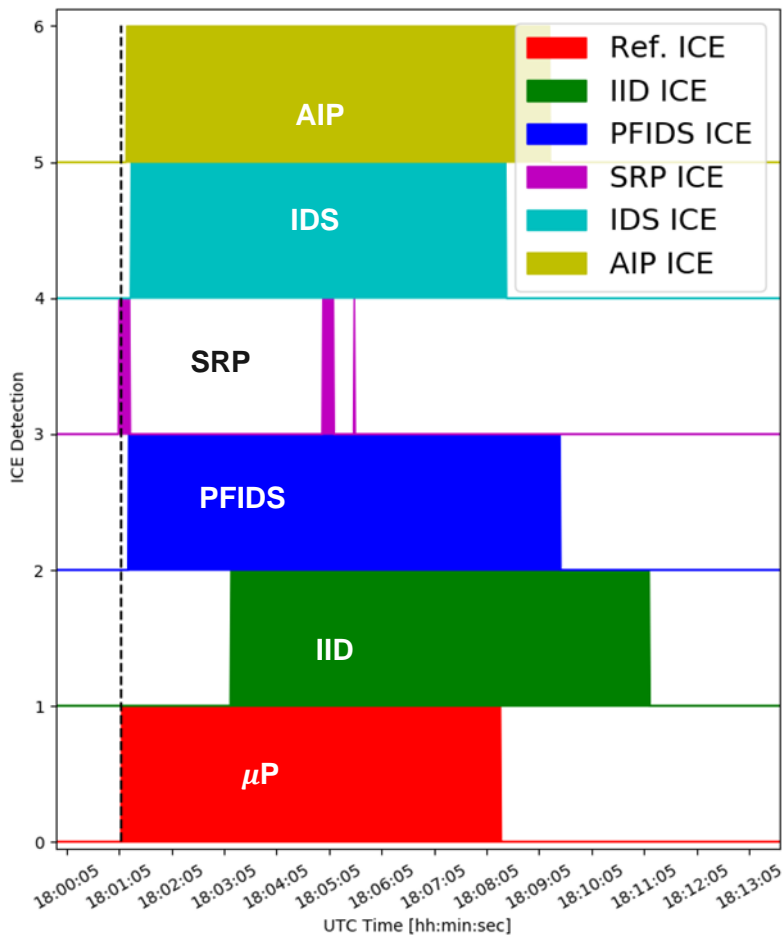


Figure 76: Ice Detection signal of DIDSs and IID for IC2 of FT1475-2 From the bottom to the top:  $\mu P$ , IID, PFIDS, SRP, IDS and AIP.

In order to keep an early ice detection and to monitor the A/C performance even when the A/C exits the icing clouds, the Arbitration flag encloses perfectly both DIDS and IID Ice flags (for SENS4ICE FT we used  $\Delta t = 0$ ): the HIDS ICE flag is raised as soon as there is a DIDS detection and dropped when the IID ice flag drops. Moreover, the HIDS ICE flag can be equal to 2, if based on DIDS measurements (IAR or LWC), the IC can be considered as a severe IC (see the Arbitration results for the couple PFIDS/IID in Figure 77), or it can assume a negative value if the encountered condition is an App. O condition. Therefore, HIDS Arbitration output (i.e. HIDS ICE flag) can assume the following values:

- 0: no ice
- 1: ice
- 2: severe ice
- negative sign: App O conditions

The HIDS **Arbitration status** (the last subplot in Figure 77 and Figure 78) provides some details on how the Arbitration result has been built:

- Arbitration status = 0 → both DIDS and IID outputs are unavailable
- Arbitration status = 1 → only DIDS outputs are available and reliable
- Arbitration status = 2 → only IID outputs are available and reliable
- Arbitration status = 3 → both DIDS and IID are available and reliable

Thanks to this approach, even if only one detection source is available, HIDS will provide ice detection information. This is what happened for IC1 of FT 1475-2.

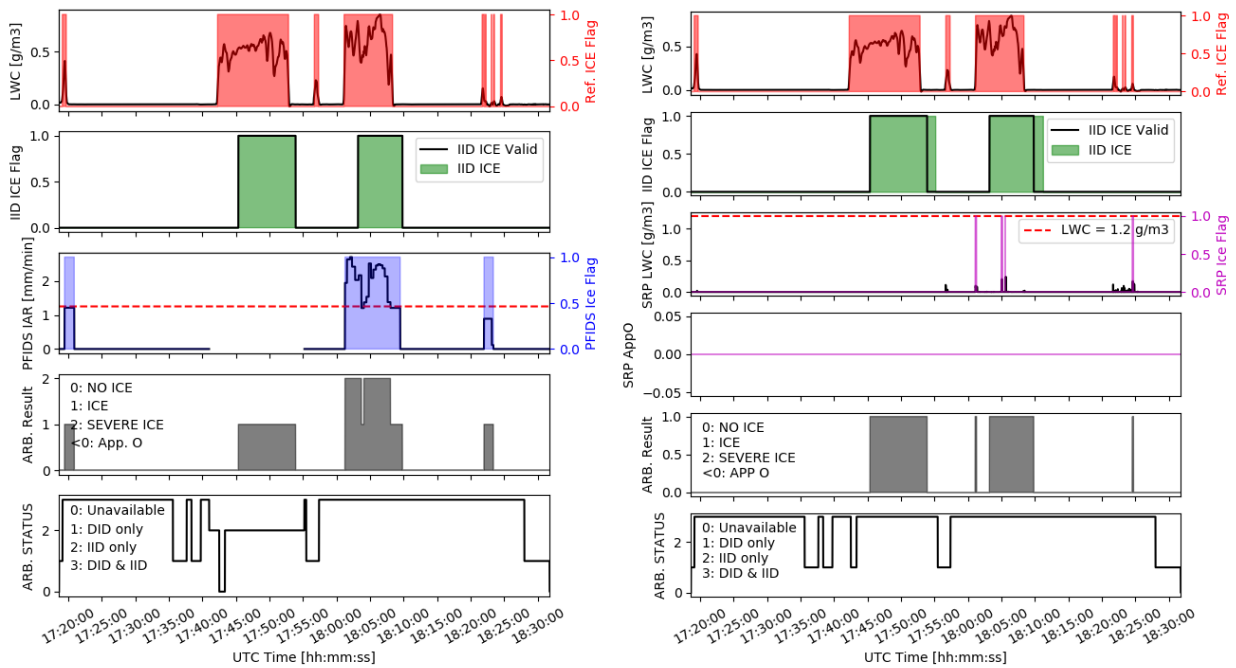


Figure 77: FT1475-2 Results of HIDS arbitration for the couple PFIDS/IID, on the left, and the couple SRP/IID, on the right. From the top to the bottom: LWC curve and  $\mu\text{P}$  ice flag; IID ice flag; DID IAR or LWC curve and ice flag; DID App O flag (not available for PFIDS since it cannot discriminate); HIDS Arbitration results; HIDS Arbitration status.

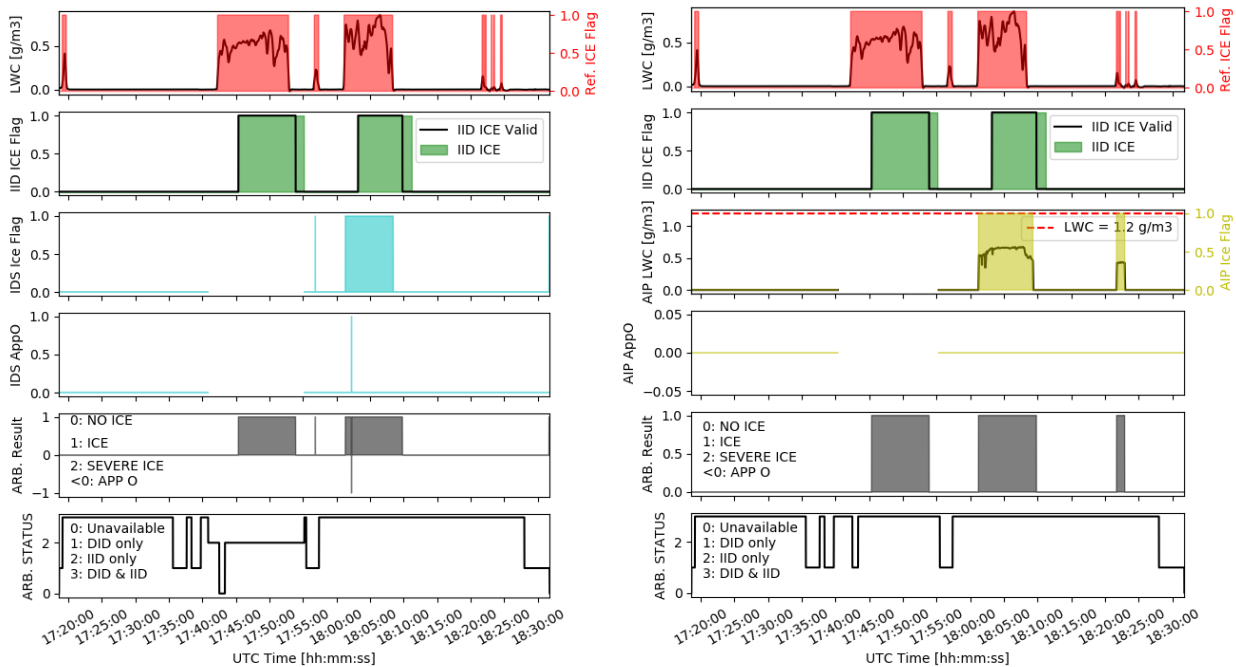


Figure 78: FT1475-2 Results of HIDS arbitration for the couple IDS/IID, on the left, and the couple AIP/IID, on the right. From the top to the bottom: LWC curve and  $\mu\text{P}$  ice flag; IID ice flag; DID IAR or LWC curve (if available) and ice flag; DID App O flag; HIDS Arbitration results; HIDS Arbitration status.



## FT1476-1

As displayed in Figure 79, FT1476-1 was characterized by 5 IC classified as App. O encounters. The parameters characterizing these IC, as well as the theoretical IAR and detection time are reported in Table 9.

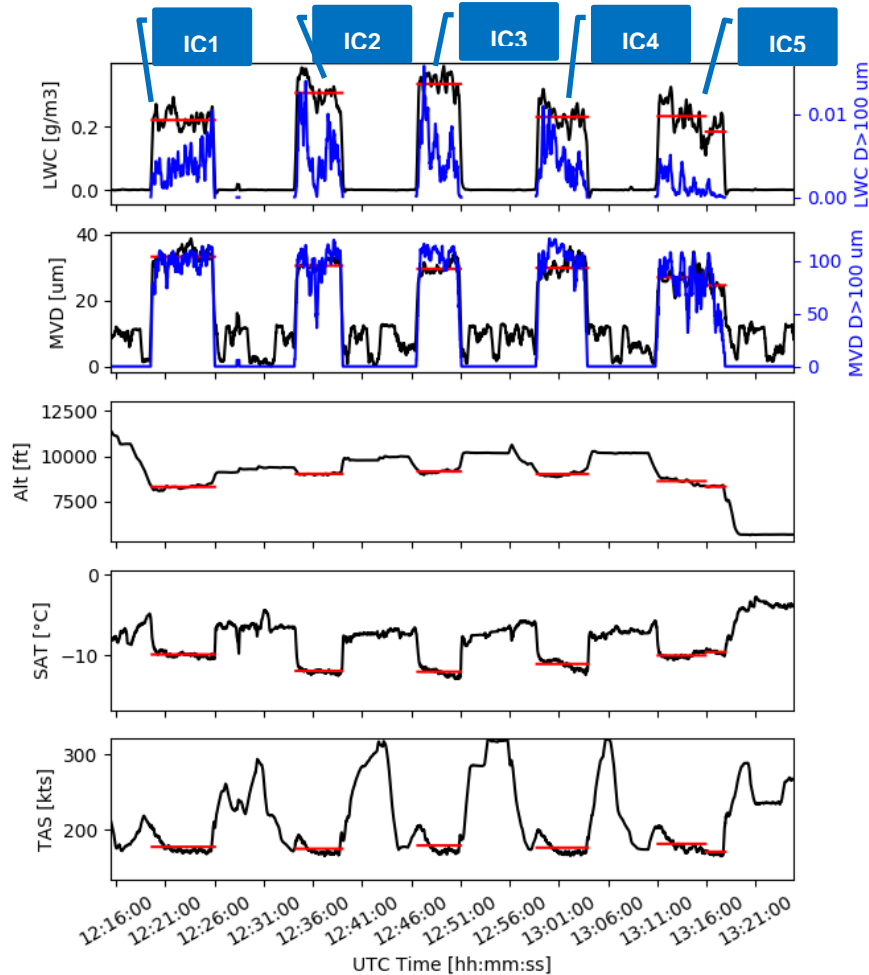


Figure 79:  $\mu$ Physics and A/C data for FT1476-1. The red lines represent the calculated average values of each parameters during the icing encounters. Such values are reported in Table 9.

IC	ICE START ( $\mu$ P)	ICE END ( $\mu$ P)	Duration ( $\mu$ P)	LWC [g/m <sup>3</sup> ]	MVD [micron]	Alt [ft]	SAT [°C]	TAS [kts]	ED103 IAR [mm/min]	ED103 Resp time [s]
1	12:19:37	12:25:58	00:06:21	0.22	32.91	8309.41	-9.82	177.97	1.15	15.66
2	12:34:14	12:39:05	00:04:51	0.30	29.79	9038.41	-11.76	175.31	1.52	11.85
3	<b>12:46:38</b>	<b>12:51:07</b>	<b>00:04:29</b>	<b>0.33</b>	<b>28.97</b>	<b>9165.32</b>	<b>-11.91</b>	<b>180.03</b>	<b>1.70</b>	<b>10.58</b>
4	12:58:47	13:03:55	00:05:08	0.23	29.83	9008.57	-11.00	176.47	1.18	15.19
5	13:10:58	13:17:51	00:06:53	0.22	26.10	8549.39	-9.83	178.73	1.10	16.38

Table 9: Characteristics of IC1, IC2, IC3, IC4 and IC 5 for FT1476-1.





The detection signals of DIDSS and IID are compared with the reference  $\mu P$  ice flag in Figure 80: the detectors were able to detect the 5 conditions and SRP and IDS, which can discriminate between App. C and App. O, considered the 5 encounters as App. O conditions, as displayed by Figure 81. Table 10 reports the number of detections for each detector.

Unfortunately, during this flight Aerotex AIP faced some issues, for this reason its data are not available.

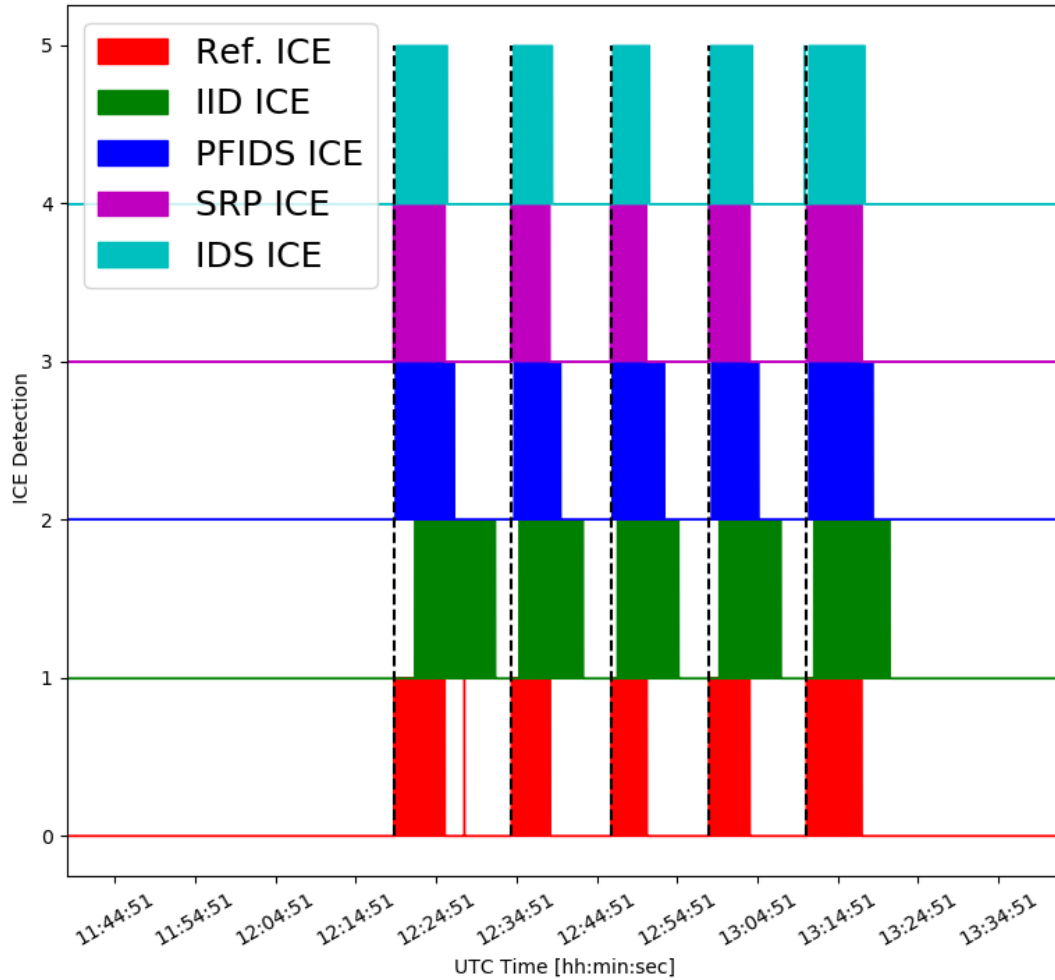


Figure 80: Ice Detection signal of DIDSS and IID for the icing encounters of FT1476-1. From the bottom to the top:  $\mu P$ , IID, PFIDS, SRP, IDS.



Flight 1476 leg1 of North America FT campaign

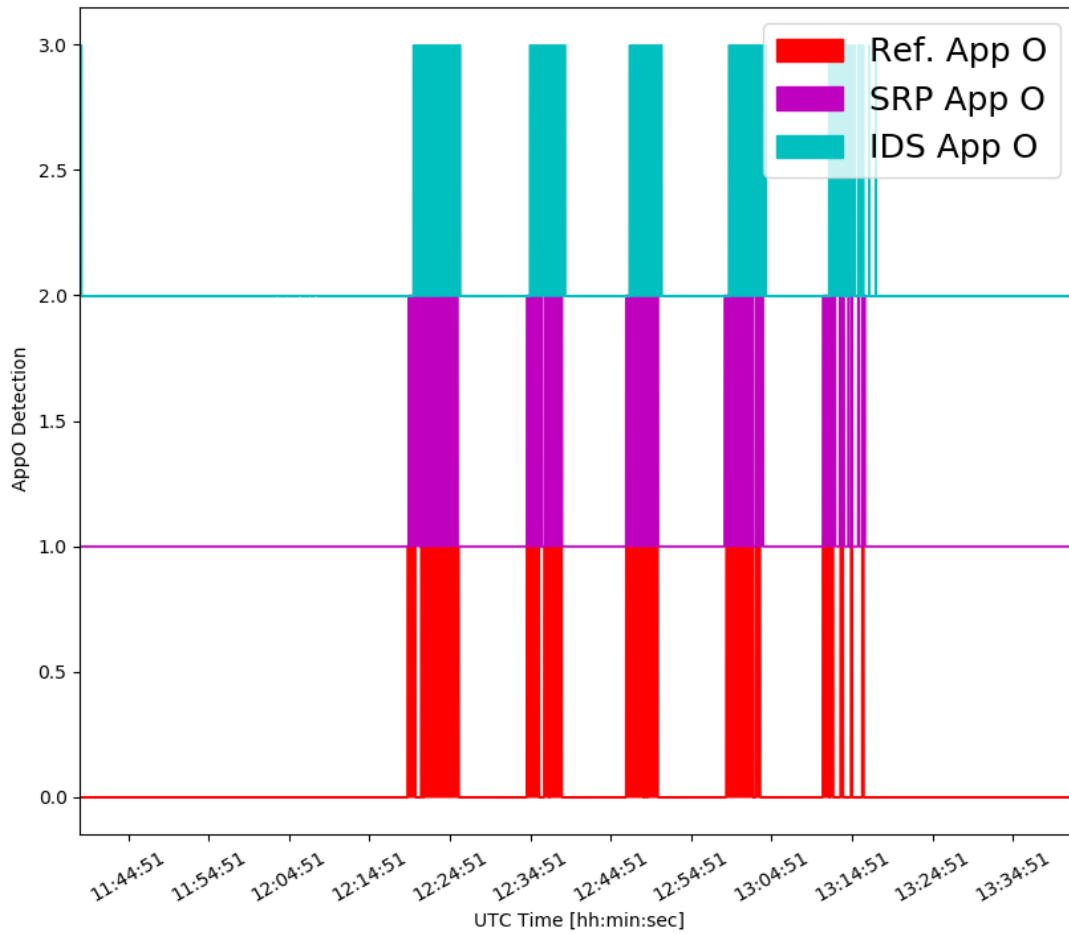


Figure 81: App O detection signals of DIDSs for the icing encounters of FT1476-1. From the bottom to the top:  $\mu P$ , SRP, IDS.

	$\mu P$	IID	PFIDS	AIP	SRP	IDS
<b>IC / APP O Flags</b>	6 / 5	5 / -	5 / -	-	5 / 5	5 / 5

Table 10: Number of icing encounters for FT 1475-1 and number of IC /APP O Flags raised by each detector. Note that IID and PFIDS are not able to discriminate between App. C and App. O icing conditions.

The response times reported in Table 11 show that DIDS are able to detect very fast each encounter, in particular SRP detected the conditions even before the  $\mu P$  probe. It is interesting to note that IID, even if not compliant to ED103 response time, seems to detect App. O conditions faster than App. C. In particular, if we focus our attention on IC3, see Figure 82, which has a theoretical IAR close to the IC2 of FT1475-2, i.e. about 1.7 mm/min, IID response time is more than halved.



IC	ICE START ( $\mu P$ )	ED103 Resp time [s]	IID ICE	IID Resp. time wrt $\mu P$	PFIDS ICE	PFIDS Resp. time wrt $\mu P$	SRP ICE	SRP Resp. time wrt $\mu P$	IDS ICE	IDS Resp. time wrt $\mu P$
1	12:19:37	15.66	12:22:08	02:31	12:19:49	00:12	12:19:34	-00:03	12:19:49	00:12
2	12:34:14	11.85	12:35:07	00:53	12:34:35	00:21	12:34:11	-00:03	12:34:24	00:10
3	12:46:38	10.58	12:47:21	00:43	12:46:48	00:10	12:46:34	-00:04	12:46:46	00:08
4	12:58:47	15.19	13:00:01	01:14	12:59:09	00:22	12:58:47	00:00	12:58:54	00:07
5	13:10:58	16.38	13:11:48	00:50	13:11:16	00:18	13:10:59	00:01	13:11:11	00:13

Table 11: IID and DIDSs response time for the 5 App O conditions of FT 1476-1.

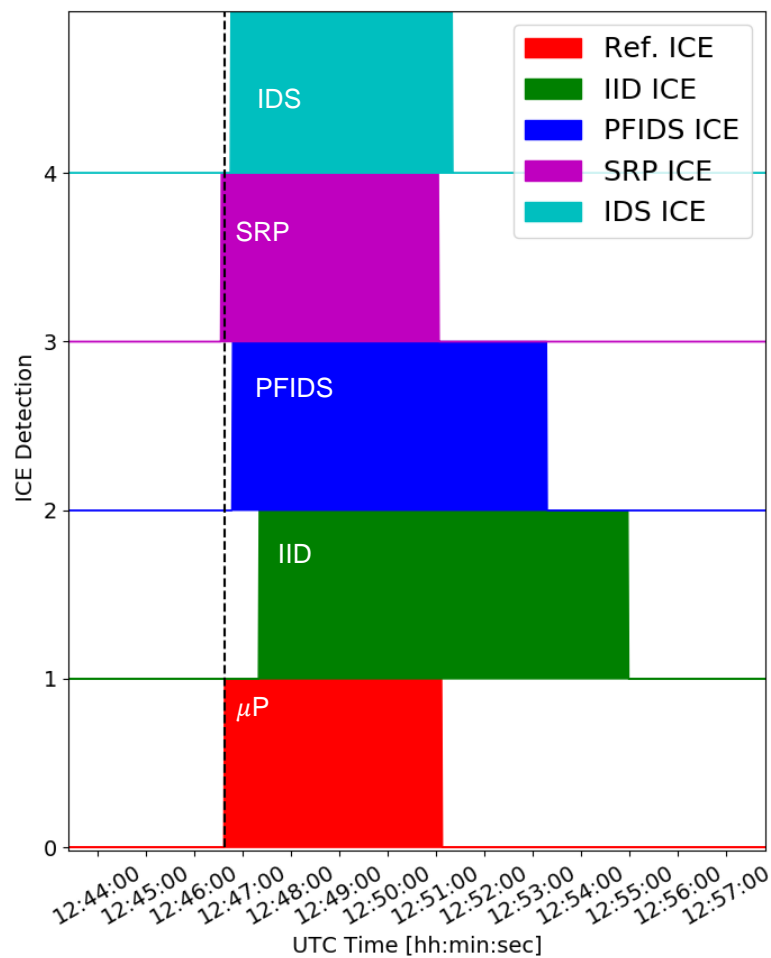


Figure 82: Ice Detection signal of DIDSs and IID for IC3 of FT1476-1. From the bottom to the top:  $\mu P$ , IID, PFIDS, SRP, IDS.

Even for this flight, IID Ice flag dropped a few minutes after the A/C exits the icing cloud. Once again, Embraer engineers confirmed that the A/C left the cloud with ice accreted on the unheated surface and it entered in the new condition with still some ice.

Figure 83 and Figure 84 report the results of HIDS arbitration function for each couple DIDS/IID. As for the previous flight, HIDS ICE flag encloses perfectly both DIDS and IID Ice flags.



Based on PFIDS IAR measures, the 5 conditions can be considered as severe conditions, HIDS flag = 2, see Figure 83 on the left. For the couple SRP/IID and IDS/IID, the HIDS ice flag switches from 1 to -1, since the two detectors classified these encounters as App. O conditions.

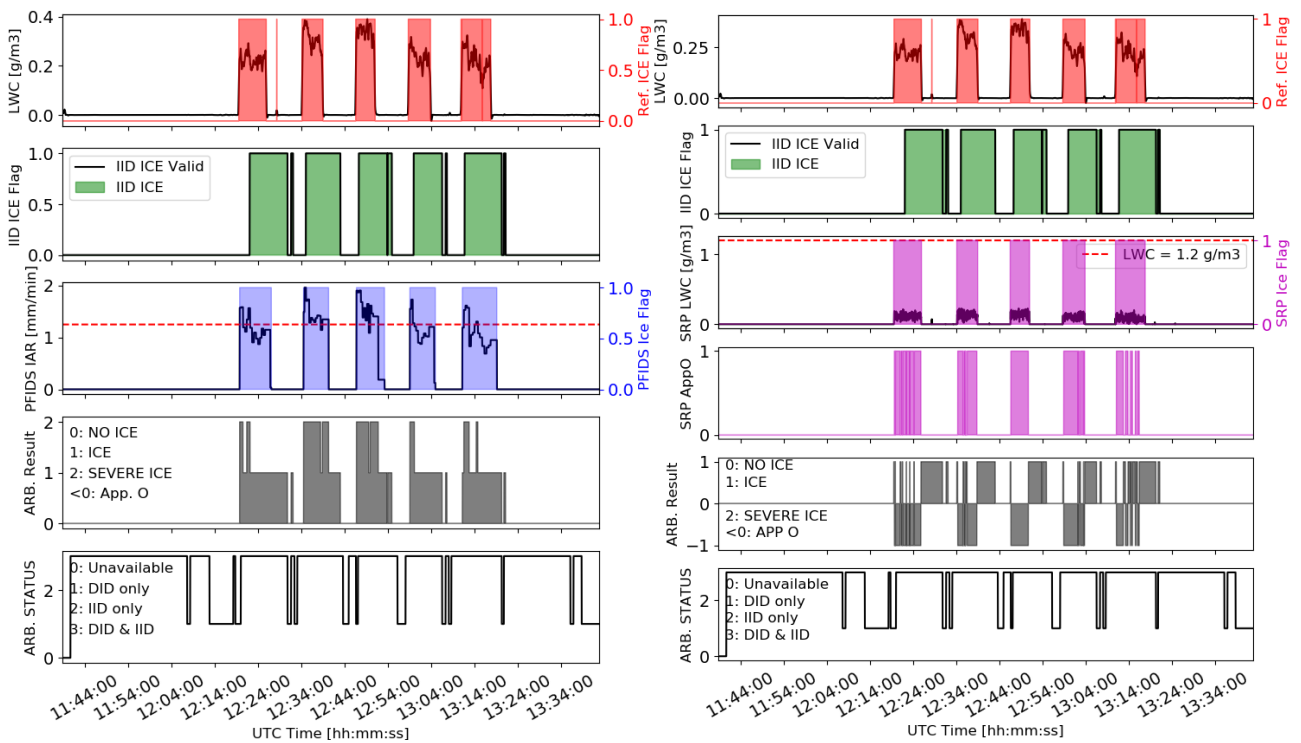


Figure 83: FT1476-1 Results of HIDS arbitration for the couple PFIDS/IID, on the left, and the couple SRP/IID, on the right. From the top to the bottom: LWC curve and  $\mu P$  ice flag; IID ice flag; DID IAR or LWC curve and ice flag; DID App O flag (not available for PFIDS since it cannot discriminate); HIDS Arbitration results; HIDS Arbitration status.

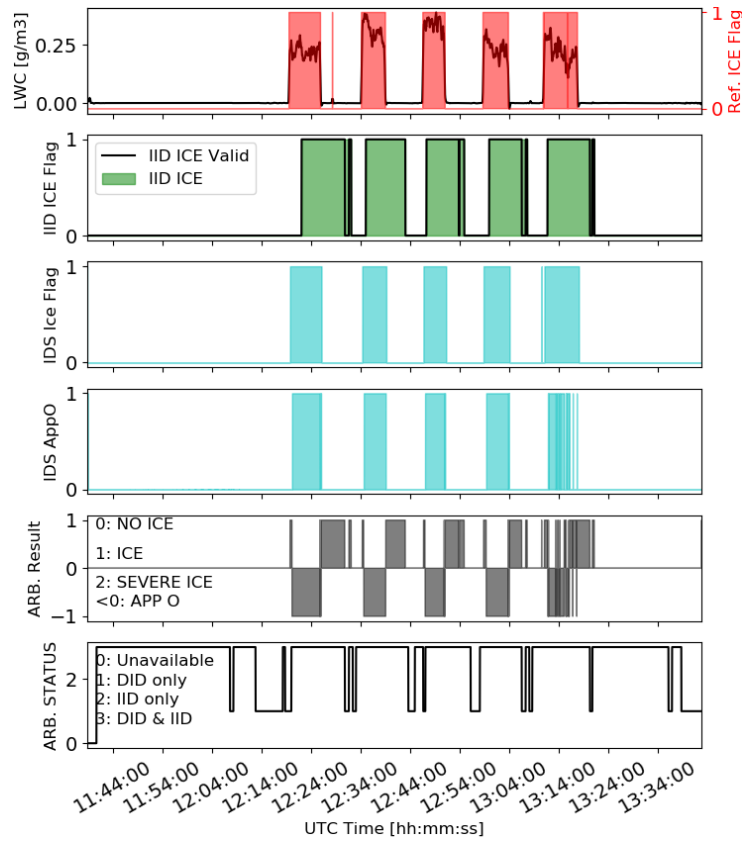


Figure 84: FT1476-1 Results of HIDS arbitration for the couple IDS/IID. From the top to the bottom: LWC curve and  $\mu P$  ice flag; IID ice flag; IDS ice flag; IDS App O flag; HIDS Arbitration results; HIDS Arbitration status.

### 3.3 HIDS results for European FT campaign

In this section three different flights of the European FT campaign are evaluated:

- as230018;
- as230021;
- as230022.

During these flights several icing conditions were encountered, including App. C and App. O conditions. With respect to the North America FT campaign, the icing clouds characterizing the European FT campaign were less homogenous and, sometimes, they contained high concentration of ice crystals, see [1] and [7]. Moreover, the overall LWCs were lower. All these aspects make the characterization of the icing conditions a complex task and the ice detection even more difficult.

As for the North America FT campaign, the results of the analyses here described were obtained by replaying offline the whole FT scenario by using post-processed data for IID, microphysics and DIDSSs.

#### Flight as230018

In Figure 85 are reported A/C data,  $\mu P$  data and IID main outputs for the flight as230018. Note that for HIDS evaluation the IID outputs obtained by considering the 10% threshold for relative drag increase are used, see §2.4.

Flight as230018 lasted more than 4 hours and several icing clouds were encountered as demonstrated by RICE probe, the legacy ice accretion detector, and the  $\mu P$  measures. Actually, the ATR42 flew through some clouds characterized by the presence of SLD and Ice Crystal too.



For safety reason, Safire’s pilots activate the Ice Protection Systems (pneumatic boots) when the A/C enters in icing conditions and ice accretion is visible on the “visual clue” outside the cockpit windows. After a while in icing conditions, the pilots exit the cloud by reducing the altitude in order to fly in warm air layer to ensure a full de-icing of the aircraft. The IPS are switched off during this phase.

Such de-icing cycle occurred 8 times during the flight, see the first subplot in Figure 85.

Indeed, a good correlation between the indirect ice detections and the period of activation of the ATR42 pneumatic boots can be observed, meaning that the indirect ice detection matches the pilots’ observations.

In Figure 85 a summary of the number of IPS systems activations (both wings and horizontal tail IPS), the RICE probe detections,  $\mu P$  ice flags and App. O flags is reported. Note that the RICE probe signals were considered severe for the following evaluation and assessment when the ice thickness on the probe is above 0.02 inch, corresponding to engineering judgement. As already stated, because of the nature of the encountered icing clouds,  $\mu P$  probes detected several very short icing encounters.

IPS activation	9
RICE ice detection	20
RICE severe ice	11
$\mu P$ ice detection	251
$\mu P$ App O detection	34
IID ice detection	8

Table 12: Summary of the number of IPS activation, reference ice flags and indirect ice detection for the flight as230018.

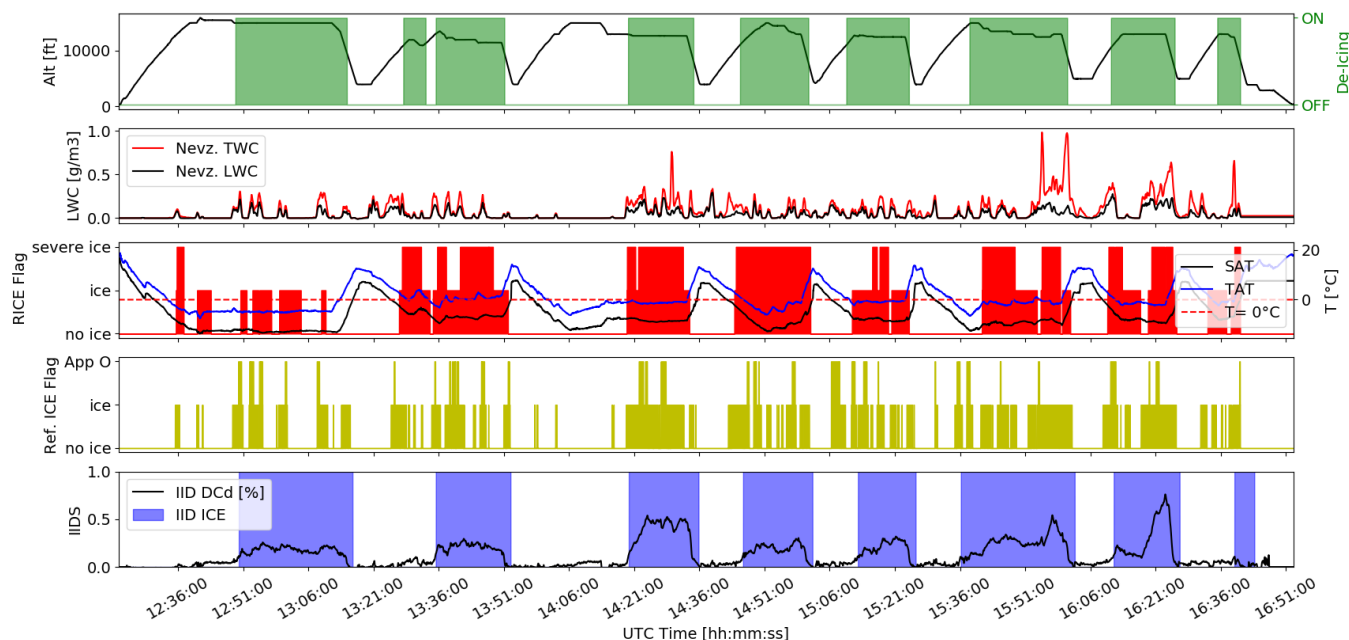


Figure 85: Flight as230018 A/C data,  $\mu P$  data, reference icing flags and IID outputs. From the top to the bottom: A/C altitude time history and IPS activation; Nevzorov measurements of LWC and TWC; Temperature time history (both SAT and TAT) and RICE probe ice flags;  $\mu P$  ice flags; IID relative drag increase and ice flags.



As illustrated in Figure 86, all the DIDSS were able to detect the icing encounters. As expected, the AMPERA icing flags are well correlated with the  $\mu P$  ones, while LILD and IID match up the RICE signals. The FOD detected as well several icing encounters, in agreement with the  $\mu P$  flags, but it was not able to hold the ice signal and to properly detect the exit from the cloud.

In effect, the FOD detection algorithm is based on the observation of abrupt temperature changes at the sensor surface due to the ice accretion. Thus, the exit from the icing cloud should correspond to a temperature decrease due to the convection heat flux. During the European FT campaign, because of the heterogeneous nature of the icing clouds, the temperature did not rise to its equilibrium temperature and therefore the convection could not cause an abrupt decrease of the temperature. For this reason, FOD developers preferred to modify the detection algorithm in order to detect each temperature changes and to display the ice presence in a discrete manner.

Neither LILD, nor FOD, detected the presence of SLD during this flight.

For this flight, the analysis is focused on two time intervals:

1. IC1: [14:19:00 – 14:28:00] UTC time
2. IC2: [14:42:00 – 15:01:00] UTC time

These two time intervals are characterized by two different icing encounters, detected by both the RICE probe and  $\mu P$ . In particular, the first encounter was characterized by a visible ice formation on the airframe, see Figure 36, and the IID measures a relative drag increase of more than 50% compared to the nominal value, see §2.4. The two conditions are characterized by SLD presence.

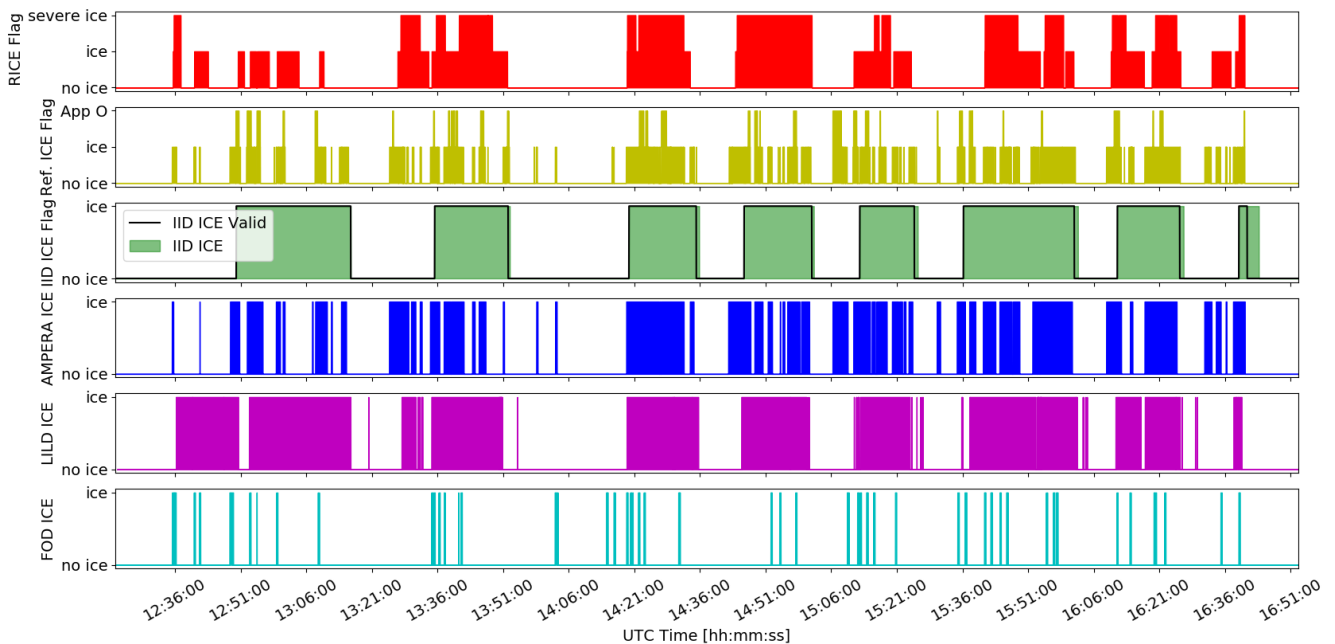


Figure 86: Flight as230018 Ice Detection signal of DIDSS and IID for icing encounters. From the top to the bottom: RICE,  $\mu P$ , IID, AMPERA, LILD, FOD.

In Figure 87 are reported for the selected time interval [14:19:00 – 14:28:00] UTC, the LWC, MVD, SAT and TAS time histories, reference icing flags and the concentration of large aspherical particles (LAS N), figure on the left, and the ice detection of DIDSS and IID w.r.t. the reference ones, figure on the right. It is important to observe that the LAS N is always lower than 1/L (i.e. 1 per litre, corresponding to 0.001 per  $\text{cm}^3$ ), this means that the MVD evaluation was not affected by the presence of ice crystals, see [7]. Average values of LWC, MVD, SAT, ALT and TAS have been used to evaluate the ED103 theoretical IAR and response time for the encountered icing condition. This allows to compare DIDSS performances. The detectors response time w.r.t. the RICE probe, the legacy ice detector, for IC1 are reported in Table 13. Note that in this Table the IID response time is reported as well even if ED103 is addressed only to direct detectors. IID raised the icing flag



30s after RICE, while all the DIDS were more sensitive and raised an ice flag before RICE, in agreement with the  $\mu P$  flag.

ED103 Resp. time [s]	ED103 IAR [mm/min]	$\mu P$ ICE FLAG [hh:min:sec]	RICE ICE FLAG [hh:min:sec]	IID Resp. Time w.r.t. RICE [s]	AMPERA Resp. Time w.r.t. RICE [s]	LILD Resp. Time w.r.t. RICE [s]	FOD Resp. time w.r.t. RICE [s]
26	0.70	14:19:04	14:19:16	30s	-7s	-1s	-7s

Table 13: IID and DIDSs response time for the icing encounter during the time interval [14:19:00 – 14:28:00] UTC of flight as230018.

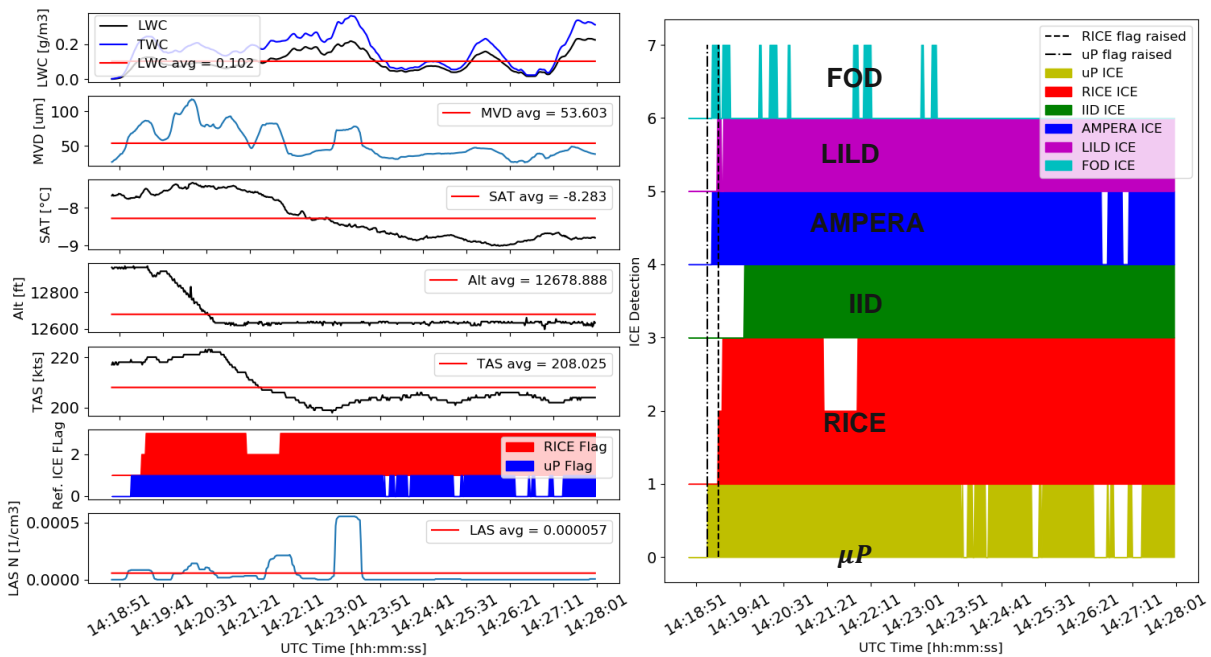


Figure 87: Flight as230018 time interval [14:19 – 14:28] UTC IC1 On the right,  $\mu P$ , A/C data and reference ice flags. On the left: DIDSs, IID and reference ice flags.

In Figure 88 are reported the time histories of LWC, MVD, SAT, TAS, reference ice flag and the concentration of large aspherical particles (LAS N), figure on the left, and, the ice detection of DIDSs and IID w.r.t. the reference ones over the time interval [14:42:00 – 15:01:00] UTC, figure on the right.

Detectors response time w.r.t RICE are indicated in Table 14. IC2 is characterized by a lower IAR than IC1, this explains the higher response time of ice accretion detectors, such as LILD, FOD and IID as well. Once again, AMPERA, which is an atmospheric sensor, guaranteed an early detection in agreement with  $\mu P$  ice flag.

ED103 Resp. time [s]	ED103 IAR [mm/min]	$\mu P$ ICE FLAG [hh:min:sec]	RICE ICE FLAG [hh:min:sec]	IID Resp Time wrt RICE [s]	AMPERA Resp Time wrt RICE [s]	LILD Resp Time wrt RICE [s]	FOD Resp time wrt RICE [s]
60	0.30	14:42:38	14:44:03	122	-95	84	486

Table 14: IID and DIDSs response time for the icing encounter during the time interval [14:42:00 – 15:01:00] UTC of flight as230018.



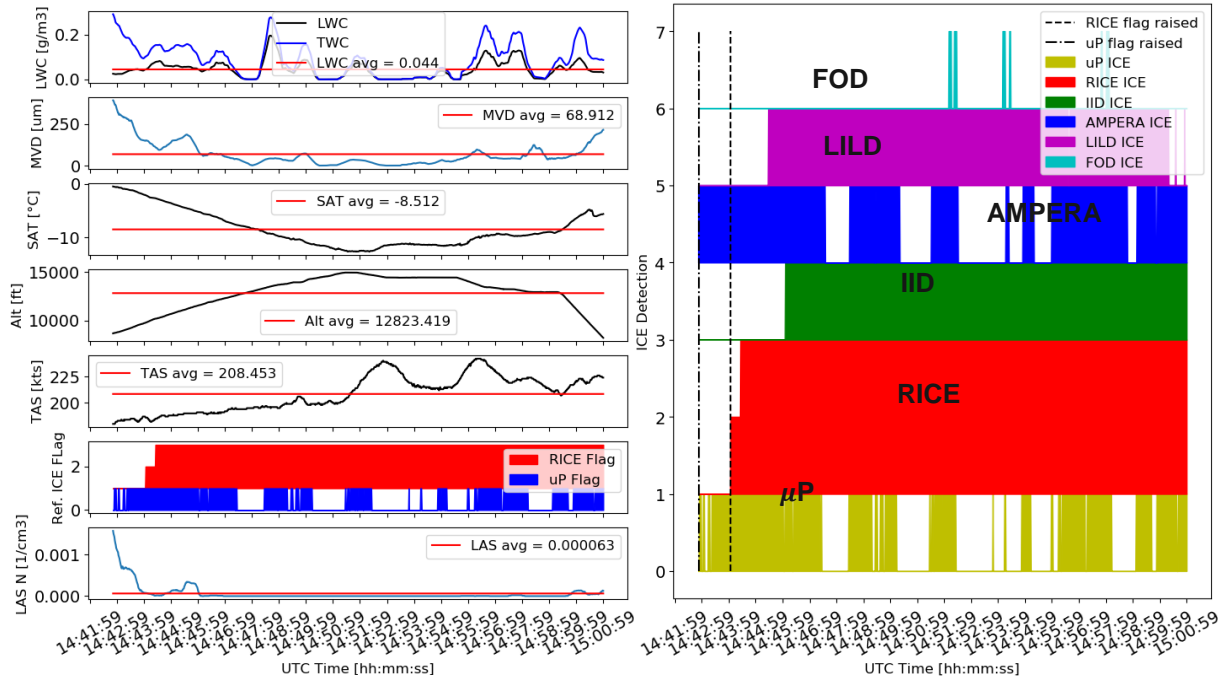


Figure 88: Flight as230018 time interval [14:42 – 15:01] UTC IC2 On the right,  $\mu P$ , A/C data and reference ice flags. On the left: DIDS, IID and reference ice flags during the time interval [14:42 – 15:01] UTC. On the left: DIDS, IID and reference ice flags.

From Figure 89 to Figure 91, the results of HIDS arbitration, coupling each DIDS with IID, are reported. As for the North America FT campaign, HIDS ICE flag encloses perfectly both DIDS and IID Ice flags ( $\Delta t = 0s$ ) in order to guarantee an early detection based on DIDS signals, and the continuous monitoring of A/C performances provided by IID even after the exit from the icing clouds.

The **IID ICE Valid** signal used by the arbitration function, as explained in §3.2, truncates detections above the upper limit  $TAT_{cr}$ . In the European campaign, this value is  $10^{\circ}C$ . Note that this limit [ $TAT_{cr}$ ] should ideally be provided by the aircraft manufacturer, according to the aircraft performance.

Figure 89 shows a very good correlation between AMPERA TWC and Nevzorov measurements, while both LILD and FOD provided higher IAR values than expected (theoretical) ones, see the second subplot from the top of Figure 90 and Figure 91. Actually for both detectors, the results of the arbitration indicate some severe icing encounters (i.e.  $IAR > 1.25$  mm/min).

For FOD, the IAR is evaluated indirectly, by resolving the classical *Messinger* balance equation, ref. [8]. The observed overestimation could be due again to the heterogeneous nature of the icing clouds and a possible overestimation of the convective heat transfer coefficient.

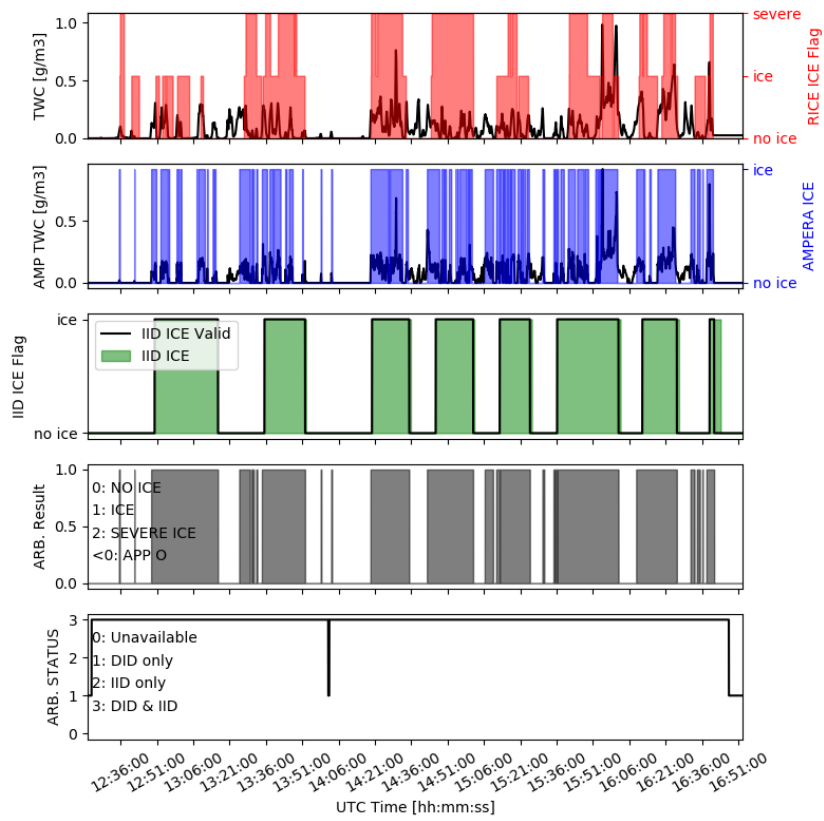


Figure 89: Flight as230018 Results of HIDS arbitration for the couple AMPERA/IID. From the top to the bottom: TWC curve and RICE ice flag; AMEPRA TWC measurements and ice flags; IID ice flags; HIDS Arbitration results; HIDS Arbitration status.

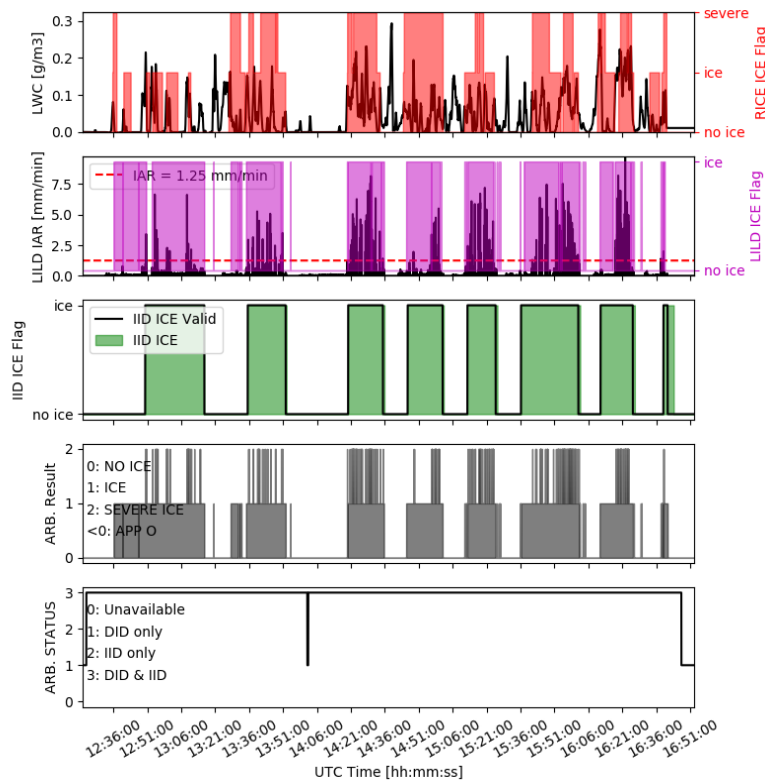


Figure 90: Flight as230018 Results of HIDS arbitration for the couple LILD/IIID. From the top to the bottom: LWC curve and RICE ice flag; LILD IAR measurements and ice flags; IID ice flags; HIDS Arbitration results; HIDS Arbitration status.

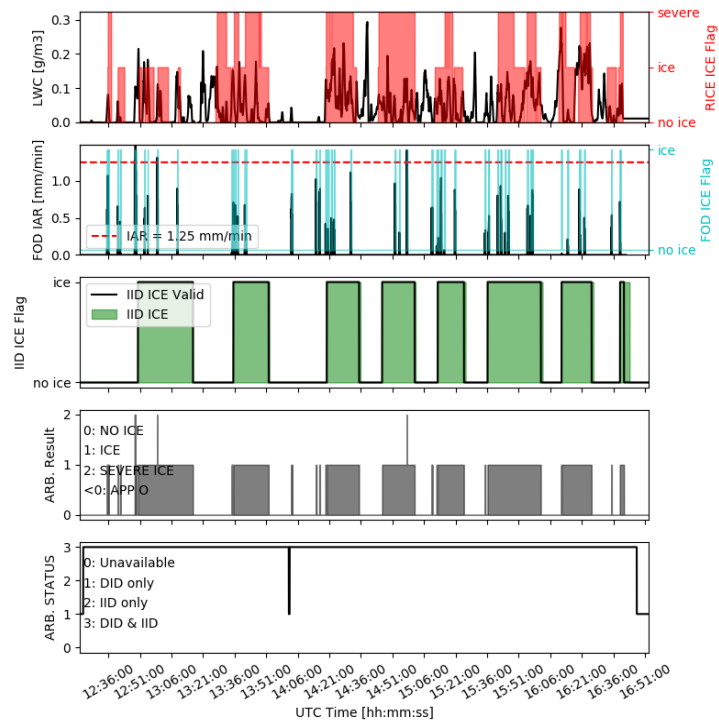


Figure 91: Flight as230018 Results of HIDS arbitration for the couple FOD/IIID. From the top to the bottom: LWC curve and RICE ice flag; FOD IAR measurements and ice flags; IID ice flags; HIDS Arbitration results; HIDS Arbitration status.



## Flight as230021

This flight lasted more than 3 hours and offered several icing encounters, especially in App. C conditions. As for flight a230018, the presence of ice crystals was observed. In Figure 92 are reported the time histories of both A/C and  $\mu P$  data, together with reference ice detection flags (both RICE probe and  $\mu P$ ) and main outputs of IID. This time, the legacy ice detector and the  $\mu P$  flags are less in agreement: some encounters characterised by lower LWC and TAT close to 0°C was not detected by RICE. As well as, when the  $\mu P$  ice flag dropped because the LWC was below the detection threshold (i.e. 0.025 g/m<sup>3</sup>, see ref. [7]), the RICE probe continued to warn for an ice accretion, such as during the time interval [14:42:00 – 14:52:00] UTC.

In Table 15 the summary of IPS activation, reference ice detections and indirect ice detection outputs. As explained in §2.4, the IID was not able to detect the first icing encounter, between [13:43:00 -13:58:00], by using the 10%  $\Delta C_D$  threshold since it was characterized by a very low performance degradation.

Figure 93 shows that all DIDSS were able to detect all the icing encounters. Again, a good correlation between AMPERA and  $\mu P$  flags is observed.

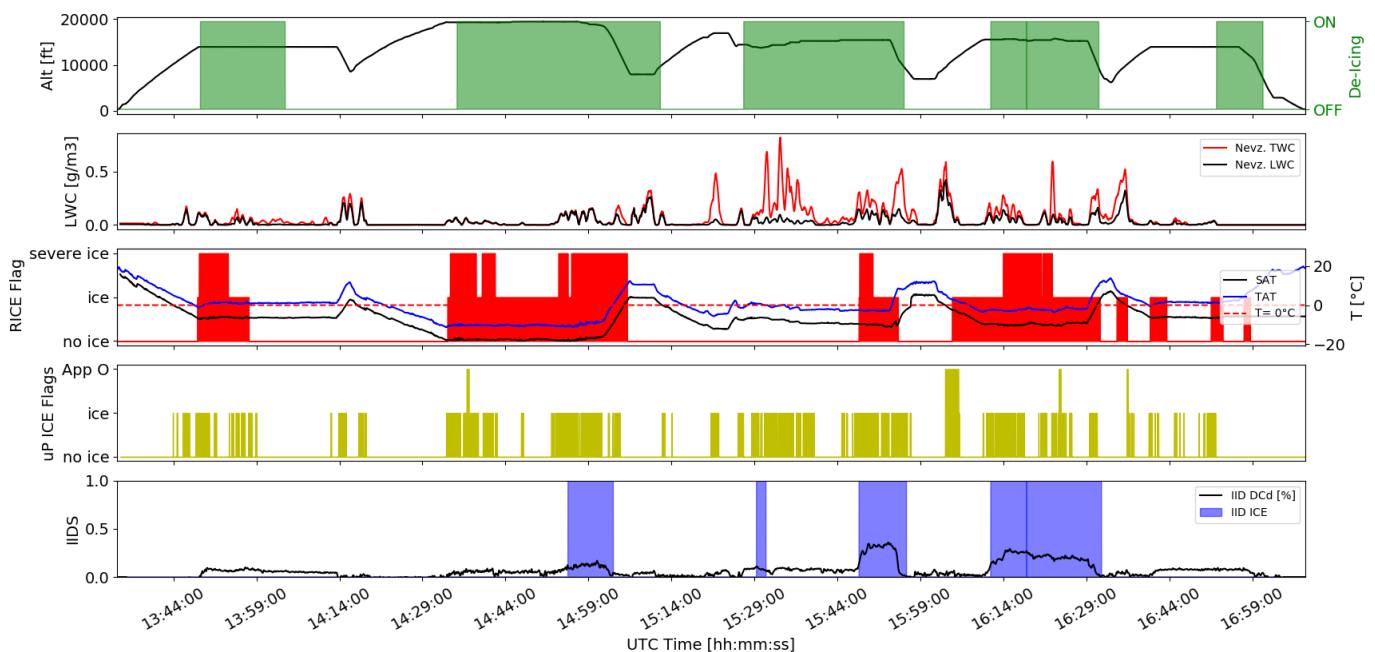


Figure 92: Flight as230021 A/C data,  $\mu P$  data, reference icing flags and IID outputs. From the top to the bottom: A/C altitude time history and IPS activation; Nevzorov measurements of LWC and TWC; Temperature time history (both SAT and TAT) and RICE probe ice flags;  $\mu P$  ice flags; IID relative drag increase and ice flags.

IPS activation	5
RICE ice detection	8
RICE severe ice	4
$\mu P$ ice detection	317
$\mu P$ App O detection	5
IID ice detection	4

Table 15: Summary of the number of IPS activation, reference ice flags and indirect ice detection for the flight as230021.

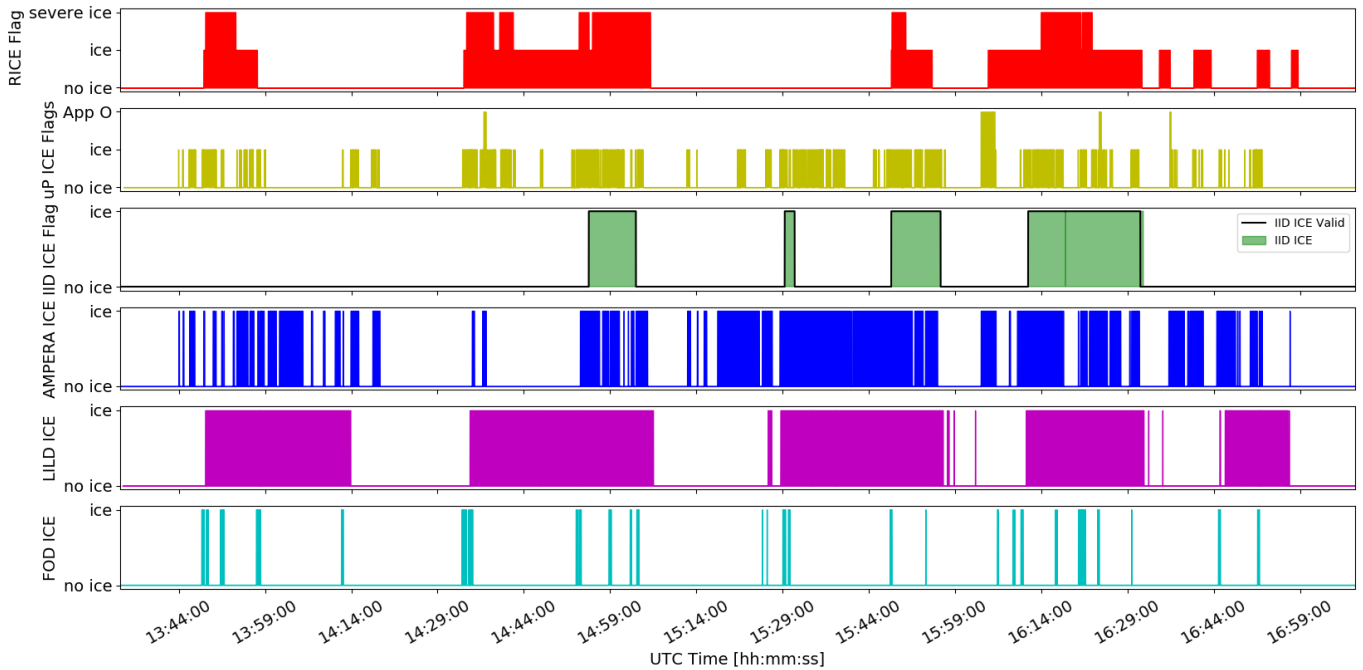


Figure 93: Flight as230021 Ice Detection signal of DIDS and IID for icing encounters. From the top to the bottom: RICE,  $\mu P$ , IID, AMPERA, LILD, FOD.

For this flight, our analysis is focused on two time intervals:

1. IC1: [14:52:00 – 15:01:00] UTC time
2. IC2: [15:46:00 – 15:57:00] UTC time

As illustrated in Figure 94, the RICE probe was already detecting an ice accretion, such as LILD. Maybe these two detectors were not completely de-iced after the previous encounter. For this reason, the DIDS response times are evaluated w.r.t. the  $\mu P$  flag. Table 16 shows that the detectors did not meet the ED103 requirement. IID as well raised an ice flag 3 minutes later  $\mu P$ . As explained in §2.4, the relative drag increase exceeds the 10% threshold, very slowly.

ED103 Resp. time [s]	ED103 IAR [mm/min]	$\mu P$ ICE FLAG [h:min:s]	RICE ICE FLAG [h:min:s]	IID Resp. Time w.r.t. $\mu P$ [s]	AMPERA Resp. Time w.r.t. $\mu P$ [s]	LILD Resp. Time w.r.t. R $\mu P$ [s]	FOD Resp. time w.r.t. $\mu P$ [s]
37	0.49	14:52:16	NA	182	90	NA	50

Table 16: IID and DIDSs response time for the icing encounter during the time interval [14:52:00 – 15:01:00] UTC of flight as230021.

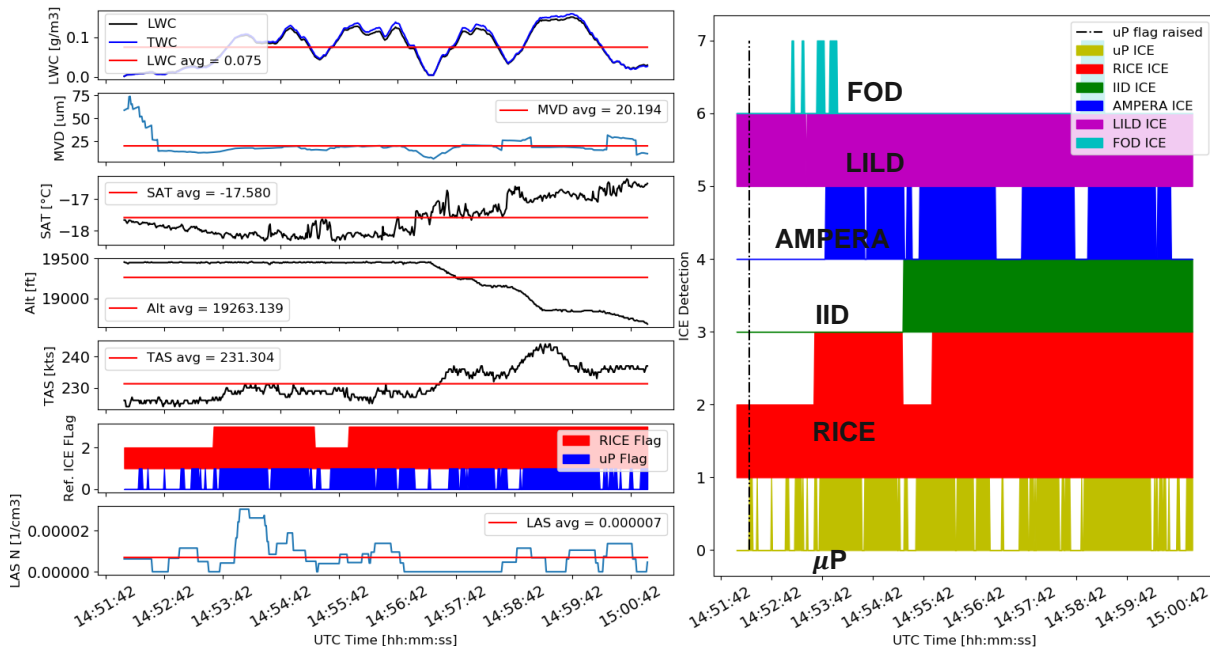


Figure 94: Flight as230021 time interval [14:52 – 15:01] UTC IC1 On the right,  $\mu P$ , A/C data and reference ice flags. On the left: DIDSs, IID and reference ice flags.

In Table 17 the response times of DIDSs and IID are reported for IC2. This time, both AMPERA and LILD were already detecting the presence of an ice condition, while both FOD and IID raised an ice flag in agreement with the legacy detector. With respect to IC1, IID detected a faster and higher relative drag increase.

ED103 Resp. time [s]	ED103 IAR [mm/min]	$\mu P$ ICE FLAG [h:min:s]	RICE ICE FLAG [h:min:s]	IID Resp. Time w.r.t. RICE [s]	AMPERA Resp. Time w.r.t. RICE [s]	LILD Resp. Time w.r.t. RICE [s]	FOD Resp. time w.r.t. RICE [s]
34.45	0.52	15:46:41	15:47:50	4	NA	NA	-8

Table 17: IID and DIDSs response time for the icing encounter during the time interval [15:46:00 – 15:57:00] UTC of flight as230021.

The results of HIDS arbitration for each DIDS/IID couple are reported in Figure 96, Figure 97 and Figure 98. It is important to highlight that, thanks to the coupling between direct and indirect detection, all the icing encounters were properly detected. Moreover, the DIDSs developed within the SENS4ICE project turned out to be more sensitive than the legacy detector.

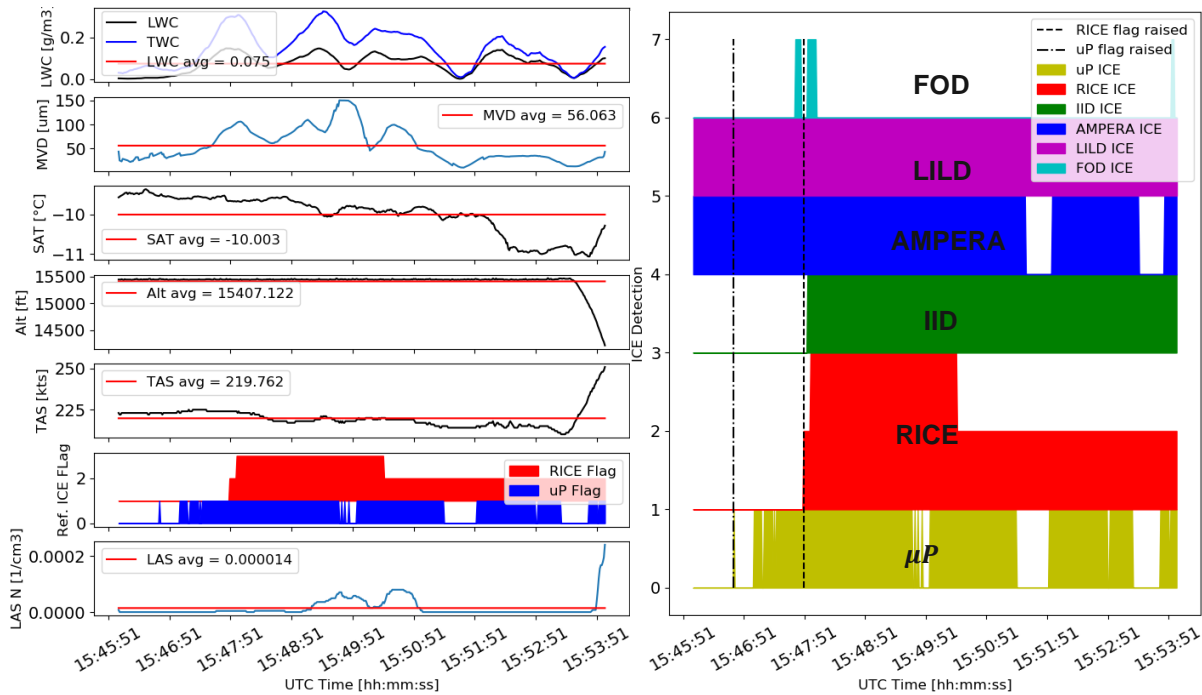


Figure 95: Flight as230021 time interval [15:46 – 15:54] UTC IC2 On the right,  $\mu P$ , A/C data and reference ice flags. On the left: DIDSs, IID and reference ice flags.

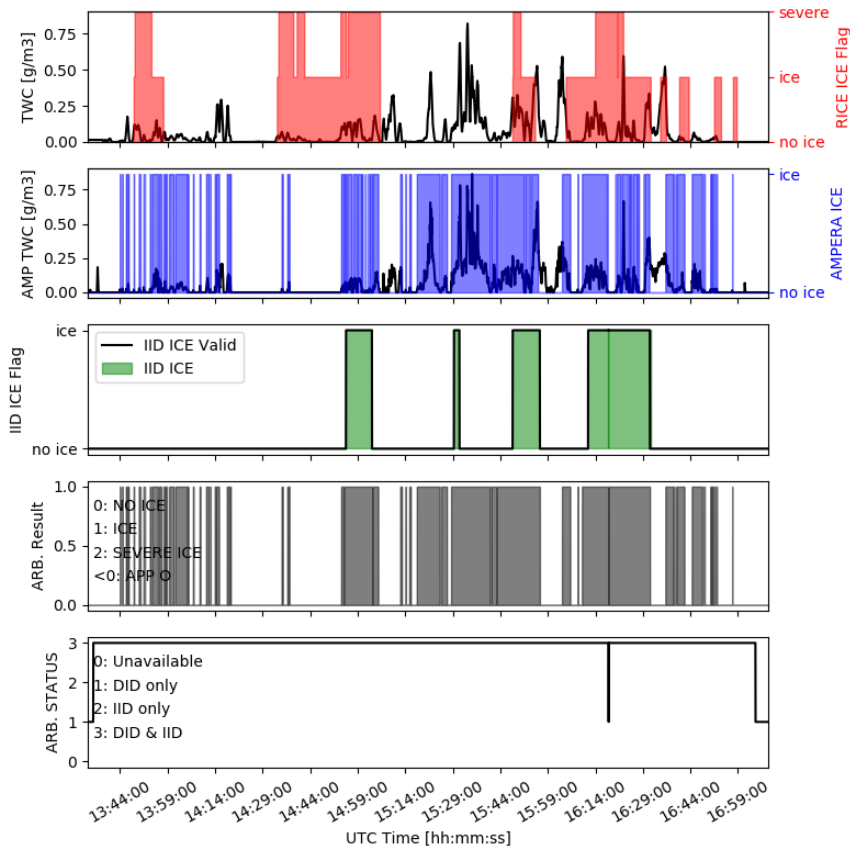


Figure 96: Flight as230021 Results of HIDS arbitration for the couple AMPERA/IID. From the top to the bottom: TWC curve and RICE ice flag; AMPERA TWC measurements and ice flags; IID ice flags; HIDS Arbitration results; HIDS Arbitration status.

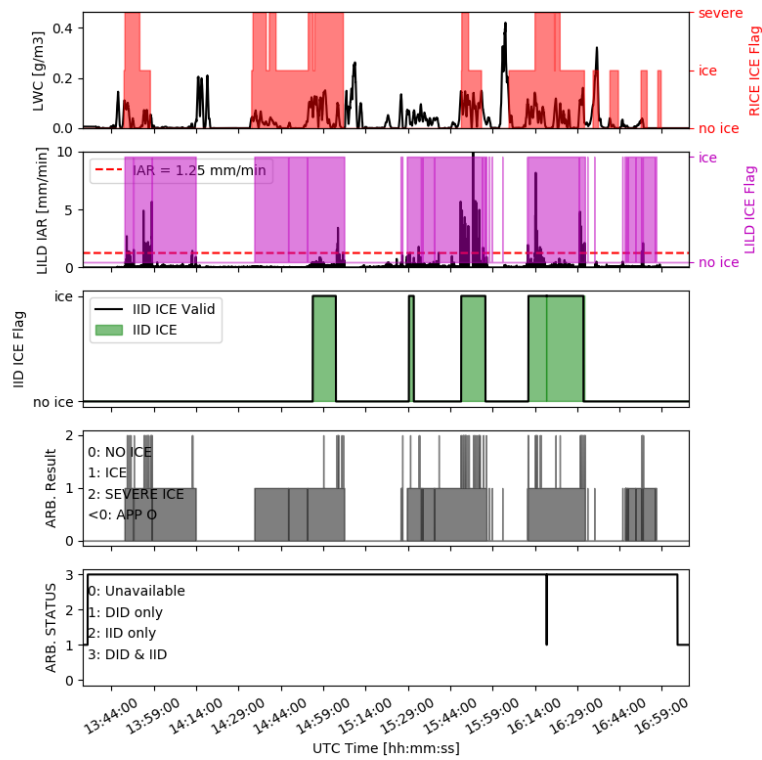


Figure 97: Flight as230021 Results of HIDS arbitration for the couple LILD/IIID. From the top to the bottom: LWC curve and RICE ice flag; LILD IAR measurements and ice flags; IID ice flags; HIDS Arbitration results; HIDS Arbitration status.

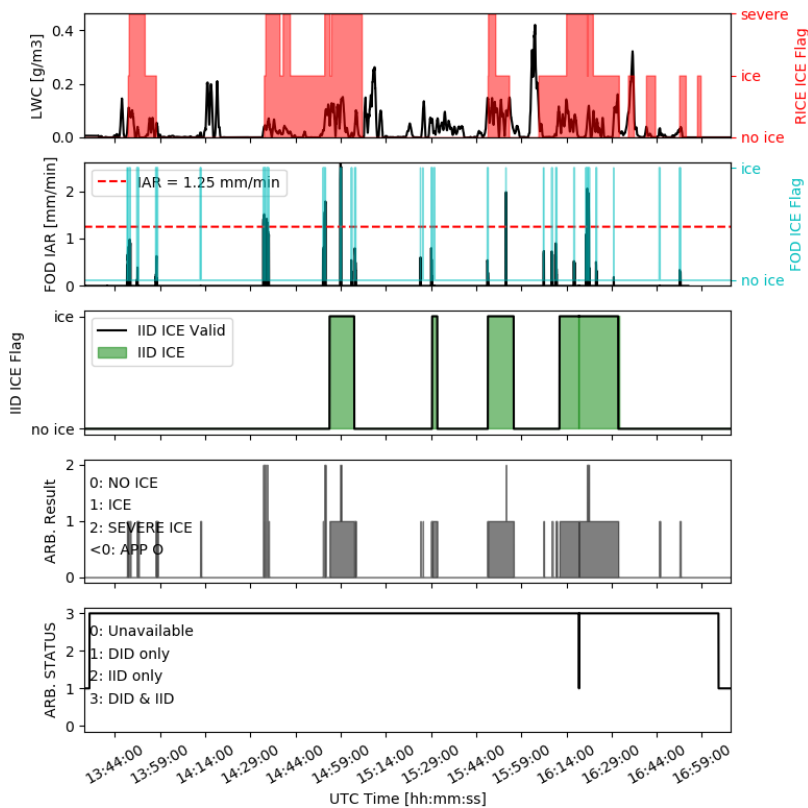


Figure 98: Flight as230021 Results of HIDS arbitration for the couple FOD/IIID. From the top to the bottom: LWC curve and RICE ice flag; FOD IAR measurements and ice flags; IID ice flags; HIDS Arbitration results; HIDS Arbitration status.



## Flight as230022

This flight lasted more than 3 hours, and was characterized by many icing encounters, mainly App. C conditions, as illustrated by RICE and  $\mu P$  detection reported in Figure 99. During this flight, ice crystals were observed as well.

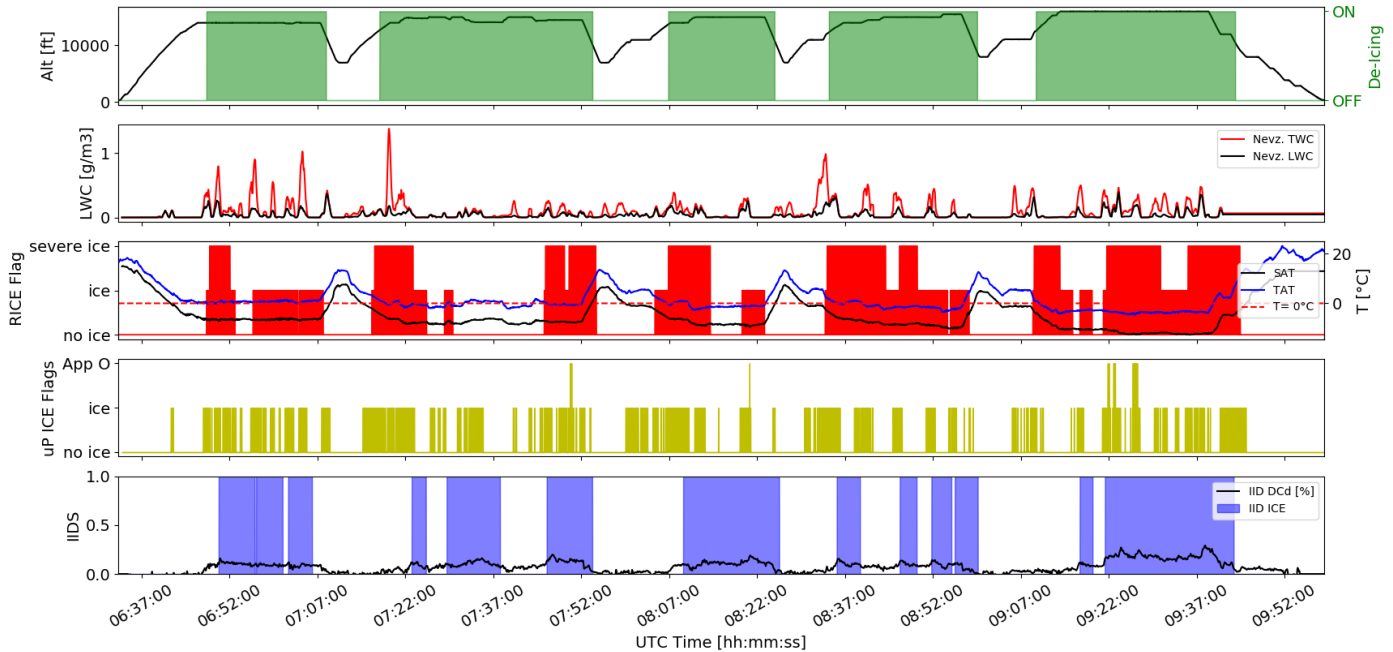


Figure 99: Flight as230022 A/C data,  $\mu P$  data, reference icing flags and IID outputs. From the top to the bottom: A/C altitude time history and IPS activation; Nevzorov measurements of LWC and TWC; Temperature time history (both SAT and TAT) and RICE probe ice flags;  $\mu P$  ice flags; IID relative drag increase and ice flags.

The summary of IPS activations and reference and IID icing flags are reported in Table 18. Figure 100 shows that DIDSs were able to detect all the icing encounters.

For this flight, the following icing encounters are analysed in details:

1. IC1: [07:14:00 – 07:23:00] UTC time
2. IC2: [09:20:00 – 09:39:00] UTC time

As shown in Table 19 and in Figure 101, all the detectors, but AMPERA, detected the IC1 with some delay. In particular, IID raised an ice flag almost 7 minutes later than the RICE probe, which considered this encounter as a severe icing condition. Note that for about one minute during IC1 (starting around 07:19 UTC) the concentration of large aspherical particles (LAS N) is exceeding the limit for reliable MVD reference measurements, so these particular reference results for this short period may be questionable and would need further analysis.

IPS activation	5
RICE ice detection	13
RICE severe ice	7
$\mu P$ ice detection	269
$\mu P$ App O detection	5
IID ice detection	13

Table 18: Summary of the number of IPS activation, reference ice flags and indirect ice detection for the flight as230022.

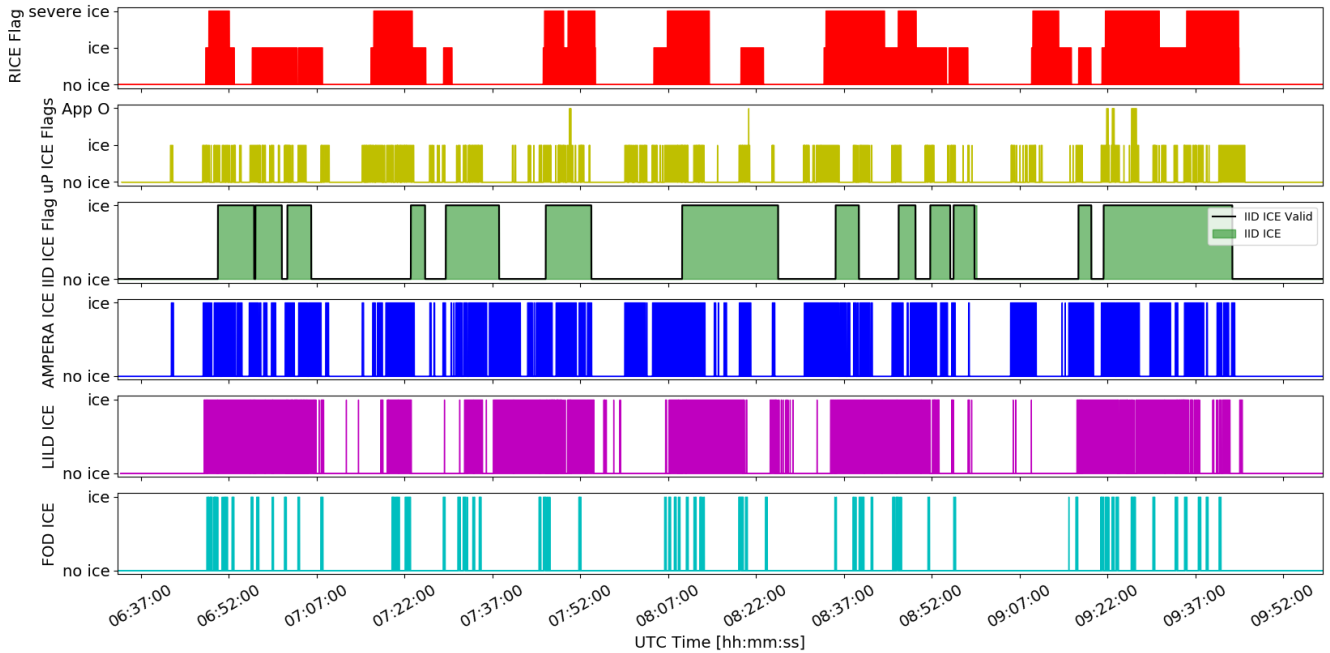


Figure 100: Flight as230022 Ice Detection signal of DIDSs and IID for icing encounters. From the top to the bottom: RICE,  $\mu P$ , IID, AMPERA, LILD, FOD.

ED103 Resp. time [s]	ED103 IAR [mm/min]	$\mu P$ ICE FLAG [h:min:s]	RICE ICE FLAG [h:min:s]	IID Resp. Time w.r.t. RICE [s]	AMPERA Resp. Time w.r.t. RICE [s]	LILD Resp. Time w.r.t. RICE [s]	FOD Resp. time w.r.t. RICE [s]
39.75	0.45	07:14:42	07:16:17	408	-94	96	211

Table 19: IID and DIDSs response time for the icing encounter during the time interval [07:14:00 – 07:23:00] UTC of flight as230022.

Different is the behaviour of DIDSs and IID during IC2, the last icing encounter of flight as230022. Even if the characteristics of this encounter are close to IC1 (i.e. same LWC and theoretical IAR) all the detectors met the ED103 response time requirement, as demonstrated by Figure 101 and Figure 102.

Since this encounter is very close to the previous one, and the A/C did not realise a full de-icing by flying through a warmer air layer, LILD was not de-iced and was already detecting ice presence on its sensitive surface. Both AMPERA and FOD detected earlier than the RICE probe.

ED103 Resp. time [s]	ED103 IAR [mm/min]	$\mu P$ ICE FLAG [h:min:s]	RICE ICE FLAG [h:min:s]	IID Resp. Time w.r.t. RICE [s]	AMPERA Resp. Time w.r.t. RICE [s]	LILD Resp. Time w.r.t. RICE [s]	FOD Resp. time w.r.t. RICE [s]
33.57	0.54	09:20:52	09:21:05	16	-11	NA	-17

Table 20: IID and DIDSs response time for the icing encounter during the time interval [09:20:00 – 09:39:00] UTC of flight as230022.

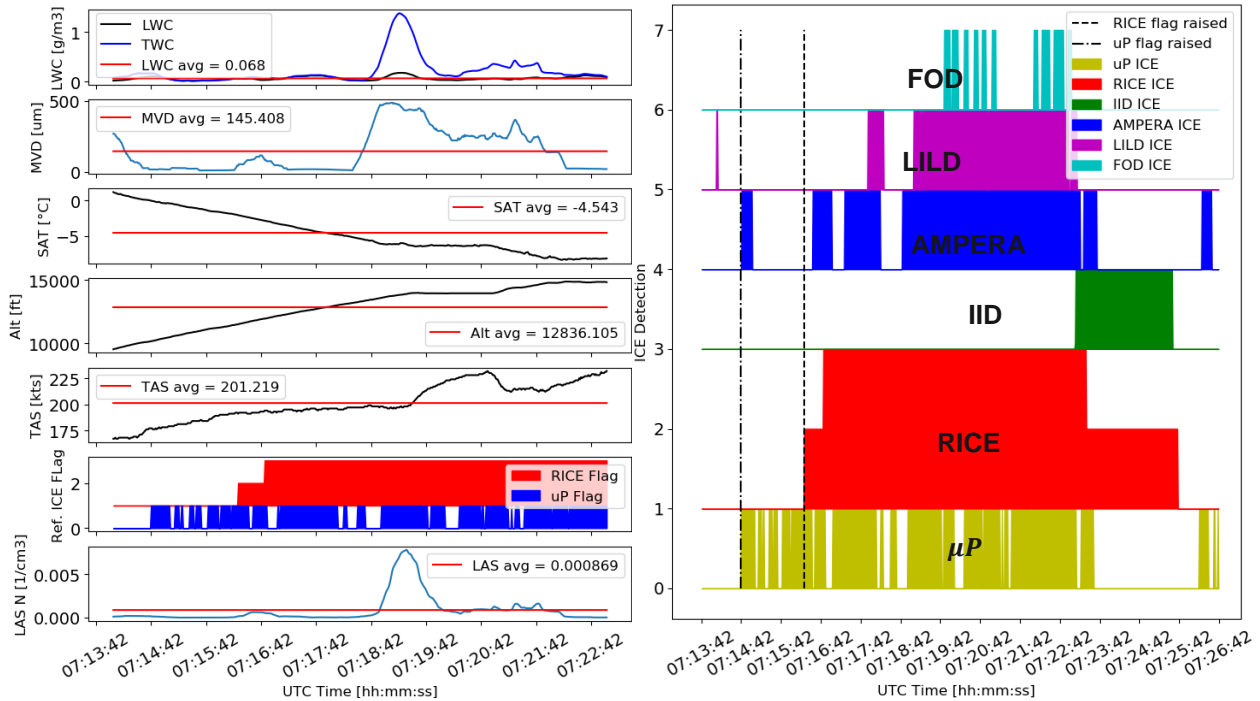


Figure 101: Flight as230022 IC1 On the right,  $\mu P$ , A/C data and reference ice flags during the time interval [07:14 – 07:23] UTC. On the left: DIDSS, IID and reference ice flags during the time interval [07:14 – 07:27] UTC.

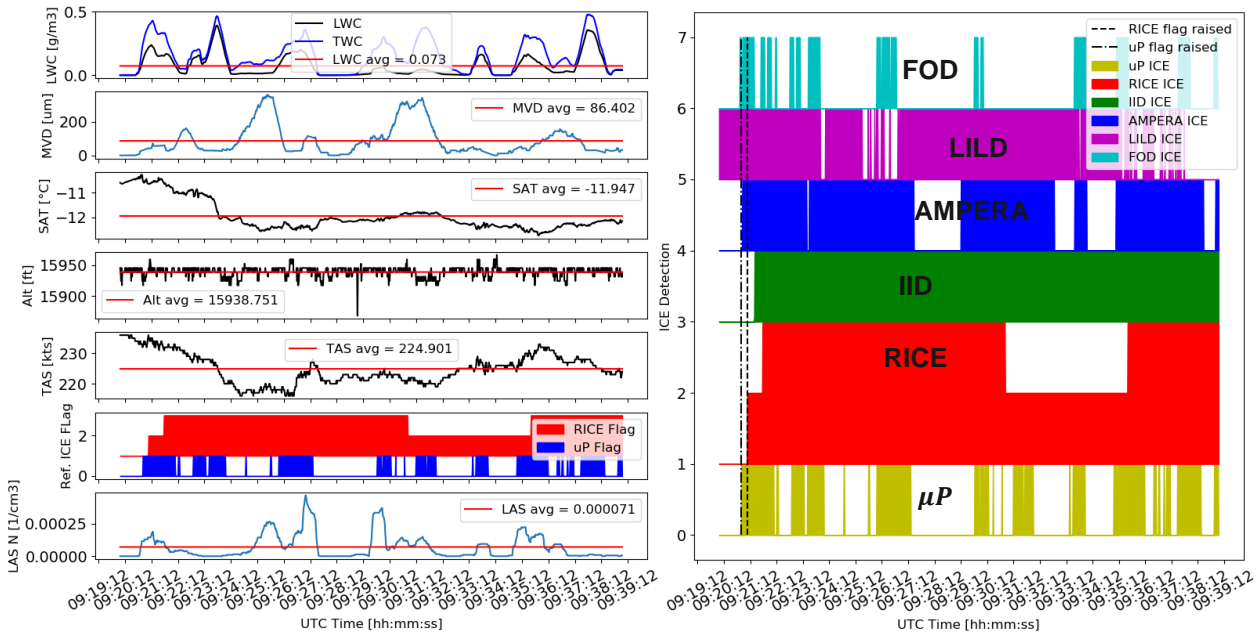


Figure 102 Flight as230022 time interval [09:20 – 09:39] UTC IC2 On the right,  $\mu P$ , A/C data and reference ice flags. On the left: DIDSS, IID and reference ice flags.

The results of the HIDS Arbitration function for each DIDS/IID couple are reported in Figure 103, Figure 104 and Figure 105.





Even for this flight, AMPERA TWC measurements are in good agreement with the  $\mu P$  ones, while both LILD and FOD overestimated the IAR. Nevertheless, the coupling between direct and indirect detection guarantees the detection of all the encountered ICs.

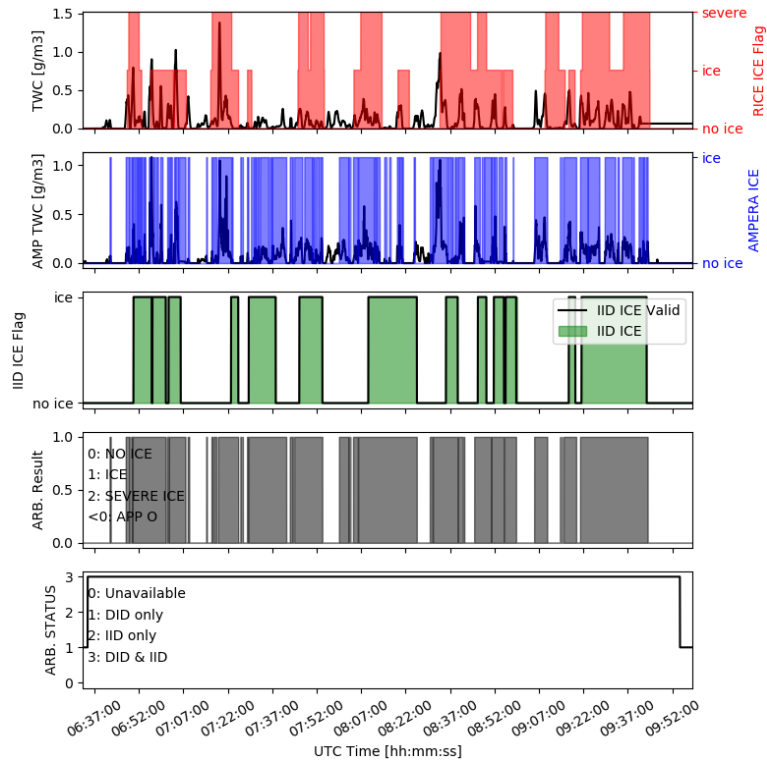


Figure 103: Flight as230022 Results of HIDS arbitration for the couple AMPERA/IID. From the top to the bottom: TWC curve and RICE ice flag; AMPERA TWC measurements and ice flags; IID ice flags; HIDS Arbitration results; HIDS Arbitration status.

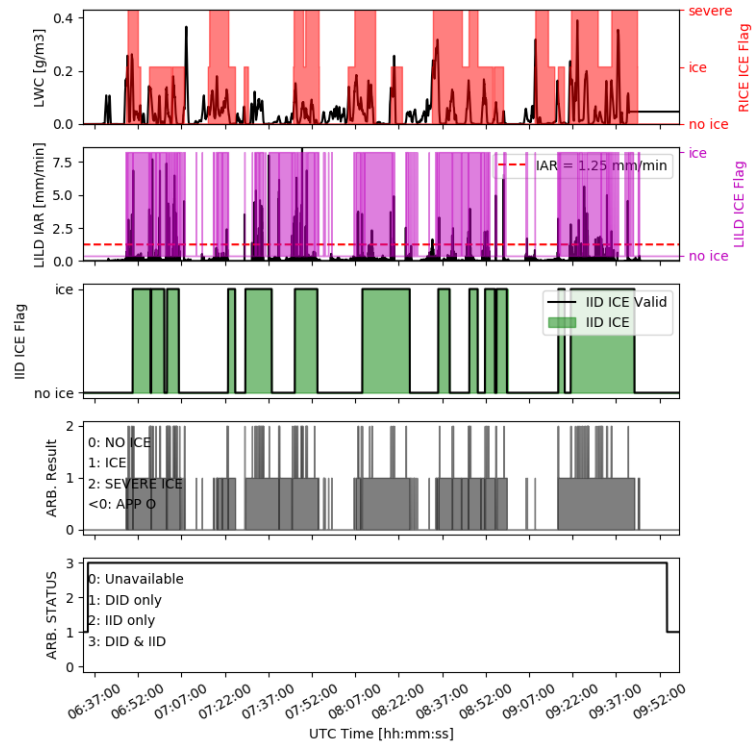


Figure 104: Flight as230022 Results of HIDS arbitration for the couple LILD/IID. From the top to the bottom: LWC curve and RICE ice flag; LILD IAR measurements and ice flags; IID ice flags; HIDS Arbitration results; HIDS Arbitration status.

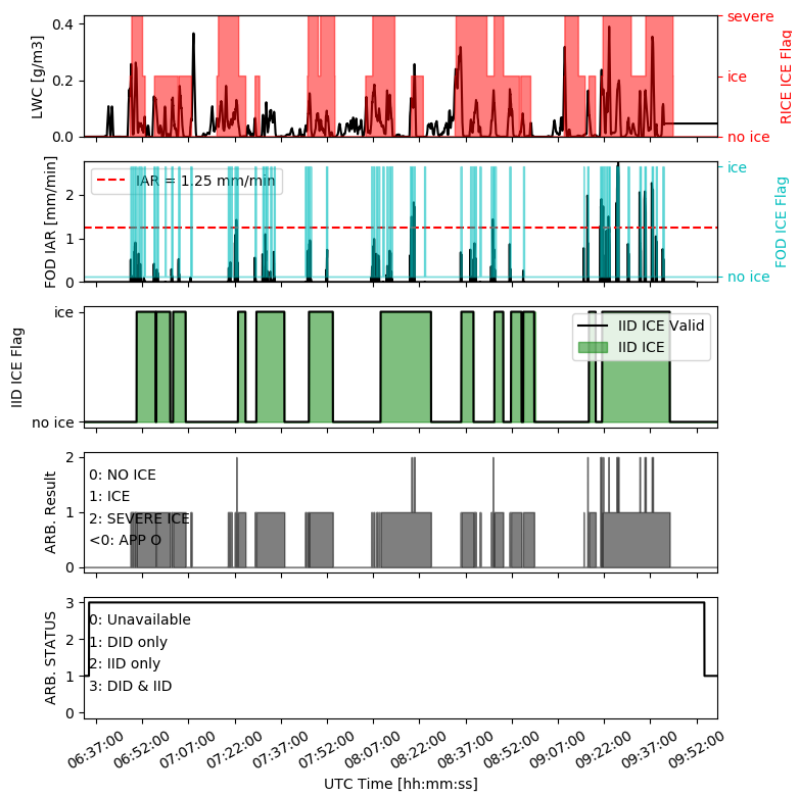


Figure 105: Flight as230022 Results of HIDS arbitration for the couple FOD/IID. From the top to the bottom: LWC curve and RICE ice flag; FOD IAR measurements and ice flags; IID ice flags; HIDS Arbitration results; HIDS Arbitration status.



### 3.4 Ways forward for HIDS

The results of the two SENS4ICE flight campaigns are very promising: HIDS, indeed, appears to be a more robust and reliable ice detection system than the legacy one.

Association of a direct sensors with the IID makes the HIDS the only system that can perform both an early ice detection, and a continuous monitoring of remaining ice, after leaving the icing clouds.

These characteristics could make the HIDS a possible Primary Ice Detection System. As illustrated in Figure 106, HIDS could offer both the control and the monitoring of A/C IPS: when DIDS detects an icing encounter the IPS shall be switched on, then, IID continuously monitors the IPS efficiency. If a performance degradation is detected after the exit from the icing clouds, some residual ice is still present on the airframe. This could be due to an inefficiency of IPS or to ice accretion on unprotected surfaces, for example due to SLD or runback ice. The pilot is then aware of the real performance of the aircraft, and can apply corrective actions if needed.

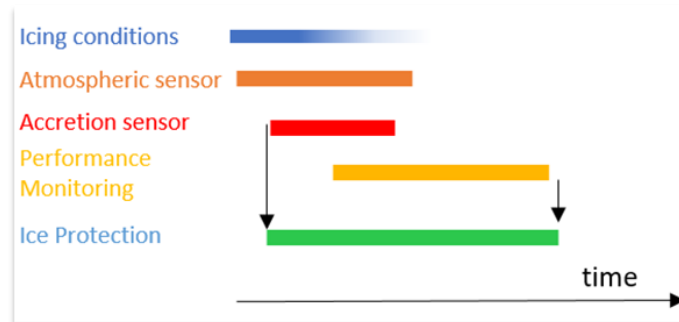


Figure 106: Schematic activation and monitoring of IPS provided by HIDS.

Moreover, direct detection may be limited because it measures only very local characteristics of the flow or accretion, therefore global drag increase effects measured by IID can reduce false alarms and consolidate the early detection, and can be used to alert the pilot only when the A/C performance is reduced by the encounter condition. In order to properly consolidate the hybrid output, as explained in §3.1, the delay applied to the DIDS ice signal to wait for the indirect ice detection confirmation shall be adjusted. This can only be done once the A/C, the IID and the Direct Ice detector performances are known.

In this way, the IPS activation can be strongly optimized. Indeed, HIDS could enable significant reduction in fuel consumption thanks to a more efficient use of IPS, associated to the monitoring of remaining ice.

This requires to determine the IID detection thresholds: after the confirmed detection of the performance degradation, safety margins for envelope protection become relevant. These are subject to the individual aircraft and must be defined accordingly. With a feedback of this information to the flight management system, the further flight operation can be planned and optimized, in order to maintain the original flight plan if possible. The performance degradation, and the respectively drag increase further, mainly indicated the presence of ice but does not directly allow a correlation to the ice formation itself. As the certification is mainly related to an admissible ice formation for certified icing operations, the information about a performance degradation must be transferred to a potentially admissible impact on flight performance for icing operations.

Probably, such an innovation in the ice protection domain will require a new certification approach, to be developed in collaboration with the certification authorities and aircraft manufacturers.



## 4. Conclusions

The SENS4ICE project was mainly focused on the development of a hybrid ice detection approach combining the advantages of dissimilar technologies in order to mitigate their shortages and to provide a more comprehensive understanding of icing condition and the aircraft behaviour.

During the flight test campaigns in natural icing conditions with two different aircraft types, enough data about the performance of the individual direct detectors as well as the indirect ice detection was gathered in order to make a first assessment of the hybrid approach and make some relevant conclusions.

The main conclusions about the HIDS (hybrid ice detection system) can be summarized as follows:

- The coupling of each direct ice detector with the indirect ice detection algorithm, through the HIDS Arbitration function, gives extensive information on the aircraft status during an icing encounter, since it provides details on the icing conditions, ice accretion and remaining aircraft capabilities.
- Direct and indirect ice detection are not directly comparable but complementary technologies: direct ice detection technologies allow detecting icing conditions or local ice accretion fast and reliably, whereas the indirect ice detection methodology uses the aircraft as a sensor and gives an information about the performance degradation after ice formation.
- Preliminary analyses of flight test data show that the direct detection technologies tested are very promising and demonstrate a good agreement with ED103B standards, in particular regarding response time.
- The indirect ice detection was able to announce the performance degradation during all icing encounters of the SENS4ICE flight test campaigns. Although the algorithm is only reactive to conditions where the flight performance is already degraded due to ice accretion on the aircraft surfaces, it provides a high potential for applications where no direct sensing technology could be applied or is too complex or expensive, like smaller aircraft of the general aviation, unmanned aerial vehicles or new advanced air mobility vehicles. It further allows a reliable operational envelope monitoring for envelope protection and flight performance calculations, (e.g., endurance and range) if the reserves are limited.
- During flight testing, the indirect ice detection algorithm and the hybrid detection approach have shown their advantages for application on new and existing aircraft.
- Certification is mainly related to demonstration of safe operations in the icing environment or successful sense-and-exit operations. SENS4ICE flight test results have shown that especially for SLD conditions, the sensing with direct detection technologies is still a challenging task. Thanks to the ice detection approach developed within SENS4ICE, which allows more comprehensive information on the encountered icing situation and the aircraft capabilities, aircraft operations throughout the wide App. O envelope might be possible. Nevertheless, the hybrid ice detection approach is currently not reflected by the certification rules and this would require an agreement on acceptable mean of compliance.

With the SENS4ICE project, via the development of HIDS and the analysis of flight campaign results, a big step to a more comprehensive view on the aircraft icing has been made.

Actually, thanks to the flight campaigns, the hybrid detection approach has been validated in a relevant environment and, hence, it can be considered as TRL5, according to the Horizon 2020 TRL definitions.

Nevertheless, additional research for further maturation is still required as the technologies are currently only tested for a relatively small part of the App. O envelope leaving a wide part of the envelope not considered yet. Additional flight test to also understand the actual SLD appearance during flight and the specific impact on the aircraft flight characteristics will be required to make a more complete assessment of the technologies and allow a better definition of required acceptable means of compliance for a potential system certification.

On a system level, implementation of the Hybrid detection function might be very dependent on the platform. Availability, frequency, reliability of all required data, may have a strong impact on the performance and reliability of the results. Furthermore, the selection of direct sensors used during SENS4ICE in the HIDS could be changed to further enhance and optimise the system. Hence, definition, test and validation of the HIDS implementation is a significant task that is peculiar to each aircraft.





## DISCLAIMER

The Phenom 300 flight test data analyzed is based on an experimental prototype. This aircraft prototype has embedded additional flight test instrumentation and features that do not represent any certified Phenom 300 aircraft model. Therefore, the analysis and performance estimations assessed in this study and within the SENS4ICE project do not represent the Phenom 300's certified performance.

Airborne data was obtained using the aircraft managed by Safire, the French facility for airborne research, an infrastructure of the French National Center for Scientific Research (CNRS), Météo-France and the French National Center for Space Studies (CNES). Distributed data are processed by SAFIRE.

## 5. References

- [1] Jurkat et al. "Overview of Cloud Microphysical Measurements during the SENS4ICE Airborne Test Campaigns: Contrasting Icing Frequencies from Climatological Data to First Results from Airborne Observations". SAE Technical Paper 2023-01-1491, 2023, doi:10.4271/2023-01-1491.
- [2] Schwarz C. "SENS4ICE EU Project Preliminary Results". SAE Technical Paper 2023-01-1496, 2023, doi:10.4271/2023-01-1496.
- [3] "HIDS demonstrator description document". SENS4ICE deliverable D2.6, December 2022
- [4] EUROCAE ED-103B. *Operational Performance Standard for InFlight Icing Detection Systems*. April 2022.
- [5] "Sensor evaluation results and final roadmaps for future technology development and exploitation". SENS4ICE deliverable D4.1, 2023.
- [6] Orazzo A. & Thillays B. "Hybrid Ice Detection System: development and validation". SAE International Conference on Icing of Aircraft, Engines, and Structures 2023, Vienna, Austria, June 20–22, 2023, 23ICE-0049.
- [7] "Final report on airborne demonstration and atmospheric characterization". SENS4ICE deliverable D4.3, 2023
- [8] B.L. Messinger. "Equilibrium Temperature of an Unheated Icing Surface as a Function of Air Speed". Journal of the Aeronautical Sciences (Institute of the Aeronautical Sciences), January 1953, doi:10.2514/8.2520.
- [9] Christoph Deiler and Falk Sachs. "Design and testing of an indirect ice detection methodology." Vienna, Austria, June 20th - 22nd 2023. SAE International Conference on Icing of Aircraft, Engines, and Structures, SAE International, Paper 2023-01-1493.
- [10] Christoph Deiler and Nicolas Fezans. "Performance-based ice detection methodology." Journal of Aircraft, 57(2):209–223, March 2020. DOI:10.2514/1.C034828.
- [11] Anon. Ice accretion simulation. AGARD Advisory Report 344, Advisory Group for Aerospace Research & Development (AGARD) - Fluid Dynamics Panel Working Group 20, North Atlantic Treaty Organization (NATO), Neuilly-Sur-Seine, France, December 1997.
- [12] Christoph Deiler. "Evaluation of aircraft performance variation during daily flight operations." Friedrichshafen, Germany, Sept. 2018. Deutscher Luft- und Raumfahrtkongress, Deutsche Gesellschaft für Luft- und Raumfahrt (DGLR). DOI:10.25967/480025.
- [13] Christoph Deiler, "A smart data approach to determine an aircraft performance model from an operational flight data base". National Harbor, Maryland, USA, January 2023. AIAA Scitech Forum, American Institute of Aeronautics and Astronautics, Inc. (AIAA). DOI:10.2514/6.2023-0797

